Fall 1-31-2007

Hydrodynamics investigation of in-vitro dissolution testing

Ge Bai
New Jersey Institute of Technology

ABSTRACT

HYDRODYNAMICS INVESTIGATION OF IN-VITRO DISSOLUTION TESTING

by
Ge Bai

Dissolution testing is routinely carried out in the pharmaceutical industry to determine dissolution rate of solid dosage forms. The United States Pharmacopoeia (USP) Dissolution Apparatus II is the device most commonly used for this purpose. Despite its widespread use, dissolution testing remains susceptible to significant error and test failures. Limited information is available on the hydrodynamics of this apparatus, although hydrodynamic effects can play a major role on test performance.

Laser-Doppler Velocimetry (LDV) and Computational Fluid Dynamics (CFD) were used here to experimentally map and computationally predict the velocity distribution inside a standard USP Apparatus II under the typical operating conditions mandated by the dissolution test procedure. The flow in the apparatus is strongly dominated by the tangential component of the velocity, but a low recirculation zone exists in the lower part of the hemispherical vessel bottom where the tablet dissolution process takes place. The velocities in this region change significantly over short distances along the vessel bottom, implying that small variations in the location of the tablet on the vessel bottom caused by the randomness of the tablet descent through the liquid result in significantly different velocities and velocity gradients near the tablet.

CFD was also used to study the hydrodynamics when the impeller was placed at four different locations, all within the limits specified by USP. Small changes in impeller

location, especially off-center, produced extensive changes in the velocity profiles and shear rates. The blend time to homogenize the liquid content was also obtained for a number of operating conditions using different experimental methods, a CFD-based computational approach, and a semi-theoretical model. Excellent agreement between data and predictions was obtained. The CFD results show that blend time is inversely proportional to the agitation speed, and that blend time is some two orders of magnitude smaller than the time typically required for appreciable tablet dissolution during the typical dissolution test, implying that the contents of this device can be considered to be well mixed during the typical test.

Finally, dissolution tests with prednisone and salicylic acid tablets were conducted, in which the tablets were placed at different locations in the dissolution vessel in order to study the effect of local hydrodynamics on dissolution. The results show that tablet location has a major effect, and that statistically significant differences exist in the dissolution profiles between centrally located tablets and tablets positioned off-center, at it is often the case during testing. The dissolution process was modeled using an approach based on the use of experimentally determined mass transfer coefficients, mass transfer coefficient equations, CFD-predicted velocity profiles, and mass balances. The results can satisfactorily predict the data.

The hydrodynamics of dissolution testing depends strongly on small differences in equipment configurations and operating conditions, which can have a profound effect on the flow field and shear rate experienced by the oral dosage form being tested, and hence the solid-liquid mass transfer and dissolution rate.

HYDRODYNAMICS INVESTIGATION OF IN-VITRO DISSOLUTION TESTING

by
Ge Bai

A Dissertation
Submitted to the Faculty of
New Jersey Institute of Technology
in Partial Fulfillment of the Requirements for the Degree of
Doctor of Philosophy in Chemical Engineering

Otto York Department of Chemical Engineering

January 2007

APPROVAL PAGE

HYDRODYNAMICS INVESTIGATION OF IN-VITRO DISSOLUTION TESTING

Ge Bai

Dr. Piero M. Armenante, Dissertation Advisor — Date
Distinguished Professor of Chemical Engineering, NJIT

Dr. Robert B. Barat, Committee Member — Date
Professor of Chemical Engineering, NJIT

Dr. Rajesh N. Dave, Committee Member — Date
Distinguished Professor of Chemical Engineering, NJIT

Dr. Russell V. Plank, Committee Member — Date
Senior Research Fellow, Merck & Co., Inc.

Dr. Laurent Simon, Committee Member — Date
Assistant Professor of Chemical Engineering, NJIT

BIOGRAPHICAL SKETCH

Author: Ge Bai

Degree: Doctor of Philosophy

Date: January 2007

Undergraduate and Graduate Education:

- Doctor of Philosophy in Chemical Engineering,
  New Jersey Institute of Technology, Newark, NJ, 2007

- Bachelor of Engineering in Chemical Engineering,
  Dalian University of Technology, Dalian, P. R. China, 1999

Major: Chemical Engineering

Presentations and Publications:

Bai, G., Armenante, P.M., Plank, R. V.,
"Velocity Distribution and Shear Rate Variability Resulting from Changes in the Impeller Location in the USP Dissolution Apparatus II," Pharmaceutical Research. Submitted.

Bai, G., Armenante, P.M., Plank, R. V.,
"Experimental and computational determination of blend time in USP dissolution testing apparatus II," Journal of Pharmaceutical Science, accepted for publication in 2007.

Bai, G., Armenante, P.M., Plank, R. V., Gentzler, M., Ford, K., Harmon P.,
"Hydrodynamic Investigation of USP Dissolution Test Apparatus II," Journal of Pharmaceutical Science, 2006, in press.

Armenante, P. M., Bai, G., Plank, R. V., Ford, K., Gentzler, M., Harmon P.,
"Quantitative Determination of the Role of Geometric and Operating Variables on the Hydrodynamics of the USP Dissolution Apparatus II," presented at *2005 AIChE Annual Meeting*, Cincinnati, OH, Oct. 30 – Nov. 4, 2005.

Bai, G., Armenante, P.M., Plank, R. V., Gentzler, M., Ford, K., Harmon, P., Gandek, T., "Effect of Operating and Geometric Factors on the Hydrodynamics of the USP Dissolution Apparatus II," presented at the MIXING XX Conference (Biennial North American Mixing Forum Conference), Parksville, British Columbia, Canada, June 26-July 1, 2005.

Akiti, O., Yeboah, A., Bai, G., Armenante, P.M., "Hydrodynamic effects on mixing and competitive reactions in laboratory reactors", Chemical Engineering Science, Volume 60, Issues 8-9, April-May, 2005, Pages 2341-2354.

Armenante, P.M., Bai, G., Plank, R., Gentzler, M., Ford,.K., Harmon, P., "Computational and Experimental Determination of the Velocity Distribution in the USP Dissolution apparatus II under Different Operating Conditions," Annual meeting of American Institute of Chemical Engineers, Austin, Texas, 2004.

Bai, G., Armenante, P.M., Akiti, O., Yeboah, A., "Mixing Effectiveness of Small-Scale Laboratory Reactors for Pharmaceutical Research," Annual meeting of American Institute of Chemical Engineers, Austin, Texas, Nov. 8, 2004.

Akiti, O., Yeboah, A., Bai, G., Armenante, P.M., "Hydrodynamic Effects on Mixing and Competitive Reactions in Laboratory Reactors," the 5^{th} International Symposium on Mixing in Industrial Process, Seville, Spain, June, 2004.

Armenante, P.M., Bai, G., Uehara-Nagamine, E., Plank, R., Gentsler, M., Ford, K., Harmon, P., "Hydrodynamic Investigation of the USP Dissolution Apparatus II via LDV and CFD," Annual meeting of American Institute of Chemical Engineers, San Francisco, California, 2003.

谨以此博士论文，献给我最亲爱的父亲、母亲

To my beloved wife for her love, support and encouragement

ACKNOWLEDGMENT

I would like to express my deepest appreciation to Dr. Piero M. Armenante, who not only served as my research supervisor, providing valuable and countless resources, insight, and intuition, but also constantly gave me support, encouragement, and reassurance. Special thanks are given to Dr. Robert B. Barat, Dr. Rajesh N. Dave, Dr. Russell Plank and Dr. Laurent Simon for actively participating in my committee and their considerations and helps.

The helps from Mr. John Hoinowsky and Mr. Yogesh Gandhi are highly appreciated.

This work was partially supported through a grant from Merck & Co., West Point, PA, whose contribution is gratefully acknowledged. The author also wish to thank Dr. Michael Gentzler, Mr. Kenneth Ford, Mr. Paul Harmon and Mr. Scott Reynolds for their contribution and support.

TABLE OF CONTENTS

TABLE OF CONTENTS
(Continued)

Chapter **Page**

TABLE OF CONTENTS
(Continued)

Chapter **Page**

TABLE OF CONTENTS
(Continued)

Chapter **Page**

LIST OF TABLES

LIST OF FIGURES

LIST OF FIGURES
(Continued)

Table **Page**

LIST OF FIGURES
(Continued)

Table **Page**

LIST OF FIGURES
(Continued)

LIST OF FIGURES
(Continued)

Table **Page**

LIST OF FIGURES
(Continued)

Table **Page**

LIST OF FIGURES
(Continued)

Table **Page**

CHAPTER 1

INTRODUCTION

1.1 Background

Solid dosage forms, such as tablets, are a convenient way of administering drugs to patients. Upon ingestion, tablets disintegrate into smaller fragments in the body compartment where absorption by the body is initiated, typically in the stomach or the upper intestine. These fragments dissolve in the digestive juices and can become absorbed by an epithelial layer such as the lining of the upper intestine. This complex *in vivo* process is routinely simulated in *in vitro* dissolution tests mandated by the Food and Drug Administration (FDA) and specified in United States Pharmacopoeia (USP).

Dissolution testing is routinely carried out in the pharmaceutical industry to determine the rate of dissolution of solid dosage forms. In addition to being routinely used by pharmaceutical companies to demonstrate adequate drug release *in vivo* (through *in vivo/in vitro* (IVIVC) correlation), *in vitro* dissolution testing is used to assist with formulation design, process development, and especially the demonstration of batch-to-batch reproducibility in production. Dissolution testing is one of the several tests that pharmaceutical companies typically conduct on oral dosage formulations (e.g., tablets) to determine compliance and to release products for distribution and sales.

Although the USP lists several different dissolution test apparatuses (USP 29-NF24, 2005), most dissolution tests are currently conducted with USP Dissolution Test Apparatuses I and II. The USP Dissolution Apparatus II is the most commonly and widely used apparatus specified by the USP, and it is the focus of the hydrodynamic study presented in this work. The dimensions, characteristics, and operating conditions

of USP Dissolution Apparatus II are detailed by the USP and all users must conform to these prescriptions when conducting dissolution tests.

The USP Dissolution Apparatus II comprises a glass vessel and an agitation system. The glass vessel is a cylindrical glass tank with a semispherical bottom, and a working volume of 900 mL (Figure 1.1). The agitation system consists of a two-blade paddle impeller mounted on a shaft centrally located in the vessel and profiled to follow the hemispherical portion of the vessel. In the industrial practice, replicate dissolution tests are typically conducted in parallel using commercially available systems containing six or more individual USP Dissolution Apparatus II units (Figure 1.2). These systems allow the agitation system (motor and impellers) to be lifted above the rack holding the vessels, as shown in this figure, in order to prepare the system for the actual test. Each vessel is filled with a prescribed amount of a fluid simulating gastric or intestinal fluids, and maintained at constant temperature of 37°C by either a water bath or a heating jacket.

The test consists of lowering the agitation system so that the paddles reach their predetermined location inside the vessels, as required by the USP, starting the agitation so that the paddles rotate at 50 RPM (in some instances 75 RPM or 100 RPM), adding a single dosage form unit, such as a tablet, to each vessel simultaneously, drawing liquid samples over time from a prescribed location within the vessel, analyzing the drug concentration in each sample, and determining the dissolution profile over time. These profiles must be within a predefined range, and cannot differ significantly from the dissolution profile that the drug manufacturer has initially submitted to the FDA when the drug was approved. Any dissolution profile that is found to be statistically different, according to a predefined criterion (Moore and Flanner, 1996), from the reference profile

established for that dosage form implies failure of the test and non-compliance of the production batch being tested. When this occurs, the batch cannot be released for commercialization and it is often disposed of. The cost of such failure is often significant given the typical high value of the product.

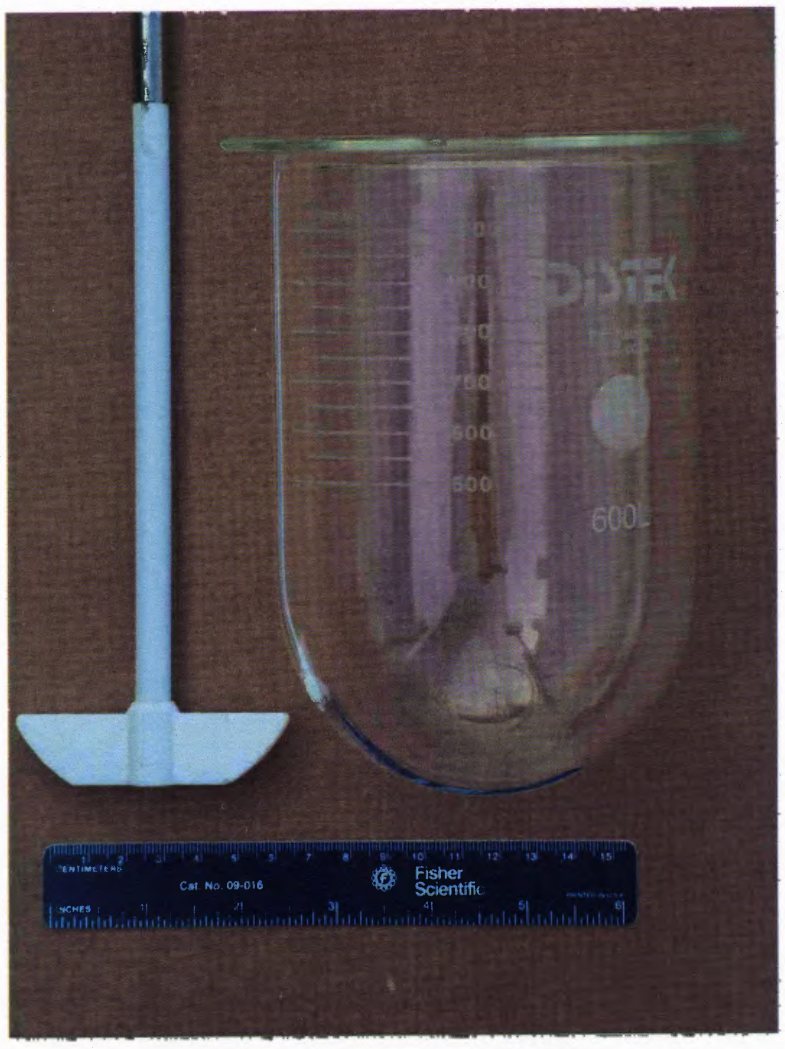

Figure 1.1 USP Dissolution Apparatus II: paddle impeller and glass vessel.

1.2 Literature Review

The USP Dissolution Apparatus II has been used in the pharmaceutical industry for decades, since this test was first officially introduced almost 30 years ago (Cohen et al. 1990). Nevertheless, and despite its widespread use in the industry, dissolution testing remains susceptible to significant error and test failures. A review of the literature shows

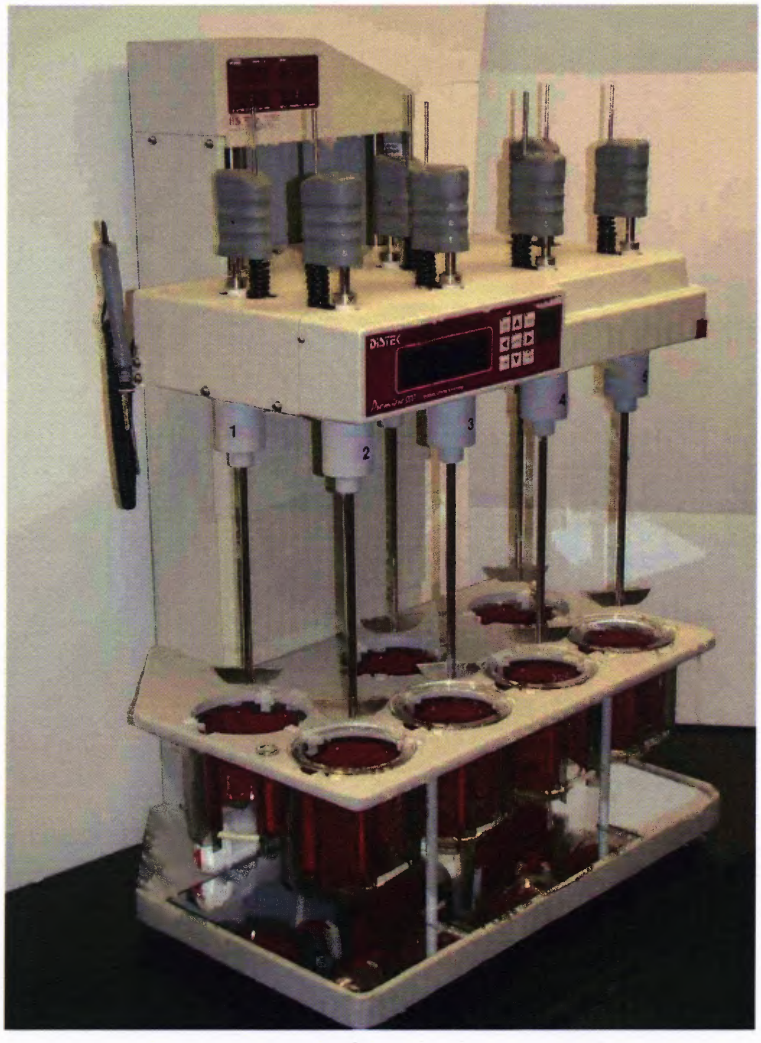

Figure 1.2 USP Dissolution Apparatus II: typical commercial dissolution testing systems containing seven Apparatus II units (Distek 5100 bathless dissolution apparatus).

that there have been numerous reports describing high variability of test results (Mauger et al. 2003, Moore et al. 1995, Qureshi and McGilveray, 1999, Qureshi and Shabnam, 2001, Costa and Lobo, 2001, Bocanegra et al. 1990, Cox and Furman, 1982, Cox et al. 1983) even when the so called "calibrator tablets" (i.e., tablets manufactured for the sole purpose of testing the proper operation of the dissolution test equipment) are used (Moore et al. 1995, Qureshi and Shabnam, 2001, Cox and Furman, 1982, Kukura et al. 2003, Baxter et al. 2005) Failures linked to dissolution testing resulted in 47 product recalls during the period 2000–2002, representing 16% of non-manufacturing recalls for oral solid dosage forms (FDC Reports, 2001, FDC Reports, 2002, FDC Reports, 2003)Irrespective of the underlying causes (such as incorrect use of the equipment or deviation of dissolution profile from the standard caused by incorrect tablet formulation) failed dissolution tests can result in product recalls, costly investigations, potential production delays, which, in turn, can have a significantly negative financial impact.

Some of the same studies have indicated that the hydrodynamics of the USP dissolution II appears to play a major role in the poor reproducibility of dissolution testing data and the inconsistency of dissolution results. This is hardly surprising considering that the USP Dissolution Apparatus II is a small, unbaffled vessel with a hemispherical bottom provided with a slowly rotating paddle, in which a tablet (or another dosage form) is dropped. This system can be expected to be associated with a complex hydrodynamics resulting in fluid velocities whose directions and intensities are highly dependent on the location within the vessel. To complicate the issue farther, tablets have often been reported to land at different locations at the bottom of the vessel

after they are dropped in the vessel at the beginning of a test, making the dissolution process even more susceptible to hydrodynamic factors.

Until recently, limited information has been available on the hydrodynamics of the dissolution apparatus and the effects of operating and geometric variables on the velocity distribution in the system. Such information is critical to advance the fundamental understanding of the dissolution rate process, enhance the reliability of dissolution testing, and eliminate artifacts associated with test methods, especially since dissolution measurements have often been reported to be inconsistent and poorly reproducible. A literature review shows that a few investigators have conducted hydrodynamic studies. Bocanegra et al. (1990)measured the flow field by Laser Doppler Anemometry, the first experimental measurement of this kind in dissolution vessels. These researchers generated data only for very limited regions of the vessel. More recently, Kukura et al. (2003) obtained experimental flow patterns using Particle Image Velocimetry (PIV) and Laser-Induced Fluorescence (LIF), and computed the velocity flow field using Computational Fluid Dynamics (CFD). However, they presented very limited quantitative comparison between the experimental data and the predictions. Other researchers also made an effort to determine the flow field inside the USP Apparatus II vessel through CFD. Kukura et al. (2004)and Baxter et al. (2005)predicted the flow pattern and shear effects with CFD. McCarthy et al. (2003, 2004) predicted the flow field with CFD and compared the CFD predictions with the limited experimental results from previous research (Bocanegra et al. 1990). Only a few researchers (Kukura et al. 2004, Baxter et al. 2005) have conducted dissolution test in which drug tablets were fixed at different locations along the bottom of the USP Dissolution Apparatus II.

One key issue that has not been addressed in previous studies is how homogeneous the content of the USP Apparatus II vessel is at any given time. This question is especially relevant if one considers that, according to the USP, liquid phase samples to determine the dissolved drug concentration as a function of time can be withdrawn anywhere "from a zone midway between the surface if the Dissolution Medium and the top of the rotating basket or blade, not less than 1 cm from the vessel wall" (USP, 2005). Unless the drug concentration in this relatively large region is uniform at any give time, one could expect that the choice of the exact location of the sampling point could introduce additional variability in the test results.

In order to answer this question, one can look the dissolution apparatus as a liquid mixing/blending device, and examine what occurs during the test. After a tablet is added to the vessel, the tablet or the fragments that it may form begin to release material, which becomes dissolved in the liquid immediately surrounding the tablet. This is a mass transfer process dominated by the available solid-liquid interfacial area, the local mass transfer coefficient, and the concentration gradient across the boundary layer around the tablet. The dissolved drug then distributes itself throughout the vessel according to a blending process typically control by the overall hydrodynamics of the system and the local turbulence intensity. This process is not instantaneous, and it may take an appreciable amount of time, the so-called blend time, for the system to become homogenized to a significant and usually pre-defined degree.

The experimental determination and semi-theoretical prediction of the blend time in mixing vessels has been a topic of significant interest. An examination of the literature shows that the experimental determination of blend time typically consists of adding a

small amount of a miscible tracer to the liquid in the mixing system and following the concentration of the tracer with time at different locations throughout the system. Typically, the local tracer concentration at a given point in the system fluctuates with time. However, the amplitudes of the concentration fluctuations decrease over time and eventually the local concentration converges asymptotically toward the ultimate homogeneous concentration value corresponding to a uniform dispersion of the tracer in the entire system. The blend time, θ (also commonly referred to as "mixing time" or "macromixing time" in the literature), is defined as the time required by the tracer-liquid system to reach a desired and pre-defined level of tracer concentration uniformity at a pre-defined location. It is common to choose a 95% uniformity level as the end point of the blending process (corresponding to a 95% blend time, θ_{95}), although other uniformity levels and corresponding blend times are possible (e.g., θ_{99}, $\theta_{99.9}$). It is always possible to calculate the blend time to achieve a desired level of uniformity once the blend time at another level of uniformity is known Brown et al. 2004.

Only a limited number of researchers have determined the effect of the impeller rotation speed on the hydrodynamics in the USP Dissolution Apparatus II. McCarthy et al. (2004) found that the velocities of the fluid are linearly proportional to the impeller rotation speed. However, this conclusion was only applied to specific points in the USP II vessel and for certain components of the velocities (tangential and axial components). Kukura et al. (2004) and Baxter et el. (2005) produced similar results, and stated that the velocities of the flow in the USP Dissolution Apparatus II increase proportionally with increased impeller rotation speed. They also found that increasing the impeller rotation

speed cannot change the fact that the distribution of strain rate along the vessel wall is not uniform if other operating conditions are not changed as well.

Only one previous research group used particle tracking in their study of USP Dissolution Apparatus II (Kukura et al. 2004). However, the purpose of particle tracking in that work was to study the flow pattern in Apparatus II. In the CFD simulation they conducted, they used mass-less particles. Thus, this previous study cannot be used to evaluate the ability of the USP Dissolution Apparatus II to suspend disintegrating particle fragments from a drug tablet.

No previous study was found in the literature on the effects of locations of the impeller and the fill volume of dissolution medium on the flow field in the USP Dissolution Apparatus II. Similarly, no previous studies were found on power consumptions for the USP Dissolution Apparatus II.

1.3 Objectives

The literature review presented in Section 1.2 shows that our current knowledge of the hydrodynamics of dissolution testing systems is still greatly incomplete, and that there is a significant need for work aimed at fully quantifying the hydrodynamics in the USP Apparatus II both computationally and experimentally.

The overall goal of this research work is to use both computational Fluid Dynamics (CFD) and Laser Doppler Velocimetry (LDV) to quantify the flow field in the USP Apparatus II under typical operating conditions mandated by the dissolution test procedure, as well as determine the effect on the vessel hydrodynamics that can be produced by changing the operating conditions of the test (such as those, voluntarily or involuntarily introduced by the operator or the improper calibration of the dissolution testing apparatus).

Table 1.1 lists the cases (i.e., operating conditions for the USP dissolution Apparatus II) that were studied in this research work. LDV was only applied to the experimentally measurement of the velocity profiles in the USP II vessel for Operating Condition 1, the standard operating condition. CFD was used to predict the flow filed in the USP dissolution apparatus II under all operating conditions.

Additional goals of the project include the determination of mixing/dissolution characteristics of Apparatus II. Such overall goals include the study of the important mixing characteristics of Apparatus II, such as the determination of blend time and power dissipation, the evaluation of the particle suspension capability of the apparatus, such as the agitation intensity to prevent particle settling and avoid "coning" effects, and the experimental determination and, to a lesser extend, the computational/theoretical

prediction, of the dissolution profiles of calibrator tablets as a function of key operating variables, such as the effect of tablet location on dissolution.

Table 1.1 Different Operating Conditions of USP II Vessel Studied in This Research Work

Operating Conditions	Agitation Speed (RPM)	Fill Volume (mL)	Impeller Location	Presence of non-dissolving tablet
1	50	900	Standard (i.e., centrally located and 25 mm off the vessel bottom)	No
2	75	900	Standard	No
3	100	900	Standard	No
4	50	500	Standard	No
5	50	900	25 mm up from standard location	No
6	50	900	25 mm down from standar d location	No
7	50	900	2 mm off center	No
8	50	500	Standard	Yes
9	100	900	Standard	Yes

Therefore, the specific objectives of this research work are to:

1. Quantify the hydrodynamics in a standard USP II dissolution vessel by experimentally mapping (via LDV) and computationally predicting (via CFD) the velocity distribution and the turbulent intensity inside the vessel under Operating Condition 1;

2. Using the validated CFD approaches described above, predict the flow field inside USP Apparatus II under the operating conditions other than Operating Condition 1 listed in Table 1.1, and quantify the hydrodynamics in the USP II dissolution vessel as a function of those variables (impeller agitation speed, dissolution media fill volume, impeller off bottom location, off-center radial distance of the impeller from the vessel centerline, presence of a non-dissolving tablet on the bottom of

the dissolution vessel) that are most likely to influence the flow field and the dissolution testing results;

3. Computationally predict (via CFD) and experimentally determine the blend time to homogenize the contents of the hemispherical USP II dissolution vessel under different operating conditions. The values of time scale required to homogenize the liquid content of the vessel could then be compared to the time scale required for tablet dissolution, in order to determine whether the former phenomenon could affect the latter process. Such knowledge can in turn be used to determine the sensitivity of the dissolution apparatus to sampling at different locations in the apparatus;

4. Computationally predict (via CFD) the power consumption and power number of USP II dissolution vessel under different operating conditions;

5. Experimentally and numerically determine the agitation requirements to suspend particles commonly found in solid dosage formulation, and prevent particle settling/map agitation space where particle settling can occur;

6. Conduct dissolution testing experiments with disintegrating and non-disintegrating calibrator tablets (10-mg Prednisone tablets (NCDA #2) and 300-mg Salicylic Acid tablets (USP)) to determine the effect of tablet location on dissolution profiles, and develop models, when appropriate, that can be used to explain and predict the resulting dissolution profiles.

CHAPTER 2

EQUIPMENT, MATERIALS, AND METHODS

2.1 Dissolution Vessel and Agitation System

A standard USP Apparatus II dissolution vessel consisting of an unbaffled, cylindrical, transparent, glass tank with a hemispherical bottom, and having an internal diameter, *T*, of 100.16 mm and an overall capacity of 1 L was used in all experiments (Figure 1.1). The agitation system consisted of a standard USP II two-blade paddle impeller mounted on a shaft. The exact geometry of each component of the impeller was obtained by measuring the actual dimensions with a caliper, which were found to be as follows: shaft diameter, 9.53 mm; length of the top edge of the blade, 74.10 mm; length of the bottom edge of the blade, 42.00 mm; height of the blade, 19.00 mm; and thickness of the blade, 5.00 mm. When the vessel was filled with 900 mL of dissolution media, the corresponding liquid height, *H*, as measured from the bottom of the vessel, was 12.88 cm; when the vessel was filled with 500 mL of dissolution media, the corresponding liquid height, *H*, as measured from the bottom of the vessel was 7.86 cm. Real dissolution media were filled into the USP II vessel when studies were carried out under Operating Condition 1, Operating Condition 8 and Operating Condition 9 listed in Table 1.1

This impeller was provided by the Merck researchers and had a slightly larger diameter shaft at the blade, resembling a collar, as opposed to the uniform shaft diameter, including the portion at the blade, typical of the USP design. The radius of this collar was only 1.6 mm larger than that of the rest of the shaft. The experiments and the computational results were obtained with this impeller in order to insure exact conformity to the Merck system. However, the geometric differences between this system and the

typical USP system are so minimal that the result obtained here are expected to be equally valid for the USP impeller with no collar.

Since only the hydrodynamics of the system was of interest here, the dissolution vessel and paddle were not assembled in a full dissolution system similar to that shown in Figure 2.1 Instead, the impeller was connected to a 1/8-HP motor controlled by an external controller (G. K. Heller Corp, Model 202P6518) which was used here to rotate at a constant agitation speed of 50 RPM, the conventional Operating Condition specified in the USP for the test. The corresponding impeller tip speed was 0.194 m/s and the impeller Reynolds number was 4,939. The Reynolds number was calculated from equation 2.1:

$$R_e = \frac{\rho N D^2}{\mu} \tag{2.1}$$

where, ρ is the density of water in kg/m^3, N is the tip speed of impeller in revolution per second (RPS), D is the diameter of the impeller in meter, μ is the viscosity in Poise (P). The motor-impeller system was mounted on a bracket above the vessel so that the impeller was centered in the vessel and the impeller clearance off the vessel bottom was 25 mm, as mandated by USP. The vessel was filled with 900 mL of de-ionized water, as in the Operating Condition 1.

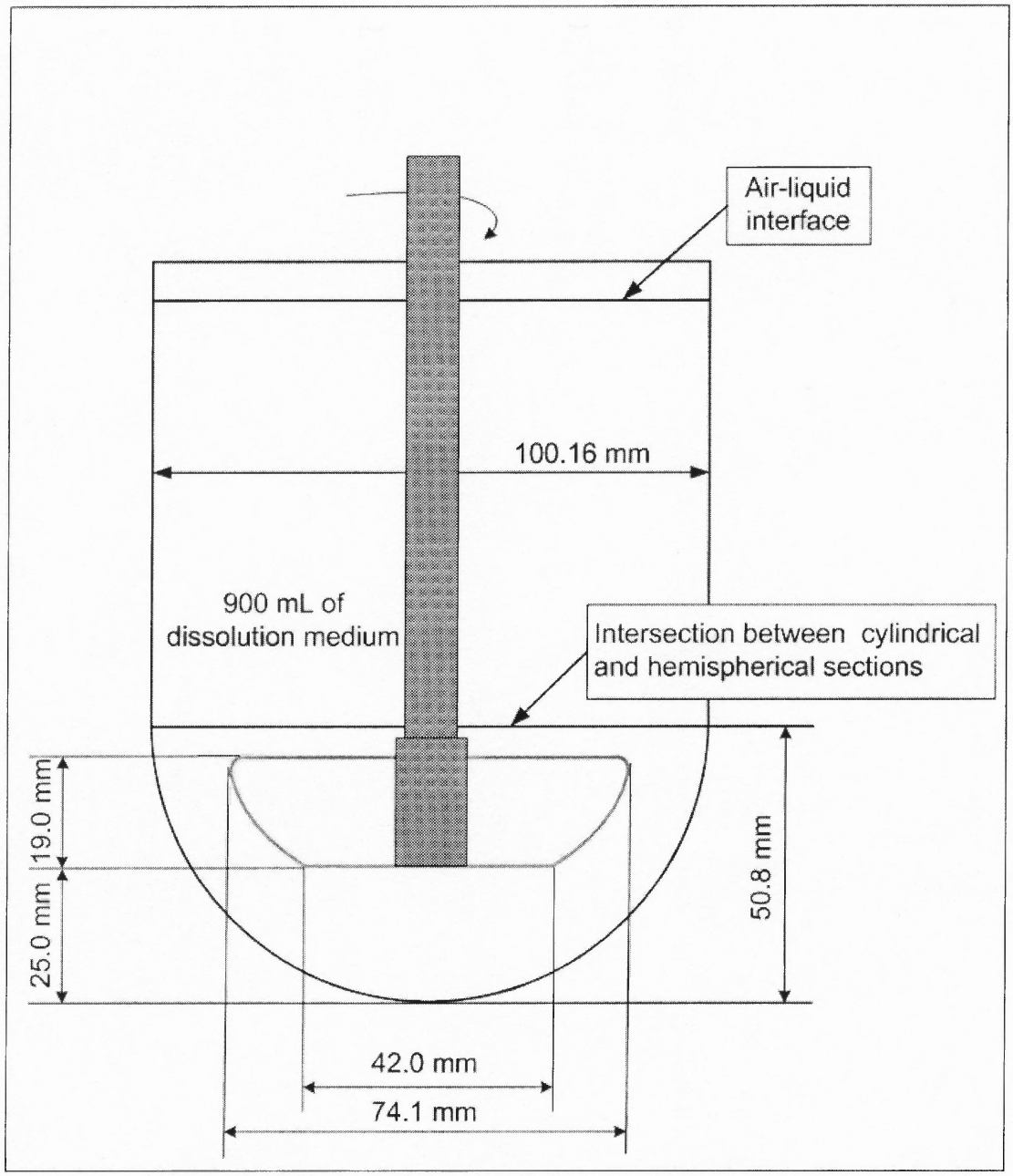

Figure 2.1 Basic geometry of USP Dissolution Apparatus II vessel and agitation system.

2.2 Laser Doppler Velocimetry (LDV) System

Laser-Doppler Velocimetry (LDV) is a non-intrusive experimental method used to determine the local velocity distribution (including its fluctuating component) in a fluid inside any transparent piece of equipment. More than forty years after its first use, LDV has been proved a material experimental method and extensively used by several investigators (Ranade and Josh, 1989; Kresta and Woods, 1993a, 1993b; Armenante *at el.*, 1994; Armenante and Chou, 1996; Schaefer *at el.*, 1997; Armenante *at el.*, 1997; Akiti and Armenante, 2004;) to quantify the flow characteristics of mixing vessels and reactors. It has several advantages. First of all, it is non-intrusive. That means LDV can measure the flow field without contacting and disturbing it at all. It needs no calibration. It presents well-defined directional response. Also, The LDV measurements are independent of media and temperature. .

In this project, a Dantec 55X series LDV apparatus (Dantec Measurement Technology USA, Mahwah, NJ, USA) was used to determine the velocity flow field and turbulence intensity inside the vessel (Figure 2.1). The LDV system comprised a 750 mW argon-ion laser (Ion Laser Technology, Inc.) producing a single multicolored laser beam passing through an optical filter to generate a monochromatic green beam (wavelength: 512 nm). The resulting beam passed through a beam splitter from which two beams emerged, one of which was passed through a Bragg cell to lower the frequency by 40 MHz and distinguish between positive and negative velocity measurements (TSI, 1979). The beams then passed through a beam expander system and a final focusing lens with a focal length of 330 mm. This lens made the beams converge so that they intersected each other to form a small control volume in the interrogation

region where the velocity was to be measured. In an actual measurement, the beams were made to converge inside the USP II vessel.

The USP II vessel was suspended from a bracket specifically built so that the vessel could be placed in an external Plexiglas square tank filled with water, in order to minimize optical distortion during LDV measurements. The dissolution media in the USP Dissolution Apparatus II vessel was seeded with small amount of neutrally buoyant silver coated particles with a diameter of 1.5 μm (T.S.I. Inc., Minneapolis, MN, USA). The particles were selected because they follow the flow field pattern closely. When the particles traveled through the small elliptical control volume formed by the two laser beams, they scatter the light. The scattered light then collected by the receiving optics composed of a variable focus lens and a photomultiplier. The 2201 Digital Storage Oscilloscope (Tektronix, Inc., Beaverton, Oregon, USA) was used to monitor the quality of the signal when conducting the measurements. Data validation and signal processing were carried out with the help of DANTEC 58N10 Doppler signal processor. The analog signals were converted from the receiving optics to instantaneous burst detection by the Doppler signal analyzer. The data were acquired, processed and presented by a computer with Dantec's software SIZEware® installed.

The receiver and the data acquisition system are capable of taking large amount of measurements in the same location in a very short time. In this work, the system took about 5000 measurements in sixty seconds measurement time.

The USP Dissolution Apparatus II vessel was suspended from a bracket specifically designed for this purpose, so that it could be placed in an external Plexiglas square tank filled with water, in order to minimize optical distortion during LDV measurements. The vessel-tank assembly was mounted on an x-y-z traversing system that enabled the velocity components in all three directions at any locations in the vessel.

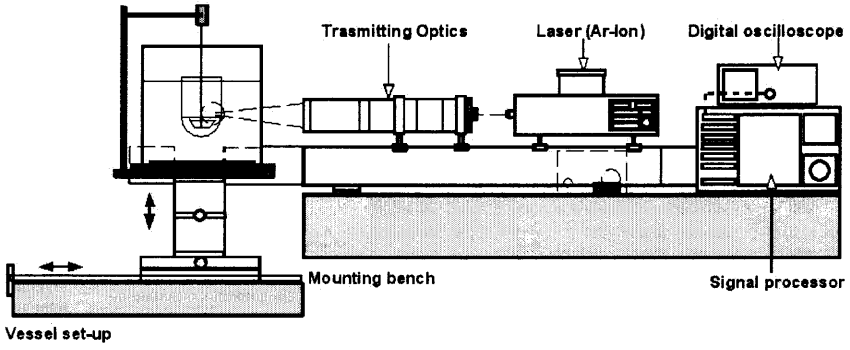

Figure 2.2 Laser-Doppler Velocimetry (LDV) apparatus used in this work, after Uehara Nagamine, 2001.

Data analysis was performed to generate the local mean and fluctuating velocity components in the direction parallel to that of the plane of the two laser beams. LDV apparatus used in this project was a 1-D system. That means it can only measure one of the three velocity components at one time. Thus, appropriate rotation of the laser beam assembly and translation of the vessel-tank assembly yielded the velocity components in all three directions at any location. This is summarized in Figure 2.3.

Assume the horizontal plane where the cylindrical and hemispherical portions of the vessel intersect is taken as plane z=0, ten virtual iso-surfaces at different vertical (z) positions were chosen from the top to the bottom potion of the vessel to make the analysis easier at z=65 mm, z=50 mm, z=25 mm, z=-0.75 mm, z=-6.75 mm, z=-15.75

mm, z=-25.75 mm, z=-31.75 mm, z=-37.75 mm and z=-43.75 mm (Shown as in Figure 2.4). The iso-surfaces at z=-6.75 mm, z=-15.75 mm and z=-25.75mm are the planes in which the top edge of the impeller blade, the middle of the impeller blade and the bottom edge of the impeller lie, separately. The density of the iso-surfaces increases from the top of the vessel to the bottom of the vessel because the bottom portion of the USP Dissolution Apparatus II vessel is the most important region of the system, where the dissolution process of the solid dosage form takes place.

On the iso-surfaces above the impeller, LDV measurements were made at seven evenly spaced radial locations between the shaft and the vessel wall. However, because of the hemispherical shape of the vessel bottom and the presence of the impeller blades, fewer measurement locations were used in the impeller region and the bottom region. At each measurement location, three velocity components (tangential, axial, and radial) were obtained by LDV.

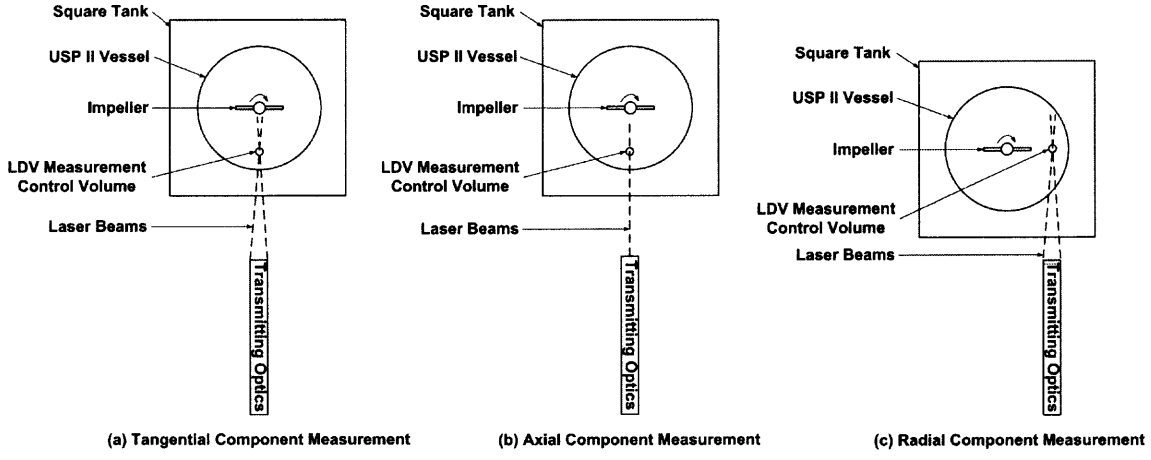

Figure 2.3 Positioning of USP Dissolution Apparatus II vessel and the LDV assembly for different velocity components measurements, top view.

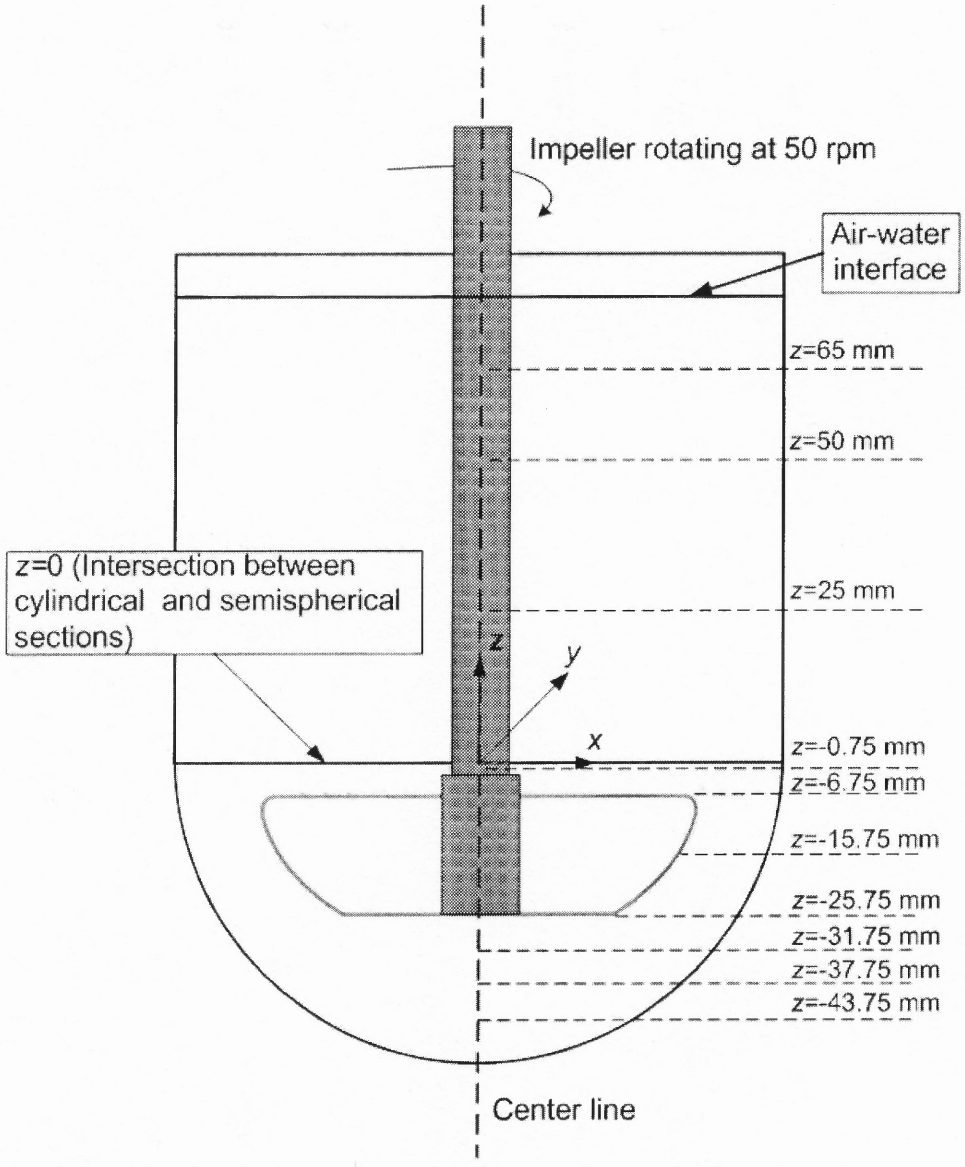

Figure 2.4 Ten iso-surfaces at different vertical positions, on which, LDV measurements were conducted..

2.3 Experimental Determination of Power Dissipation

Power dissipation is an important parameter when studying mixing device. An unsuccessful attempt was made to experimentally measure the power dissipated by the impeller using an apparatus previously used to determine the power dissipation in baffled tanks provided with larger and more power dissipating impellers. The apparatus and method are described in detail elsewhere (Armenante et al. 1999; Armenante and Chang, 1998). Briefly, the apparatus consisted of a system of strain gages mounted on a shaft and electrically connected to a signal conditioner and an amplifier system (2120A system, Measurement Group Co.) via a slip ring assembly (Airflyte Electronics Co., Bayonne, NJ, Part No. CAY1030-12-2), so that the torque applied by the impeller on the shaft as the impeller rotated in the liquid resulted in straining the shaft (and the strain gages mounted on it). The gage signal was directly proportional to the torque applied to the shaft. Knowing the torque and the power dissipated by an impeller, the power number N_p could be determined. In these experiments, the USP II paddle impeller was secured at the end of this shaft rotated at 50 RPM. The system was calibrated by applying know torques and measuring the resulting strain gage signal.

The main problem with this approach was that the power dissipated by the USP II paddle rotating at 50 RPM (or even 100 RPM) in the unbaffled USP II vessel was exceedingly small, probably of the order of 10^{-4}-10^{-3} Watts. Therefore, the resulting strain gage signal was of the same order of magnitude of the system noise, and accurate torque readings could not be obtained. Instead, the power dissipation obtained via CFD simulation was compared with literature equation for unbaffled systems.

2.4 Experimental Determination of Blend Time

Blend time was measured using a tracer approach (Hass and Nienow, 1989, Manna, 1997, Nienow, 1997). The USP Apparatus II dissolution vessel/paddle assembly shown in Figure 2.1 was modified in this work in order to make suitable for tracer injection. The modified vessel consisted of the standard USP Apparatus II unbaffled, cylindrical, transparent, glass vessel with a hemispherical, fitted with two small copper tubes passing through holes drilled through the bottom of the glass vessel, and glued to the vessel itself (Figure 2.5) so that a tracer could be added at either location. The tubes were mounted flush with the inside wall of the vessel and were used as injection points. One injection point (defined as Injection Point 1) was centrally located exactly below the impeller, and the other was 48.6° away from the vertical centerline along the vessel bottom (defined as Injection Point 2).

Figure 2.6 shows the locations of the two injection points. Each tube was provided with a valve and a septum through which the needle of a syringe containing the tracer could be inserted. Blend time was experimentally measured only under the standard Operating Condition, listed in Table 1.1.

A typical experiment began by preparing the system, charging the vessel with deionized water and the appropriate reactant (if required by the detection method, as described below), and starting the agitation. Then, one of the two valves was open, the syringe needle was inserted in the septum, the content of the syringe was emptied inside the agitated vessel, and the stopwatch was started. The time required to achieve a predefined level of tracer homogeneity at either one of two pre-selected monitoring points was recorded. Two blend time monitoring points were defined, both located

points was recorded. Two blend time monitoring points were defined, both located midway between the impeller shaft centerline and the vessel wall. Monitoring Point 1 and Monitoring Point 2 were, respectively, 25 mm and 50 mm above the z=0 location, defined as the intersection between the cylindrical and hemispherical portions of the vessel (Figure 2.6). Two methods were used to experimentally determine blend time in this work.

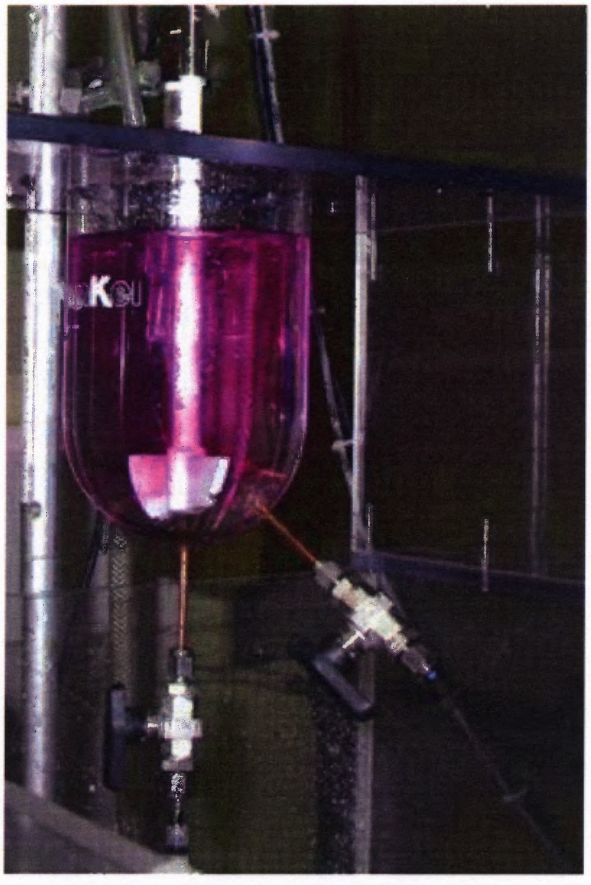

Figure 2.5 Modification USP dissolution testing system used for experimental determination of bland time in the absence of the conductivity probe.

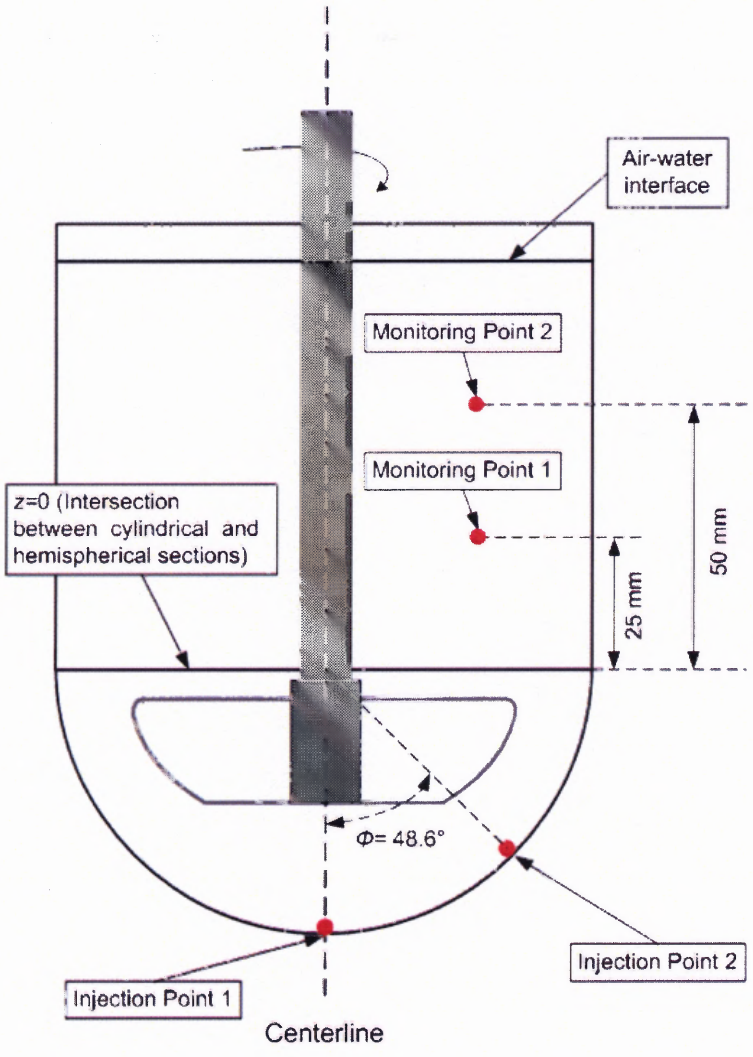

Figure 2.6 Locations of two injection points and two monitoring points for experimental determination of bland time.

Method 1 is the conductivity measurement. A cylindrical conductivity probe, 1 cm in diameter (Orion, Cat No. 990101), was connected to a conductivity meter (Orion, MOD 101) and was placed inside the vessel with its tip located at one of the two monitoring points described above. At t=0, 3 mL of a 1.0 mol/L NaOH solution were injected from Injection Point 1. Conductivity was monitored over time. The time at which the conductivity measurement reached 95% of the final asymptotic value, and remained above that value, was recorded. Experiments were repeated in quintuplicate.

Method 2 is discoloration approach. An aliquot of 3 mL of a 1.0 mol/L NaOH solution was added to the vessel together with 6 drops of phenolphthalein indicator, turning the solution in the vessel pink (Figure 2.5). At t=0, 3 mL of a 1.2 mol/L HCl solution were injected from one of the injection points. The time at which the solution became visually clear at the predefined monitoring point was recorded. Experiments were repeated in quintuplicate.

Discoloration tests were conducted both in the presence and in the absence of the conductivity probe. The presence of the conductivity probe introduces a baffle effect. It is well known that baffling increases the turbulence of any agitated vessels, promotes axial recirculation, and reduces blend time (Nishikawa et al. 1979, Myers et al. 2002, Nere et al. 2003). Hence, blend times obtained in experiments conducted in the presence of the conductivity probe were considered less representative of the true blend time in the unbaffled USP II system. However, a comparison of the results obtained using both methods, in both cases in the presence of the probe, was found to be useful to interpret the data even when other experiments were conducted in which the conductivity probe was not present and the blend time could only be detected with the discoloration method.

The approach was as follows. Similar experiments using the two methods were conducted, all in the presence of the conductivity probe. The level of tracer uniformity, obtained through conductivity measurement, at the time when local discoloration was achieved was recorded. In this way, the results of the two methods could be related to each other. This calibration of the discoloration method against the conductivity method was important in those experiments in which no conductivity probe was present and only the discoloration method could be used, since it allowed for the indirect estimation of the

level of uniformity achieved in the discoloration experiments in the absence of the conductivity probe.

The level of non-uniformity, X, defined as:

$$X(t) = \frac{C_{Final} - C(t)}{C_{Final} - C_o} \tag{2.2}$$

could be experimentally obtained with the conductivity method. In this equation, $C(t)$ is the local concentration of the tracer. The time required to reach 95% homogeneity (i.e., X=0.05), was recorded. This was the 95% blend time, θ_{95}. Assuming that the oscillation dampening follows an exponential decay, it can be shown that the blend time, θ_U, to achieve any desired level of local tracer uniformity U=1-X is given by the following equation (Brown et al. 2004):

$$\frac{\theta_U}{\theta_{95}} = \frac{\ln(1-U)}{\ln(1-95\%)} = \frac{\ln X}{\ln(0.05)} \tag{2.3}$$

From the discoloration experiments conducted in the presence of the conductivity probe θ_U could be experimentally determined, although the value of U at which discoloration was achieved was unknown. However, from Equation 2.3, it was then possible to determine the value of $U(X)$ at which discoloration occurred. The knowledge of $U(X)$ at discoloration, and hence X, was used to analyze the results of the discoloration experiments in which no probe was present.

2.5 Experimental Determination of the Effect of Locations of Tablet on Dissolution under Operating Conditions 8 and 9

2.5.1 Experiment Setup and Method

All dissolution experiments were conducted using a Distek 5100 Bathless Dissolution Apparatus II (Distek Inc, North Brunswick, NJ), shown in Figure 1.2. Although this equipment is provided with seven standard 1-L individual dissolution vessels, only two of the vessels were used at a time.

Dissolution studies were carried out with two types of tablets, i.e., 10 mg prednisone calibrator tablets (disintegrating tablets, NCDA #2), kindly provided by Dr. Zongming Gao (FDA, St. Louis, MO), and 300 mg salicylic acid calibrator tablets (non-disintegrating tablets; USP Lot Q0D200), purchased from USP, Rockville, MD. The dissolution medium for prednisone consisted of de-aerated and de-ionized water, in accordance with the Dissolution Test Performance Standard #2 (Division of Drug Analysis, 1995). The dissolution medium for salicylic acid tablets consisted of a 0.05 M monobasic potassium phosphate buffer to which an NaOH solution (50% w/w concentration) was added to reach a final pH value of 7.4±0.05 (USP Certificate, 2006). The media were de-aerated according to the degassing method developed by Moore (Moore, 1996) (Figure 2.7). The temperature of the dissolution medium was raised to 37±0.5 °C prior to its use in the experiments.

In order to test the effect of tablet position on dissolution, a tablet was initially fixed at a predefined location on the bottom of the dissolution vessel with a very small bead of a commercial available high-viscosity polymer (polybutene). Four tablet locations were tested, i.e., at the center of the vessel bottom, 10° off-center, 20° off-

center and 40° off-center. All angles originated from the center of the sphere comprising the hemispherical vessel bottom, and were measured starting from the vertical centerline to the point of interest, (e.g., the angle would be zero for the central point below the impeller).

After the vessel and the fixed tablet were placed in the dissolution equipment, the appropriate volume of dissolution medium (500 mL for prednisone tablets, and 900 mL for salicylic acid tablets) was slowly poured into the dissolution vessel in order to minimize initial dissolution. The first sample was taken right after the medium addition, and immediately after that, the agitation was started at the prescribed rotational speed (50 rpm for prednisone tablets, and 100 rpm for salicylic acid tablets). This was defined as the zero-time point. All experiments lasted 45 minutes. Obviously, the procedure outlined here is slightly different from the procedure described in the USP (USP 2006), which requires that the tablet be dropped into the vessel after the medium has been added and the agitation started.

Samples were manually taken at five-minute intervals for 45 minutes by removing 5-mL aliquots with a 5-mL syringe connected to a cannula, 2 mm in diameter, inserted only when a sample was taken. A total of 10 samples were taken in each experiment. The volume of medium removed by sampling was not replaced, in accordance to USP (USP, 2005; Baxter et al., 2005). The sampling point was horizontally located midway between the impeller shaft and the vessel wall, and midway between the top edge of the impeller and the surface of the dissolution medium, i.e., within the sampling zone prescribed by the USP. About 2 mL of each sample were discarded and the rest was filtered with a double layer PTFE/PES 0.8-μm filter (Drummond Scientific Co.,

Broomall, PA). The filtered samples were stored in small glass vials until analyzed. All samples were analyzed with a UV-visible spectrophotometer (Varian CARY 50 Bio) at the specified wavelengths, i.e., 242 nm for prednisone and 296 nm for salicylic acid. (Division of Drug Analysis, 1995, USP Certificate, 2006). The results were compared to 9-point calibration curves generated using reference standards obtained with solutions with know concentrations.

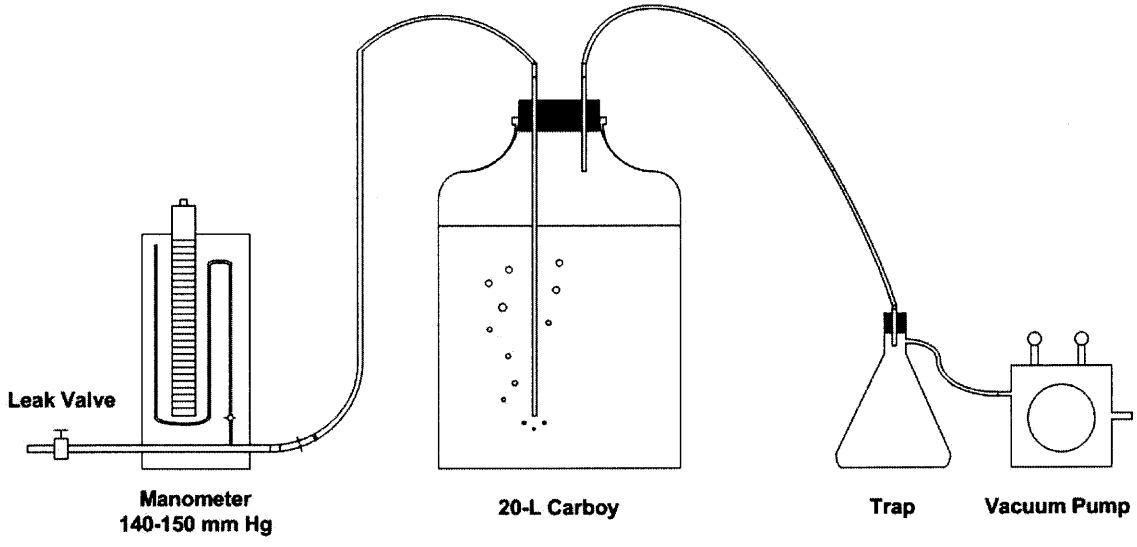

Figure 2.7 Equipment used to de-aerate the dissolution medium (after Moore, 1996).

All experiments in which the tablets were placed at the central location were performed in triplicates to determine reproducibility.

2.5.2 Data Analysis

The dissolution profiles obtained with tablets at off-center locations were compared to those obtained with the centrally located tablets in order to determine whether the results were statistically different. Two approaches were used. The first approach consisted of using a model-independent method based on the similarity factor (f_1) and difference factor (f_2) proposed by Moore and Flanner (Moore and Flanner, 1996; Baxter et al. 2005):

$$f_1 = \left\{ \frac{\sum_{t=1}^{n} |R_t - T_t|}{\sum_{t=1}^{n} R_t} \right\} \times 100 \tag{2.4}$$

$$f_2 = 50 \times \log_{10} \left\{ \left[1 + \frac{1}{n} \sum_{t=1}^{n} (R_t - T_t)^2 \right]^{-0.5} \times 100 \right\} \tag{2.5}$$

where R_t is the reference assay at time t, T_t is the test assay at the same time, and n is the number of points. The higher the similarity factor f_1 (which can be in the range 0 to 100), the higher the average difference between reference and test curves is. The higher the difference factor f_2, (which can be in the range $-\infty$ to 100) the lower the average difference between reference and test curves (Costa and Lobo, 2001). Public standards have been set by Food and Drug Administration (FDA) for f_1 and f_2. Accordingly, statistical similarity between the two curves being compared requires that both $0 < f_1 < 15$ and $50 < f_2 < 100$ (FDA, 1997; Baxter et al. 2005).

The second approach to evaluate the similarity of dissolution profiles was based of the analysis of variance and the calculation of the P values using a standard Student's t-tests.

2.5.3 Determination of Tablet-Medium Mass Transfer Coefficient From Experimental Dissolution Data

In order to determine how the mass transfer process is affected by the location of the tablet, at least for the case in which the tablet is eroding and not disintegrating, the mass transfer coefficient must be extracted from the experimental data. This can be done by rearranging and integrating the basic mass transfer equation. The rate of dissolution of a chemical species, such as a drug, from a solid surface, such as a tablet, into the adjacent liquid, such as the dissolution medium, can be expressed as follows:

$$\frac{dC}{dt} = \frac{kA}{V_L}(C_s - C) \tag{2.6}$$

where, C is the drug concentration in the dissolution medium, C_s is the solubility concentration of the drug, k is mass transfer coefficient, A is the tablet surface area exposed to the dissolution medium, and V_L is the volume of dissolution medium, assumed to be well mixed.

Of interest here is the determination of the mass transfer coefficient k from the experimental data:

$$k = \frac{V_L}{A(C_s - C)}\frac{dC}{dt} \tag{2.7}$$

As time progresses and the tablet erodes, the surface area A, is reduced. If the tablet is cylindrical and if it retains its original height-to-diameter ratio, β, during the dissolution process (a reasonable assumption is the mass transfer coefficient is similar on all exposed surfaces), then A can be calculated knowing the ratio:

$$\beta = \frac{h_T}{d_T} \tag{2.8}$$

where, h_T and d_T are, respectively, the height and the diameter of the tablet. In the case of the salicylic acid tablet, h_T and d_T were measured with a caliper and found to be 9.57 mm and 3.33 mm, respectively, yielding a β value equal to 0.348. If only the top and side surface of the tablet are exposed to the dissolution medium, the interfacial area available for mass transfer is:

$$A = \pi d_T^2 \left(\frac{1+4\beta}{4} \right) \tag{2.9}$$

From a mass balance for the drug disappearing from the tablet and appearing in the dissolution medium it is, at any time:

$$C = \frac{\rho_T \left(V_{T0} - V_T \right)}{V_L} + C_0 \tag{2.10}$$

where, ρ_T, V_{T0}, and V_T are, respectively, the density, initial volume and volume at time t for the tablet, and C_0 is the initial concentration of the drug in the dissolution medium (equal to zero in this work). Since the tablets are cylindrical, the tablet volume is given by:

$$V_T = h_T \frac{\pi d_T^2}{4} = \beta \frac{\pi d_T^3}{4} \tag{2.11}$$

By substituting this equation into Equations 2.10, one can get the tablet volume as it changes with time:

$$d_T = \left[d_{T0}^3 - \frac{4\left(C - C_0\right) V_L}{\pi \beta \rho_T} \right]^{1/3} \tag{2.12}$$

Substituting this equation into Equation 2.9, gives an expression for A as a function of C, as the concentration of drug in solution increases with time:

$$A(C)=\pi\left[d_{T0}^3-\frac{4(C-C_0)V_L}{\pi\beta\rho_T}\right]^{2/3}\left(\frac{1+4\beta}{4}\right) \tag{2.13}$$

An estimate of the mass transfer coefficient k, assumed to be constant with time and changing tablet volume, can be obtained by substituting this expression for A in Equation 2.7 and integrating it, resulting in:

$$k=\frac{1}{tV_L}\int_{C_0}^{C_t}\pi\left[d_{T0}^3-\frac{4(C-C_0)V_L}{\pi\beta\rho_T}\right]^{2/3}\left(\frac{1+4\beta}{4}\right)\left(\frac{1}{C_s-C}\right)dC \tag{2.14}$$

where, C_t is the drug concentration in the dissolution medium at time t. Since experimental data of C vs. t are available, this equation can be used to calculate k from by numerical integration, at least for the case of salicylic acid tablets, since these tablets do not disintegrate.

2.5.4 Prediction of the Tablet-Medium Mass Transfer Coefficients

In order to determine whether the experimentally derived tablet-medium mass transfer coefficients could be predicted theoretically or computationally for the non-disintegrating salicylic acid tablets the following approach was used. The equations available in the literature for mass transfer coefficients in systems that approximately represent the tablet-medium interaction in the dissolution vessel were obtained. Since these equations are typically based on boundary layer theory, they require as input the approaching velocity of the incoming fluid. Such a velocity was estimated from CFD.

For the case of a centrally located tablet, it was assumed that the tablet-dissolution medium mass transfer process at the top tablet surface is similar to the mass transfer between a rotating disk and the surrounding fluid, although here the tablet is stationary

and the fluid is rotating. The rotating disk model predicts that the mass transfer coefficient is (Middleman, 1998, Bird et al. 2002):

$$k_{top} = 0.62 D_{AB}^{2/3} \nu^{-1/6} \omega^{1/2} \tag{2.15}$$

where, k_{top} is the mass transfer coefficient in cm/s, D_{AB} is the diffusivity between the solute and the solvent in cm^2/s, ν is the kinematic viscosity of the liquid in cm^2/s, and ω is the angular velocity of the rotating disk in rad/s. In order to adapt this equation to the tablet-dissolving medium case, it was assumed that ω is the rotational angular velocity of the dissolving medium above the tablet. Since the medium in this region of the USP Apparatus II was previously found to move with solid body rotation (Bai et al., 2006), ω was calculated by dividing the tangential velocity of the fluid at a location above the tablet by the radial distance of that location from the vessel centerline. Accordingly, it was found that ω=12.94 rad/s. For comparison purposes, the angular velocity of the impeller for the salicylic acid case is 10.47 rad/s (corresponding to N=100 rpm). These results are in agreement with previous work, which showed, both experimentally and computationally, that the angular velocity of the fluid in the lower region of a USP Apparatus II is slightly larger than that of the impeller (Bai et al., 2006). The kinematic viscosity in Equation 2.15 was taken as that of water at 37 °C (0.70×10^{-2} cm^2/s). The diffusivity of salicylic acid in water was estimated from the Wilke-Chang correlation (Geankoplis, 2003, Bird et al. 2002):

$$D_{AB} = 1.173\times10^{-16}(\phi M)^{1/2} \frac{T}{\mu V_A^{0.6}} \tag{2.16}$$

where M is the molecular weight of the solvent in kg/kg-mol (18.02 for water), Φ is an association parameter of the solvent (2.6 for water), T is the temperature in K (310 in this case), V_A is the solute molar volume at its normal boiling point in m^3/kg mol (0.09592 m^3/kg mol in this case, assuming the molar volume of salicylic acid at boiling point is the same as that at room temperature) The diffusivity value, D_{AB}, for salicylic acid-water system was calculated to be 1.47×10^{-5} cm^2/s.

In order to estimate the tablet-dissolution mass transfer coefficient on the side of the centrally located tablet it was assumed that this process is similar to the mass transfer between a rotating cylinder and the surrounding fluid, although here the tablet is stationary and the fluid is rotating. The rotating cylinder model predicts that the mass transfer coefficient k_{side} is as follows (Labraga, and Berkah, 2004):

$$\frac{k_{side}\, d_T}{D_{AB}} = 0.135\left[0.5\,\mathrm{Re}_\Omega^2\, Sc\right]^{1/3} \tag{2.17}$$

where Sc is the Schmidt Number, $Sc=\mu/(D_{AB}\cdot\rho_L)$ and Re_Ω is defined as:

$$\mathrm{Re}_\Omega = \frac{d_T u_\Omega \rho_L}{\mu} \tag{2.18}$$

with u_Ω being the velocity at the periphery of the rotating cylinder. In order to adapt this equation to the tablet-dissolving medium case, it was assumed that u_Ω is the tangential velocity of the dissolving medium next to the tablet, and appropriately scaled.

A different approach was used to calculate the mass transfer coefficient when the tablet was off-center. The mass transfer coefficients for the top and side surfaces of the off-center tablets were estimated using the mass transfer models for a flow parallel a flat plate (top surface) and past a single cylinder (side surface). The solid-liquid mass

transfer coefficient when a liquid moves parallel to flat plate was calculated from (Bird et al. 2002, Geankoplis, 2003):

$$k_{top} = 0.99 \cdot u \cdot (\mathrm{Re})^{-0.5} (Sc)^{-2/3} \tag{2.19}$$

where, u is the approaching velocity of the liquid to the flat plate, Sc is the Schmidt number and Re is the Reynolds number, defined as (Bird et al. 2002, Geankoplis, 2003):

$$\mathrm{Re} = \frac{Lu\rho_L}{\mu} \tag{2.20}$$

In the original equation for a flat plate, L is the distance from the beginning of the plate in the direction of the flow. Here it was assumed that L is equal to the diameter of the tablet, d_T. The density of the fluid, ρ_L, was taken to be that of water at 37 °C (995.73 kg/m^3). The approaching velocity of the rotating liquid flowing over the tablet top surface, u, was obtained by calculating, through CFD, the tangential velocity of the liquid at eight equally spaced locations in the azimuthal direction on the plane where the tablet was located and at the same radial distance as the tablet radius. These values were averaged to determine the average velocity of the medium approaching the tablet in Equation 2.19.

The solid-liquid mass transfer coefficient on the cylindrical side of the tablet was obtained from the equation describing the mass transfer around cylinders (Bird et al. 2002, Geankoplis, 2003):

$$k_{side} = 0.6 \cdot u \cdot (\mathrm{Re})^{-0.487} (Sc)^{-2/3} \tag{2.21}$$

where, Re was calculated as before, and the approaching velocity u was predicted as just described above.

2.6 Particle Suspension Experiments

"Coning" is the phenomenon that occurs when a tablet undergoing dissolution testing in a USP Apparatus II disintegrates, and the fragments form a cone of solids slowly rotating under the impeller as a result of the gentle agitation that it generates. An attempt was made here to determine the agitation conditions under which the "coning" effect appear, and to model the process. The experiments consisted of adding a small number of particles to 900 mL of de-ionized water in a USP Dissolution Apparatus II and observing the motion of the particles in the vessel as a function of the agitation speed.

Initially, Microcrystalline Cellulose particles (Avicel PH 102, FMC Corporation, Philadelphia, PA) and spherical beads of ion exchange resin were used as dispersed solids.

Avicel PH 102 is a white powder with particles of irregular shapes. It has a very broad size distribution from 1 micron to 400 microns. The particle size was measured with a Laser Diffraction Particle Size Analyzer, Beckman Coulter LS 230, and the volume average size was found to be about 100 microns. It is highly porous material and has sponge-like properties. When placed in water, Avicel PH 102 particles absorb water and swell. Avicel PH 102 is typically used as a filler and disintegrator in solid dosage formulations. However, because of the absorption of water, the true density of Avicel PH 102 in water is different from that of dry Avicel PH 102. Since the density of Avicel PH 102 is needed for CFD simulation of particle suspension and no previous literatures could be found on this topic, its density was determined experimentally.

Dry Avicel PH 102 particles were placed in a beaker with water for 30 minutes to swell. The particles were then placed in a glass cylindrical container with a fritted disk at the end and spun in basket centrifuge (Safty-Head Centrifuge, Clay Adams, Parsippany, NJ) at 5000 rpm for 10 minutes in order to remove the interparticle water but not the intraparticle water inside the individual Avicel particle. The density of the centrifuged "wet" particles was then measured with a pychnometer. The measurements were repeated in quintuplicate.

Resins particles were taken from a deionization ion exchange cartridge (Fisher Scientific Catalog No. D8901). The particles are light yellow in color with a spherical shape. The resins have larger average size than Avicel PH 102. They have a very broad size distribution ranging from 250 microns to more than 800 microns (measured with stacked sieves). The density of the resin was experimentally determined with a pychnometer, and the measurements were also repeated in quintuplicate.

During a suspension experiments, 900 mL of de-ionized water were initially added to the dissolution vessel. The temperature was maintained at 37±0.5 °C. 400 mg of Avicel PH 102 or small amount of resin particles (with particle size range between 250 microns and 300 microns, measured with sieves) were dropped in the USP dissolution test apparatus with the impeller rotating at different rotation speeds. The motions of the particles were visually observed and recorded.

CHAPTER 3

NUMERICAL SIMULATION WITH COMPUTATIONAL FLUID DYNAMICS (CFD)

3.1 Computational Fluid Dynamics (CFD)

Computational Fluid Dynamics (CFD) is a computational tool designed to solve the momentum and mass balance equations under laminar or turbulent regimes to predict the flow field and mass transfer in complex geometries (such as mechanically stirred mixing vessels). CFD computations are typically conducted on mainframe computers or dedicated workstations. All numerical simulations in this work were carried out on a Dell Precision 650 Workstation, equipped with two Intel XEON 2.8 Gigahertz processors and 2 gigabytes of random access memory (RAM). When simulating the flow field, the convergence standards were set as the following: 10^{-5} for continuity, 10^{-4} for velocity components and turbulence parameters (k, ϵ, ω) and at the same time, the velocity magnitudes on one or two points within the domain do not change with time. It took about 7 hours to have 10,000 iterations for this work on the workstation mentioned above. It typically took about no less than 35 hours to get a converged numerical simulation run depending on the complexity of the simulation setup and number of cells.

Numerical simulations of the velocity distribution, power consumption, blend time, solid particle suspension and strain rate distribution inside the USP Dissolution Apparatus II vessel were conducted using a commercial mesh generator, GAMBIT v2.1.6, coupled with a Computational Fluid Dynamic (CFD) package, FLUENT v6.1.22. The full 360°-tank geometry was incorporated in the simulations.

3.2 Mesh Generation and Mesh Quality

Figure 3.1 shows the mesh used in the CFD simulations for Operating Condition 1. In order to save computation time and effectively increase the simulation convergence, a structured Cooper-type hex mesh was created in the cylindrical portion of the vessel and in the upper section of the hemispherical vessel bottom above section A-A in Figure 3.1, panel c. An unstructured, tetrahedral mesh was generated in the lower section of the hemispherical bottom to follow the curved shape more closely. Accordingly, the liquid volume was computationally partitioned into two sub-volumes. The meshes in each sub-volume were created starting from the same starting face (Figure 3.1), i.e., the horizontal cross section of the vessel located where the lower edge of the impeller blade lies (section A-A in Figure 3.1c). On this starting face, the curves resulting from the intersection of the horizontal plane with vertical solid surfaces such as the vessel wall (resulting in a circle) or the impeller blade edge (resulting in a rectangle) were identified. These curves were partitioned into small elements by specifying points on them from which the grid line started. This approach resulted in the generation of a larger number of smaller cells in the regions near the impeller and the tank wall in order to capture the steep velocity gradients in those regions. From the pre-meshed starting surface (Figure 3.1a), a hex grid was generated with a Cooper-scheme approach, by extending and projecting the pre-meshed surface both upward, up to the liquid-air interface (Figure 3.1b), and downwards, reaching down to the iso-surface 12.35 mm below the lower edge of the impeller (Figure 3.1c, C-C). A much finer tetrahedron mesh was created below this iso-surface, in order to capture the flow near the vessel bottom.

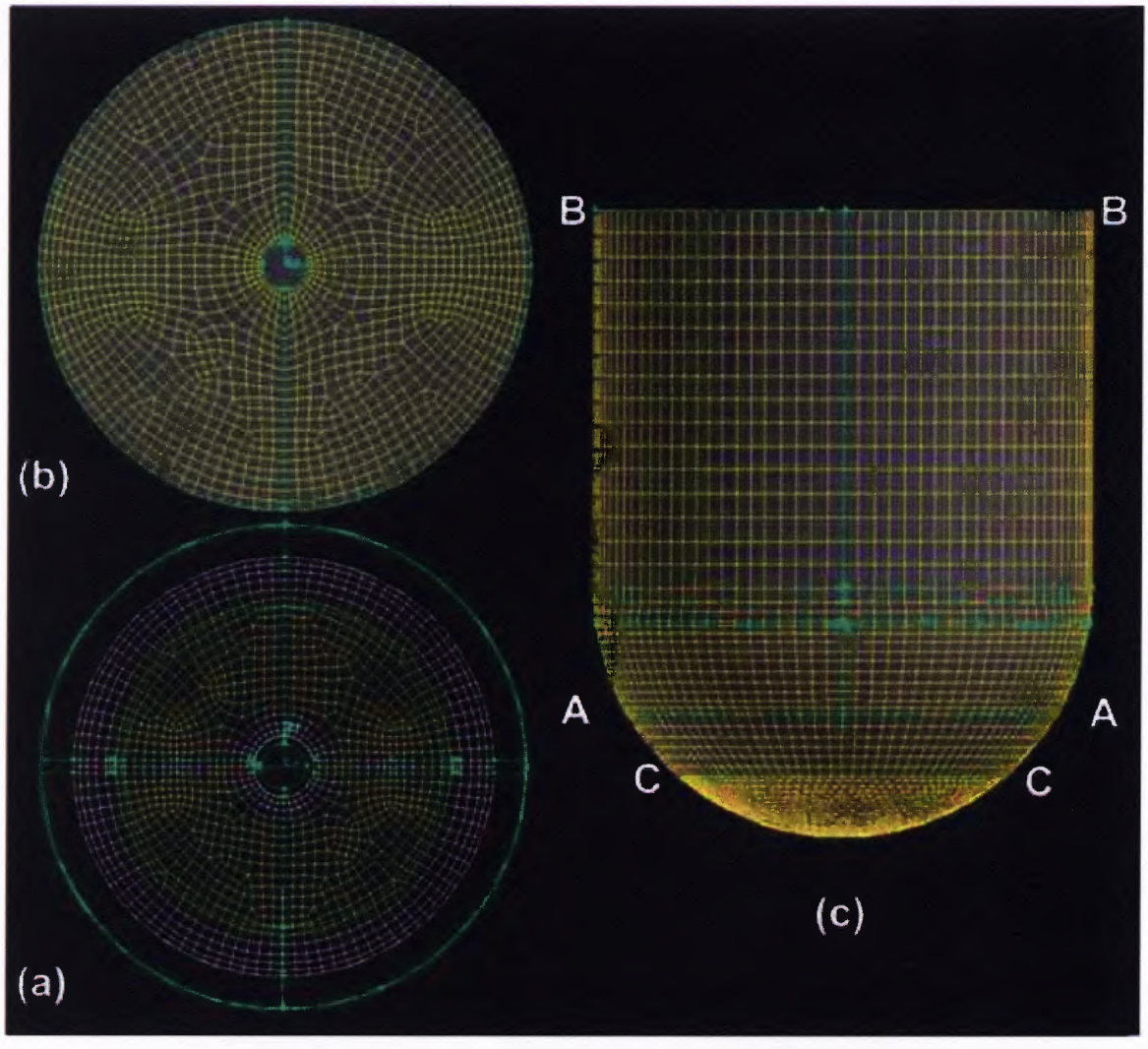

Figure 3.1 Mesh used in CFD simulation for Operating Condition1: (a) starting face on iso-surface at A-A; (b) top face on iso-surface at B-B; (c) axial, side view of mesh, the interface between upper and lower mesh domain is at C-C.

The mesh contained 80,262 cells, 219,590 faces, and 62,472 nodes. Simulations with a mesh containing 258,310 cells (finer mesh) were also run, in order to evaluate the effect of grid number to the numerical solution. The two CFD predictions were not appreciably different. In fact, the results with the coarser mesh matched the LDV data marginally better.

Significant attention was paid to the generation of a high quality mesh for Operating Condition 1, since this determined whether the simulation converged to a stable solution or not. The average EquiAngle Skew parameter (one of the most important parameters to determine the quality of the mesh) was typically in the range 0.3 to 0.4 (0-best; 1-worst) and was no larger than 0.809 for any individual cell. The size variation was very smooth in the complete domain. There was no hex cell with a high aspect ratio in the domain. The cell elements were fine enough to capture the high gradient of the geometry in the area of impeller blade and the bottom of the vessel.

Meshes for other Operating Conditions with 900 mL fill volume listed in Table 1.1 were generated with similar approach described above and contain similar number of cells. Meshes for Operating Conditions with 500 mL fill volume listed in Table 1.1 were generated with similar approach described above but contain about 65,000 cells. All meshes have similar quality as that of the mesh generated for Operating Condition 1.

3.3 Modeling the Turbulent Flow Field

Numerical simulations of the flow fields inside the USP Dissolution Test Apparatus vessels under different Operating Conditions were carried out with a general purpose, commercial, Computational Fluid Dynamics (CFD) Package, FLUENT 6.1.22. The software numerically integrates the transport equations. Combined with the user-defined boundary conditions, it can quantitatively provide the descriptions of the flow fields. Under different Operating Conditions, the flow fields inside the USP Dissolution Apparatus II vessels are turbulent. Appropriate turbulence models must be incorporated into the numerical simulation to account for the turbulent effects.

CFD programs such as FLUENT numerically solve the general equations representing the conservation of mass and momentum. In Cartesian coordinates, the continuity equation for an *incompressible fluid* written using the summation convention can be written as:

$$\frac{\partial u_i}{\partial x_i} = 0 \tag{3.1}$$

Similarly, the momentum balance equation for the same incompressible fluid (Navier-Stokes equation) can be written as:

$$\frac{\partial u_i}{\partial t} + u_j \frac{\partial u_i}{\partial x_j} = -\frac{1}{\rho}\frac{\partial P}{\partial x_i} + \nu \nabla^2 u_i + g_i \tag{3.2}$$

In Eq. 3.2, the second term on left hand side accounts for the convective momentum transport, while the terms on the right hand side represent, respectively, pressure forces, viscous transport, and body forces, such as gravity.

In turbulent flow, it is customary to assume that the velocity at any point can be taken to be the sum of the mean (time-averaged) and fluctuating components, i.e.:

$$u_i = \overline{u}_i + u_i' \tag{3.3}$$

Using this equation the continuity equation can be rewritten as:

$$\frac{\partial \overline{u}_i}{\partial x_i} = 0 \tag{3.4}$$

And the time-averaged momentum equation, which can be used for the prediction of the velocities in turbulent flow, becomes:

$$\frac{\partial \overline{u}_i}{\partial t} + \overline{u}_j \frac{\partial \overline{u}_i}{\partial x_j} = -\frac{1}{\rho}\frac{\partial \overline{P}}{\partial x_i} + \nu \nabla^2 \overline{u}_i + g_i - \frac{\partial}{\partial x_j}\left(\overline{u_i' u_j'}\right) \tag{3.5}$$

The last term in Eq. 3.5 represents the Reynolds stresses containing the product of the fluctuating velocity components. Since the Reynolds stresses cannot be predicted from first principles, they are typically calculated by making some assumptions about their relationship with other variables (closure problem). A number of different turbulence models are available for this purpose. Software packages such as FLUENT offer different turbulence models to solve the closure problem.

However, it is unfortunately that there is no single turbulence model can be superior for all classes of problems. The choice of turbulence model depends on the nature of the flow system, the accuracy level, the available computational resources *etc.* Based on the nature and the Operating Conditions of the USP Dissolution Apparatus II vessel, considering the specialty of the turbulence models provided by the simulation solver FLUENT 6.1.22 and the computing resources on hand, for the current project, to account for the turbulent effects during the numerical simulations, CFD simulations were conducted for Operating Condition 1 using different turbulence models, i.e., the k-ω model with low Reynolds number correction, RNG k-ϵ model, and Realizable k-ε model(Wilcox, 1998, Hanjalic et al. 2003), or with no turbulence model at all, i.e.,

assuming laminar flow. The simulation results from all models were compared to experimental results from Laser Doppler Velocimetry (LDV). After preliminary results were obtained, as described in Chapter 4, the k-ω model with low Reynolds number correction was selected and used throughout this work for all Operating Conditions.

3.3.1 RNG and Realizable k-ε Turbulence Model

Both of this two turbulence models were developed from standard k-ε model (Launder and Spalding, 1974), which is a semi-empirical model based on model transport equations for the turbulence kinetic energy (k) and its dissipation rate (ε). The model transport equation for k is derived from the exact equation, while the model transport equation for ε was obtained using physical reasoning and bears little resemblance to its mathematically exact counterpart. In the derivation of the k-ε model, it was assumed that the flow is fully turbulent, and the effects of molecular viscosity are negligible. The standard k-ε model is therefore valid only for fully turbulent flows.

The governing transport equations for the standard k-ε model are:

$$\frac{\partial k}{\partial t}+\bar{u}_i\frac{\partial k}{\partial x_i}=\frac{\partial}{\partial x_i}\left(\frac{\nu_t}{\sigma_k}\frac{\partial k}{\partial x_i}\right)+\nu_t\left(\frac{\partial \bar{u}_i}{\partial x_j}+\frac{\partial \bar{u}_j}{\partial x_i}\right)\frac{\partial \bar{u}_i}{\partial x_j}-\varepsilon \tag{3.6}$$

and

$$\frac{\partial \varepsilon}{\partial t}+\bar{u}_i\frac{\partial \varepsilon}{\partial x_i}=\frac{\partial}{\partial x_j}\left(\frac{\nu_t}{\sigma_\varepsilon}\frac{\partial \varepsilon}{\partial x_i}\right)+C_{1\varepsilon}\frac{\varepsilon}{k}G-C_{2\varepsilon}\frac{\varepsilon^2}{k} \tag{3.7}$$

Where G is the generation of k and is given by:

$$G = \nu_t \left(\frac{\partial \bar{u}_i}{\partial x_i} + \frac{\partial \bar{u}_j}{\partial x_i} \right) \frac{\partial \bar{u}_i}{\partial x_j} \tag{3.8}$$

The turbulent viscosity is then related to k and ε by the expression:

$$\nu_t = C_\mu \frac{k^2}{\varepsilon} \tag{3.9}$$

The coefficients C_μ, $C_{1\varepsilon}$, $C_{2\varepsilon}$, σ_k and σ_ε are constants which have the empirically derived values of 0.09, 1.44, 1.92, 1.0 and 1.3(Launder and Spalding, 1974).

The RNG-based k-ε turbulence model is derived from the instantaneous Navier-Stokes equations, using a mathematical technique called "renormalization group" (RNG) methods. The analytical derivation results in a model with constants different from those in the standard k-ε model, and additional terms and functions in the transport equations for k and ε (FLUENT Inc., 2005). RNG-based k-ε turbulence model provides not only accuracy but also efficiency when modeling turbulence flow. It is expected to provide better prediction for rapidly strained flows and the flows with streamline curvature.

The governing transport equations for the RNG k-ε Turbulence Model are:

$$\frac{\partial k}{\partial t} + \bar{u}_i \frac{\partial k}{\partial x_i} = \nu_t S^2 - \varepsilon + \frac{\partial}{\partial x_i} \left(\alpha \nu_t \frac{\partial k}{\partial x_i} \right) \tag{3.10}$$

and

$$\frac{\partial \varepsilon}{\partial t} + \bar{u}_i \frac{\partial \varepsilon}{\partial x_i} = C_{\varepsilon 1} \frac{\varepsilon}{k} \nu_t S^2 - C_{\varepsilon 2} \frac{\varepsilon^2}{k} - R + \frac{\partial}{\partial x_i} \left(\alpha \nu_t \frac{\partial \varepsilon}{\partial x_i} \right) \tag{3.11}$$

Here ν_0 is the molecular viscosity and

$$S^2 = 2 S_{ij} S_{ij} \tag{3.12}$$

is the magnitude of the rate-of-strain. $C_{\varepsilon 1}$, $C_{\varepsilon 2}$ and α are constants which have individual value of 1.42, 1.68 and 1.39. (Choudhury, 1993).

In addition to the standard and RNG-based k-ε models, FLUENT also provides the so-called realizable k-ε model (Shih et al. 1995). The term "realizable" means that the model satisfies certain mathematical constraints on the normal stresses, consistent with the physics of turbulent flows. The realizable k-ε model was intended to address those deficiencies of traditional k-ε models by adopting the following (Shih et al. 1995): a new eddy-viscosity formula involving a variable C_{μ} originally proposed by Reynolds (1987); a new model equation for dissipation ε based on the dynamic equation of the mean-square velocity fluctuation (FLUENT Inc., 2005).

The governing transport equations for the RNG k-ε Turbulence Model are:

$$\frac{\partial}{\partial t}(\rho k)+\frac{\partial}{\partial x_j}(\rho k u_j)=\frac{\partial}{\partial x_j}\left[\left(\mu+\frac{\mu_t}{\sigma_k}\right)\frac{\partial k}{\partial x_j}\right]+G_k+G_b-\rho\varepsilon-Y_M+S_k \tag{3.13}$$

and

$$\frac{\partial}{\partial t}(\rho \varepsilon)+\frac{\partial}{\partial x_j}(\rho \varepsilon u_j)=\frac{\partial}{\partial x_j}\left[\left(\mu+\frac{\mu_t}{\sigma_\varepsilon}\right)\frac{\partial \varepsilon}{\partial x_j}\right]+\rho C_1 S\varepsilon-\rho C_2\frac{\varepsilon^2}{k+\sqrt{\nu\varepsilon}}+C_{1\varepsilon}\frac{\varepsilon}{k}C_{3\varepsilon}G_b+S_\varepsilon \tag{3.14}$$

Where

$$C_1=\max\left[0.43,\frac{\eta}{\eta+5}\right] \tag{3.15}$$

$$\eta=S\frac{k}{\varepsilon} \tag{3.16}$$

$$S = \sqrt{2S_{ij}S_{ij}} \tag{3.17}$$

In these equations, G_k represents the generation of the turbulence kinetic energy due to the mean velocity gradients. G_b is the generation of turbulent kinetic energy due to buoyancy. Y_M represents the contribution of the fluctuating dilatation in compressible turbulence due to the overall dissipation rate. C_2 and $C_{1\varepsilon}$ are constants. σ_k and σ_ε are turbulent Prandtl numbers for k and ε. S_k and S_ε are user-defined source terms (FLUENT Inc., 2005).

3.3.2 *k-ω* Turbulence Model with Low-Reynolds-Number Correction

The standard *k-ω* model is an empirical model based on model transport equations for the turbulence kinetic energy (*k*) and the specific dissipation rate (*ω*), which can also be thought of as the ratio of ε to *k*.

The standard *k-ω* model was first introduced by Wilcox, D. in 1998. The *k-ω* model has been modified over the years, production terms have been added to both the *k* and ω equations, which have improved the accuracy of the model for predicting free shear flows. It has lower sensitivity to boundary conditions. It has good performance for free shear and low Reynolds number flows. (FLUENT Inc., 2005, Zhang and Kleinstreuer, 2003).

The governing equations for the standard *k-ω* model are:

$$\frac{\partial}{\partial t}(\rho k) + \frac{\partial}{\partial x_i}(\rho k u_i) = \frac{\partial}{\partial x_j}\left(\Gamma_k \frac{\partial k}{\partial x_j}\right) + G_k - Y_k \tag{3.18}$$

$$\frac{\partial}{\partial t}(\rho\omega) + \frac{\partial}{\partial x_i}(\rho\omega u_i) = \frac{\partial}{\partial x_j}\left(\Gamma_\omega \frac{\partial \omega}{\partial x_j}\right) + G_\omega - Y_\omega \tag{3.19}$$

where, the term G_k represents the generation of turbulence kinetic energy due to mean velocity gradients. G_ω represents the generation of ω. Γ_k and Γ_ω respectively represent the effective diffusivity of k and ω. Y_k and Y_ω are the dissipation of k and ω due to turbulence.

$$\Gamma_k = \mu + \frac{\mu_t}{\sigma_k} \tag{3.20}$$

$$\Gamma_\omega = \mu + \frac{\mu_t}{\sigma_\omega} \tag{3.21}$$

where σ_k and σ_ω are the turbulent Prandtl numbers for k and ω. The turbulent viscosity, μ_t, is computed by combining k and ω as follows:

$$\mu_t = \alpha^* \frac{\rho k}{\omega} \tag{3.22}$$

The k-ω model with low-Reynolds-number Correction is from a modification of the standard k-ω model by defining a different form of α^*. The coefficient α^* damps the turbulent viscosity causing a low-Reynolds-number correction. It is given by:

$$\alpha^* = \alpha_\infty^* \left(\frac{\alpha_0^* + \mathrm{Re}_t / R_k}{1 + \mathrm{Re}_t / R_k}\right) \tag{3.23}$$

Where

$$\mathrm{Re}_t = \frac{\rho k}{\mu \omega} \tag{3.24}$$

$$R_k = 6 \tag{3.25}$$

$$\alpha_0^* = \frac{\beta_i}{3} \tag{3.26}$$

$$\beta_i = 0.0072 \tag{3.27}$$

In standard k-ω model, $\alpha^* = \alpha_\infty^* = 1$. k-ω turbulence model with low-Reynolds-number correction is better than the standard k-ω model when predicting transitional flow.

However, good convergence cannot be easily achieved by using k-ω models. Under relaxation parameters need to be adjusted carefully to get well converged simulation results.

3.4 Boundary Conditions

Proper boundary conditions must properly assigned to the fluid system prior to solving the Computational Fluid Dynamics (CFD) simulation.

The no-slip condition in the appropriate frame of reference was assumed at all solid surfaces. The air-water interface was always assumed to be flat, since the agitation speed in this work was low enough (less than 100 RPM) to prevent the formation of a vortex, as visually confirmed in the experiments. The air-water interface was modeled as a frictionless surface, and the normal gradients of all variables were zero at this interface.

As mentioned in Chapter 2, the LDV apparatus can determine only the average velocity (separately for each component) at a given location, by measuring the instantaneous local velocities at that location over a period of time, typically 60 seconds, during which the impeller rotates but the measurement location relative to the (fixed) vessel does not. The instrument then determines the time-averaged velocity component at that location as well as other statistics. By contrast, the CFD simulations produce time-invariant three-dimensional flow predictions where the velocities vary with position, including the azimuthal position. However, since the dissolution vessel is unbaffled under Operating Condition 1 and the flow field is symmetrical, the CFD-predicted flow can also be viewed as a time-dependent flow in which the velocity at a given fixed location is a function of the its azimuthal position relative to the rotating impeller. Therefore, in order to compare the LDV data with the CFD predictions under Operating Condition 1, the CFD-predicted velocities at a given axial and radial position but different azimuth must be averaged along the circumference passing through that point in

order to generate an average azimuthal velocity that can be compared with the time-averaged velocity of the LDV at the same axial and radial position.

When predicting velocity profile for Operating Condition 1,2 and 3, for each velocity component, the CFD-predicted velocities at eight different azimuth positions at the same radial location on a given iso-surface were averaged to give a single value of the azimuth ensemble-averaged velocity component at that location. The ensemble-average local velocity component values so obtained could be compared with the time-averaged velocity measurements obtained experimentally with the LDV.

3.5 Reference Frame

A rotating reference frame approach was used in simulations for all Operating Conditions (Operating Condition 1, 2, 3, 4, 5 and 6) for which the computation domains were symmetric. In this frame of reference, the vessel wall was assumed to be rotating, and the impeller was stationary, although the appropriate body forces were included in the computation to account for the non-inertial characteristics of the rotating reference frame.

When the equations of motion are solved in a rotating reference frame, the acceleration of the fluid is augmented by additional terms that appear in the momentum equations (Batchelor, 1967). The absolute velocity $\vec{v}$ and the relative velocity in the reference frame are related by the following equation:

$$\vec{v}_r = \vec{v} - (\vec{\Omega} \times \vec{r}) \tag{3.28}$$

where, $\vec{\Omega}$ and $\vec{r}$ are the angular velocity vector and the position of the vector in the rotating reference frame respectively. The left-hand side of the momentum equations appears as follows for an inertial reference frame:

$$\frac{\partial}{\partial t}(\rho\vec{v}) + \nabla \cdot (\rho\vec{v}\vec{v}) \tag{3.29}$$

For a rotating reference frame, the left-hand side written in terms of absolute velocities becomes:

$$\frac{\partial}{\partial t}(\rho\vec{v}) + \nabla \cdot (\rho\vec{v}_r\vec{v}) + \rho(\vec{\Omega} \times \vec{v}) \tag{3.30}$$

In terms of relative velocities the left-hand side becomes:

$$\frac{\partial}{\partial t}(\rho\vec{v}_r) + \nabla \cdot (\rho\vec{v}_r\vec{v}_r) + \rho(2\vec{\Omega} \times \vec{v}_r + \vec{\Omega} \times \vec{\Omega} \times \vec{r}) + \rho\frac{\partial\vec{\Omega}}{\partial t} \times \vec{r} \tag{3.31}$$

Figure 3.2 shows the relation between origin reference frame and the rotating reference frame.

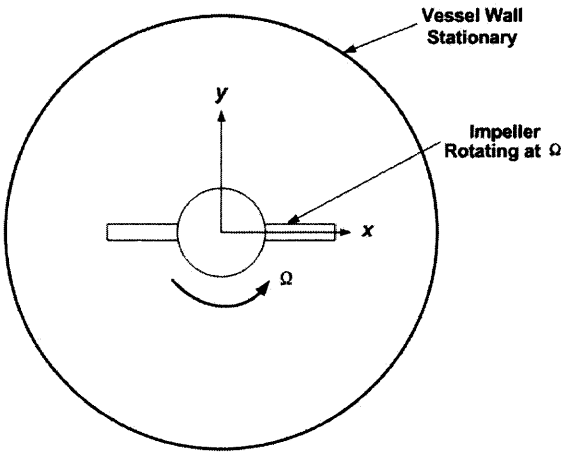

(a) Original Reference Frame

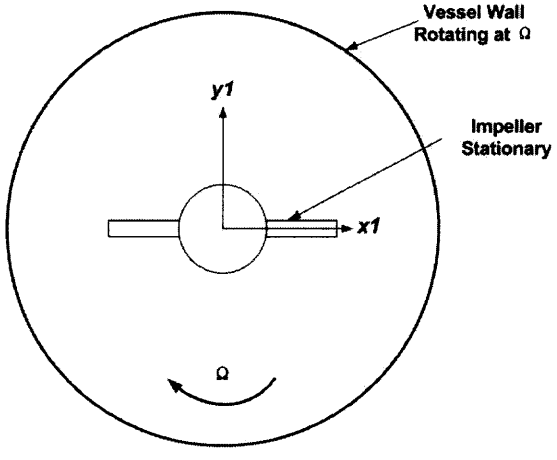

(a) Rotating Reference Frame

Figure 3.2 Transforming coordinates from absolute frame to a rotating reference frame, top view.

Simulations were also conducted in systems that were not symmetric, as in those Operating Conditions (Operating Conditions 7, 8 and 9) where a tablet was present at an offset location at the bottom of the vessel, or the impeller was placed off center to simulate slight misalignment. In these Operating Conditions, a single frame or reference could not be used because there exists strong intrinsic periodic unsteadinesses due to the relative motion between the impeller and the tablet or the asymmetry of the domain.

The most accurate way to simulate these kinds of systems is to carry out a fully time dependent CFD simulation. However, this approach will be extremely expensive in terms of memory use and computational time. In such situation, small time steps are defined prior to starting the simulation. Convergence must be achieved at each time step before moving to the next one. This procedure keeps being repeated until "a time dependent steady state achieved" (Coy 1996; Harvey III and Rogers 1996).

A less expensive approach has been developed and applied to overcome the limitations of using steady state boundary conditions while permits the unsteady features to be retained. This approach is termed Multiple Reference Frames (MRF) model (Luo et al. 1994; Luo et al. 1993, Akiti and Armenante, 2004; Akiti et al. 2004). The MRF approach overcomes some of the problems associated with a completely steady-state approach while still solving an inherently unsteady-state system. This translates into considerable savings in computer resources if compared to the more accurate but time-consuming fully time-dependent CFD simulation approach. In MRF, the volume is divided into two domains: an inner cylindrical domain including the impeller, and an outer domain comprising the vessel wall possibly including the tablet or in an offset position with respect to the impeller. In the inner domain frame, the conservation

equations are transformed into a rotating reference frame and the flow is computed in a steady state manner, thus reducing an inherently time-dependent process as a steady-state flow. The outer domain is modeled at steady state in a stationary reference frame. The results are transformed back to stationary reference frame at the end of the simulation. Figure 3.3 shows the rotating and stationary frames of reference for MRF model.

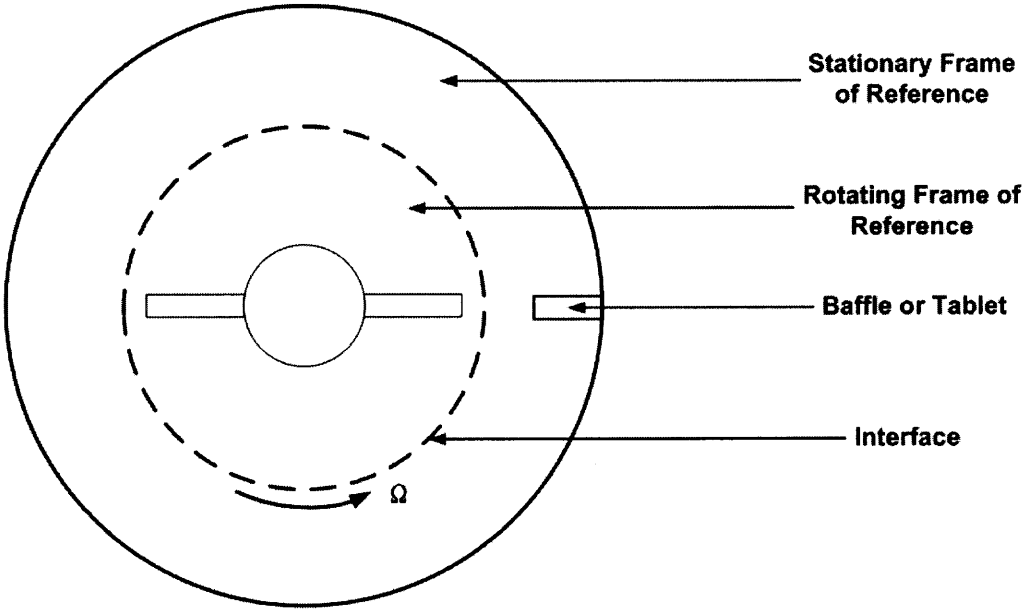

Figure 3.3 Frames of reference for MRF model, top view.

Since the MRF formulation involves the solution of the model equations in two different frames of reference, it is possible that in some regions (in particular at the interface between the rotating reference frame and the stationary reference frame) the solution of a particular variable will depend on the values of other variables in portions of the solution domain that may not be in the same frame of reference. In such a situation, appropriate transformations from one frame to the other are performed to ensure that the

solution is performed in a frame of reference consistent with the variable of interest. Details are provided elsewhere (Akiti and Armenante, 2004).

3.6 Numerical Simulation for Blend Time Study

CFD has been proven to be a valuable tool to predict blend time in a stirred vessel (Jaworski and Dudczak, 1998, Murthy and Jayanti, 2002, Zhou et al. Campolo and Soldati, 2004, Yoeh et al. 2005). CFD simulations were applied to predict the blend time for Operating Conditions 1, 2, 3, 5 and 6. The simulation results for Operating Condition 1 were compared with the results from blend time experiments. The starting point to predict blend time for each Operating Conditions mentioned above was the converged simulation of the flow field with the k-ω model with low Reynolds number correction described in section 3.3.

Once the velocity distribution is computed, the CFD solver can simulate species transport phenomena in the computational domain. This is accomplished by calculating the local mass fraction of each species, Y_i, obtained solving the mass balance equation for the generic ith species, incorporating convective-diffusive mass transfer. The conservation equation has the following general form (FLUENT Inc., 2005):

$$\frac{\partial}{\partial t}(\rho Y_i) + \nabla \cdot (\rho \bar{v} Y_i) = -\nabla \cdot \vec{J}_i + R_i + S_i \tag{3.32}$$

where R_i is the net rate of production of species i by chemical reaction (equal to zero in blend time simulations because there is no chemical reaction), S_i is the rate of creation by addition from the dispersed phase plus any user-defined sources (equal to zero here), and $\vec{J}_i$ is the diffusion flux of species i, which arises because of the concentration gradients. For laminar and dilute flows:

$$\vec{J}_i = -\rho D_{i,m} \nabla Y_i \tag{3.33}$$

For turbulence flows:

$$\vec{J}_i = -\left(\rho D_{i,m} + \frac{\mu_t}{Sc_t}\right)\nabla Y_i \tag{3.34}$$

where $D_{i,m}$ is the diffusion coefficient for species i in the mixture, Sc_t is the turbulent Schmidt number, and μ_t is the turbulent viscosity.

During the tracer transport simulations, the unsteady solver in FLUENT was turned on, and a "tracer" chemical species with the same physical and chemical properties of the fluid in the vessel was numerically "injected" into the vessel at time t=0. The tracer concentration throughout the vessel was calculated by the solver at the end of each time step (equal to 0.1 seconds in this work). Two probe points were defined in FLUENT to have the same positions of the two monitoring points in the blend time experiments for Operating Condition 1. The concentrations of the tracer as a function of time was predicted at each probe point. Blend time was numerically obtained when the tracer concentrations reached same relative concentration level obtained from the discoloration experiments without the conductivity probe at a selected monitoring point.

3.7 Determine the Power Dissipation and Power Number for the System

The power delivered by the impeller to the system is an important design parameter for any mixing device. Computational Fluid Dynamics (CFD) software used in this work, FLUENT 6.1.22, sums the cross product of the radius vector and the force vector at all nodes on the impeller surface to get the total torque ($\vec{\tau}$) of the system, which is directed along the shaft axis. The force on the impeller includes both shear and normal forces. Tangential velocity gradients from the surface are used to calculate the shear force and surface pressure and cell area are used to calculate the normal forces. The production of the total torque and the impeller rotation speed allows calculate the power imparted by the impeller to the system:

$$P = \omega\tau = 2\pi N\tau \tag{3.35}$$

where, ω is the angular rotation speed of the impeller in RPS.

Based on experimental data, power dissipated by the impeller into the system, P, is proportion to the cube of the rotation speed of the impeller, the fifth power of the impeller diameter and fluid density with the following relationship:

$$P = N_p N^3 D^5 \rho \tag{3.36}$$

Where N_p is a dimensionless constant for a certain stirred mixing system, defined as power number. From Equation 3.36, one can get:

$$N_p = \frac{P}{\rho N^3 D^5} \tag{3.37}$$

In this work, the calculated power, P and power number, N_p for USP Dissolution Apparatus II under different Operating Conditions were only compared to the published correlations (Nagata, 1975).

3.8 Numerical Modeling of Particle Suspension

FLUENT 6.1.22 could predict the trajectory of a discrete phase particle (or droplet or bubble) by integrating the force balance on the particle, which is written in a Lagrangian reference frame. This force balance equates the particle inertia with the forces acting on the particle, and can be written (for the x direction in Cartesian coordinates) as:

$$\frac{d_{u_p}}{d_t} = F_D\left(u - u_p\right) + \frac{g_x(\rho_p - \rho)}{\rho_p} + F_x \tag{3.38}$$

where, $g_x(\rho_p - \rho)/\rho_p$ is the body force, u is the fluid phase velocity, u_p is the particle velocity, ρ is the fluid density, ρ_p is the density of the particle. Term $F_D\left(u - u_p\right)$ is the drag force per unit particle mass and

$$F_D = \frac{18\mu}{\rho_p d_p^2}\frac{C_D R_e}{24} \tag{3.39}$$

where, μ is the molecular viscosity of the fluid. d_p is the particle diameter. Re is the relative Reynolds number, which is defined as:

$$R_e = \frac{\rho d_p \left|u_p - u\right|}{\mu} \tag{3.40}$$

The drag coefficient, C_D, can be taken from:

$$C_D = a_1 + \frac{a_2}{R_e} + \frac{a_3}{R_e^2} \tag{3.41}$$

where, a_1, a_2, a_3 are constants that apply to smooth spherical particles over several ranges of Re given by Moris and Alexander (1972). C_D could be expressed in another way as:

$$C_D = \frac{24}{R_{e_{sph}}}\left(1 + b_1 {R_{e_{sph}}}^{b_2}\right) + \frac{b_3 R_{e_{sph}}}{b_4 + R_{e_{sph}}} \tag{3.42}$$

where

$$b_1 = \exp\left(2.3288 - 6.4581\phi + 2.4486\phi^2\right) \tag{3.43}$$

$$b_2 = 0.0964 + 0.05565\phi \tag{3.44}$$

$$b_3 = \exp\left(4.905 - 13.8944\phi + 18.4222\phi^2 + 15.8855\phi^3\right) \tag{3.45}$$

$$b_4 = \exp\left(1.4681 + 12.2584\phi - 20.7322\phi^2 + 15.8855\phi^3\right) \tag{3.46}$$

which are taken from Haider and Levenspiel (1989). The shape factor, ϕ, is defined as:

$$\phi = \frac{s}{S} \tag{3.47))}$$

where s is the surface area of a sphere having the same volume as the particle, and S is the actual surface area of the particle. The Reynolds number $R_{e_{sph}}$ is computed with the diameter of a sphere having the same volume.

In Eq. 3.38 the term F_x represents some additional forces that can be important under special circumstance. The first of these is the "virtual mass" force, the force required to accelerate the fluid surrounding the particle. This force can be written as:

$$F_x = \frac{1}{2}\frac{\rho}{\rho_p}\frac{d}{d_t}\left(u - u_p\right) \tag{3.48}$$

and is important when $\rho > \rho_p$. Another additional force may arise due to the pressure gradient in the fluid is:

$$F_x = \left(\frac{\rho}{\rho_p}\right)u\frac{\partial u}{\partial x} \tag{3.49}$$

These forces are optional when using FLUENT 6.1.22 according to specific situations.

The trajectory equation is numerically integrated by FLUENT 6.1.22 to produce the velocity of the particle at each point along the trajectory, where the trajectory itself is obtained through the following equation:

$$u_{pi} = \frac{dx_i}{dt} \tag{3.50}$$

i.e.

$$x_i = \int u_{pi} dt \tag{3.51}$$

Therefore, the particle position at any time inside the USP dissolution apparatus II vessel under any agitation conditions could be tracked by simulation.

In this work, preliminary CFD simulations were conducted to determine the flow field at a particular agitation in the vessel, prior to particle tracking. The k-ω model with low Reynolds number correction described in Section 3.3 was used as the turbulence model. Simulations were conducted at two agitation speed, i.e. 50 rpm and 150 rpm. The latter, is not one of the operating condition listed in Table 1.1 This simulation was conducted only to later track the (virtual) particles.

Tracking simulations consisted of adding "virtual" particles of appropriate density and size to a computational cell, run an unsteady-state particle tracking simulation to determine the particle position at any time, and then determine whether such a particle would ultimately reside in the computation cell near the vessel bottom (indicating settling) or remain somewhere else in the vessel (indicating suspension). The simulations were run to simulate a real process lasting for a period of time of 4 minutes. Experimentally it was noticed that this was a long enough period of time for the particles to settle, if they did so. The motions of the particles were simulated using the unsteady-state FLUENT solver with a time step of 0.05 seconds.

CHAPTER 4

RESULTS AND DISCUSSION

4.1 Flow Field Characterization under Operating Condition 1

4.1.1 Selection of Turbulence Model for CFD Simulations

In a preliminary study, the results of simulations based on the use of three different turbulence models (the RNG k-ϵ model, the Realizable k-ϵ model and the Standard k-ω model with Low Reynolds-Number correction) and those obtained with no turbulence model (i.e., laminar flow model) were compared with the LDV data collected on two different iso-surfaces (z=50 mm, z=-31.75 mm) located above and below the impeller, respectively. Figure 4.1 shows that the results based on the turbulence models were of the same order of magnitude, indicating that this approach was somewhat robust.

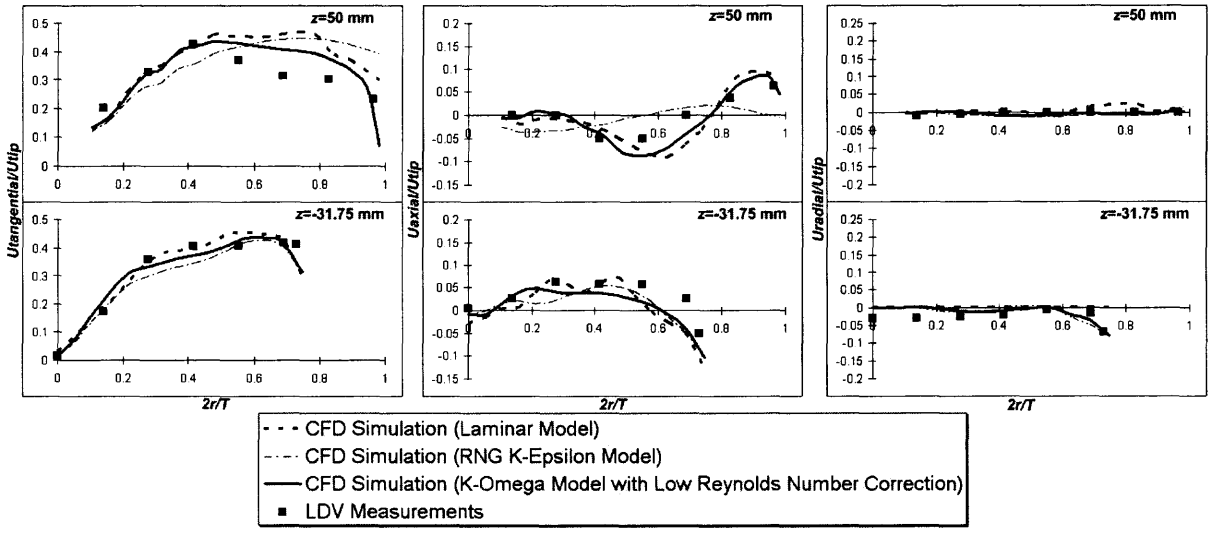

Figure 4.1 Comparison between experimental LDV velocity data and CFD predictions on iso-surface z=50 mm and z=-31.75 mm using different turbulence models under Operating Condition 1.

The k-ω simulations were generally in better agreement with the LDV data than those with any other turbulence model or in the absence of any turbulence model. For example, the highest LDV tangential velocity at z=50 mm was 43% of the impeller tip speed and was observed at relative radial position of 0.41. The k-ω simulations predicted that the peak tangential velocity was also 43% of the impeller tip speed, but at relative radial position of 0.47. By contrast, the RNG k-ϵ simulations predicted a peak velocity of 46% at relative radial position of 0.68. On the iso-surface at z=-31.75 mm, the agreement between the LDV data and the k-ω simulations was even better not only in the core region closer to the shaft, but also in the region extending beyond $2r/T$=0.27, i.e., where the velocity profiles flatten out.

As for the axial velocities, the shape and the magnitude of the velocity profiles predicted by k-ε simulations were appreciably different from the LDV data, especially for z=50 mm. The k-ω simulations predicted not only better velocity magnitudes but also shapes of the velocity profiles that were more similar to the LDV data.

Finally, the radial velocities on the iso-surface at z=50 mm were all very small (less than 3.5% of the impeller tip speed), although the k-ω prediction were much closer to the LDV data. Similarly, for z=-31.75 mm, the k-ω model predicted a better shape of the velocity profile than RNG k-ϵ model, even though the LDV data showed that the velocities were typically much smaller than 9% of the impeller tip speed.

In a separate series of simulations conducted for a slightly different geometry of the dissolution system than that used in this work another turbulence model was additionally tested, namely the Realizable k-ε model. The results obtained with this model were only marginally better than those obtained with the standard k-ε model

(results not shown). In the rest of this study, all simulations were conducted using the k-ω turbulence model with low Reynolds number correction.

4.1.2 Velocity Distribution Profiles

Figure 4.2, Figure 4.3, and Figure 4.4 show, respectively, the tangential, axial, and radial velocity profiles obtained from LDV measurements and the results of the CFD simulations based on the k-ω model with low Reynolds-Number correction. The LDV measurements on z=-6.75 mm and below were limited to locations between the hemispherical vessel wall and the impeller.

Figure 4.2 shows that all the tangential velocities, irrespective of the iso-surfaces where they were obtained, were oriented in the same direction as the impeller rotation, indicating a strong tangential flow, as in the case of other unbaffled systems (Armenante et al. 1994; Armenante and Chou, 1994; Armenante et al. 1997;Ciofalo et al. 1996; Dong et al. 1994a, 1994b; Murthy and Jayanti, 2002). Everywhere in the vessel the experimental tangential velocities were always much stronger than the other components, with peak tangential velocities ranging between 40% and 50% of the tip speed on all iso-surfaces with the exception of the iso-surfaces at z=-25.75 mm and z=-6.75 mm, where the maximum velocity was 38% to 36% of the tip speed, respectively. These velocity peaks were achieved at a radial distance $2r/T \approx 0.41$ on iso-surfaces at z=-0.75 mm and above; at a radial location very close to the blade tip on iso-surface at z=-15.75 mm (middle of the impeller blade); and at radial locations very close to the vessel wall on iso-surfaces at z=-25.75 mm and below. On the iso-surface at z=-6.75 mm, where the top

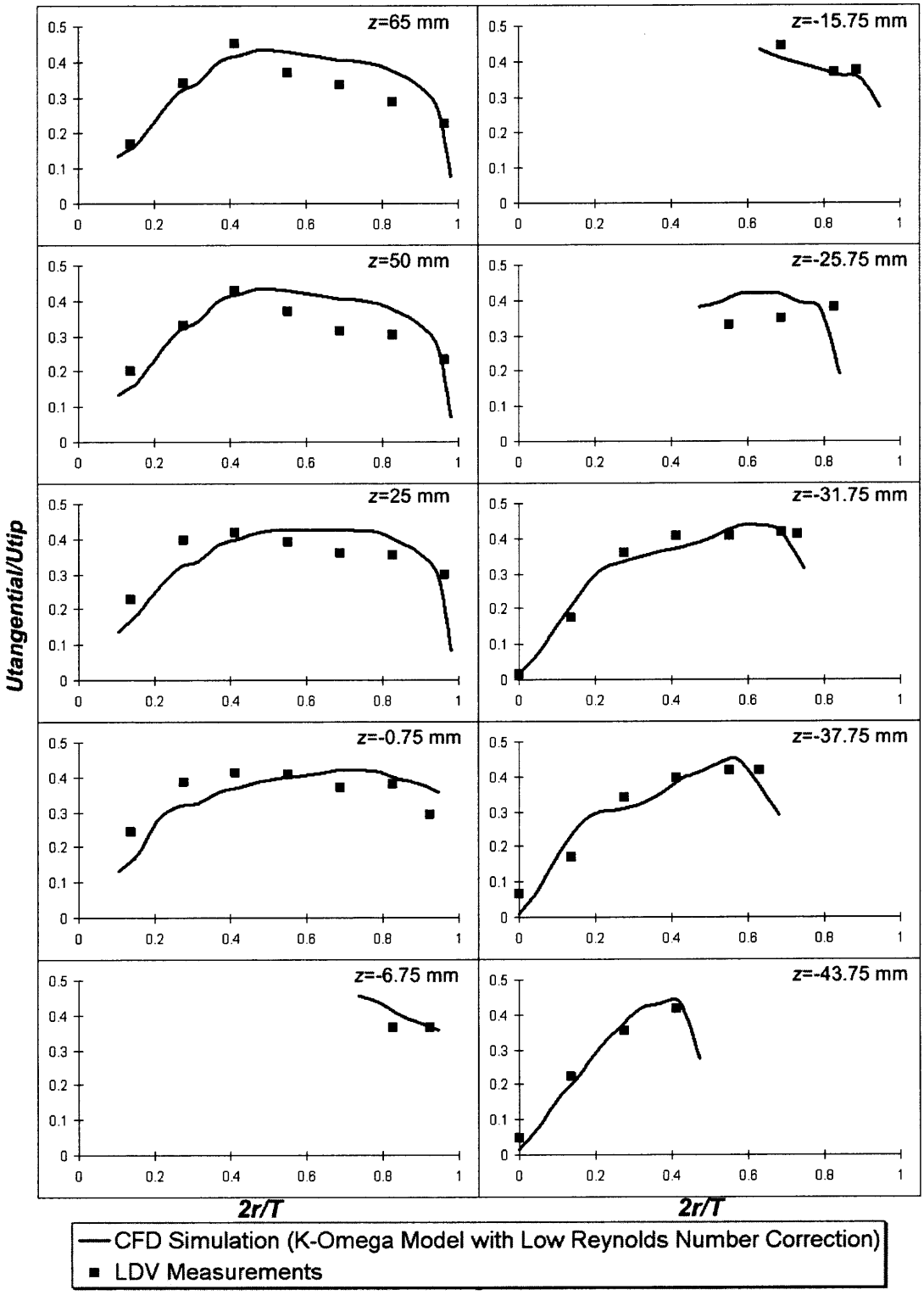

Figure 4.2 Comparison between LDV data and CFD predictions for tangential velocities on different iso-surfaces under Operating Condition 1.

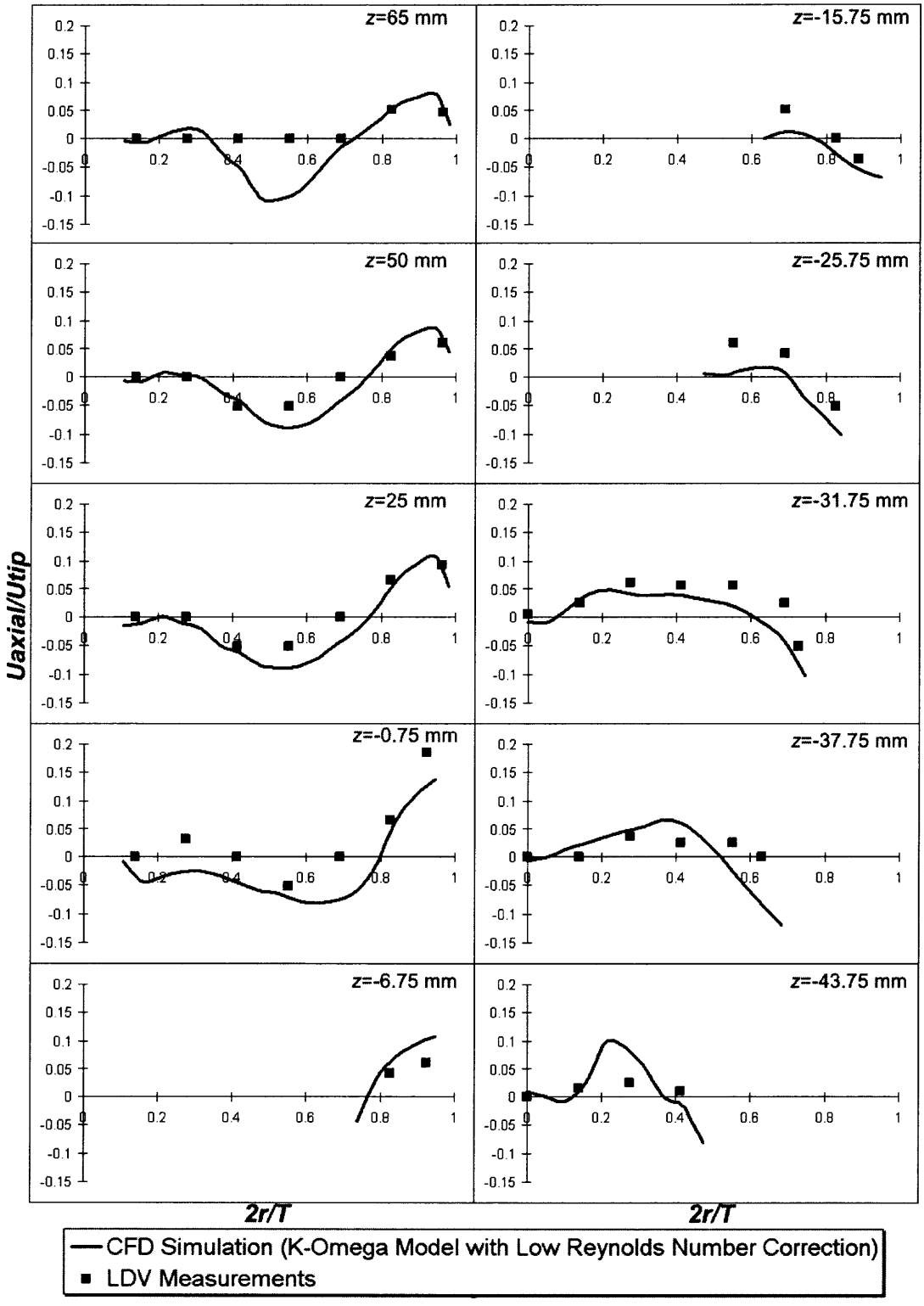

Figure 4.3 Comparison between LDV data and CFD predictions for axial velocities on different iso-surfaces under Operating Condition 1.

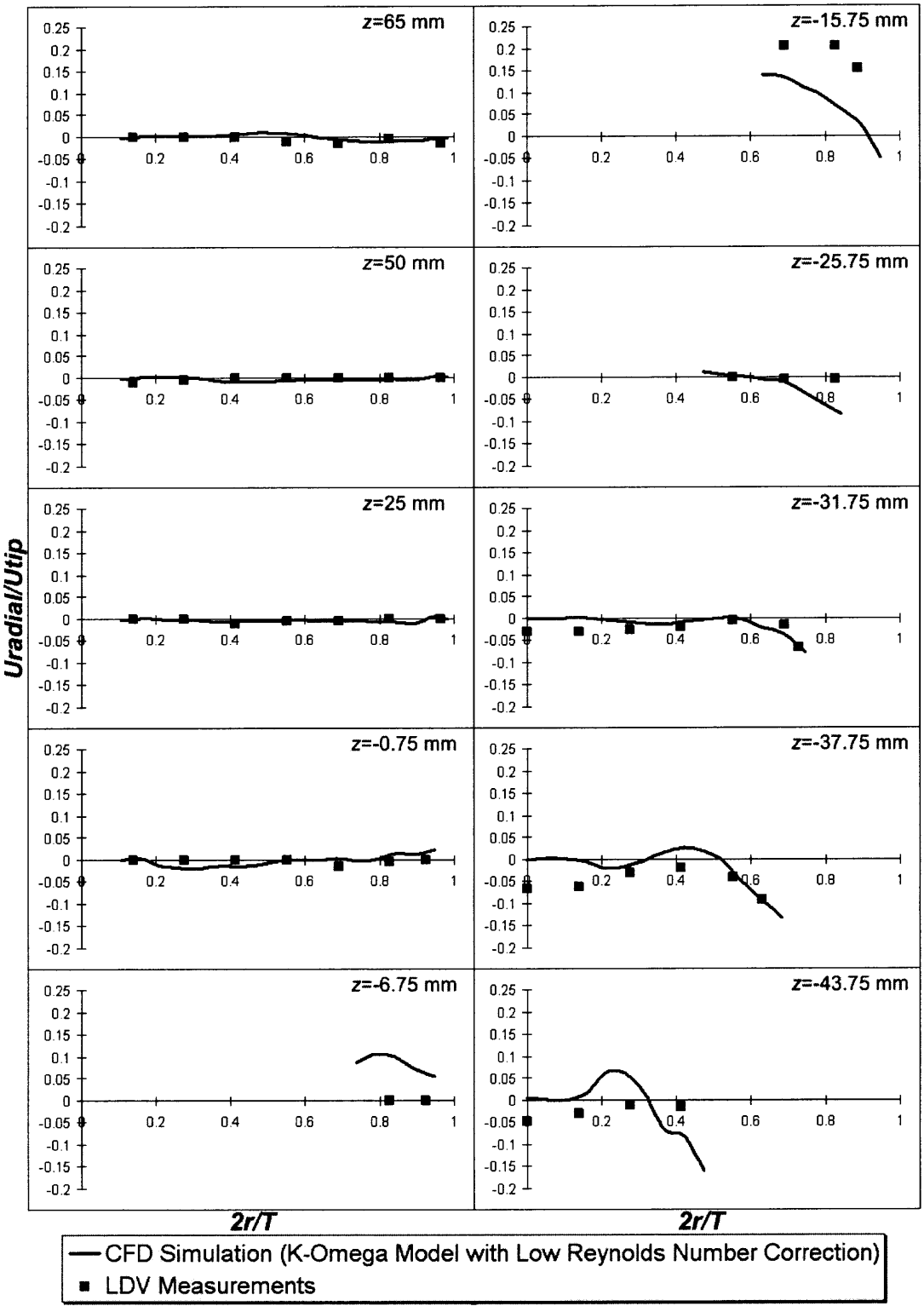

Figure 4.4 Comparison between LDV data and CFD predictions for radial velocities on different iso-surfaces under Operating Condition 1.

edge of the impeller blade is located, only two LDV measurements could be obtained. Significant although not complete agreement can be observed between the experimental data and the numerical results. Especially relevant is the good agreement between the LDV and CFD results for the tangential velocities at or below the impeller. This is the most critical region for the operation of the USP II apparatus, because of the presence of the solid dosage form somewhere on the bottom of the vessel. This is also the most difficult region where LDV measurements can be made because of the increasing curvature of the vessel with respect to the observation plane of the laser, i.e., where the laser beams enter the vessel.

In the upper region of the vessel, i.e., for $z \geq 0.75$ mm, the fluid in the inner core ($2r/T<0.4$) rotates with the shaft in solid body rotation, as indicated by the linear increase of the velocity with $2r/T$ (Figure 6). In the outer region ($2r/T>0.4$), the velocity profiles are much flatter, and decrease slowly with the radial position before dropping rapidly at the tank wall, where the fluid velocity is expected to go to zero. LDV data could not be taken too close to the wall because of the optical distortion produced by the round glass wall.

On the iso-surface z=-15.75 mm, i.e., in the middle of the impeller blade, the CFD profile matches closely the LDV measurements, showing that the peak tangential velocity occurs near the impeller tip and decreases toward the wall. For z=-6.75 mm, where the top edge of the impeller blade lies, the CFD simulation shows that the tangential velocity is higher near the impeller blade than near the wall, while the LDV measurements, although supporting the simulations, show a flat velocity profile and lower velocity magnitudes.

In the region below the impeller (z=-25.75 mm, z=-31.75 mm, z=-37.75 mm, z=-43.75 mm), both the LDV measurements and the CFD simulations show that the radial location where the peak velocity occurs is closer to the vessel wall, which is the opposite of what was observed in the region above the vessel (Figure 4.2). This can be attributed to the proximity of the impeller and to the curvature of the vessel wall, creating a fluid region where the local tangential velocity follows more closely that of the impeller.

Figure 4.3 presents the results for the axial velocities. These velocities are relatively small compared to the tangential velocities, with the magnitude of the LDV axial velocities in the 0-20% range of the tip speed, and those from the CFD simulations in the range at 0-15% of the tip speed. On most iso-surfaces, the LDV measurements and CFD the simulations produced similar axial velocity profiles, although deviations occurred. In general, the CFD simulations predicted slightly higher absolute velocity magnitudes than the LDV measurements.

The velocities on the iso-surfaces above the impeller (z=-0.75 mm, z =25 mm, z=50 mm, z=65 mm) or at the impeller top blade (z=-6.75 mm) are directed downwards near the center of the vessel and upwards near the vessel wall, creating a weak but clearly detectable top-to-bottom recirculation loop. The reverse is true in the region at or below the impeller (z=-43.75 mm, z=-37.75 mm, z=-31.75 mm, z=-25.75 mm and z=-15.75 mm), where the flow near the wall is directed downwards. This is the result of the jet emanating radially from the impeller, impinging on the vessel wall, and then creating two weak recirculation loops above and below the impeller. This is typical of most radial (paddle-like) impellers, although in the USP II vessel the hemispherical bottom, the

absence of baffles, and the relatively large size of the impeller with respect to the vessel diameter produce an even weaker flow in the region below the impeller.

On the iso-surface at z=65 mm, the LDV measurements show a flat velocity profile with almost zero velocity magnitude in the region $0.13<2r/T<0.68$, while the CFD simulations show negative velocities (Figure 7). The discrepancy between these curves is an indication that the recirculation loop in the portion above the impeller actually "closes" below the iso-surface at z=65 mm (i.e., the flow converges back toward the shaft), while the CFD simulation predicts that this recirculation effect occurs at a higher vertical location. For z=-25.75 mm, z=-6.75 mm, z=-0.75 mm, z=-15.75 mm, the LDV and CFD profiles are similar, but translated vertically with respect to each other.

Finally, Figure 4.4 presents the results for the radial velocities. In the upper portion of the vessel (iso-surfaces at z=-0.75 mm, z=25 mm, z=50 mm, z=65 mm), both the LDV measurements and CFD simulations show that the magnitude of the radial velocities is very small (less than 2.5% of the impeller tip speed), i.e., a very weak radial flow. As for the impeller region, on the iso-surface at z=-6.75 mm, the LDV measurements show an almost zero radial velocity magnitude, i.e., no radial flow. However, the CFD simulation shows positive (i.e., outward) radial velocities. For z=-15.75 mm, the reverse is true, i.e., a positive radial velocity with a relatively high velocity magnitude of 22% of the impeller tip speed was measured with the LDV. This is reasonable because in this region the impeller blade should push the fluid toward the wall. The CFD simulation also shows positive velocities, but their magnitudes are only about half of the LDV measurements. All this means that the radial velocity is over predicted by CFD near the upper edge of the blade and is under predicted it in the middle

of the impeller and near its lower edge, which implies that there is a small discrepancy between CFD predictions and LDV data about the exact location where the impeller produces the expected outward directed radial jet. Apparently, CFD predicts this point to be slightly higher than what actually observed experimentally. However, the phenomenon is adequately predicted by the CFD simulations. This change in radial flow must occur over a very small vertical distance in the small gap between the impeller blade and the vessel wall. Therefore, in this region, even a small error in the prediction of the location where this flow reversal occurs can produce a larger discrepancy with the experimental data.

Below the impeller, the radial velocity is typically negative, although still small. This is also expected since the flow must be negative near the vessel wall in this region, as the curvature of the vessel redirects the radial flow generated by the impeller inwards and toward the bottom of the vessel. This is what both the LDV measurements and CFD prediction show for lower iso-surfaces.

As already mentioned, the difference between the slightly larger shaft diameter at the blade used in this work instead of the more commonly used uniform shaft diameter is so small that the results obtained here are expected to be equally valid for the USP impeller with no collar at the impeller blade.

4.1.3 Velocity Magnitude and Velocity Vectors

Figure 4.5 shows the contours of the CFD-predicted velocity magnitude on a vertical cross section through the impeller shaft for different orientations of the impeller. The impeller plane is defined here as y-plane and the plane perpendicular to y-plane is defined as x-plane. Figure 4.6 presents the same contours plots of the velocity magnitude on iso-surfaces at different vertical (axial) locations. Additional plots show the velocity vectors on a vertical cross section through the impeller shaft at different orientations of the impeller (Figure 4.7), an expanded view of the velocity vectors in impeller region (Figure 4.8), an expanded view of velocity vectors near vessel bottom region for two different impeller orientations (Figure 4.9), and, finally, the velocity vectors on the iso-surfaces at different vertical locations (Figure 4.10). In some of these figures, the greater vector density in the lower portion of the vessel is an artifact caused by the greater concentration of computational cells in that region (Figure 3.1).

A full picture of the three-dimensional flow in the USP II vessel emerges by looking at all these figures and by combining them with the velocity profiles previously discussed (Figures 4.2 to Figure 4.4). The top portion of the vessel is dominated by a strong tangential flow. A much weaker circulation loop caused by the impeller rotation is also present on the vertical cross section in the upper region of the vessel. The radial jet generated by the rotating impeller near the top edge of the blade impinges on the wall, producing an axial upward flow near the vessel wall. This flow is confined in the outer region of the vessel ($2r/T>\sim0.7$; Figures 4.7 and Figure 4.8). The CFD simulation predicts that this loop closes very high in the tank, as indicated by the relatively stronger radial flow near the air-liquid interface (Figure 4.7). In the middle inner core region

above the impeller (~0.3<2*r/T*<~0.7), the flow is directed downwards. It should be remarked that this region does not extend all the way to the center of the vessel to include the shaft. Instead, the innermost core region (2*r/T*<~0.3) is characterized by very low axial and radial velocities (Figures 4.3 and Figure 4.4) and by tangential velocities increasing proportionally to the radial position (Figure 4.2). In other words, the inner core rotates almost as a solid body.

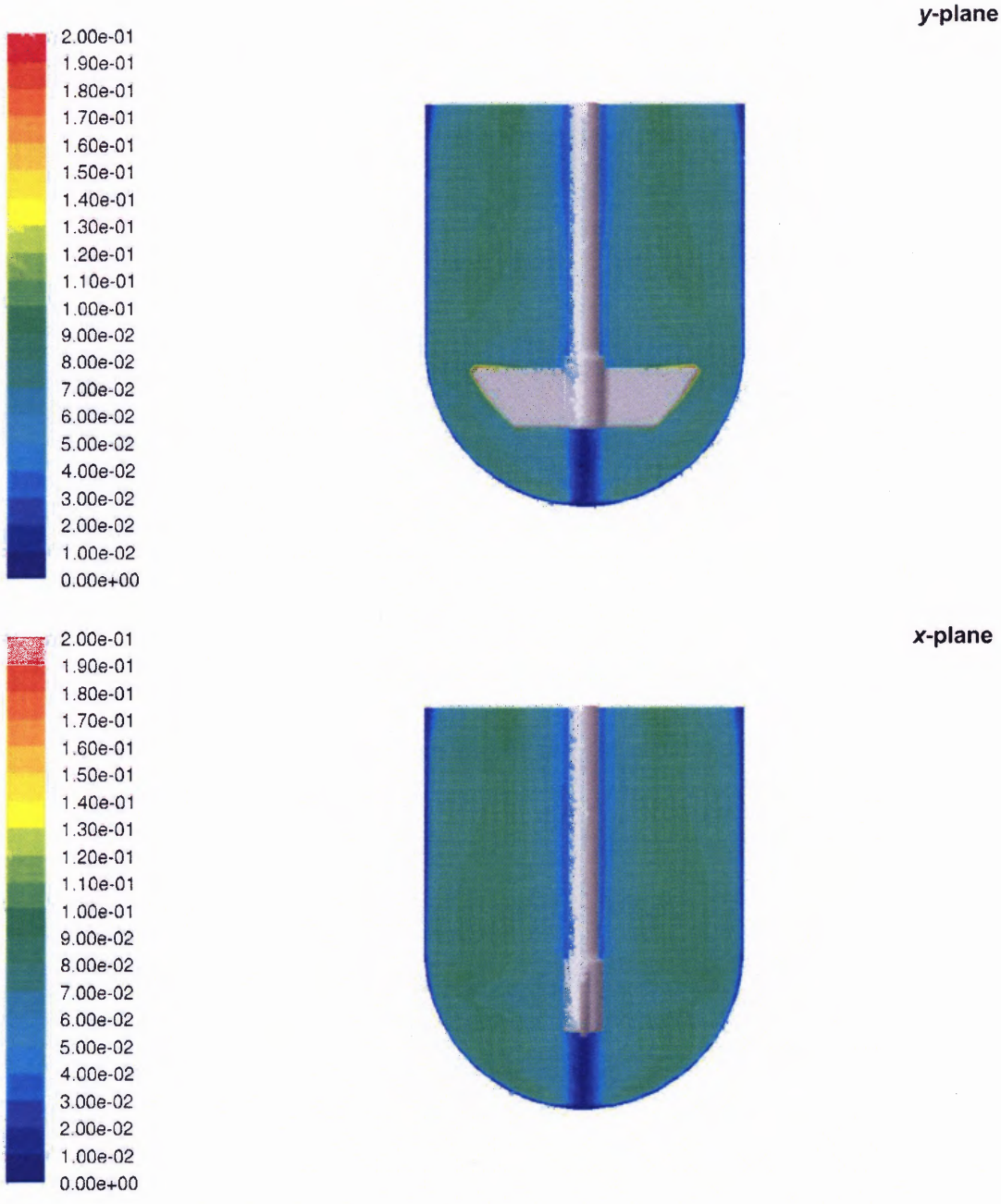

Figure 4.5 CFD predictions of the velocity magnitude on vertical cross sections through the impeller shaft for different impeller orientations under Operating Condition 1 (m/s).

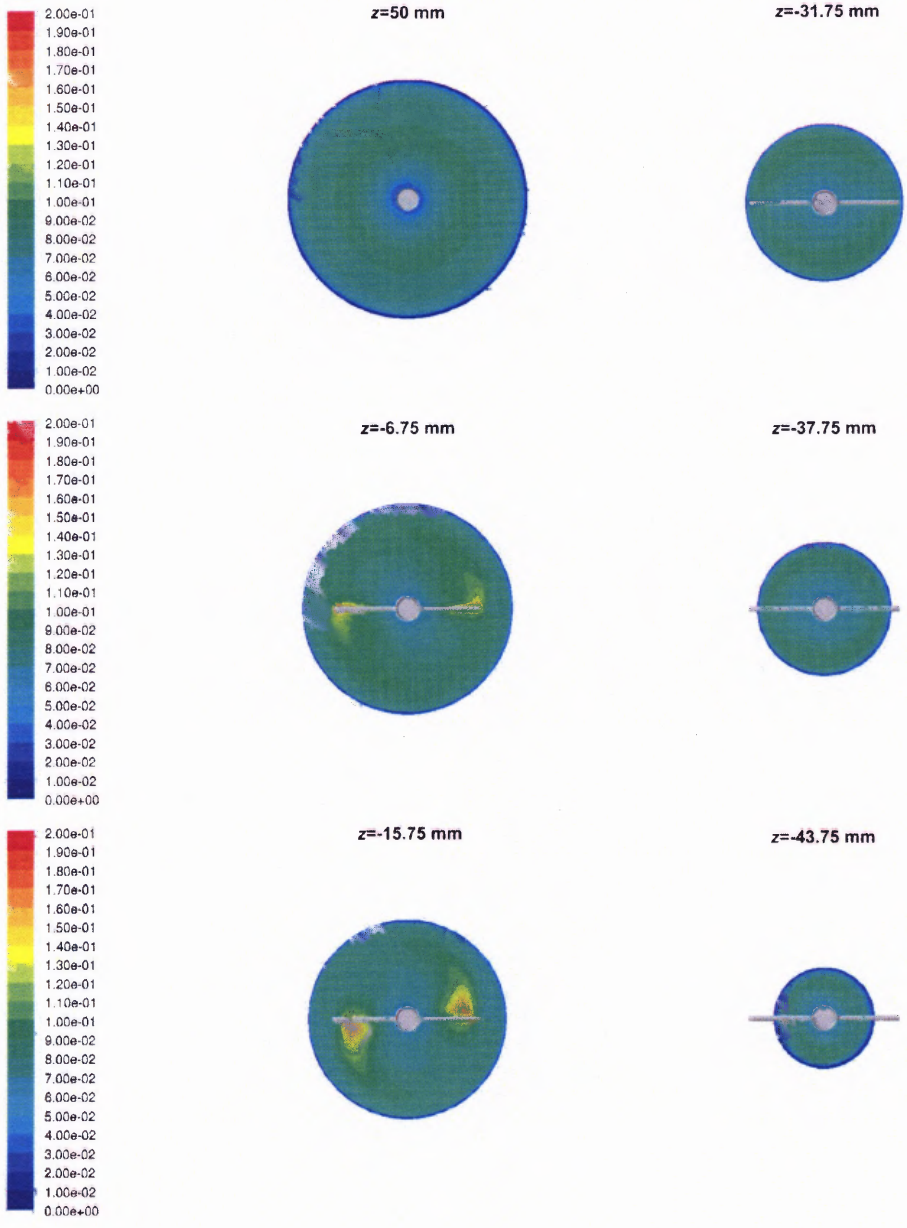

Figure 4.6 CFD predictions of velocity magnitude on different iso-surfaces under Operating Condition 1 (m/s)

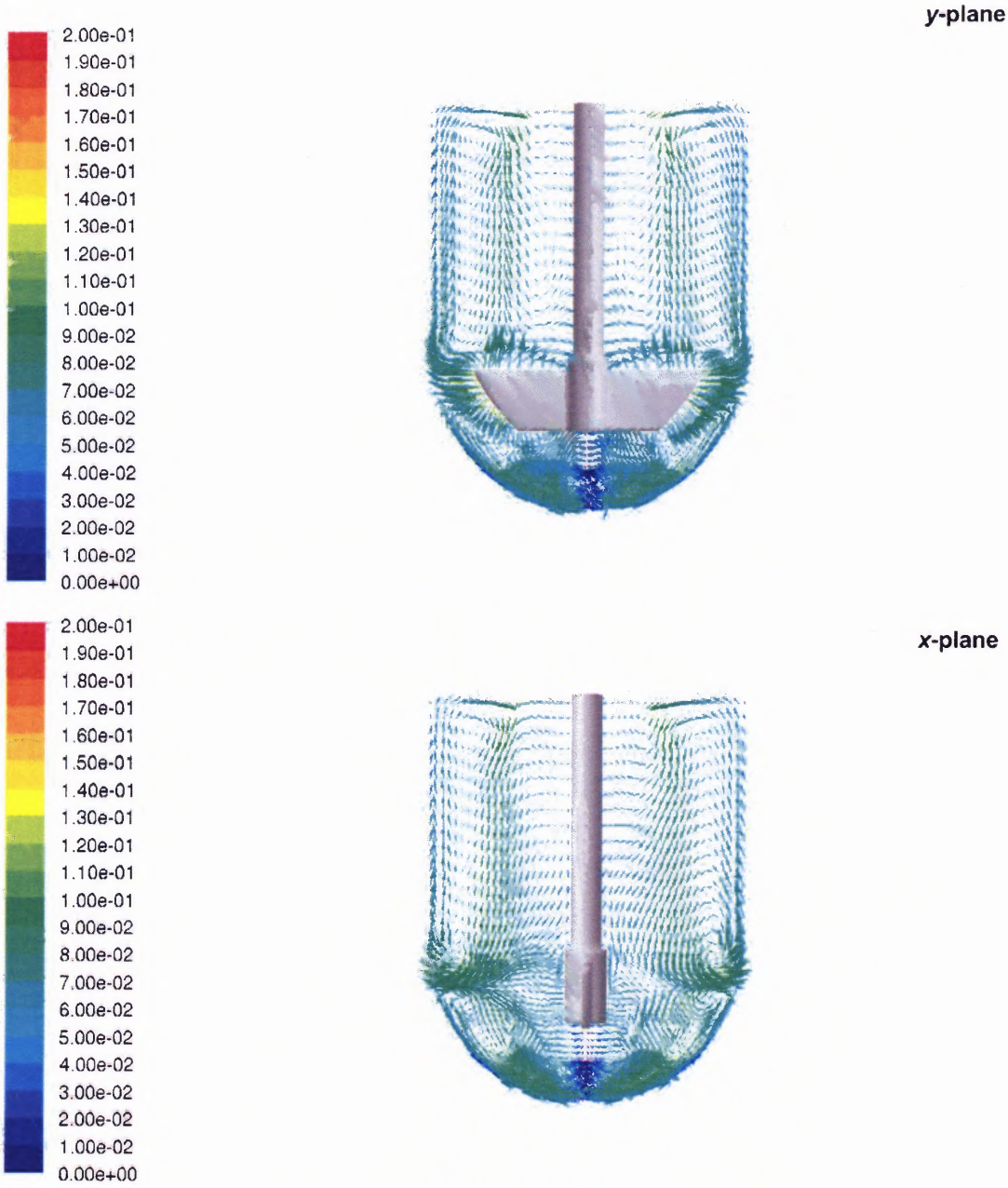

Figure 4.7 CFD predictions of velocity vectors colored by velocity magnitude on vertical cross section through the impeller shaft at different orientations under Operating Condition 1 (m/s).

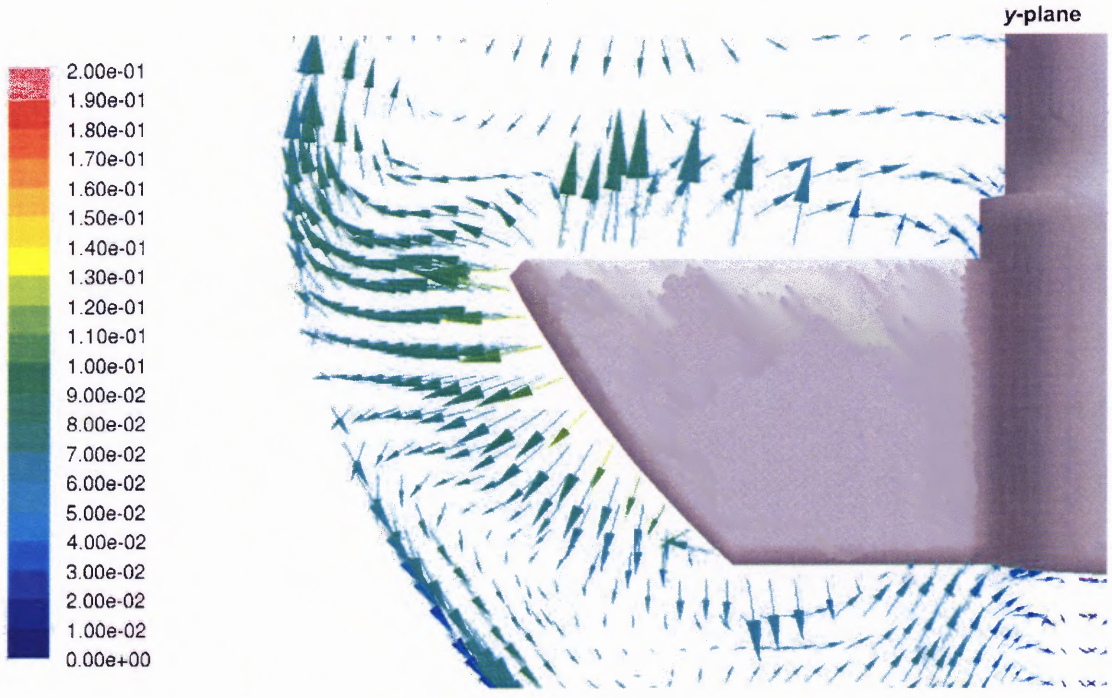

Figure 4.8 CFD predictions of velocity vectors colored by velocity magnitude on vertical cross sections through the impeller shaft for the impeller region under Operating Condition 1 (m/s).

The fluid region around the impeller is obviously dominated by the impeller rotation (Figure 4.8). The fluid velocity near the blade tip matches the tip speed. However, the fluid velocity decays rapidly, both radially and axially, away from the blade tip. For example, the velocities on the upper edge of the blade near the blade tip (z=-6.75 mm) are very similar to the tip speed, but the velocities on the iso-surface at z =-0.75 mm, which is only 6 mm above the top edge of the blade, show a significant decay in the velocity magnitude (Figures 4.7 and Figure 4.8). An even more dramatic drop in velocity occurs in the radial direction, as it can be seen by moving away from the blade tip and towards the wall in Figure 4.8

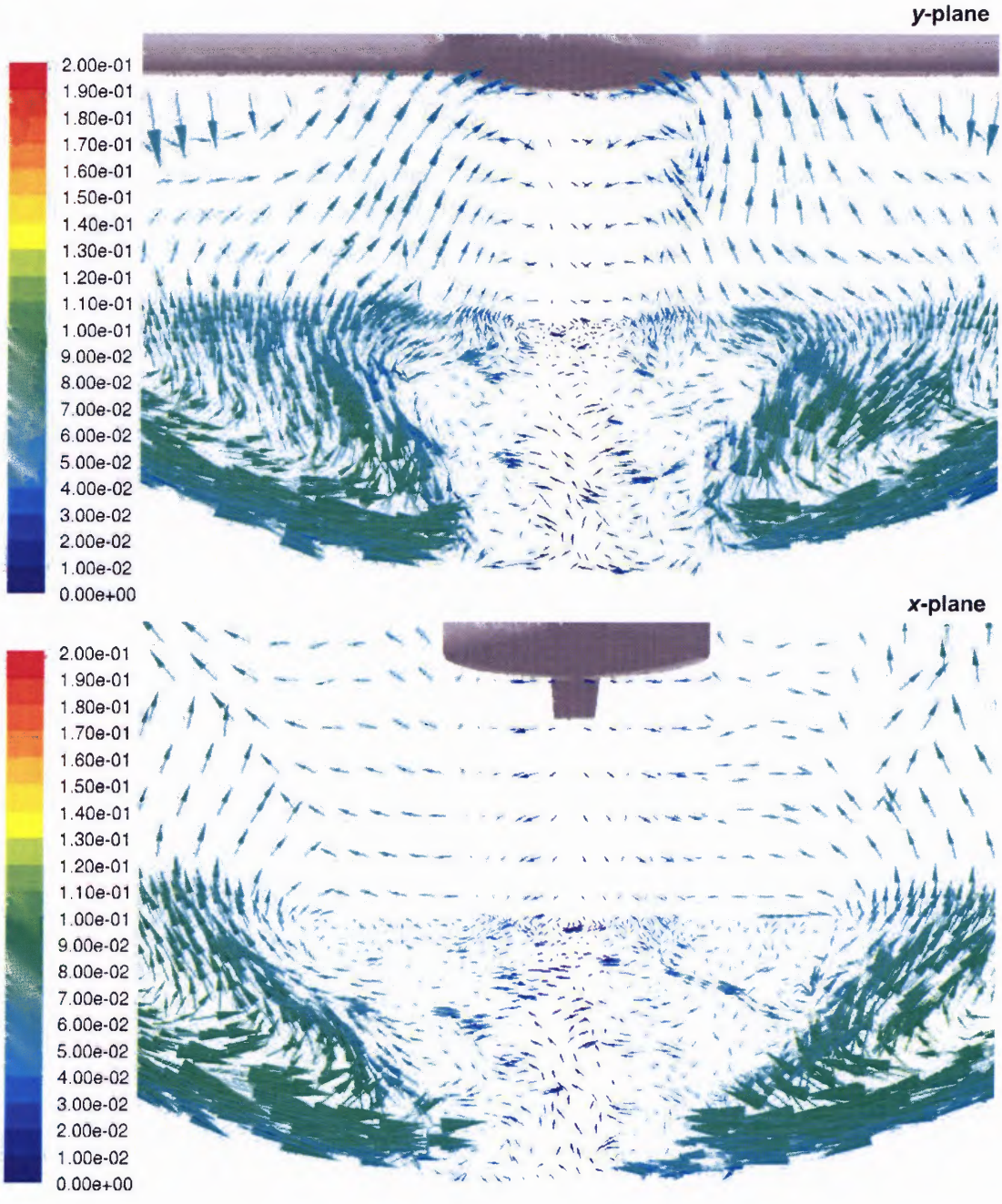

Figure 4.9 CFD predictions of velocity vectors colored by velocity magnitude on vertical cross section through the impeller shaft at different orientations, for the bottom region under Operating Condition 1 (m/s).

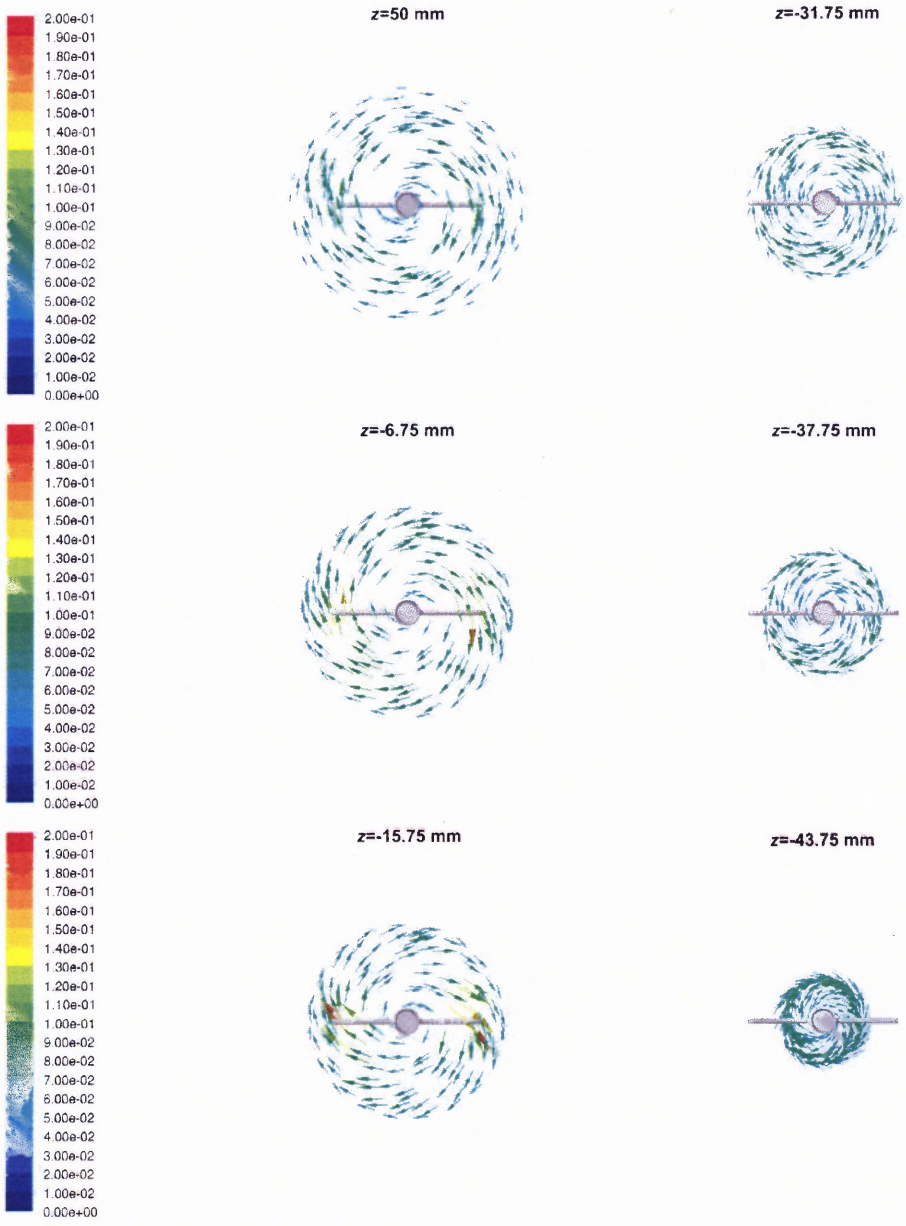

Figure 4.10 CFD predictions of velocity vectors colored by velocity magnitude on different iso-surfaces under Operating Condition 1 (m/s)

The radial jet generated by the impeller produces a complex flow in the gap between the blade tip and the vessel wall (Figure 4.8). The radial flow is rapidly converted to a more axially oriented flow, which is predicted by the CFD to be directed

upwards only near the top edge of the blade. Anywhere else in the gap, the flow is predicted to be oriented downwards. By looking at this figure, one can easily appreciate that even a minor error in the prediction of the vertical location where the flow switches direction from upwards to downwards can result in a significant discrepancy between the CFD results and the experimental LDV data. As already mentioned, this observation partially justifies the differences between the LDV and CFD results in this region.

The flow in the region below the impeller is the most complex and the most important for this work (Figure 4.9 combined with Figures 4.2 to Figure 4.4). These figures show that the flow is relatively strong in the tangential direction, even in the region below the impeller, but that the radial and axial components are generally weak, and are affected by the presence of a second vertical recirculation loop having a stronger pulsating component generated by the passing of the paddle. After the paddle has passed, the flow becomes extremely weak (Figure 4.9).

The striking feature of the flow in the region below the impeller is that this vertical recirculation loop is not able to penetrate the inner core region located just at the center under the impeller (Figures 4.5, Figure 4.7 and Figure 9). The net result is that the flow in this core is nearly stagnant in the vertical plane and it is dominated by weak tangential velocities (although stronger than the other components) on the order of 5% of the tip speed or less. This weakly swirling but otherwise nearly stagnant core region extends all the way from the vessel bottom to the lower edge of the impeller. As the impeller rotates, the stagnant core region expands (Figure 4.9, y-plane) and contracts (Figure 4.9, x-plane). The axial velocities change rapidly with time and location when moving across the vertical boundaries for this core region, while remaining very weak.

Figure 4.9 also shows that small changes in position near the bottom of the vessel are associated with large changes in the velocity magnitude. For example, by moving by a distance of only 2 to 5 mm, the velocity in the plane of the impeller can vary from near zero to 1/3 of the tip speed, and possibly higher. It is obvious that such a change in local velocity can have a dramatic effect on the local mass transfer rate at a specific location on the surface of the tablet and hence on the local dissolution rate of a solid tablet. Even more importantly, the initial location of a dissolving tablet on the bottom of the vessel (e.g., inside the semi-quiescent region under the shaft or outside it) can produce significant differences in the velocity profiles and velocity gradients experienced by the tablet, with a possible significant impact on the dissolution or erosion rate.

The CFD simulations cannot be expected to provide a full description of such a complex flow, with such small velocities, in such a small region. However, the CFD results obtained here consistently capture the main features of the flow, including the fact that the flow under the impeller is dominated by a weak tangential flow and has near zero radial and axial components. This is confirmed not only by the LDV results, but also by the robustness of the predictions in this region, which are relatively similar irrespective of the turbulence model used.

4.1.4 Turbulence Kinetic Energy (k) and Turbulence Dissipation Rate (ϵ)

Figure 4.11 and Figure 4.12 show plots of the turbulence kinetic energy and turbulent dissipation rate, respectively, on vertical cross sections through the impeller shaft at different orientations. The energy dissipation rate is potentially relevant to dissolution process since in many equations for the mass transfer between suspended solids and the

surrounding fluid the solid-liquid mass transfer coefficient k was reported to be dependent on ε. Hence, the local value of the energy dissipation rate near the vessel bottom could affect the dissolution process if tablet fragments become suspended. Appreciable turbulence levels and dissipation rates are present only in the impeller region, and especially near the blade tip. As the rotating impeller moves away from a given location in the impeller region, both turbulence and energy dissipation rate decay rapidly. Low values of k and ε are predicted anywhere else in the vessel. The turbulence kinetic energy is weak even in the region below the impeller where tablet dissolution occurs. Some higher values of energy dissipation rate appear along the vessel bottom, but not in the center where the tablet is usually located during a test.

4.1.5 Strain Rate

The shear stress tensor $\boldsymbol{\tau}$ is related to the rate-of-deformation tensor $\mathbf{S}$ through the equation:

$$\boldsymbol{\tau} = -\mu \mathbf{S} \tag{4.1}$$

For an incompressible Newtonian fluid, the components of the rate-of-deformation tensor are given by (Bird et al. 2002, FLUENT Inc., 2005):

$$S_{ij} = \frac{\partial u_i}{\partial x_j} + \frac{\partial u_j}{\partial x_i} \tag{4.2}$$

Then, the local value of magnitude of the strain rate (or simply "strain rate"), $\dot{\gamma}$, is defined as:

$$\dot{\gamma} = |\mathbf{S}| = \sqrt{\frac{1}{2}\sum_i \sum_j S_{ij}^2} \tag{4.3}$$

The strain rate represents the rate at which the velocity varies with distance when moving away from the point of interest. Since, based on boundary layer theory (Bird et al. 2002), the mass transfer boundary layer around a dissolving tablet can be assumed to be proportional to the velocity boundary layer (typically through $Sc^{1/3}$, where Sc is the Schmidt Number, $Sc=\mu/D_{AB}\cdot\rho$), information about the strain rate, i.e., knowledge of how rapidly the velocity changes when moving away from a surface (the vessel bottom in this case) can be important in estimating the relative magnitude of the local mass transfer rates. High strain rate regions can be expected to experience higher mass transfer rates, and hence more rapid dissolution rates.

Figure 4.13 and Figure 4.14 present contour plots of the strain rate, respectively, on a full vertical cross section of the vessel and, magnified, in the bottom region. As one can expect, the strain rate is high near the impeller blades and near the walls, where the velocity must eventually become zero and the velocity gradients are large. However, the strain rate is significantly higher at the wall in the region near the vessel bottom than at the wall in the cylindrical section the vessel. This phenomenon can be attributed not only to the proximity to the impeller, but also to the presence in this bottom region of steep velocity gradients resulting from the rapid variation in velocity magnitude over short distances, as indicated in the previous section.

The strain rate is not uniform in the region below the impeller. Figure 4.14 shows that the strain rate changes by more than an order of magnitude as one moves along to the hemispherical wall where the tablet is located during the dissolution test.

Figure 4.13 and Figure 4.14 can only provide a qualitative but visual description of the strain rate distribution. Quantitative CFD-based predictions of the strain rate distribution along the hemispherical portion of the vessel wall under Operating Condition 1 will be discussed in Sections 4.5.3 and 4.5.4 with comparison to other Operating Conditions.

4.1.6 Discussion of Flow Field in USP II Vessel under Operating Condition 1

This is possibly the first study aimed at completely characterizing the hydrodynamics of a USP Dissolution Apparatus II through CFD simulations and a detailed point-by-point comparison of the CFD predictions with experimental LDV data obtained for the entire dissolution vessel. Some of the results of this work can be compared with those of the few investigations available to date.

The results found here can be partially compared with those of Bocanegra et al. (1990), who obtained Laser Doppler Anemometry (LDA) data for only a few selected locations in the dissolution vessel. The tangential velocities found here at two iso-surfaces (z=-43.75 mm and z=25 mm) agree well with the experimental results of those authors.

A different group of investigators (Kukura et al. 2003; Kukura et al. 2004; Baxter et al. 2005) conducted a series of experimental studies using Particle Image Velocimetry (PIV) and compared their data with CFD predictions. Because of the nature of their experimental data, these authors only produced a qualitative comparison between data and numerical predictions. However, their velocity plots appear to compare favorably with the detailed results obtained here.

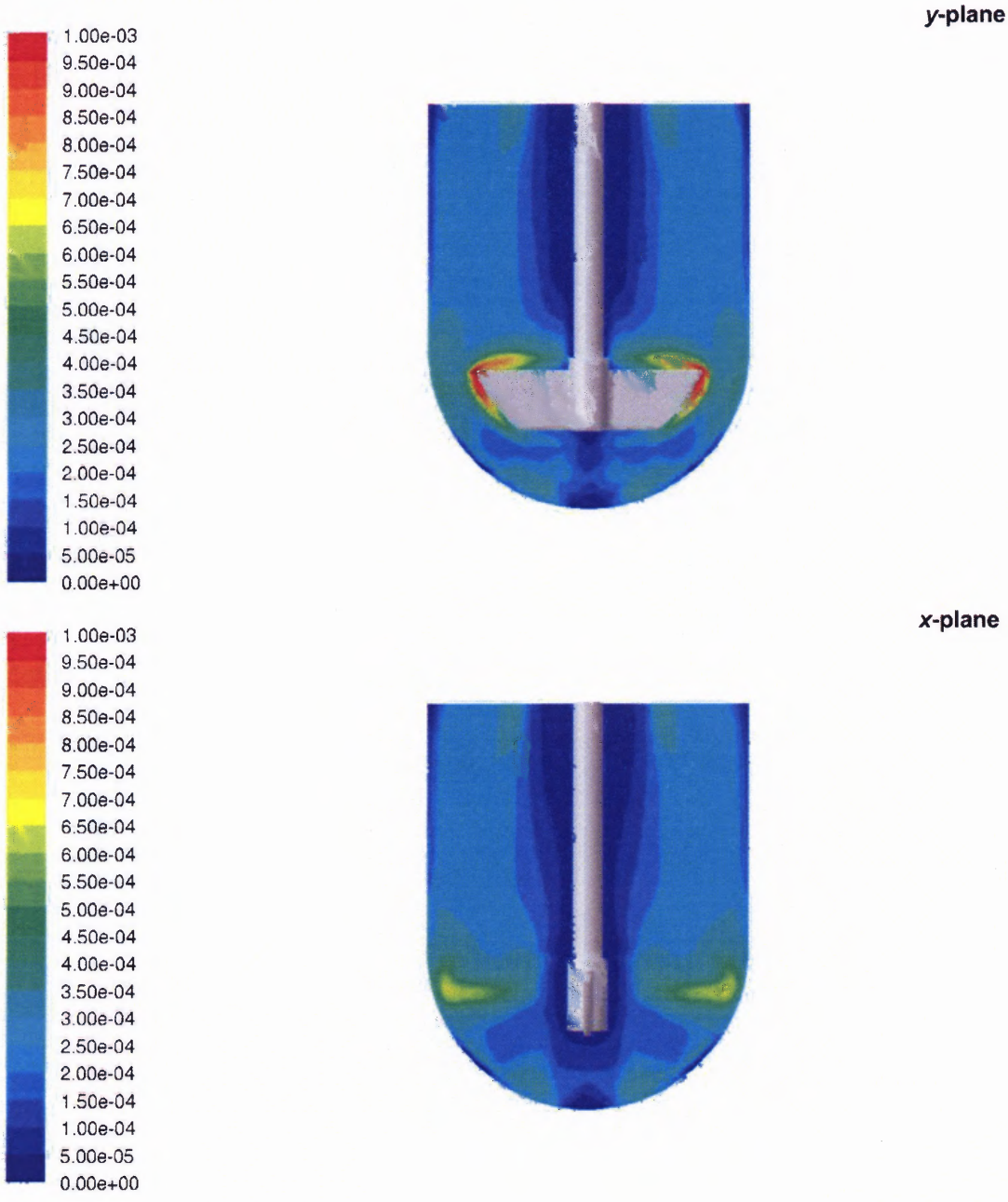

Figure 4.11 CFD predictions of the turbulence kinetic energy on vertical cross sections through the impeller shaft at different orientations under Operating Condition 1 (m^2/s^2).

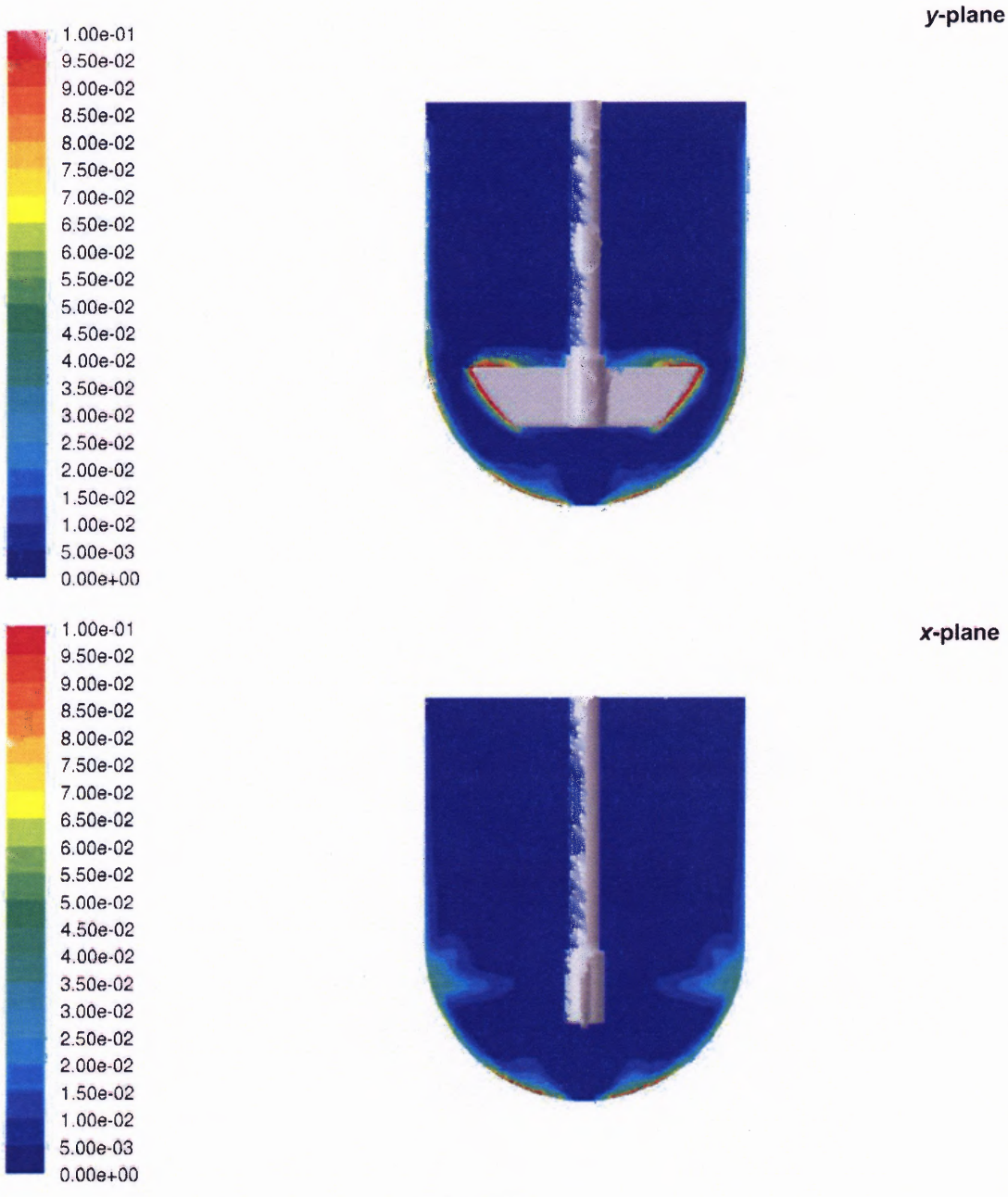

Figure 4.12 CFD predictions of the turbulence energy dissipation rate on vertical cross sections through the impeller shaft at different orientations under Operating Condition 1 (m^2/s^3).

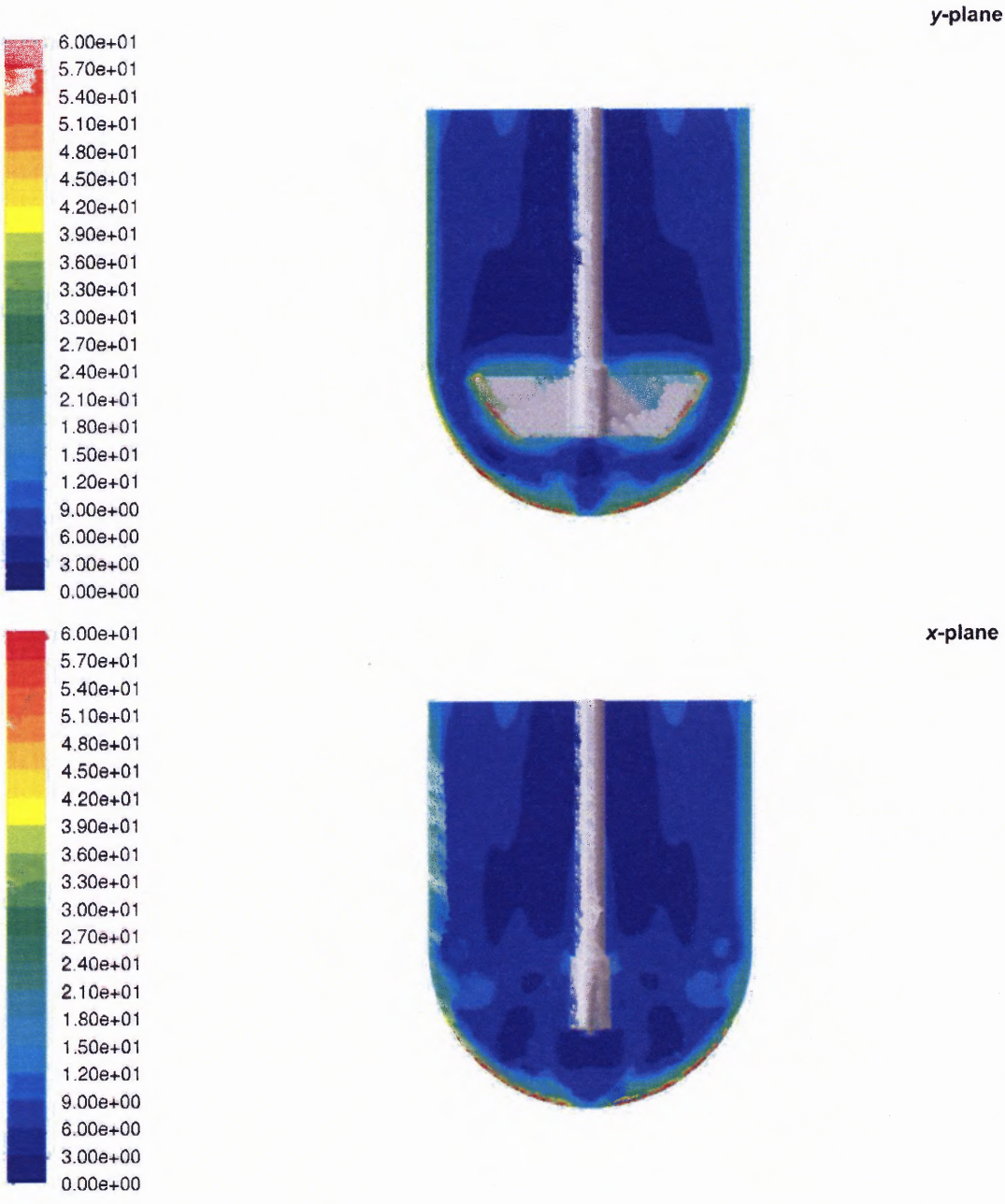

Figure 4.13 CFD predictions of strain rate on vertical cross sections through the impeller shaft at different orientations under Operating Condition 1 (1/s).

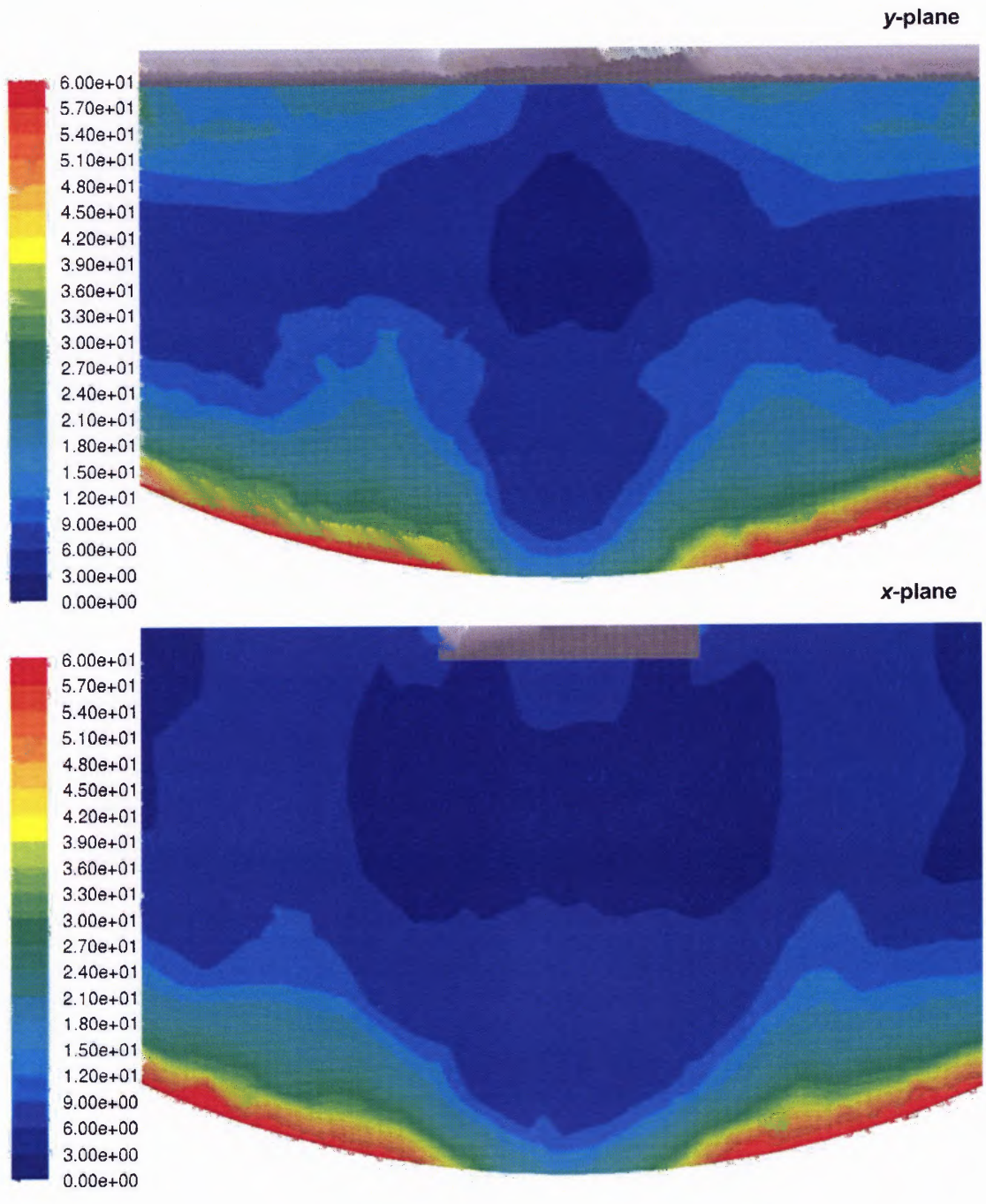

Figure 4.14 CFD predictions of the strain rate on vertical cross sections through the impeller shaft at different orientations for the bottom region under Operating Condition 1 (1/s).

Finally, another group of investigators (McCarthy et al. 2003, 2004) used a CFD approach similar to that used here, but generated no experimental data of their own. Instead, they used the limited experimental data of Bocanegra et al. (1990) to partially validate their approach. A comparison of the results of McCarthy et al.(2003) with those obtained here shows that the basic features of the flow field in the vessels, such as the main recirculation patterns and the jet flowing inwards near the vessel bottom, are similar. However, some differences can be found in the finer flow structures. For example, the flow that was predicted and experimentally validated here for the innermost core in the upper region of the vessel is weaker than that which McCarthy et al. obtained. Their results also show intermediate recirculation patterns near the wall in the upper portion of the vessel, which were neither predicted nor experimentally measured here. In this regard, the results of Kukura et al. (2003, 2004)and Baxter et al. (2005) are more similar to those found here. A more interesting difference between the results of McCarthy et al. (2003)and those of the present work is in the finer flow structure below the impeller. McCarthy et al. (2003) found a stronger and much more structured "wavy" flow below the impeller than that numerically predicted here or reported by Kukura et al. (2003, 2004) and Baxter et al. (2005). Our experimental results seem to confirm that the flow below the impeller is indeed very weak in any direction other than tangential, and that the CFD predictions generally overestimate the intensity of such a flow. It should be stressed that the k-ω model with low Reynolds number correction was used here to model turbulence effects. This model is probably superior to other standard turbulence models routinely used in simulations (Wilcox, 1998, Hanjalic et al. 2003). However, it is unclear what turbulence model McCarthy et al. (2003) used in their work.

In general, the CFD predictions obtained here agreed reasonably well with the LDV data. This is important to validate the CFD results obtained in this work, and draw more wide-ranging conclusions based on them. In addition, the agreement indicates that the turbulence model used in this work, i.e., the k-ω model with low Reynolds number correction, is appropriate for this kind of systems.

The hydrodynamics of the USP Apparatus II is dominated by two main features. The first is that anywhere in the system the main flow is strongly tangential, as in all unbaffled systems, with limited axial and radial components. Secondary flows are also present, but they form two smaller recirculation loops above and below the impeller. This has implications for the axial homogeneity of the vessel, although the small size of the vessel implies that blending is likely to occur relatively rapidly.

The second important hydrodynamic feature is that the central core region between the bottom of the vessel and the lower edge of the impeller is characterized by exceedingly small radial and axial velocities and turbulence levels. This zone rotates with the impeller, and it is surrounded by another zone, also below the impeller, with much higher radial and axial velocities. This analysis can qualitatively explain the effect of "coning" at the center of the vessel bottom. Coning is often observed when a tablet disintegrates rapidly during the dissolution test, and the resulting granules form a rotating cone of loosely aggregating particles under the impeller.

The high degree non-uniformity in the flow field near the vessel bottom can introduce a degree of uncertainty in the dissolution test. A tablet that is dropped into the gently agitated liquid in the vessel, as in a typical dissolution test, may land at a random location on the vessel bottom, and thus be exposed to very different flow fields

depending on its final position. The velocities in this region, albeit small, change significantly over short distance along the vessel bottom. This implies that small variations in the location of the tablet on the vessel bottom caused by the randomness of the tablet descent through the liquid are likely to result in significantly different velocities at the tablet location. The strain rate, which is another important factor that can affect the tablet dissolution rate, also changes significantly along the vessel bottom. The dramatic changes of both velocities and strain rate within a very small space can likely introduce variability in the dissolution test. Therefore, the vessel hydrodynamics and the initial location of the tablet after being dropped into the vessel can possibly affect the dissolution test results.

4.2 Flow Field Characterization Under Operating Conditions 2 and 3

Operating Condition 2 and Operating Condition 3 are only different from Operating Condition 1 by impeller rotation speed. Only CFD simulation was applied when studied the flow field for these two Operating Conditions. The flow field of Operating Condition 2 and 3 were also predicted with the k-ω model with low-Reynolds-number Correction. Velocity distribution profile, velocity magnitude, velocity vectors, strain rate, turbulence energy dissipation rate were compared among Operating Condition 1, 2 and 3.

4.2.1 Comparison of Velocity Distribution Profiles

Figures 4.15 through 4.17 show the CFD-predicted distribution profiles for the tangential, axial, and radial velocities for Operating Condition 1, 2, and 3. A few observations can be made about the results depicted in these figures: (a) The non-dimensional velocity profiles at a given horizontal cross section are remarkably similar irrespective of the impeller rotation speed, implying that, local velocities scale up, generally speaking, nearly linearly with impeller tip speed; (b) In general, the profiles for Operating Condition 1 and 2 are nearly superimposable, while the profiles for Operating Condition 3 are typically slightly different from the other two; (c) The tangential velocities in the upper core region in all three Operating Conditions scale up very well with the impeller tip speed. Outside this region, the non-dimensional tangential velocities are always larger for Operating Condition 3; (d) Below the impeller, the non-dimensional tangential velocity profiles are similar irrespective of the Operating Condition; (e) The non-dimensional axial velocity profiles at a given horizontal cross section are similar.

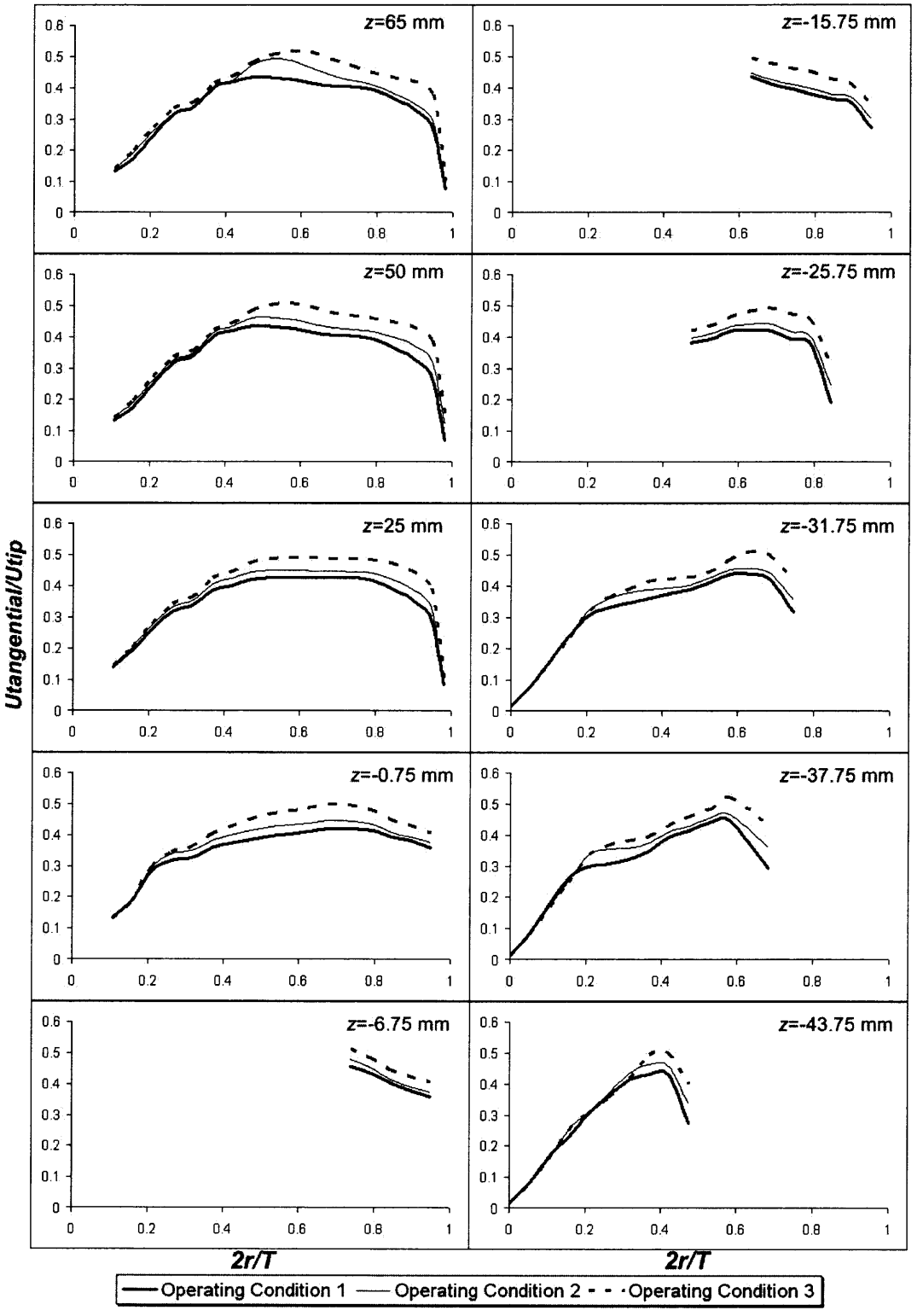

Figure 4.15 CFD predictions for tangential velocities on different iso-surfaces under Operating Condition 1, 2 and 3.

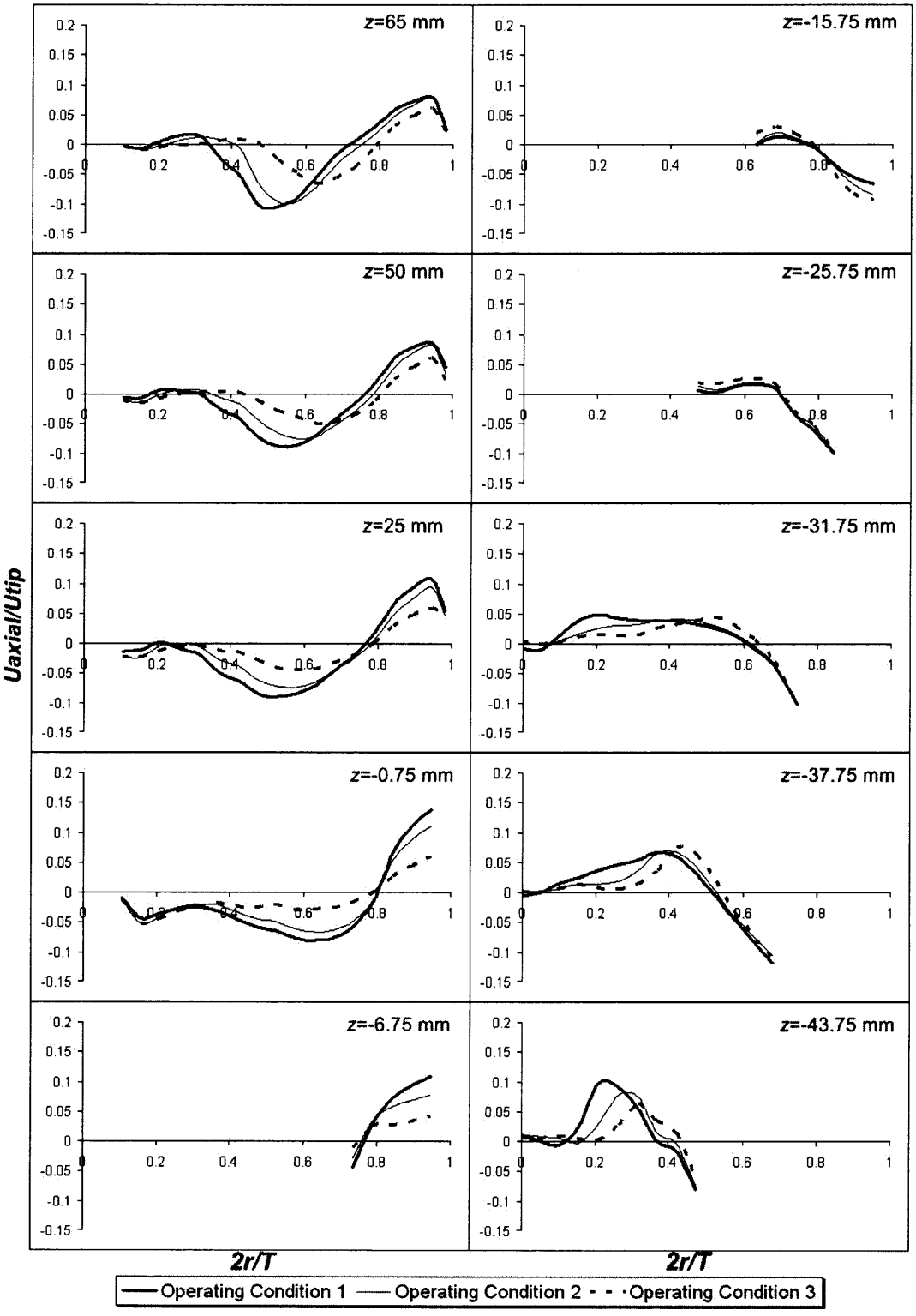

Figure 4.16 CFD predictions for axial velocities on different iso-surfaces under Operating Condition 1, 2 and 3.

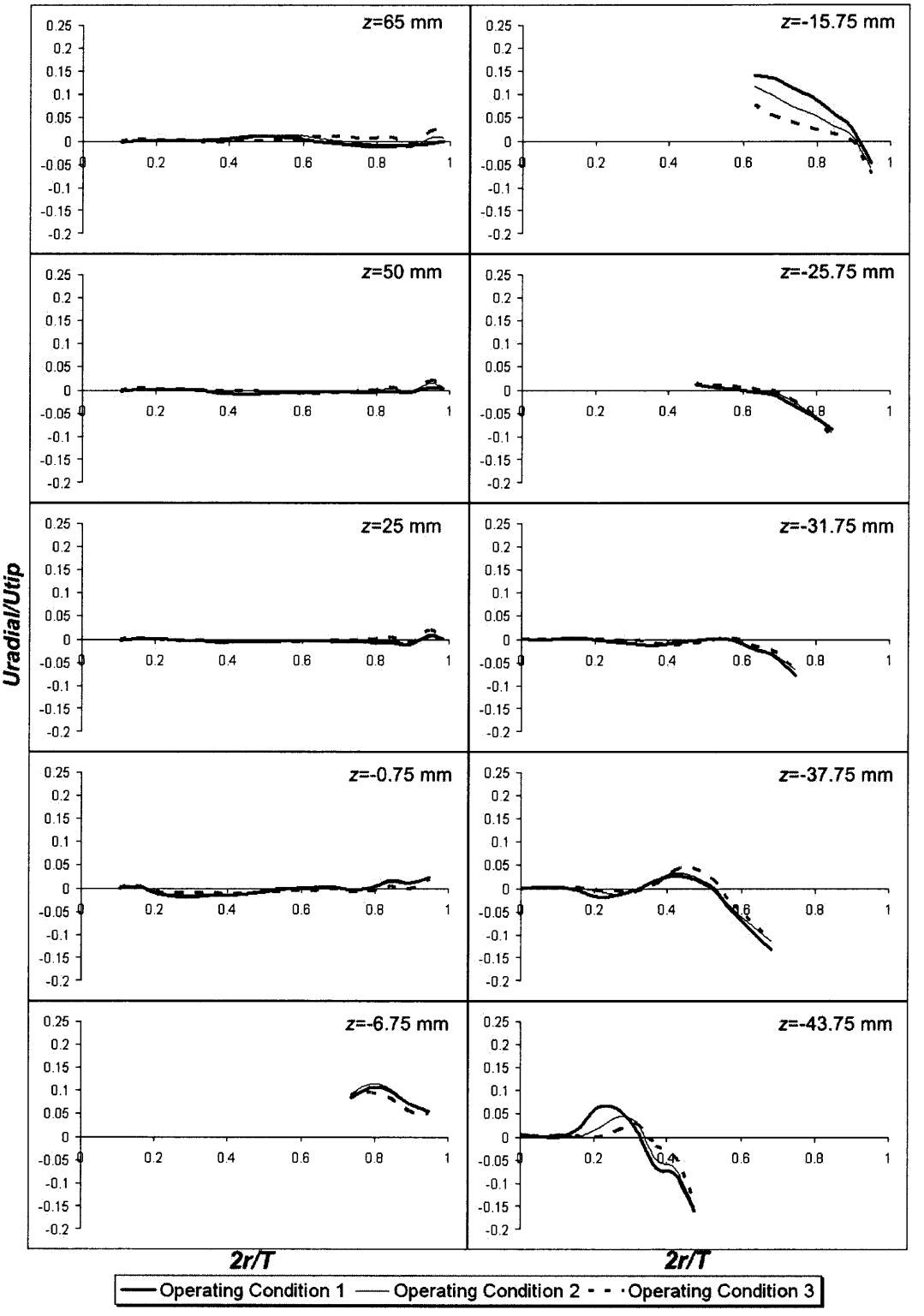

Figure 4.17 CFD predictions for radial velocities on different iso-surfaces under Operating Condition 1, 2 and 3.

However, the profiles for Operating Condition 3 are always slightly flatter then for the other two Operating Conditions, implying that the relative axial velocities for Operating Condition 3 are even smaller than the axial velocities than in the other two Operating Conditionds; (f) the non-dimensional radial velocity profiles do not change with agitation speed, and are typically nearly superimposable. However, the non-dimensional radial velocity profiles below the impeller are more appreciably different from each other, with the profile for Operating Condition 3 being flatter than the others. This observation, combined with a similar one for the axial velocities, implies that the recirculation flow under the impeller is comparatively weaker for Operating Condition 3 than in the other two Operating Conditions. In summary, increasing the agitation speed to 100 RPM results in an even larger dominance of the tangential flow over the axial/radial recirculation flow than at lower agitation speeds (50 RPM and 75 RPM). This is evident in most regions of the USP II apparatus, but especially the region below the impeller, where tablet dissolution occurs.

4.2.2 Comparison of Velocity Magnitude and Velocity Vectors

Figure 4.18, 4.19, 4.20, 4.21 present the CFD predictions of contours of velocity magnitudes and velocity vectors on the vertical cross section (y plane) and on iso-surfaces at different axial locations among Operating Condition 1, 2 and 3. Combined with Figure 4.15, 4.16 and 4.17, the three-dimensional flow in the vessel can be evinced for Operating Condition 2 and 3.

As in Operating Condition 1, strong tangential flow prevails in the top region of the vessel above the impeller, including a solid-body type of flow in the upper inner core.

A much weaker circulation loop resulting from the initial radial jet produced by the impeller (Figure 4.20) is also present in the top portion of the vessel. The same radial jet generated in the impeller region produces a complex flow in the gap between the blade tip and the vessel wall and below the impeller (Figure 4.20, 4.21).

Generally speaking, the flow patterns are very similar for all these three Operating Conditions. For Operating Condition 2, the flows are dominated by tangential component, while the radial and axial components are generally weak. A second weak vertical recirculation loop having a stronger pulsating component generated by the passing of the blade can be observed (Figures 4.19). However, the flows in the central core below the impeller is extremely weak in the vertical plane and is dominated by weak (but stronger with respect to the other components) tangential velocities. In the regions below the impeller, there is a sharp demarcation between the core region under the shaft, nearly stagnant except for the rotating component, and the outer region, dominated by a stronger pulsating flow (Figure 4.20). The exact placement of the dissolving tablet either inside the rotating core, outside it, or at its boundary can be expected to affect significantly role the dissolution process.

For Operating Condition 3, the pulsing jet is clearly much smaller than in the other two Operating Conditions. The net result is an increase in the size of the weak recirculation zone directly under the impeller. However, because of the increase in tip speed (and consequent change of scale in these figures) the absolute magnitude or the local velocities is approximately unchanged as for N=50 RPM and N=100 RPM. The situation at N=75 RPM is intermediate between the other two Operating Conditions.

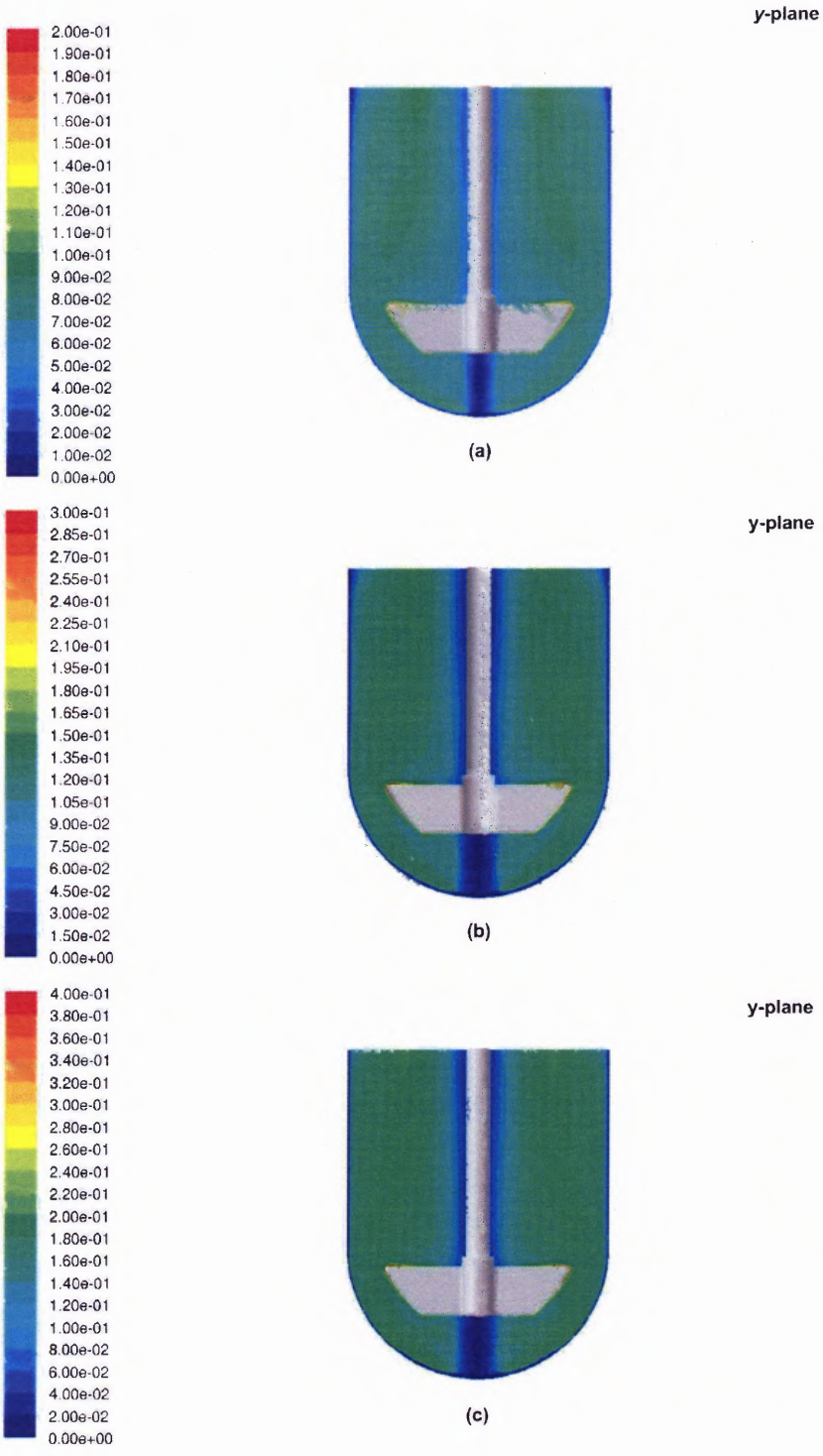

Figure 4.18 CFD predictions of contours velocity magnitude on vertical cross section (y plane) (m/s): (a) Operating Condition 1, (b) Operating Condition 2, (c) Operating Condition 3.

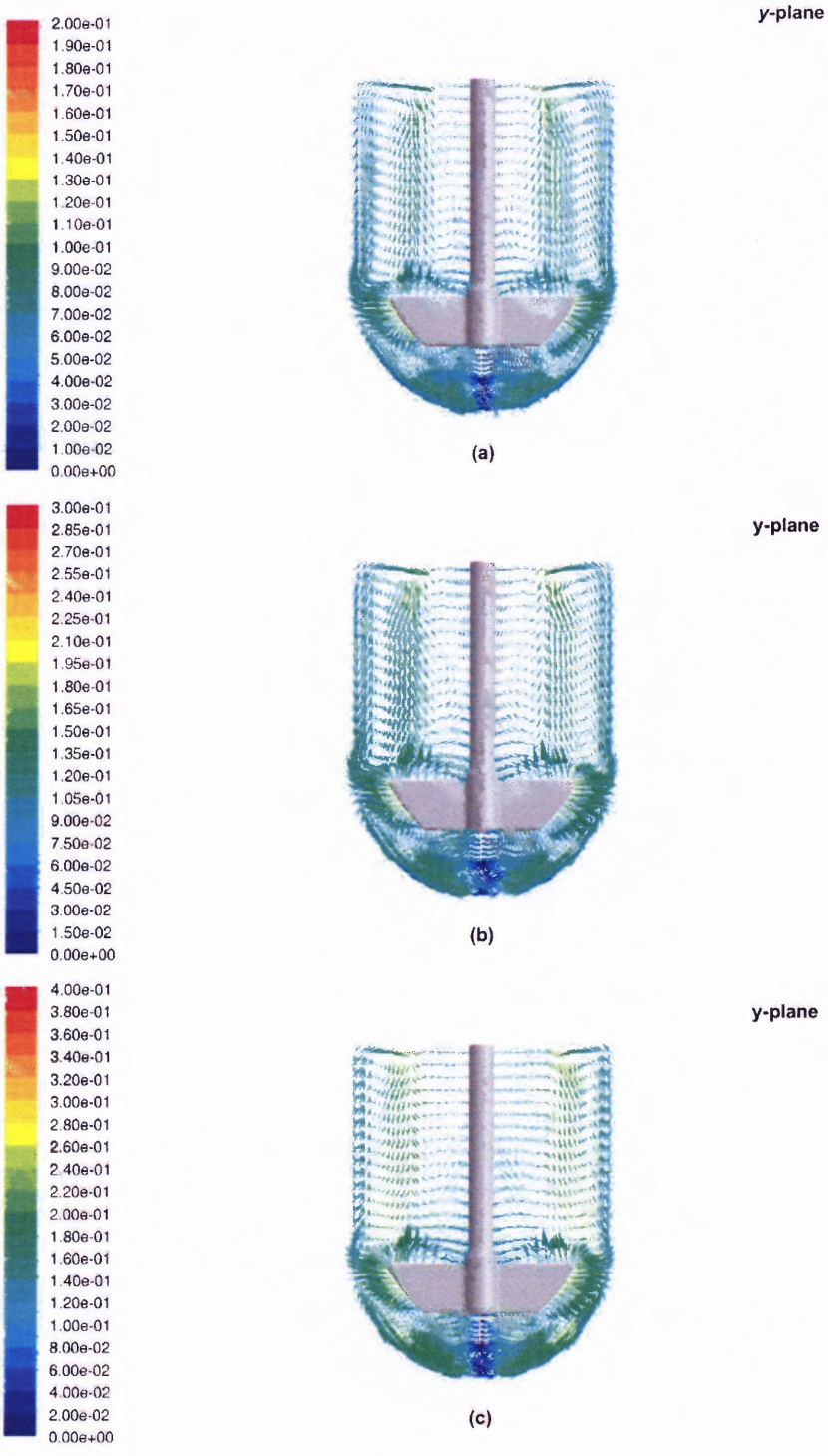

Figure 4.19 CFD predictions of velocity vectors colored by velocity magnitude on vertical cross section (*y* plane) (m/s): (a) Operating Condition 1, (b) Operating Condition 2, (c) Operating Condition 3.

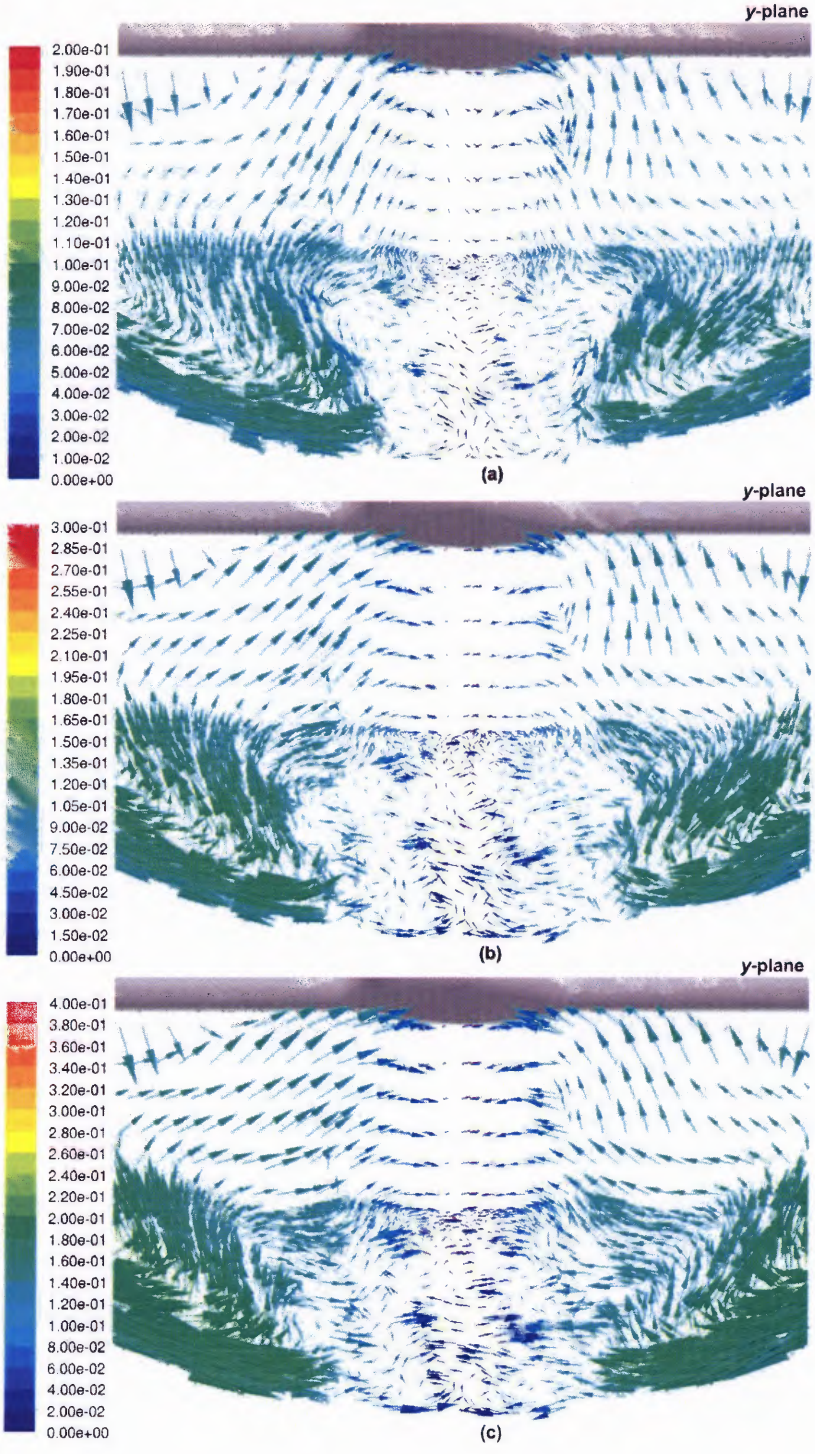

Figure 4.20 CFD predictions of velocity vectors colored by velocity magnitude on vertical cross section (y plane) for the bottom region (m/s): (a) Operating Condition 1, (b) Operating Condition 2, (c) Operating Condition 3.

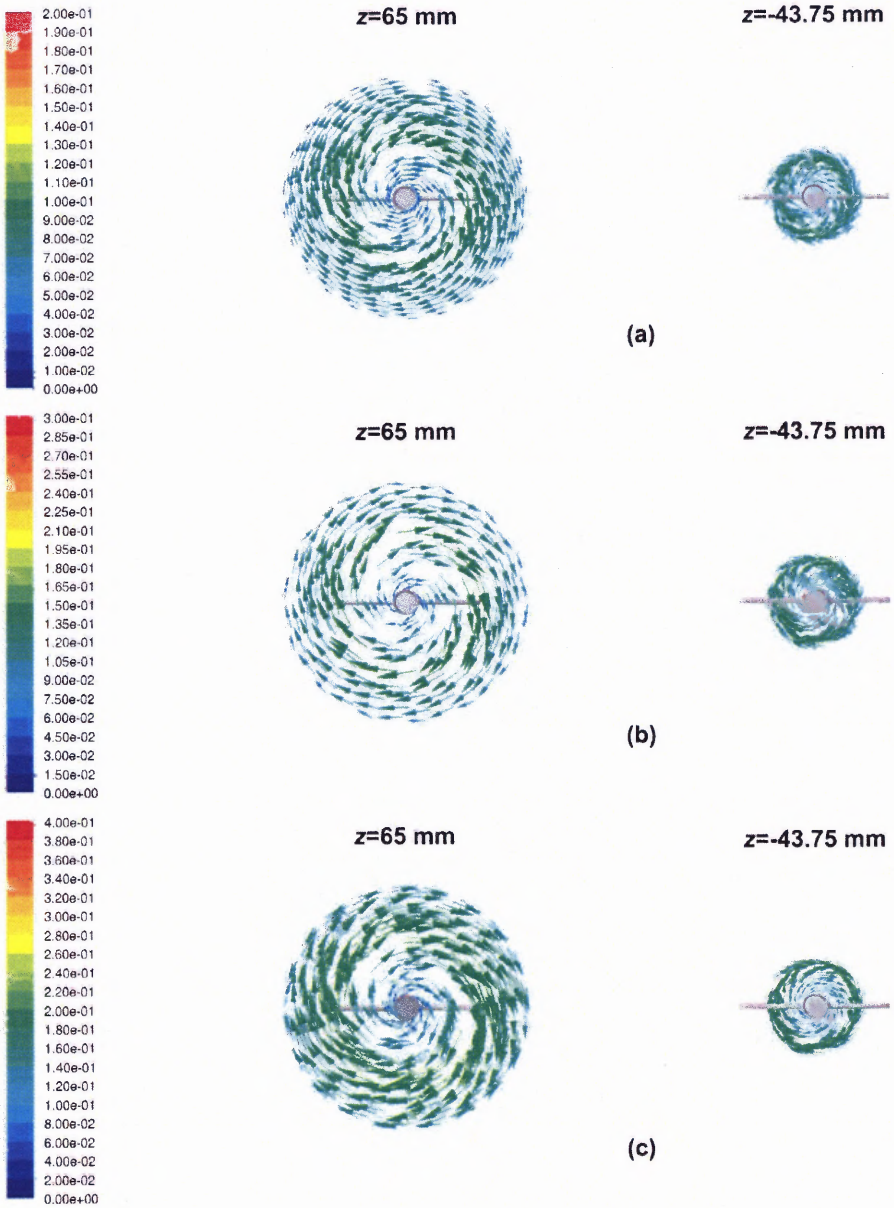

Figure 4.21 CFD predictions of velocity vectors colored by velocity magnitude on different iso-surfaces (z=65 mm and z=-43.75 mm) (m/s): (a) Operating Condition 1, (b) Operating Condition 2, (c) Operating Condition 3.

4.2.3 Comparison of Strain Rate and Turbulence Energy Dissipation Rate (ϵ)

Contour plots of the strain rate on a vertical cross section (y plane) for Operating Condition 1, 2 and 3 are given in Figures 4.22 and 4.23. As seen in Operating Condition 1, the strain rates for Operating Condition 2 and 3 are higher near the impeller blades and the walls than the other regions in the vessel, and are not uniform in the region below the impeller. In the central core region, the values of strain rates are low even for Operating Condition 2 and 3. The absolute values of strain rates are little higher in Operating Condition 2 and 3 than which in Operating Condition 1 because of higher impeller rotation speeds.

The distributions of the energy dissipation rate ϵ are shown in Figures 4.24. As seen in Operating Condition 1, there are appreciable energy dissipation rates but higher absolute values are present in the impeller region (impeller blade tips) for Operating Condition 2 and 3. However, appreciable energy dissipation rates could also be observed at the bottom of the vessel, but outside of the central core region.

Figures 4.22, 4.23 and 4.24 indicate that unless the tablet is placed outside the central region immediately under the impeller the dissolution process may not be too significantly affected by the increased agitation speed.

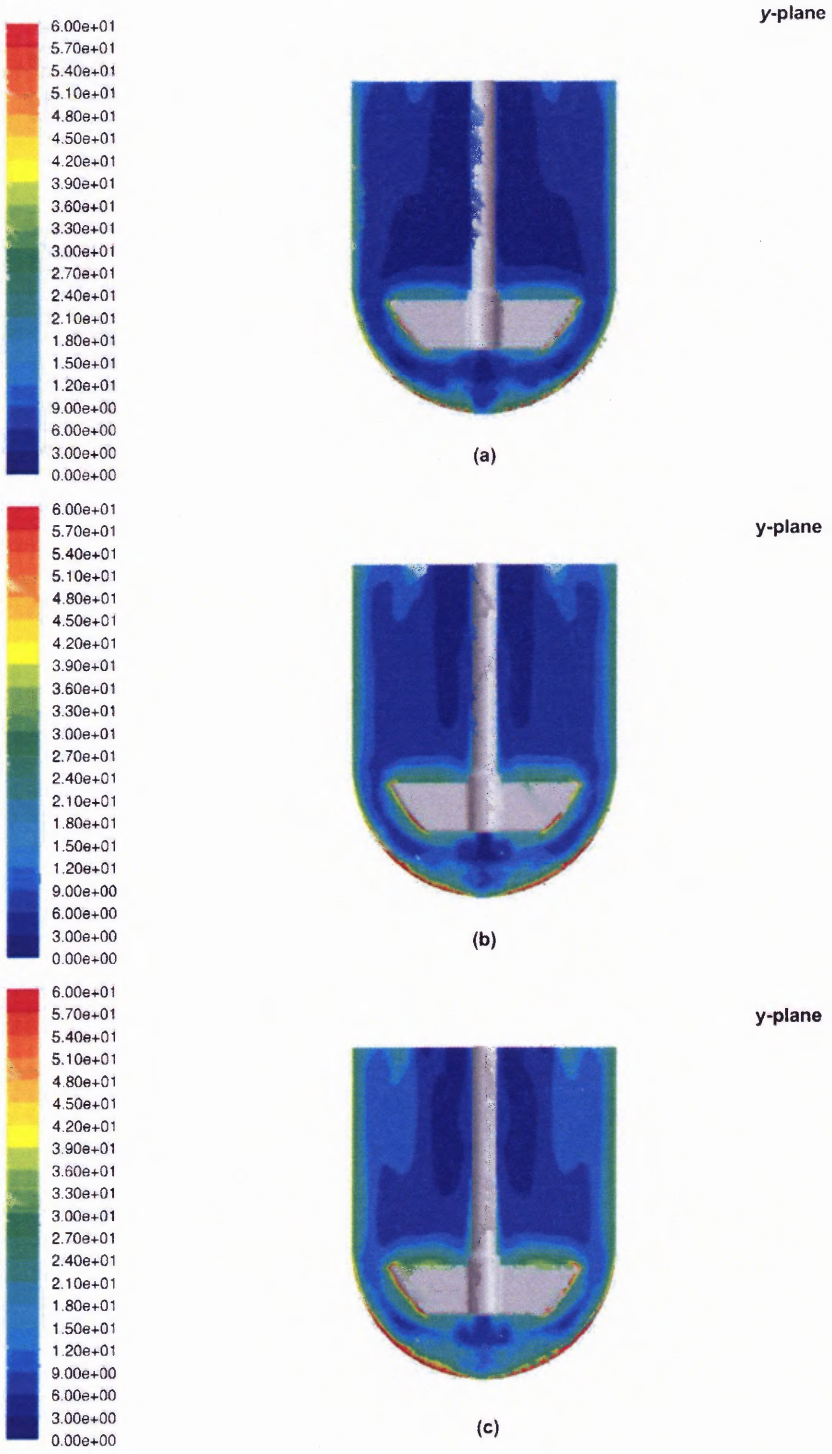

Figure 4.22 CFD predictions of strain rate on vertical cross sections (y-plane) (1/s): (a) Operating Condition 1, (b) Operating Condition 2, (c) Operating Condition 3.

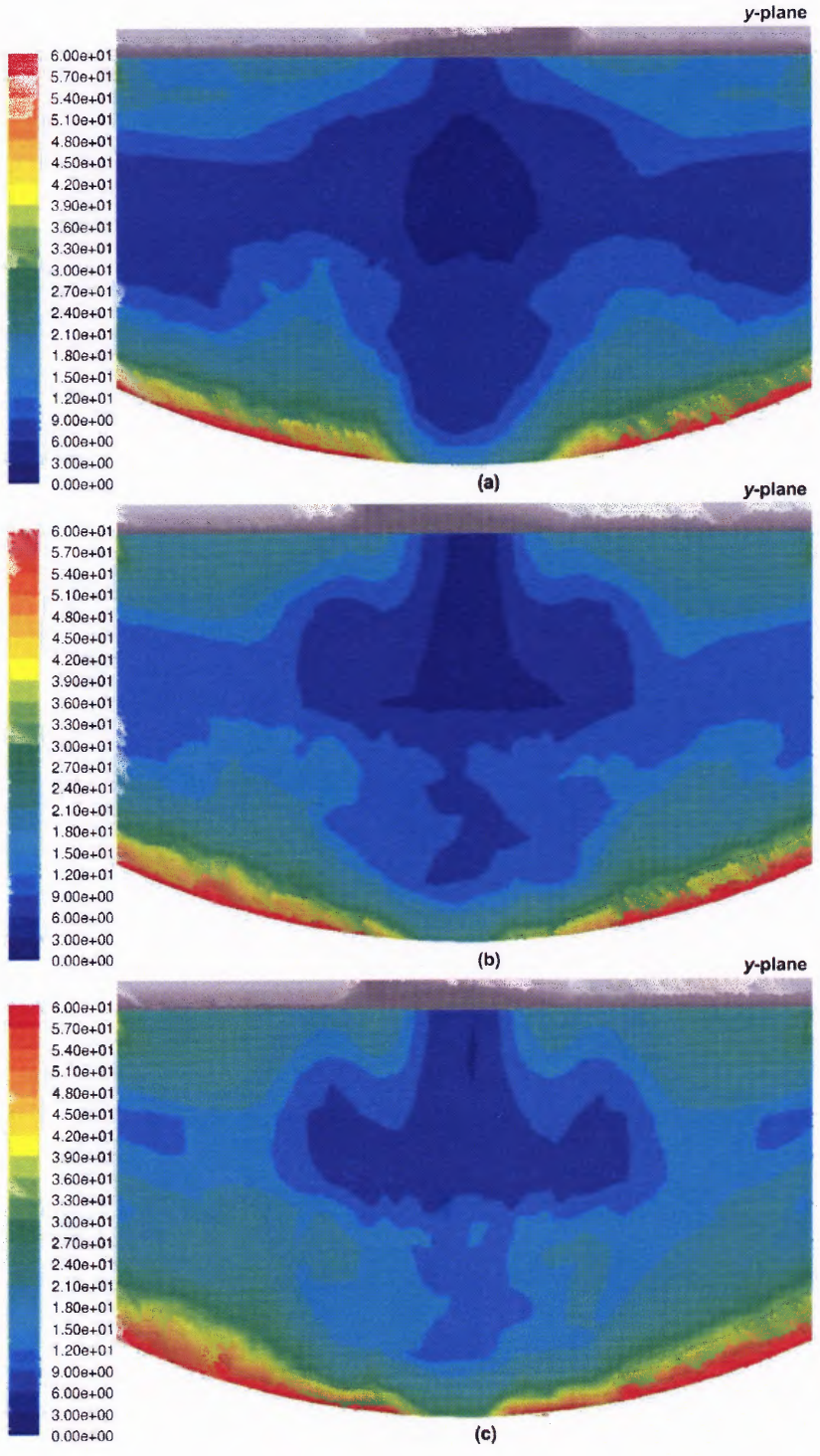

Figure 4.23 CFD predictions of the strain rate on vertical cross sections (*y*-plane) for the bottom region (1/s): (a) Operating Condition 1, (b) Operating Condition 2, (c) Operating Condition 3.

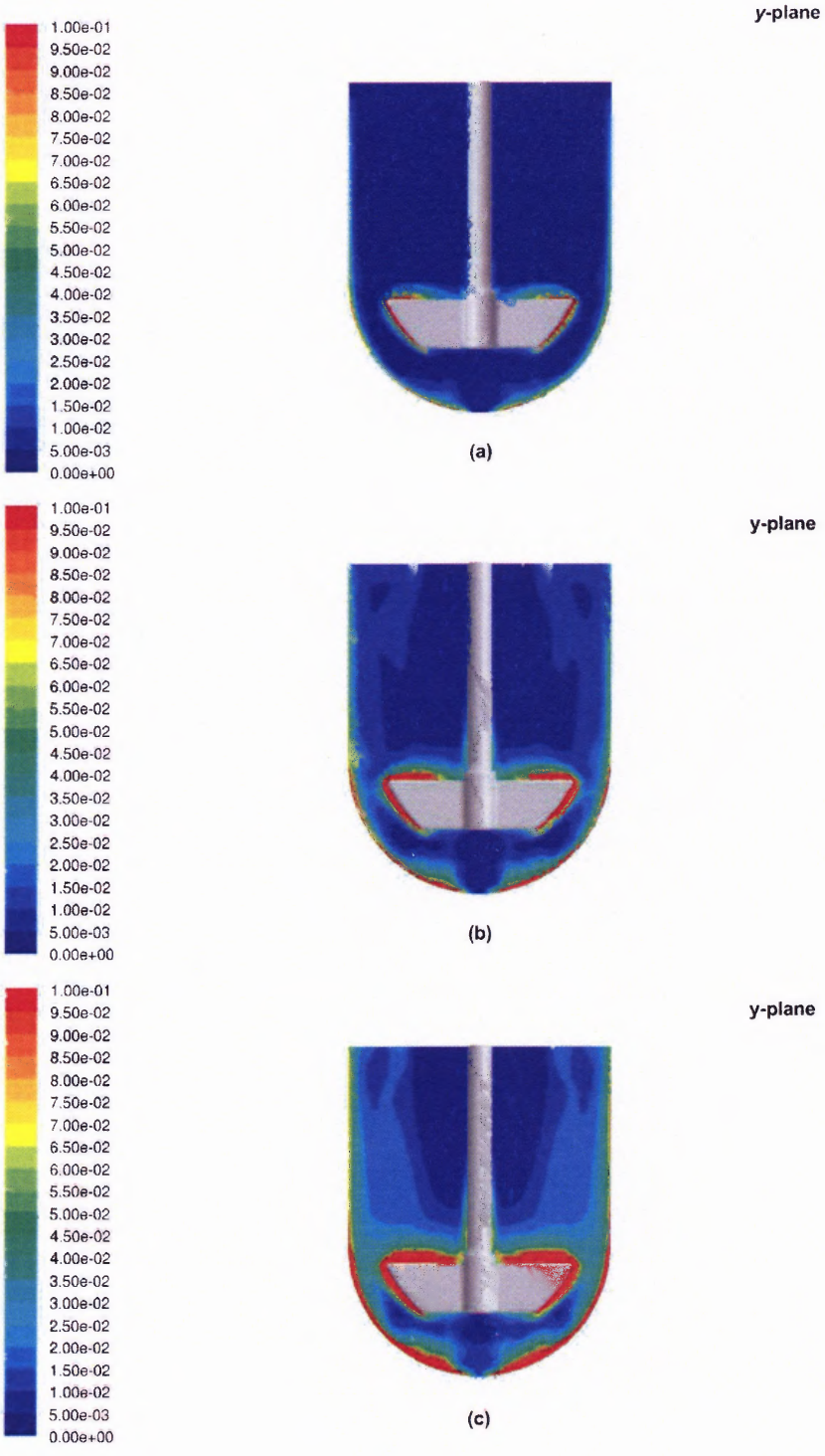

Figure 4.24 CFD predictions of the turbulence energy dissipation rate on vertical cross sections (y-plane) (m^2/s^3): (a) Operating Condition 1, (b) Operating Condition 2, (c) Operating Condition 3.

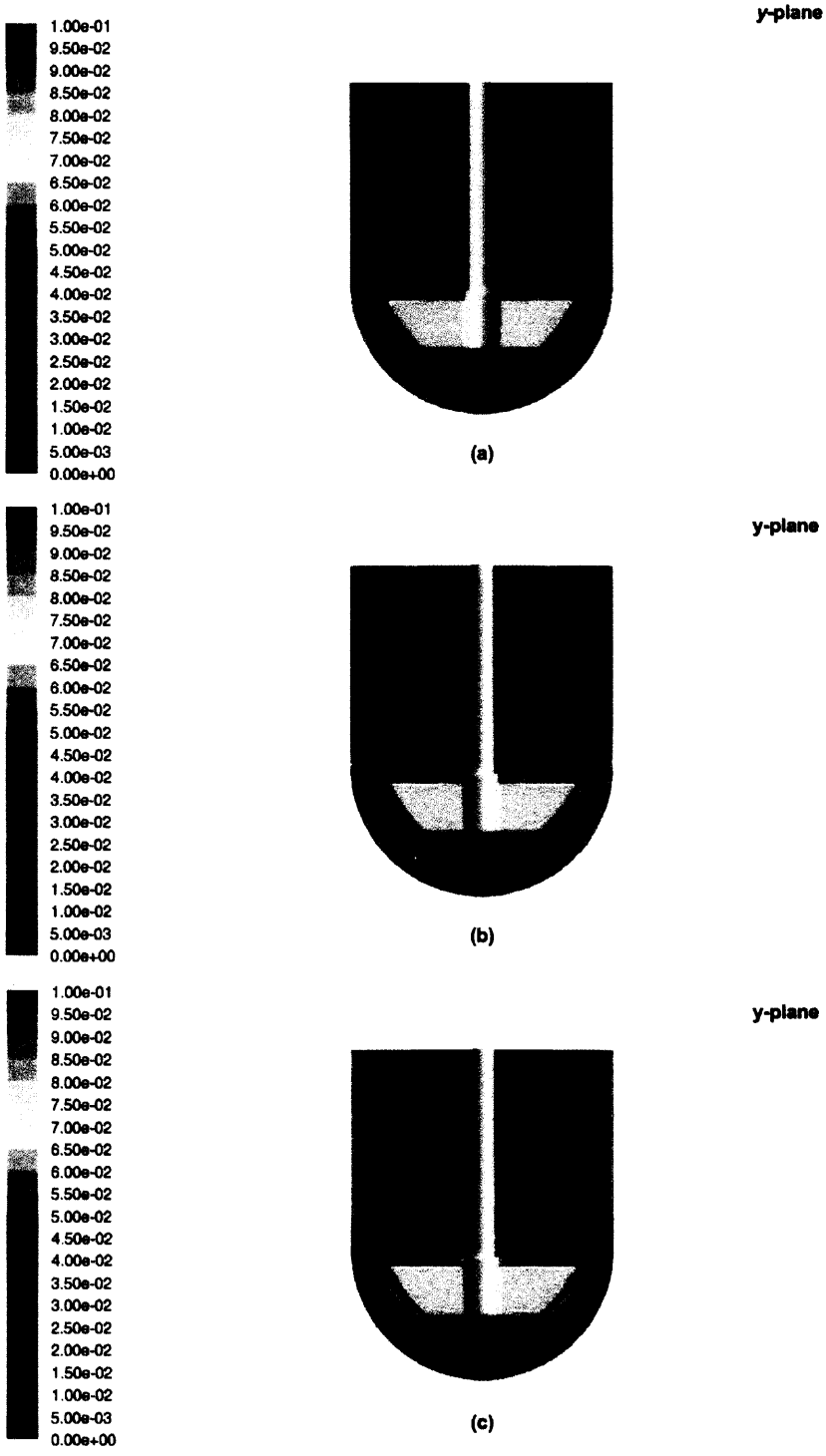

Figure 4.24 CFD predictions of the turbulence energy dissipation rate on vertical cross sections (y-plane) (m^2/s^3): (a) Operating Condition 1, (b) Operating Condition 2, (c) Operating Condition 3.

4.3 Flow Field Characterization Under Operating Condition 4

Operating Condition 4 is only different from Operating Condition 1 by dissolution media filled volume. Only CFD simulation was applied when studied the flow field for Operating Condition 4. The flow field of Operating Condition 4 was also predicted with the k-ω model with low-Reynolds-number Correction. Velocity distribution profile, velocity magnitude, velocity vectors, strain rate, turbulence energy dissipation rate were compared between Operating Condition 1 and 4.

4.3.1 Comparison of Velocity Distribution Profiles

Figures 4.25 to 4.27 show the CFD-predicted distribution profiles for the tangential, axial, and radial velocities for Operating Condition 4 and Operating Condition 1. A number of conclusions can be drawn from these figures: (a) In general, the velocity profiles for both Operating Conditions at a given horizontal cross section are similar to each other. However, appreciable differences can also be observed; (b) An inner core rotating as a solid body exists in the upper portion of the 500 mL vessel. Although the impeller rotational speed is the same in both Operating Conditions (N=50 RPM), the inner core in the 500 mL vessel rotates at a faster speed than that in the 900 mL vessel, as indicated by the steeper slope of the tangential velocity profile for the former Operating Condition at lower radial distances. This is consistent with the fact that the impeller transfers a similar amount of momentum to a smaller volume of fluid. Outside the inner core, the tangential velocities are appreciably larger in the top portion of the tank or similar to the velocities in Operating Condition 1; (c) In the gap between the impeller blade and the vessel wall the tangential velocity profiles are similar in both Operating

Conditions, implying that the impeller rotation dominates this region over any other possible effects caused by the different volumes; (d) below the impeller the flow is again strongly tangential and dominated by a solid body type of rotation; (e) Similar as seen in Operating Condition 1, two axial/radial loops are discernible above the impeller from Figures 4.26 and 4.27, as well as Figures 4.29 one next to the shaft, extending up to $2r/T \approx 0.35$, and the other in the remaining portion of the upper vessel up to the wall. Since the first of these two loops extends almost down to the impeller blade, it is likely that material in this region will not be easily exchanged with the rest of the vessel; (f) the axial velocity profiles in the gap between the impeller blade and the vessel wall are similar in both Operating Conditions, implying, again, that the proximity of the impeller dominates the flow in this region; (g) the axial velocities below the impeller are larger near the center in operating 4 than those in Operating Condition 1; (h) the radial velocities are larger in Operating Condition 4 than those in Operating Condition 1 in the upper portion of the vessel, as a result of the external second upper recirculation loop mentioned above. In the rest of the vessel, the radial velocity profiles in Operating Condition 4 are similar to that of Operating Condition 1 (including the impeller-wall gap region).

4.3.2 Comparison of Velocity Magnitude and Velocity Vectors

Figures 4.28 presents the CFD predictions on contours of velocity magnitude on the vertical cross section (y-plane) for Operating Condition 4 and Operating Condition 1. Figure 4.29 to 4.31 present CFD predictions on velocity vectors on the vertical cross

section (y-plane) and on the iso-surfaces (at z=25mm and z=-43.75 mm) for Operating Condition 4 and Operating Condition 1.

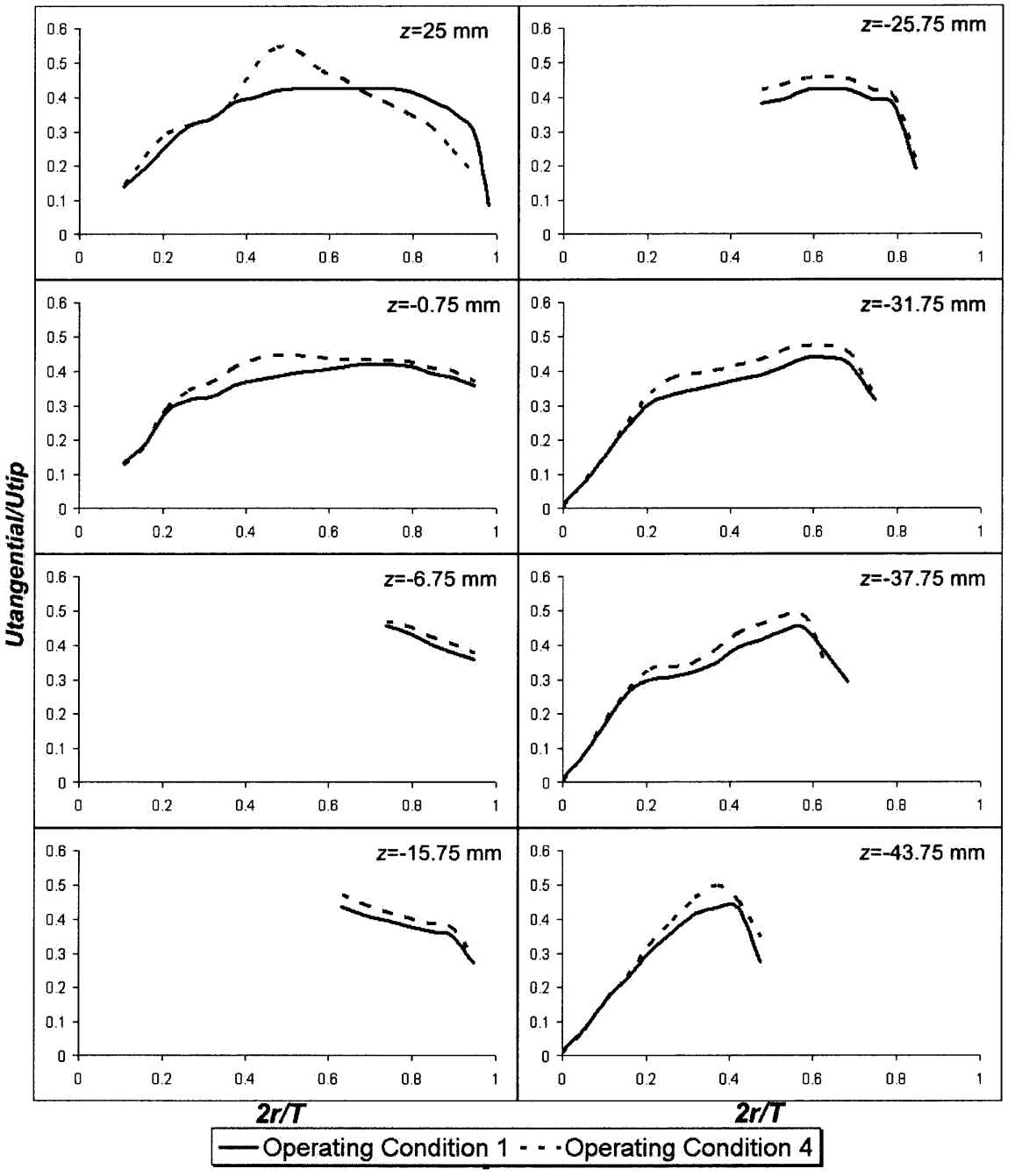

Figure 4.25 CFD predictions for tangential velocities on different iso-surfaces under Operating Condition 1 and 4.

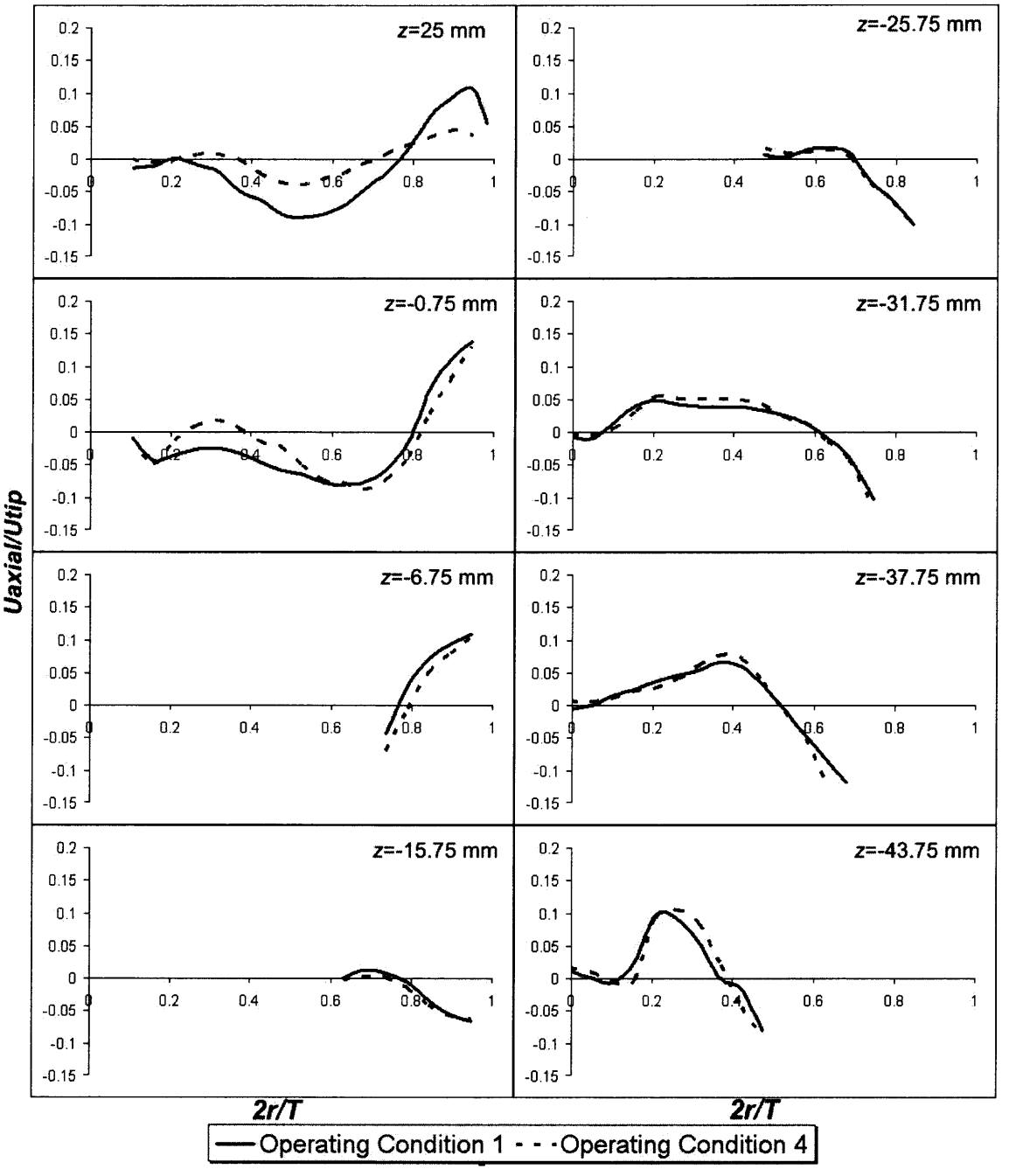

Figure 4.26 CFD predictions for axial velocities on different iso-surfaces under Operating Condition 1 and 4.

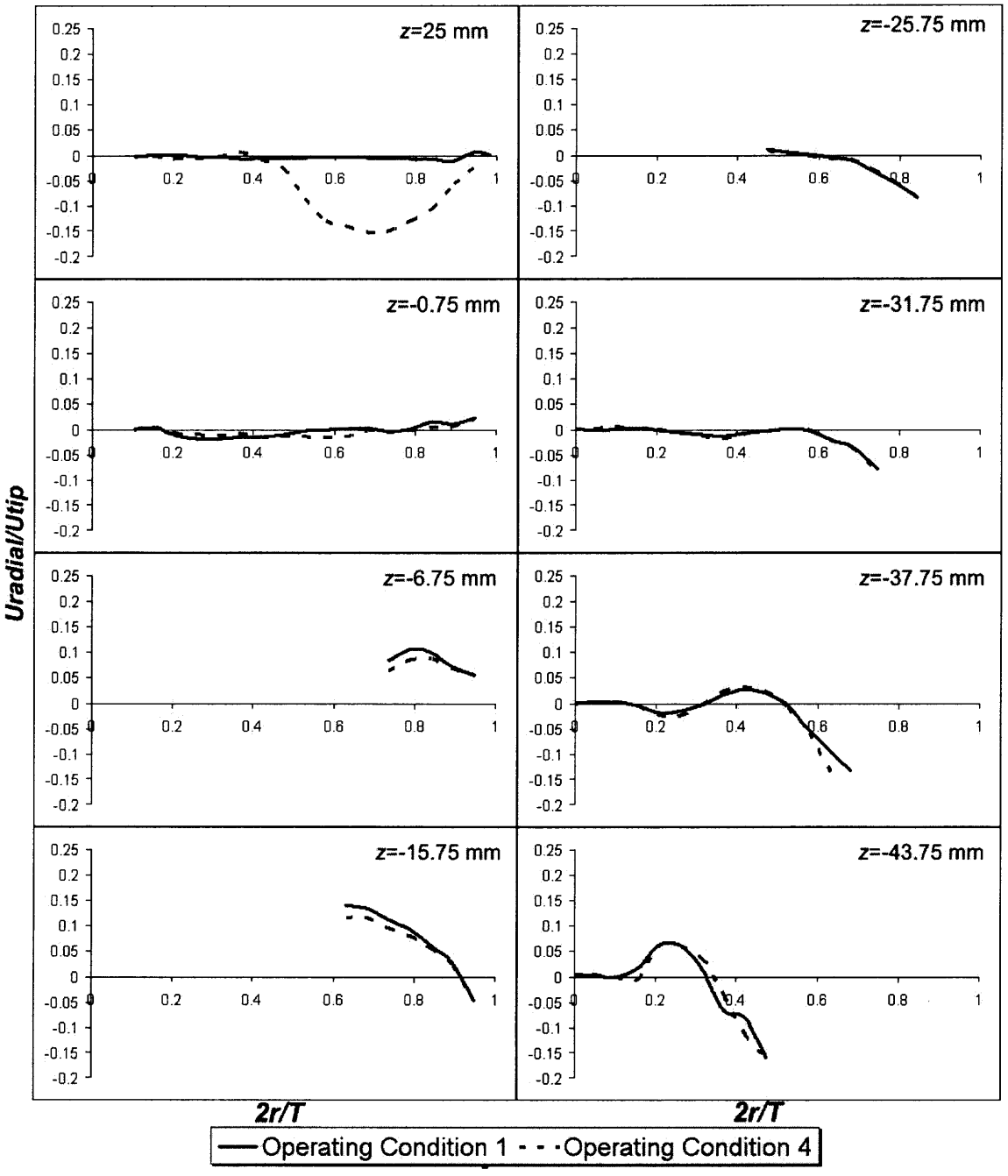

Figure 4.27 CFD predictions for radial velocities on different iso-surfaces under Operating Condition 1 and 4.

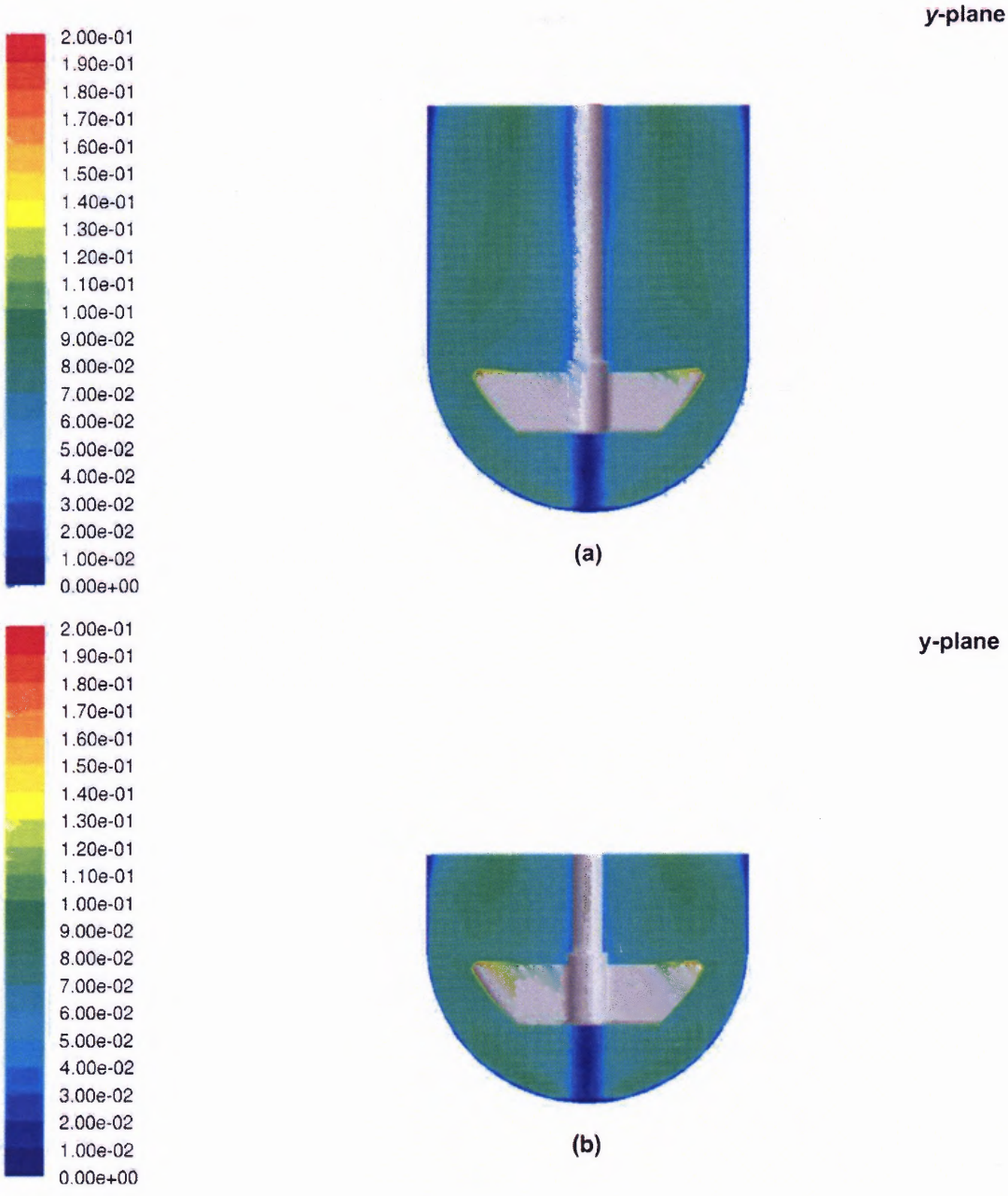

Figure 4.28 CFD predictions of contours velocity magnitude on vertical cross section (*y* plane) (m/s): (a) Operating Condition 1, (b) Operating Condition 4.

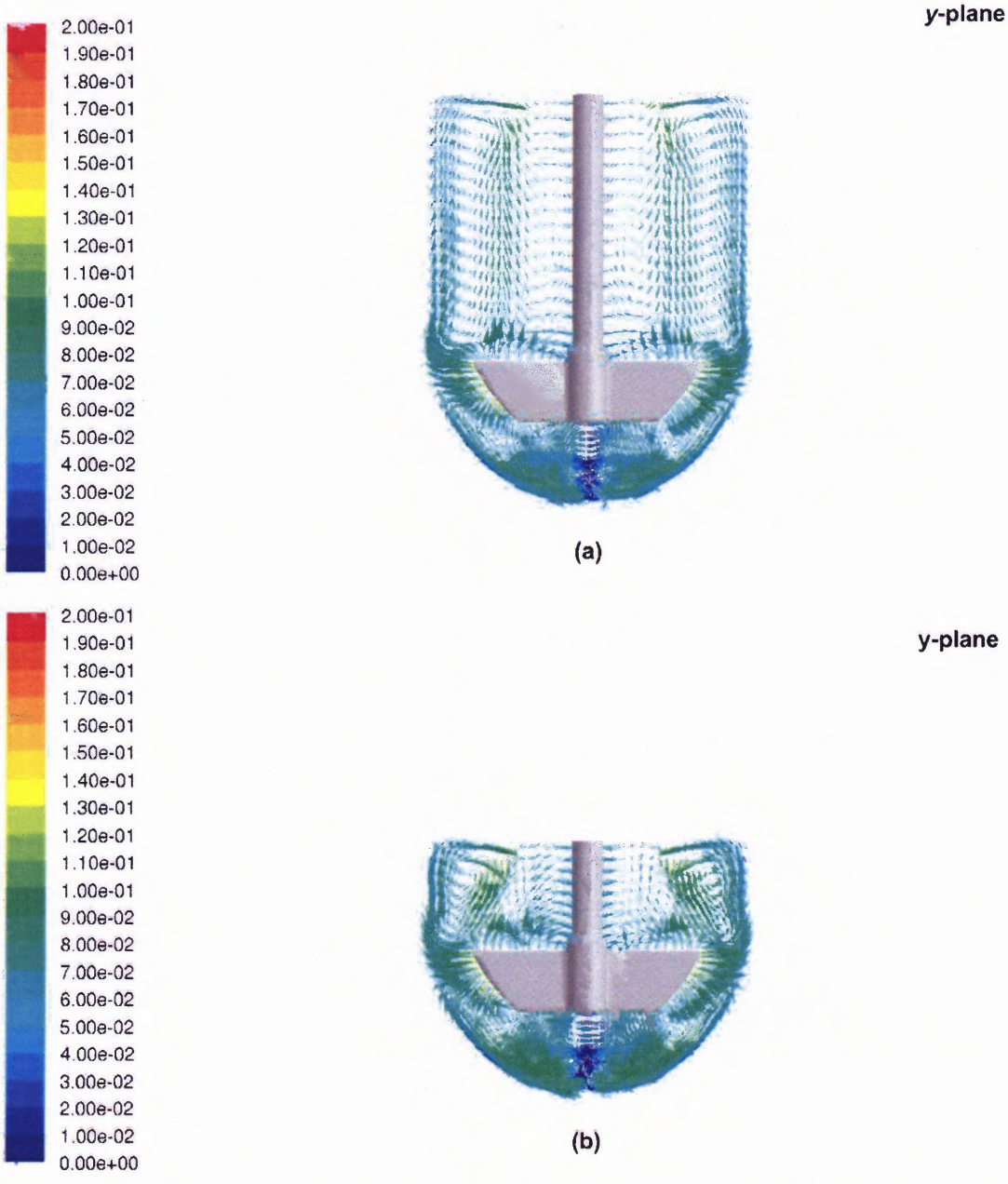

Figure 4.29 CFD predictions of velocity vectors colored by velocity magnitude on vertical cross section (*y* plane) (m/s): (a) Operating Condition 1, (b) Operating Condition 4.

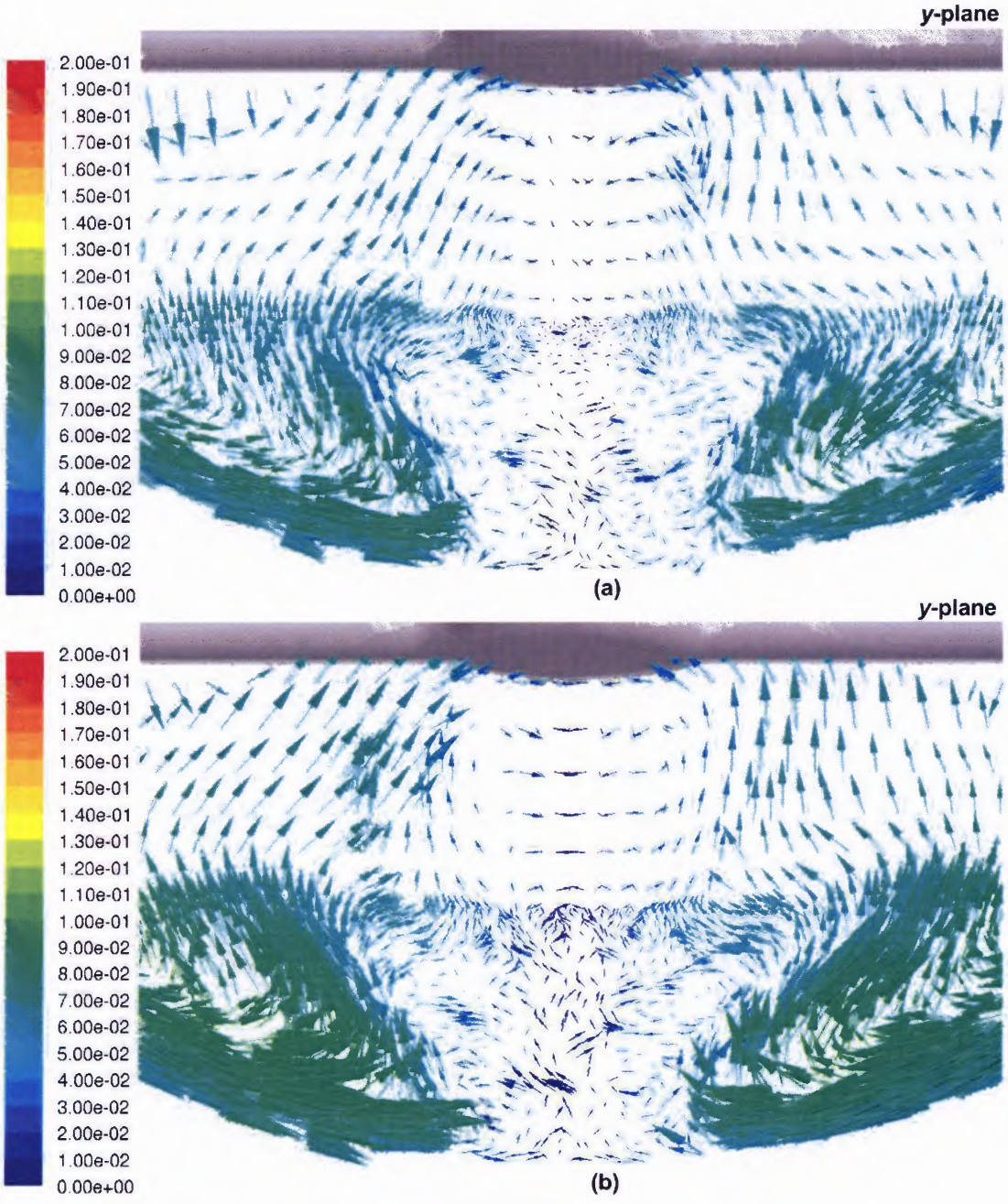

Figure 4.30 CFD predictions of velocity vectors colored by velocity magnitude on vertical cross section (y plane) for the bottom region (m/s): (a) Operating Condition 1, (b) Operating Condition 4.

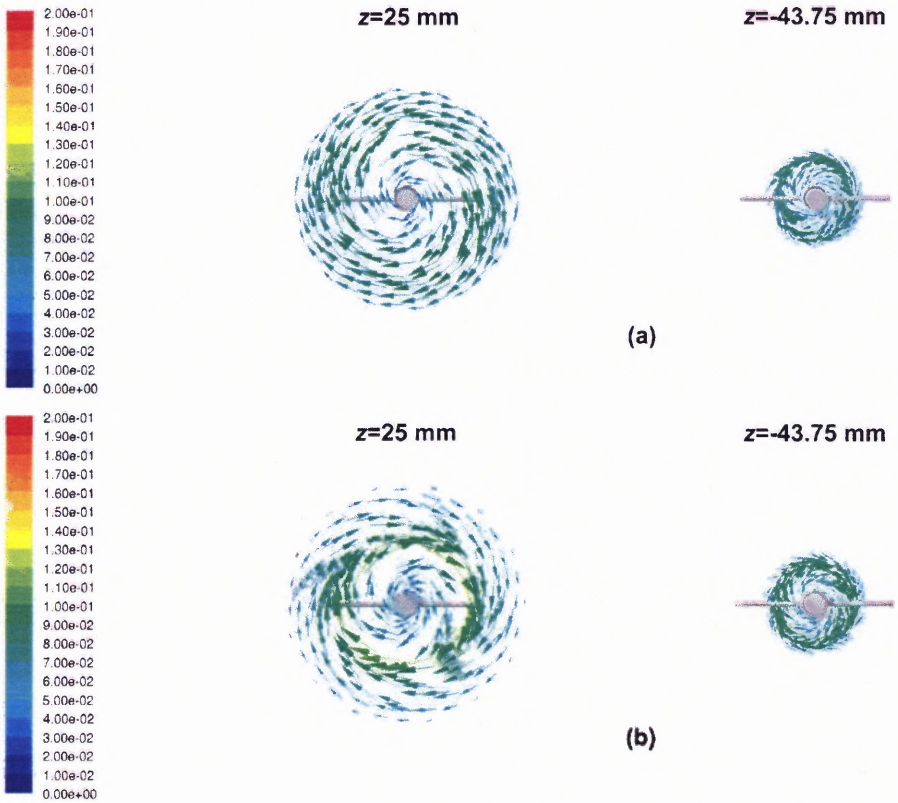

Figure 4.31 CFD predictions of velocity vectors colored by velocity magnitude on different iso-surfaces (z=25 mm and z=-43.75 mm) (m/s): (a) Operating Condition 1, (b) Operating Condition 4.

All these figures confirm the picture emerging from the analysis of the velocity profiles described in the previous section. Overall, the flow is strongly tangential, slightly even more so than in Operating Condition 1, because of the reduced volume and the unchanged agitation speed. The upper portion of the vessel contains not one but *two* recirculation flows on the vertical plane, i.e., a larger one, similar to that in Operating

Condition 1, extending radially from the wall to about the middle of the vessel, and a smaller one next to the shaft. Both recirculation flows are weak in comparison to the tangential flows, but extend vertically from the upper edge of the impeller blade to the air-liquid interface. This in an indication that the pumping action of the impeller (discharging radially from the blades, and being fed from the center) is becoming more difficult as a result of the reduced distance between the impeller blades and the air-liquid interface in Operating Condition 4 which prevents the complete closure of a single vertical loop, as in Operating Condition 1. Below the impeller, the usual picture emerges, including the low recirculation zone just under the impeller, and the swirling action both inside and outside this zone. This weak axial/radial in Operating Condition 4 is generally stronger than in Operating Condition 1, especially in the inner core below the impeller.

4.3.3 Comparison of Strain Rates and Turbulence Energy Dissipation Rate (ϵ)

Figures 4.32 and 4.33 present the CFD predictions on contours of strain rate on the vertical cross section (y-plane) for Operating Condition 4 and Operating Condition 1. Figure 4.34 present CFD predictions on contours on turbulence energy dissipation rate on the vertical cross section (y-plane) for Operating Condition 4 and Operating Condition 1.

An observation on these figures indicates that the strain rates are similar between Operating Condition 4 and Operating Condition 1, both in the impeller region and the vessel bottom.

Similar observation applies to the turbulence energy dissipation rate ϵ, shown in Figures 4.34. Actually, the regions of higher (red colored) energy dissipation rates are slightly thicker in Operating Condition 1 around the blades. Near the bottom of the

vessel, the energy dissipation rates are very similar between these two Operating Conditions. This implies that the mass transfer rates can be very similar in both Operating Conditions.

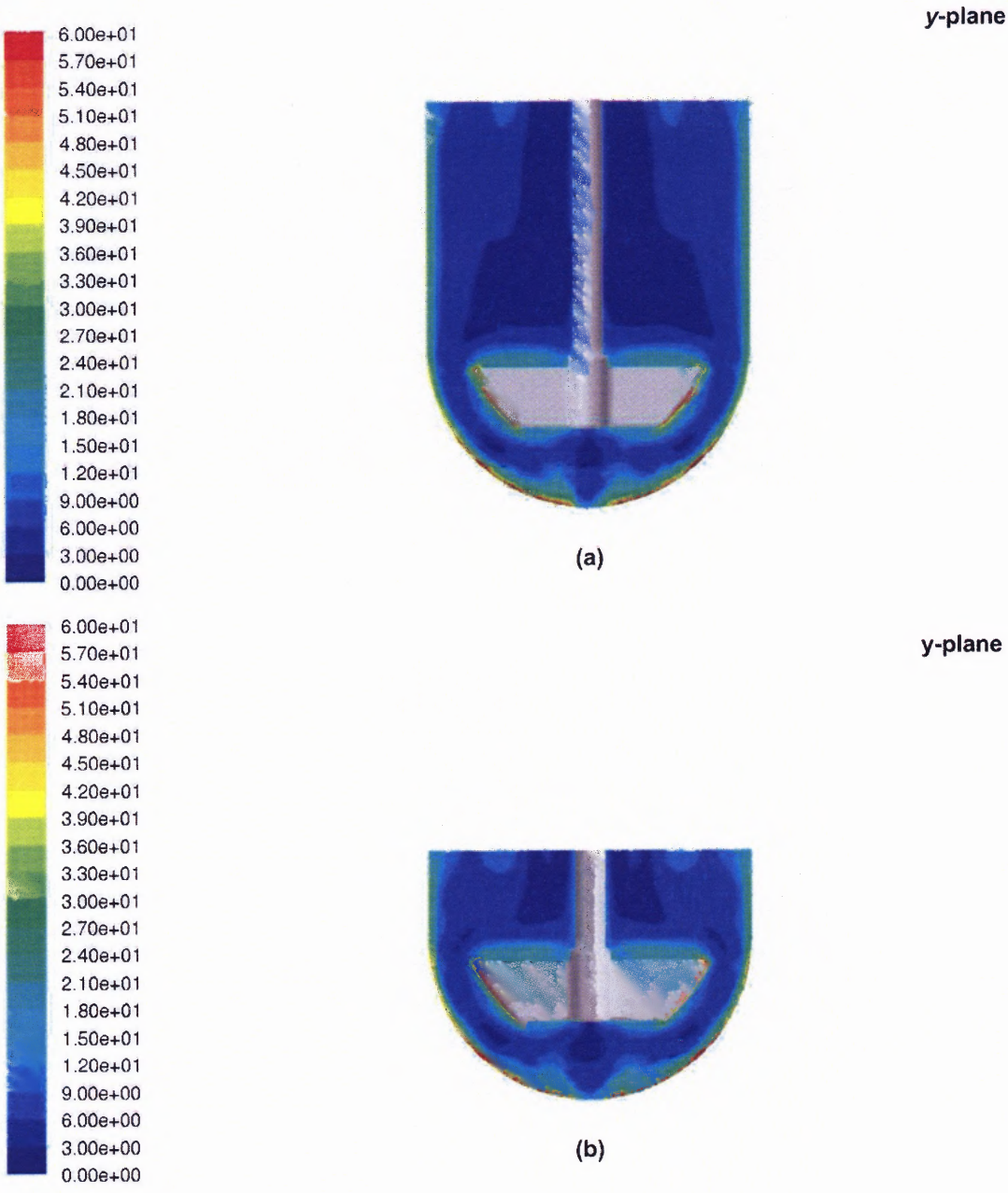

Figure 4.32 CFD predictions of the strain rate on vertical cross sections (*y*-plane) (1/s): (a) Operating Condition 1, (b) Operating Condition 4.

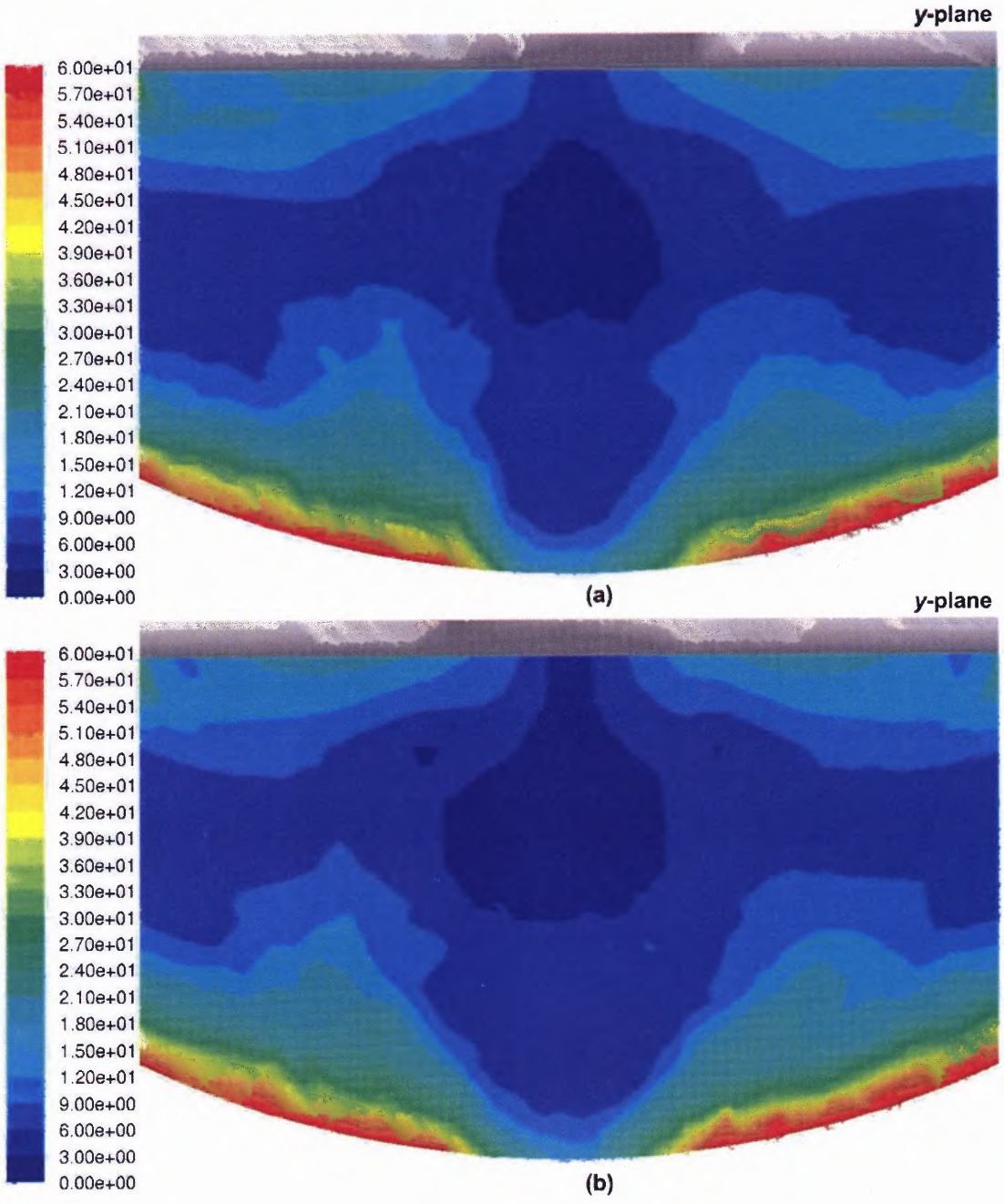

Figure 4.33 CFD predictions of the strain rate on vertical cross sections (y-plane) for the bottom region (1/s): (a) Operating Condition 1, (b) Operating Condition 4.

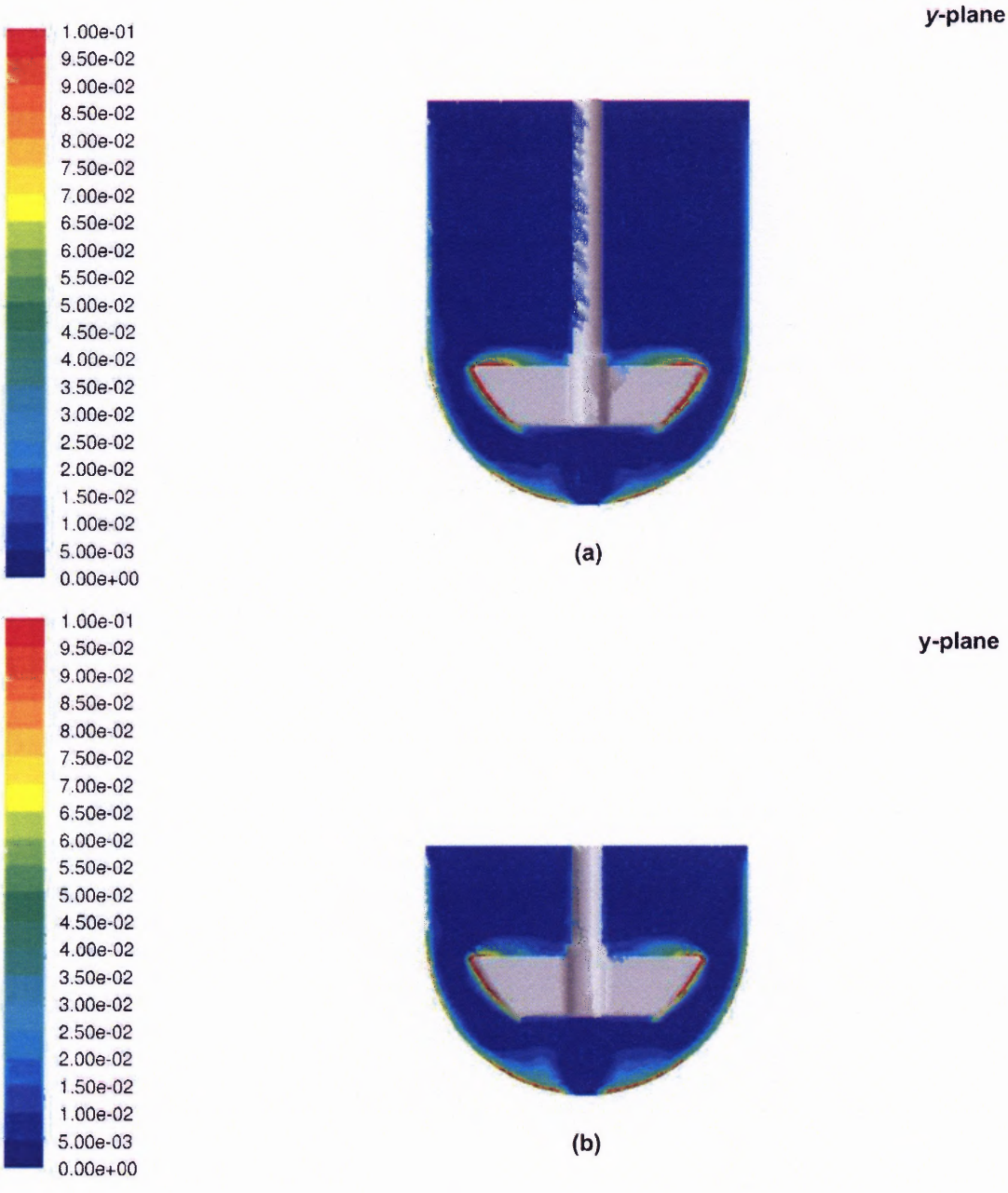

Figure 4.34 CFD predictions of the turbulence energy dissipation rate on vertical cross sections (y-plane) (m^2/s^3): (a) Operating Condition 1, (b) Operating Condition 4.

4.4 Blend Time Study Under Operating Conditions 1, 2, 3, 5 and 6

In initial experiments in which the tracer was injected through Injection Point 1, the blend time was determined with both the conductivity method and the discoloration method. The blend time to achieve 95% uniformity with the conductivity method was found to be 27.2 seconds when the conductivity probe was placed at Monitoring Point 1 and 26.5 seconds when the conductivity probe was placed at Monitoring Point 2 (averages of five experiments in each case, with standard deviations of 5.5% and 5.6% respectively). For the same geometry, i.e., in the presence of the conductivity probe, discoloration was observed at 23.1 seconds at Monitoring Point 1 and 23.9 seconds at Monitoring Point 2 (averages of five experiments in each case with standard deviations of 4.4% and 4.5%). The results of both methods were compared in order to determine the level of homogeneity, U_D, at the time the discoloration phenomenon occurred (transition from color to no color) at the location where the tip of the conductivity probe was. The method used was as follows. By using Equation 2.3, and taking the discoloration time as θ_U, the value of U_D at discoloration was found to be 92.16% (X_D=0.0784) at Monitoring Point 1 and 93.33% (X_D=0.0667) at Monitoring Point 2. Since discoloration must occur for the same value of X_D irrespective of the experiment, an average of these two values was taken, which was 0.0726. This implies that whenever discoloration was observed at any given point inside the vessel during any experiment, the local uniformity level U_D was taken to be 92.74%.

This calibration approach and the resulting knowledge of X_D at discoloration (0.0726) were then used to calculate the blend time at discoloration (where $\theta_D=\theta_{92.74}$) in all the other experiments in which the conductivity probe could not be used, conductivity could not be measured, and the discoloration method was the only usable approach. The results are presented in Table 4.1, where each experimental data point represents the average of five measurements. The standard deviation was always smaller than 5.00%.

All experimental blend times were found to have the same order of magnitude, which was about 30 seconds. The data obtained at the same monitoring point were similar in value, irrespective of the location of the injection point. However, changing the Monitoring Point from 1 to 2 produced an appreciable increase in θ_D (about 18%).

Table 4.1 Comparison of Experimental and CFD-Predicted Blend Times at Discoloration, θ_D. X_D=0.0726; U_D=92.74%, Operating Condition 1

Injection Point	Monitoring Point	Blend Time at Discoloration, θ_D (s)	
		Discoloration Experiment (average ± stand. deviation)	CFD Prediction
1	1	27.5±0.9	28.1
2	1	27.9±0.9	27.1
1	2	33.2±1.5	30.9
2	2	33.3±1.6	30.3

The exact determination of when the discoloration occurred at a specific location contains some degree of uncertainty, and more so in the absence of the probe than in its presence. Without the probe, the fluid in the upper region of the vessel near the shaft

remained colored for a significantly longer period of time (up to $t \approx 60$ s) than the rest of the tank, because of the solid body rotation of the central liquid core described in Section 4.1. This core continuously "shed" material in the form of colored filaments moving radially, making the exact determination of when complete discoloration occurred at a specific location outside the core region somewhat difficult. When the probe was present, the resulting baffling effect in the upper portion of the tank eliminated this problem almost entirely.

Figure 4.35 shows the molar concentration contours of the tracer at different times, as predicted by the CFD simulation, when the tracer was injected at Injection Point 1 under standard Operating Conditions. This figure shows that after about 30 s, the concentration distribution of the tracer did not change appreciably with time. This figure also shows that the core region in the upper portion of the vessel was the most difficult to homogenize, as experimentally observed. Qualitatively, the behavior of the experimental system was similar to that predicted through CFD.

CFD computations such as that graphically reported in Figure 4.35 were used to calculate the concentration profiles at both monitoring points as a function of time, following a tracer injection. Figure 4.36 shows these time profiles. The time at which the concentration was predicted to drop (and consistently remain) below the value corresponding to a uniformity coefficient U_D of 92.74% (i.e., intersecting the horizontal line at X_D=0.0726) was taken as the predicted θ_D value. Values of the predicted θ_D for different injection points and monitoring points are also shown in Table 2.

The results reported in this table show that the CFD-computed blend times at discoloration compare favorably with the experimental results. CFD predictions agreed with the experimental data even better when predicting blend time at Monitoring Point 1.

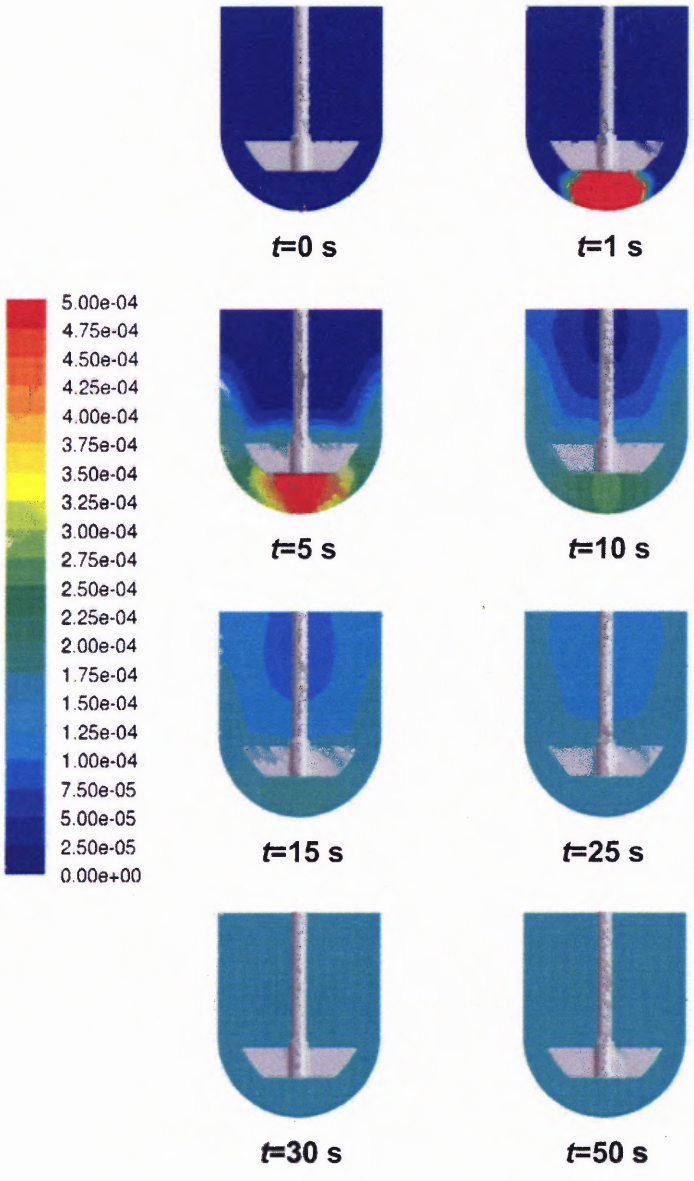

Figure 4.35 Contours of molar concentration of tracer (in kmol/m^3) as a function of time as predicted by the CFD simulation under standard Operating Conditions (Operating Condition 1): Tracer injected at Injection Point 1.

As observed in the experiments, the CFD-predicted θ_D values confirmed that the injection point does not appreciably affect θ_D, whereas the monitoring point does. The average difference between the computed and experimental blend times is 1.7 s, i.e., an average deviation of about 5%, which is quite reasonable considering the complexity of the process and the uncertainty implicit in the experimental determinations. However, the agreement is typically much better for Monitoring Point 1 (average deviation=2.7%), than for Monitoring Point 2 (average deviation=7.9%).

These results validate the CFD simulation approach used here to predict blend time in USP II Apparatuses. In addition, the order of magnitude of all these blend times (~30 seconds) is much smaller than the time of the typical dissolution test experiment, implying that once the dissolved active pharmaceutical ingredient (API) leaves the boundary around the drug tablet and enters the bulk solution, it distributes itself throughout the USP II vessel rather quickly.

Because of the favorable comparison between CFD predictions and experimental data, CFD was additionally used to estimate the effect on θ_D of different operating parameters such as agitation speed and impeller locations. The results are presented in Table 4.2 for Monitoring Point 1 and in Table 4.3 for Monitoring Point 2.

The blend times obtained under standard Operating Conditions and geometry (Operating Conditions 1, 2, and 3) and presented in Table 4.2 and Table 4.3 were plotted in Figure 4.37, showing that blend time is inversely proportional to agitation speed:

$$\theta_U \propto \frac{1}{N} \tag{4.4}$$

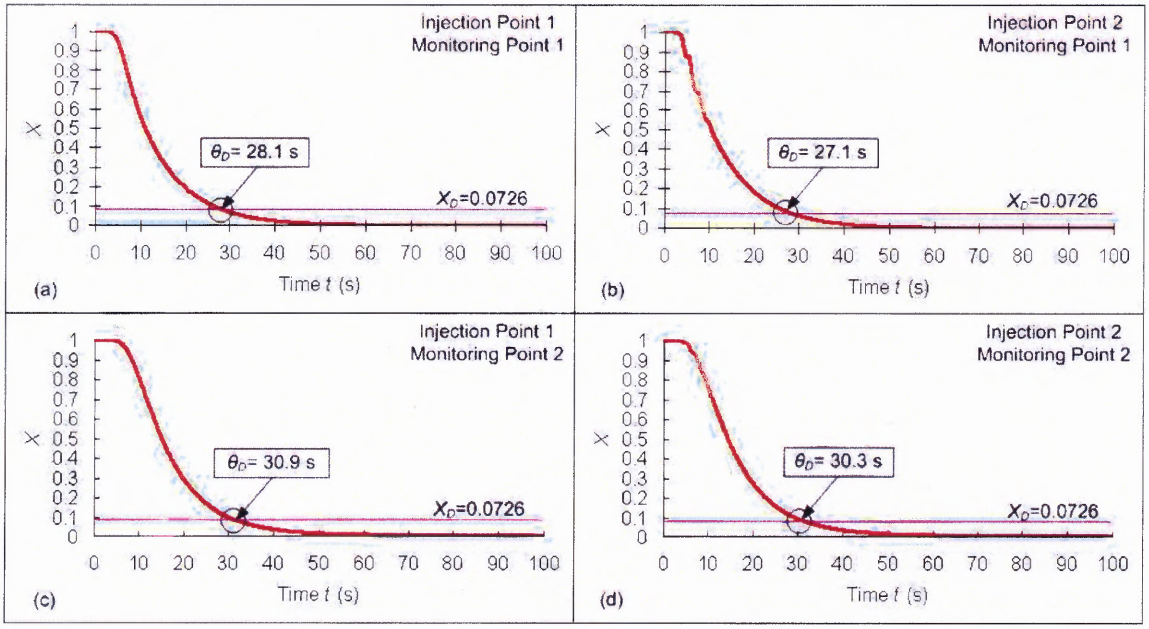

Figure 4.36 Plot of X vs. t for to predict θ_D from CFD simulations under standard Operating Conditions (Operating Condition 1): (a) Injection Point 1, Monitoring Point 1; (b) Injection Point 1, Monitoring Point 2; (c) Injection Point 2, Monitoring Point 1; (d) Injection Point 2, Monitoring Point 2.

Table 4.2 CFD-Predicted Blend Time at Discoloration, θ_D (with X_D=0.0726), at Monitoring Point 1 for Different Operating Conditions

Operating Condition	Blend Time at Discoloration, θ_D (s)	
	Tracer Injected at Injection Point 1	Tracer Injected at Injection Point 2
1 (standard)	28.1	27.1
2	16.7	16.3
3	13.8	13.2
5	25.8	25.8
6	24.4	23.9

Table 4.3 CFD-Predicted Blend Time at Discoloration, θ_D (with X_D=0.0726), at Monitoring Point 2 for Different Operating Conditions

Operating Condition	Blend Time at Discoloration, θ_D (s)	
	Tracer Injected at Injection Point 1	Tracer Injected at Injection Point 2
1 (standard)	30.9	30.3
2	18.0	17.6
3	15.7	15.2
5	28.4	28.4
6	26.8	26.2

This is consistent with the results obtained by many workers for blend time in mixing vessels and impellers of different geometries (Cox et al. 1983, Grenville and Nienow, 2004, Kresta et al. 2006). The results found here can be analyzed using previously derived semi-empirical equations for blend time. A representative of such blend time equations is the following (Grenville, 1992, Grenville and Nienow, 2004):

$$P_o^{1/3} N\theta_{95} \frac{D^2}{T^{1.5} H^{0.5}} = 5.20 \tag{4.5}$$

where P_o is the impeller power number, D is the impeller diameter, T is the vessel diameter, and H is the height of liquid. Equation 4.5 was derived by rounding off the exponents obtained from regression of the data for different impellers at different scales (Grenville, 1992). The standard deviation of the constant was ±10.0%.

Although Equation 4.5 was derived for baffled mixing tanks with common impeller geometries one can conceivably adapt this equation to the USP Dissolution Apparatus II case, since no vortex was observed in this vessel under the conditions tested

here. For an apparatus with standard geometry (impeller clearance=25 mm), D, T, H, and P_o are all constant. Then, Equation 4.5, combined with Equation 2.3, can be re-written as:

$$N\theta_D = \text{constant} \tag{4.6}$$

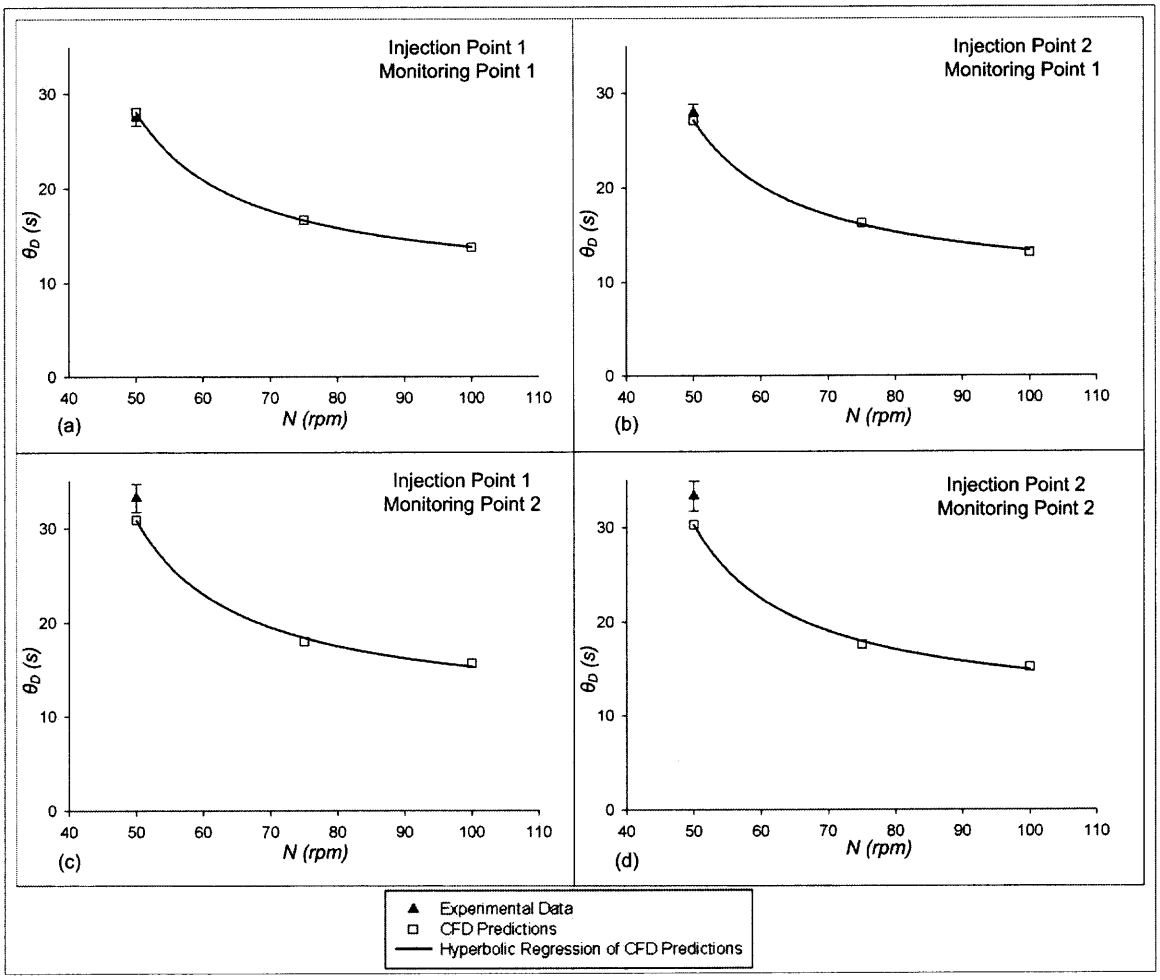

Figure 4.37 Plot of θ_D vs. N under standard Operating Conditions (Operating Condition 1): (a) Injection Point 1, Monitoring Point 1; (b) Injection Point 1, Monitoring Point 2; (c) Injection Point 2, Monitoring Point 1; (d) Injection Point 2, Monitoring Point 2.

where, the constant needs to be determined experimentally. The form of this equation is identical to that of Equation 4.4, which was shown in Figure 4.37 to appropriately fit the experimental data, confirming that the blend time process in a USP Dissolution Apparatus II is similar to that of other mixing vessels. A plot of the non-dimensional blend time number $N\theta_D$, reported in Figure 4.38, shows that $N\theta_D$ is indeed constant with respect to N. The value of the constant in Equation 4.6 is a function of the motoring point and the injection point, with the latter having a bigger impact than the former on $N\theta_D$, as shown in the regression equations reported in Figure 4.38. Considering only the monitoring point as a parameter, the following regression equations were obtained for the USP Apparatus II under Operating Conditions 1, 2 and 3 (impeller clearance=25 mm):

$$N\theta_D = 22.0 \pm 1.2 \qquad \text{(Monitoring Point 1)} \tag{4.7}$$

$$N\theta_D = 24.5 \pm 1.8 \qquad \text{(Monitoring Point 2)} \tag{4.8}$$

These equations can be used to predict the blend time in a USP II apparatus and any agitation speed in the range examined here, and possibly beyond.

Table 4.2 and Table 4.3 also present the CFD predictions for the Operating Conditions in which the vertical location of the impeller was changed. When the agitation speed was kept at 50 RPM, the blend time was found to decrease irrespective of whether the impeller was raised (Operating Condition 5) or lowered (Operating Condition 6) with respect to the standard location (Operating Condition 1). The decrease was smaller when the impeller was raised (5-8%) than when it was lowered (12-13%). Raising the impeller slightly improves blending probably because of the proximity of the impeller to the monitoring point. As for the similar effect predicted when the impeller was lowered, one can only speculate that the impeller at this location interacts more

intensively with the vessel wall generating a stronger upwards flow that reduces blend time.

In any case, the blend time at N=50 RPM is of only a few tens of seconds, irrespective of the impeller location. This blend time is still much smaller than the time required for tablet dissolution during a typical test in the USP Apparatus II, as discussed below.

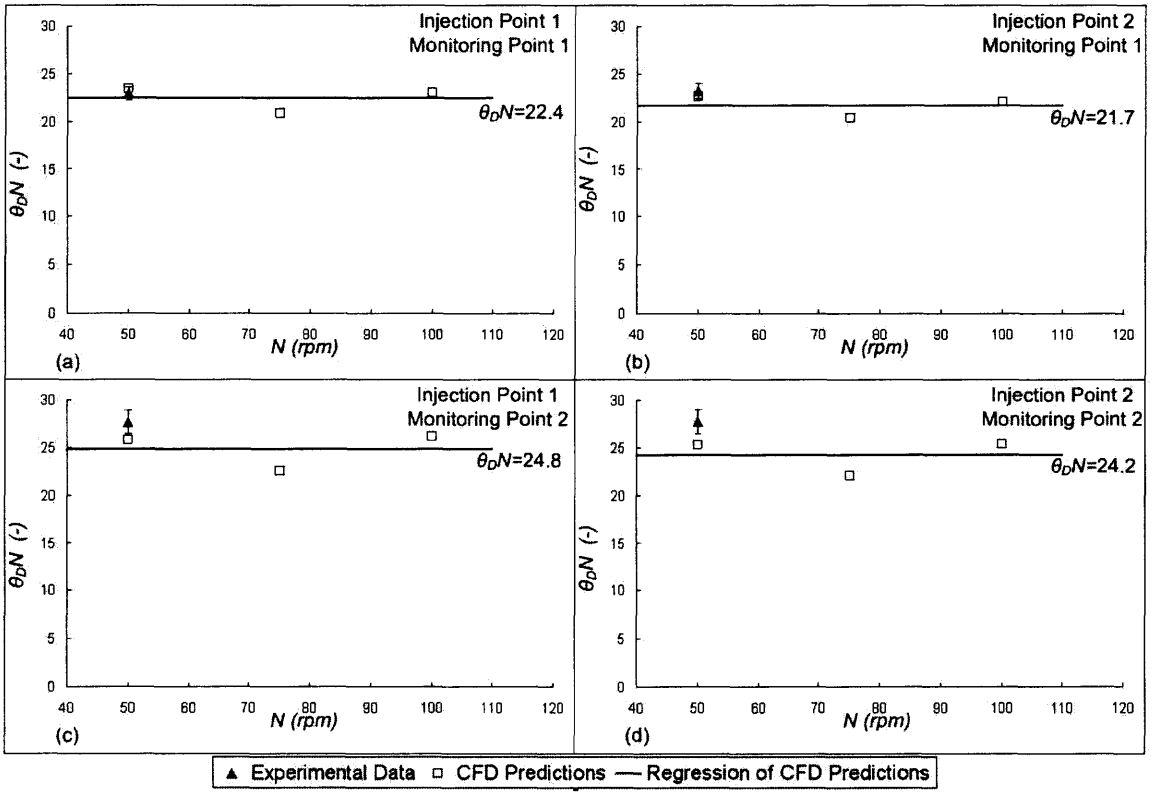

Figure 4.38 Non-dimensional blend time number, $\theta_D N$, as a function of N under Operating Conditions 1, 2 and 3: (a) Injection Point 1, Monitoring Point 1; (b) Injection Point 1, Monitoring Point 2; (c) Injection Point 2, Monitoring Point 1; (d) Injection Point 2, Monitoring Point 2.

The results of Tables 4.1, 4.2 and 4.3 show that the time needed to homogenize the vessel's content to a 92.74% uniformity level is about 30 s. Combining this result with Equation 2.3, it is possible to calculate the times required to achieve other

uniformity levels, such as the 95%, 99% and 99.9% levels, for which the blend times are 35 s, 53 s, and 79 s, respectively. These blend times can be compared with the times typically required by the tablet dissolution process to proceed to any meaningful extent.

As an example, Moore et al. (1995) conducted experiments on the dissolution of Prednisone tablets, Lot J, in a USP Apparatus II under standard Operating Conditions. Samples were taken 30 minutes after the tablet was added to the vessel. Six identical dissolution tests were run and the average percentage of the drug released at this time was found to be 52% with a standard deviation of 0.9%. Intuitively, these data indicate that the time scale for blending is much smaller that that for tablet dissolution.

A slightly more refined analysis can be obtained by comparing the rate of drug concentration change caused by dissolution (dC_P/dt) to that caused by blending ($dC_P/d\theta$), where C_P is the drug concentration is solution. The first term can be calculated using the mass transfer equation for particle dissolution (Armenante and Kirwan, 1989):

$$\frac{dC_P}{dt} = K\frac{A}{V}\left(C_{Ps} - C_P(t)\right) \tag{4.9}$$

Assuming that the concentration $C_P(t)$ is much smaller than the corresponding saturation concentration C_{Ps} (this is typically the case in the initial phase of the dissolution process), and that the surface area A and the mass transfer coefficient K do not change rapidly during dissolution, the dissolution rate becomes:

$$\frac{dC_P}{dt} \cong K\frac{A}{V}\left(C_{Ps}\right) = \alpha \tag{4.10}$$

where α is a constant.

In order to estimate ($dC_P/d\theta$), Equations 2.2 and 2.3 can be combined to calculate the blend time to reach a generic homogenization level U at a given point within the vessel:

$$\theta_U = \beta \ln X = \beta \ln \left(\frac{C_{P\,Final} - C_P(t)}{C_{P\,Final} - C_{Po}} \right) \tag{4.11}$$

where, β is a constant. Assuming that C_{Po} can be neglected with respect to $C_{P\,Final}$ and that C_p is appreciably smaller than $C_{P\,Final}$, and recalling that $\ln(1-\varepsilon) \cong -\varepsilon$ for small enough values of ε, then the previous equation becomes:

$$\theta_U \cong \beta \ln \left(\frac{C_{P\,Final} - C_P(t)}{C_{P\,Final}} \right) = \beta \ln \left(1 - \frac{C_P(t)}{C_{P\,Final}} \right) \cong -\beta \frac{C_P(t)}{C_{P\,Final}} = \beta' C_P(t) \tag{4.12}$$

where, β' is also a constant. Then, by taking the derivative with respect of θ_U the rate of homogenization of the dissolved drug product at a specific location in the vessel can be predicted from this equation to be:

$$\frac{dC_p}{d\theta_U} \cong \frac{1}{\beta'} = \gamma \tag{4.13}$$

where, γ is a constant. An estimate of the magnitude of the rate of dissolution relative to the rate of homogenization can be obtained by examining the ratio:

$$\frac{\dfrac{dC_p}{dt}}{\dfrac{dC_p}{d\theta_U}} \cong \frac{\alpha}{\gamma} = \text{constant} \tag{4.14}$$

A numerical value for this ratio can be obtained by approximating the derivatives as finite differences and using the experimental and predicted data from this work as well as the above-mentioned data of Moore et al (1995). Then:

$$\frac{\frac{dC_p}{dt}}{\frac{dC_p}{d\theta_U}} \cong \frac{\frac{\Delta C_p}{\Delta t}}{\frac{\Delta C_p}{\Delta \theta_U}} \approx \frac{\frac{52\% C_{Ps}}{30 \text{ min}}}{\frac{99.9\% C_{Ps}}{79\ s}} \cong 0.0228 = 2.28\% \qquad (4.15))$$

The small value of this ratio implies that the rate at which dissolution occurs is much slower than the rate of blending, i.e., that homogenization of the vessel's content is a much faster process than dissolution. This implies that, for all practical purposes, the vessel's content is typically well mixed.

A simpler way to reach the same conclusion is by examining what would happen during, for example, a 79 s time interval (numerically equal here to $\theta_{99.9}$) during a dissolution test. At the end of this time period, the concentration in the sample would be at least 99.9% of the value at the beginning of the time period, while tablet dissolution would have progressed by only 2.28%. By comparison, the concentration of dissolved Prednisone (Lot J) at 30 minutes should be in the range 46%-59% of the saturation value, i.e, 52.5%±6.5%. (Qureshi, 1996).

Similar results can be obtained by analyzing other data, such as those of Moore et al. (1995) for the dissolution of Salicylic Acid tablets (Lot K) with Apparatus II under standard Operating Conditions. In this case, a 99.9% homogeneity level in the vessel would be reached at the same time tablet dissolution would have progressed by only 0.77%. The concentration of dissolved Prednisone (Lot J) at 30 minutes should be in the range 13%-22% of the saturation value, i.e, 17.5%±4.5%. (Qureshi, 1996).

In summary, vessel homogenization appears to be a much faster process than tablet dissolution in the typical dissolution test utilizing the USP Apparatus II.

4.5 Flow Field Characterization under Operating Conditions 5, 6 and 7

4.5.1 Comparison of Velocity Magnitude and Velocity Vectors

Figure 4.39 and Figure 4.40 show the contours of the CFD-predicted velocity magnitude on a vertical cross section through the impeller shaft for different orientations of the impeller and different impeller locations. Figure 4.41 presents the velocity vectors for different impeller locations on a horizontal cross section 43.75 mm below the horizontal plane where the cylindrical and horizontal sections of the vessel intersect. Figure 4.42 shows the velocity vectors on a vertical cross section containing the impeller blades. Addition plots show the expanded views of velocity vectors in the vessel bottom region on a vertical cross section through the impeller shaft at two different orientations of the impeller for Operating Condition 1, 5, 6 and 7.

Panels (b) in Figure 4.39 and Figure 4.40 present the contours of the velocity magnitude for Operating Condition 7. Although the impeller was displaced sideways by only a small distance (2 mm compared to a vessel radius of 50.08 mm, i.e., a 4% translation), the velocity magnitude plots show a significant non-symmetric distribution compared to Operating Condition 1 (Figure 4.39a and Figure 4.40a).

Figure 4.41b shows that even under Operating Condition 7, the tangential component of the velocity dominates over the other velocity components, although the tangential velocity is weaker compared to Operating Condition 1 (Figure 41a), especially in the region where the impeller-wall distance is larger.

The impeller asymmetry under Operating Condition 7 produced higher axial and radial velocities in most regions of the vessel than in Operating Condition 1, especially on the side where the impeller-wall distance was smaller, both above and below the impeller. However, on the opposite side of the vessel, the regions where the velocity magnitude was very small (e.g., in upper region near the wall, and, more significantly, in the region below the impeller) actually expanded, as indicated by the enlarged darker region, especially just under the impeller. Since the impeller rotates, the different regions rotate as well, exposing different portions of the vessel to high fluctuating velocities, and promoting mixing and recirculation.

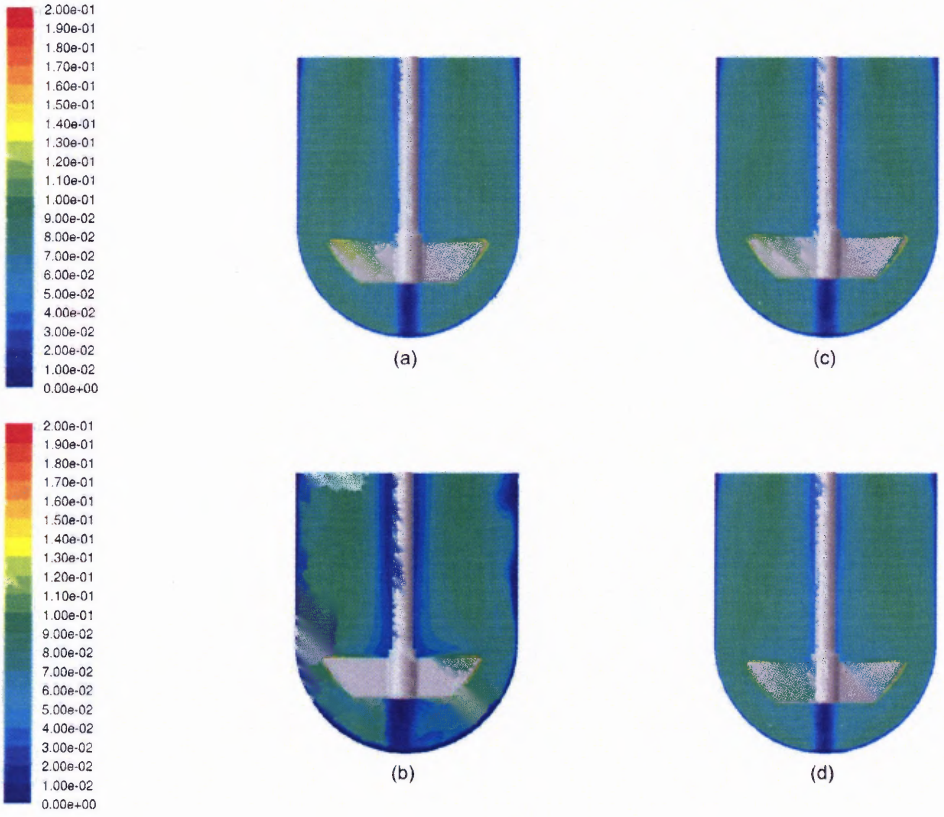

Figure 4.39 CFD predictions of contours of the velocity magnitude (m/s) on the impeller plane (y-plane) for different locations of the impeller: (a) Operating Condition 1, (b) Operating Condition 7, (c) Operating Condition 5, (d) Operating Condition 6.

The velocity vector plot (Figure 4.42b) confirms these observations. Two recirculation loops could still be observed, above and below the impeller. However, the loops are no longer symmetric. As one can anticipate, on the side where the impeller blade is 2 mm closer to the vessel wall (the left side in the figure) the loops have higher velocity magnitude than at the same radial location on the opposite side.

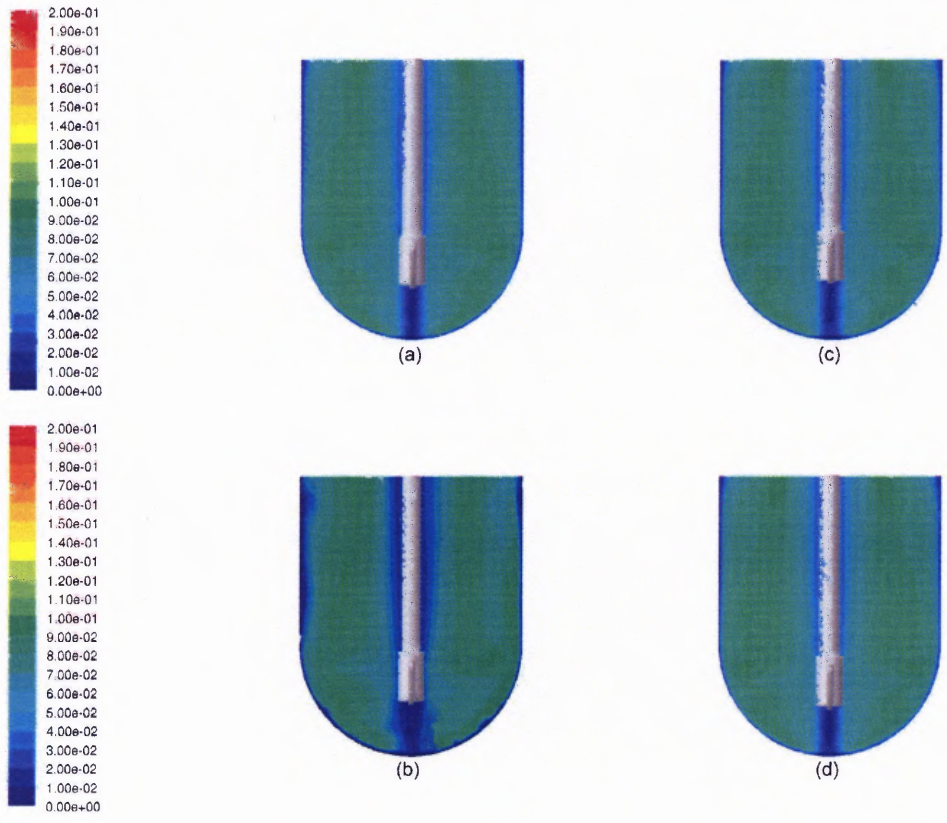

Figure 4.40 CFD predictions of contours of the velocity magnitude (m/s) on the plane perpendicular to the impeller plane (x-plane) for different locations of the impeller: (a) Operating Condition 1, (b) Operating Condition 7, (c) Operating Condition 5, (d) Operating Condition 6.

Of special interest here are the plots for the region below the impeller (Figures 4.43b and Figure 4.44b). Since the impeller is off-center, the symmetric structure and the poorly mixed region below the shaft observed under Operating Condition 1 (Figure 4.43a

and Figure 4.44a) are now largely removed. A stronger flow in the vertical plane now sweeps the entire lower region, creating alternating recirculation loops below both tips of the lower edge of the impeller. These loops move with the impellers, and the net result is that the entire vessel bottom region is affected. An eddy in the vertical plane can even be observed in Figure 4.42b and Figure 4.43b. It is also remarkable that the radially

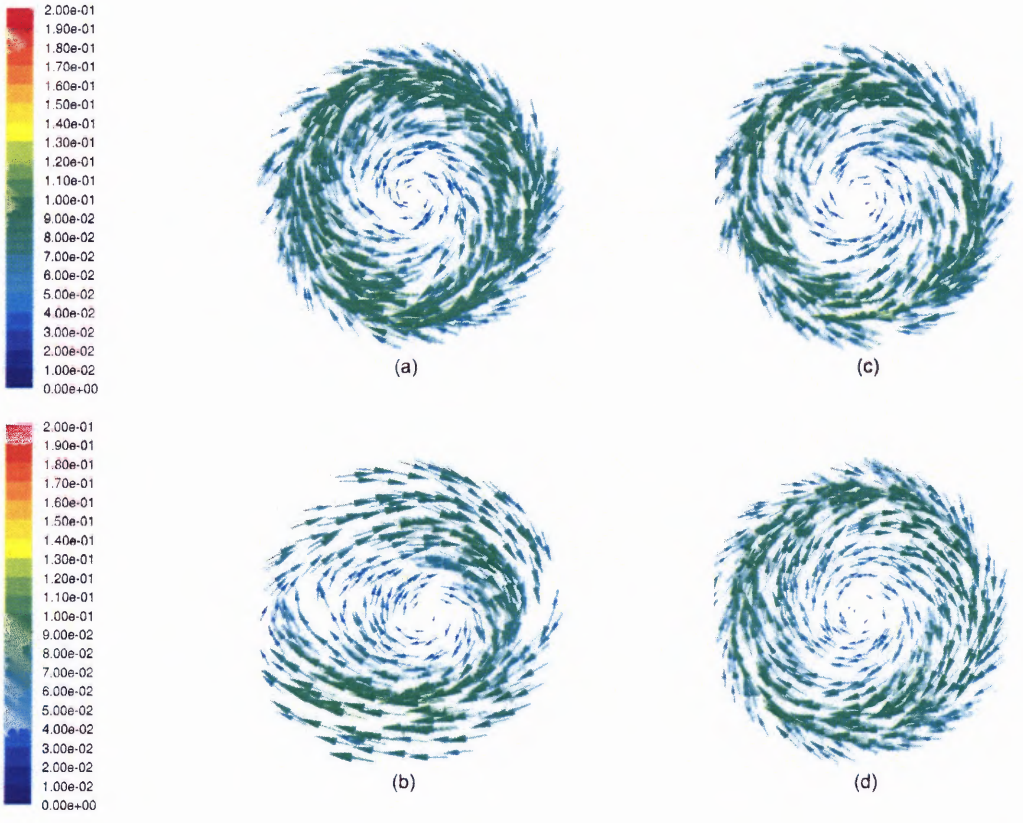

Figure 4.41 CFD predictions of velocity vectors (m/s) on a horizontal plane below the impeller at z=-43.75mm (where z=0 is the vertical plane at the intersection of the cylindrical and hemispherical regions of the vessel) for different locations of the impeller: (a) Operating Condition 1, (b) Operating Condition 7, (c) Operating Condition 5, (d) Operating Condition 6.

directed flow sweeping the central core region below the impeller now "feeds" a large upflow stream (shown on the left in the figures) which further promotes axial mixing within the vessel.

Figure 4.39c and Figure 4.40c show the contours of the velocity magnitude under Operating Condition 5. The difference in velocities between these figures and the corresponding figures for Operating Condition 1 is relatively small. The low velocity region below the impeller is larger for the higher impeller position simply because the impeller clearance is larger. A slight increase in the velocity magnitude can be detected in the center near the vessel bottom.

The tangential component of the velocity does not appear to be appreciably affected by the increased off-bottom clearance (Figure 4.41c) compared to Operating Condition 1 (Figure 4.41a), implying that the preservation of symmetry, and hence the resulting strong tangential flow, dominate over any other effects.

A comparison between the velocity vectors for the two cases (Figure 4.42c vs. Figure 4.42a) and especially in the region below the impeller (Figures 4.43c and Figure 4.44 c vs. Figures 4.43a and Figure 4.44a), shows that small velocity differences exist. Under Operating Condition 5, the low velocity region below the impeller is characterized by slightly higher velocities in the axial and radial directions, and the region just around the low-mixing core region shows a stronger upward-directed flow. The probable cause for this effect is the larger gap between the impeller blades and the vessel wall, resulting in a slightly stronger pumping action by the impeller and a stronger flow in the lower recirculation loop (Figure 4.43c and Figure 4.44c). However, the difference in velocity profiles between Operating Condition 1 and Operating Condition 4 appears to be rather

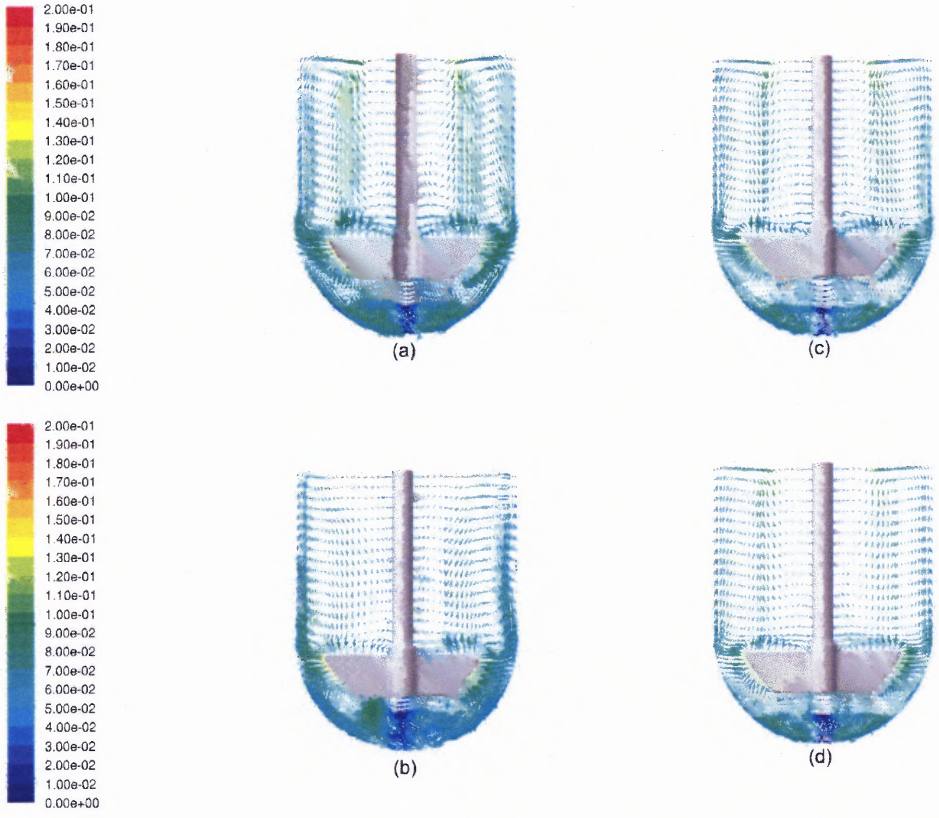

Figure 4.42 CFD predictions of velocity vectors (m/s) on the impeller plane (y-plane) for different positions of the impeller: (a) Operating Condition 1, (b) Operating Condition 7, (c) Operating Condition 5, (d) Operating Condition 6.

small. In summary, although the higher impeller position places the impeller farther away from vessel bottom, the stronger pumping action produces a slightly stronger lower recirculation loop.

Figure 4.39d and Figure 4.40d show the contours of the velocity magnitude under Operating Condition 6. In general, the velocity magnitudes for this Operating Condition are similar to those under Operating Condition 1. As in Operating Condition 5, the

tangential velocity is not significantly affected by the lower off-bottom clearance (Figure 4.41d) compared to Operating Condition 1 (Figure 4.41a). Once again, symmetry prevails over other small effects.

A closer comparison of the velocity vectors under Operating Condition 6 (Figures 4.42d, Figure 4.43d, and Figure 4.44d) with those under Operating Condition 1 shows that the differences are still small, but that the reduced volume of fluid below the impeller and the smaller gap, and hence the proximity of the fluid in this region to the impeller, promotes a slightly larger segregation of the fluid region just under the impeller from the other regions of the vessel. This can be seen from the slightly expanded low velocity region just below the impeller shaft. In other terms, it becomes increasingly difficult for the fluid jet emerging radially from the blade to penetrate the central fluid core just below the impeller. This in turn, slightly reduces the axial velocity component of the fluid just under the impeller and promotes segregation.

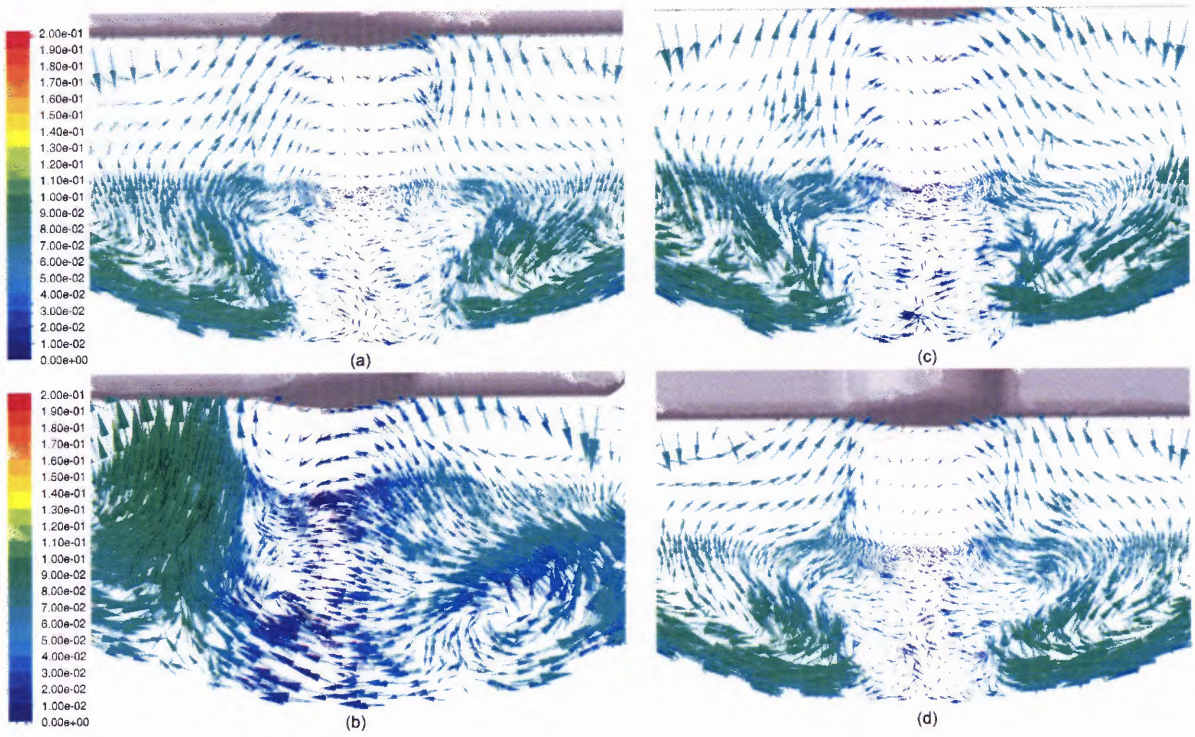

Figure 4.43 CFD predictions of velocity vectors (m/s) on the impeller plane (y-plane) at the vessel bottom for different locations of the impeller: (a) Operating Condition 1, (b) Operating Condition 7, (c) Operating Condition 5, (d) Operating Condition 6.

4.5.2 Comparison of Turbulence Energy Dissipation Rate (ε)

Figure 4.45 presents the distribution of the local CFD-predicted energy dissipation rates, ε (i.e., the rate of turbulence energy dissipation per unit mass), on the y-plane, for Operating Conditions 1, 5, 6 and 7. The CFD-predicted distributions of the energy dissipation rate in the USP Apparatus II are symmetric above and below the impeller under Operating Conditions 5 and 6 but not under Operating Condition 7 (Figure 4.45b). The highest energy dissipation rates were found around the impeller blades, near the wall in the impeller region, and near the vessel bottom. Whenever symmetry was present, ε

dropped rapidly in the wall region just under the impeller shaft. However, if symmetry was lost, as under Operating Condition 7, the energy dissipation rate was found to be more uniformly distributed below the impeller (Figure 4.45b).

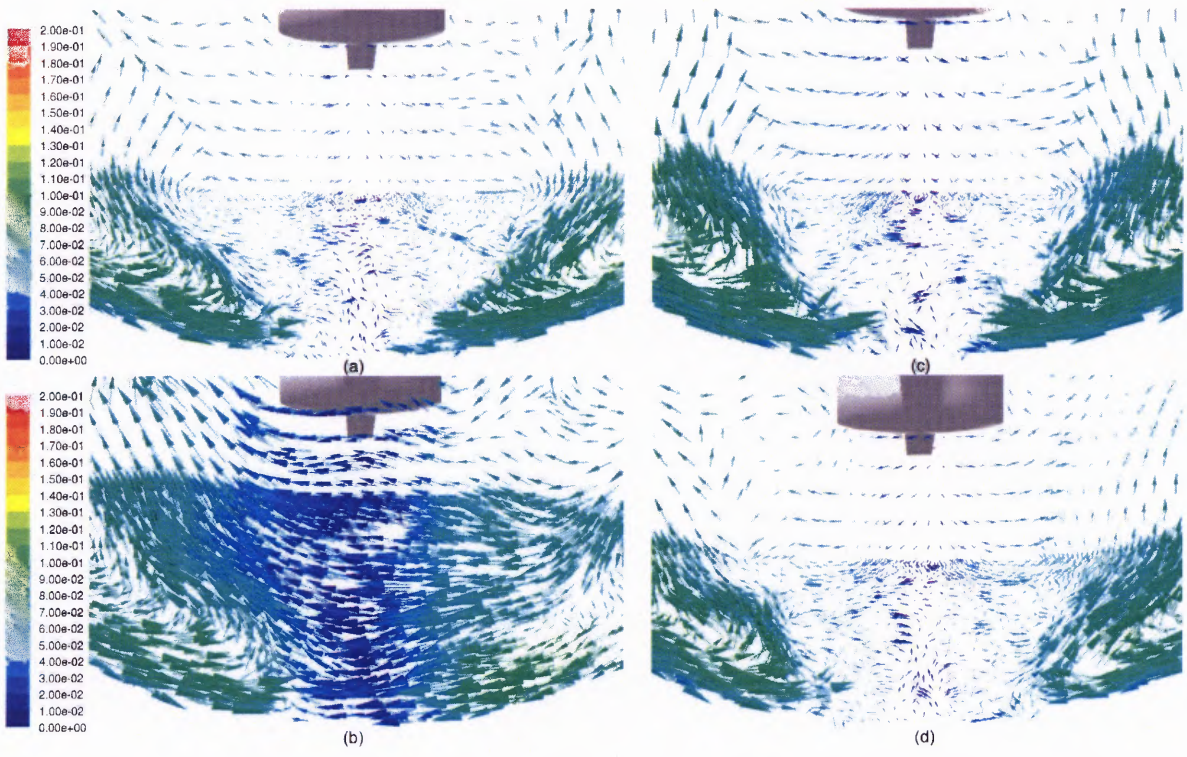

Figure 4.44 CFD predictions of velocity vectors (m/s) on the plane perpendicular to the impeller plane (x-plane) at the vessel bottom for different locations of the impeller: (a) Operating Condition 1, (b) Operating Condition 7, (c) Operating Condition 5, (d) Operating Condition 6.

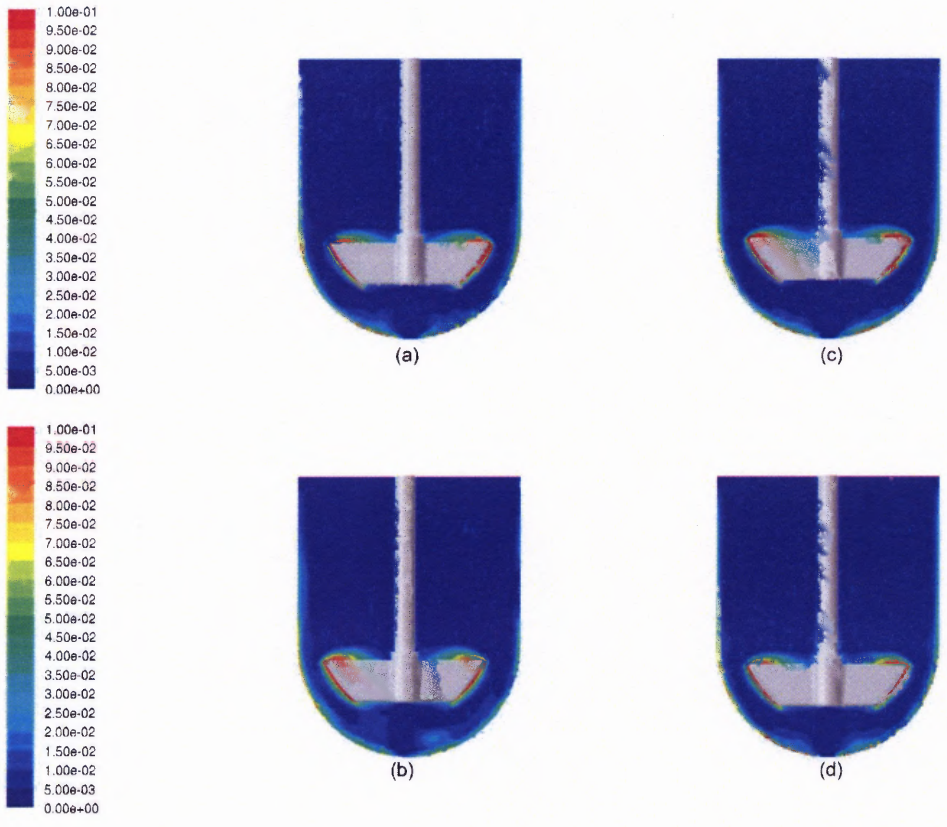

Figure 4.45 CFD predictions of the energy dissipation rate (m^2/s^3) on the impeller plane (*y*-plane) for different locations of the impeller: (a) Operating Condition 1, (b) Operating Condition 7, (c) Operating Condition 5, (d) Operating Condition 6.

4.5.3 Comparison of Strain Rate

Figures 4.46 and Figure 4.47 present the distribution of the local strain rate in the region below the impeller on the vertical plane of the impeller and on its perpendicular plane, respectively. The strain rate is generally higher next to the vessel wall under all Operating Conditions shown here, as one would expect. Panels (a), (c) and (d), corresponding to the three Operating Conditions in which the impeller is centrally located, show symmetrical strain rate distributions, all similar to each other. The impeller

clearance does not appear to affect appreciably the strain rates, as one can see by comparing Panels (a), (c) and (d) in Figures 4.46 and Figure 4.47. The only apparent difference is the size of the central low strain region midway between the impeller and the vessel bottom.

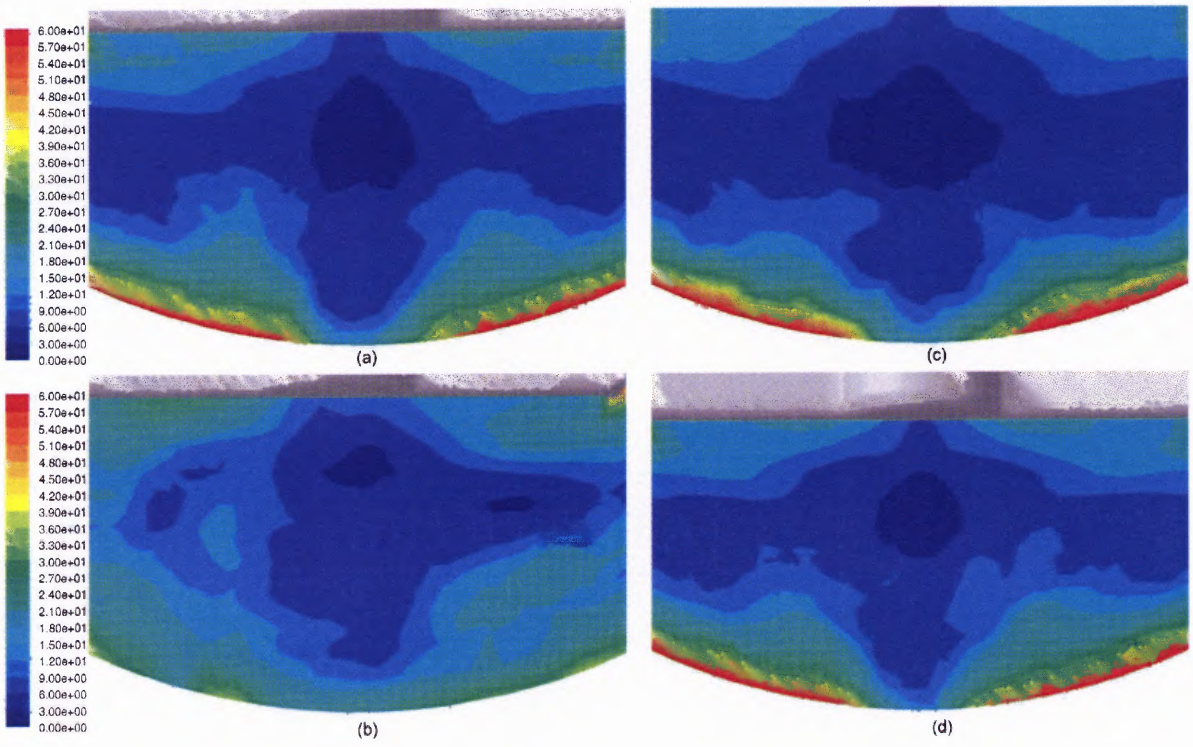

Figure 4.46 CFD predictions of contours of the strain rate (1/s) on the impeller plane (y-plane) at the vessel bottom for different locations of the impeller: (a) Operating Condition 1, (b) Operating Condition 7, (c) Operating Condition 5, (d) Operating Condition 6.

In the inner core (about 10 mm wide) just below the impeller shaft the strain rate drops significantly. This core is surrounded by a region of high wall strain rates. Hence, a rapid transition in strain rate occurs at the intersections between these two regions. The low-strain rate core region expands and contract with the blade passage as one can see by comparing corresponding panels in Figures 4.46 and Figure 4.47.

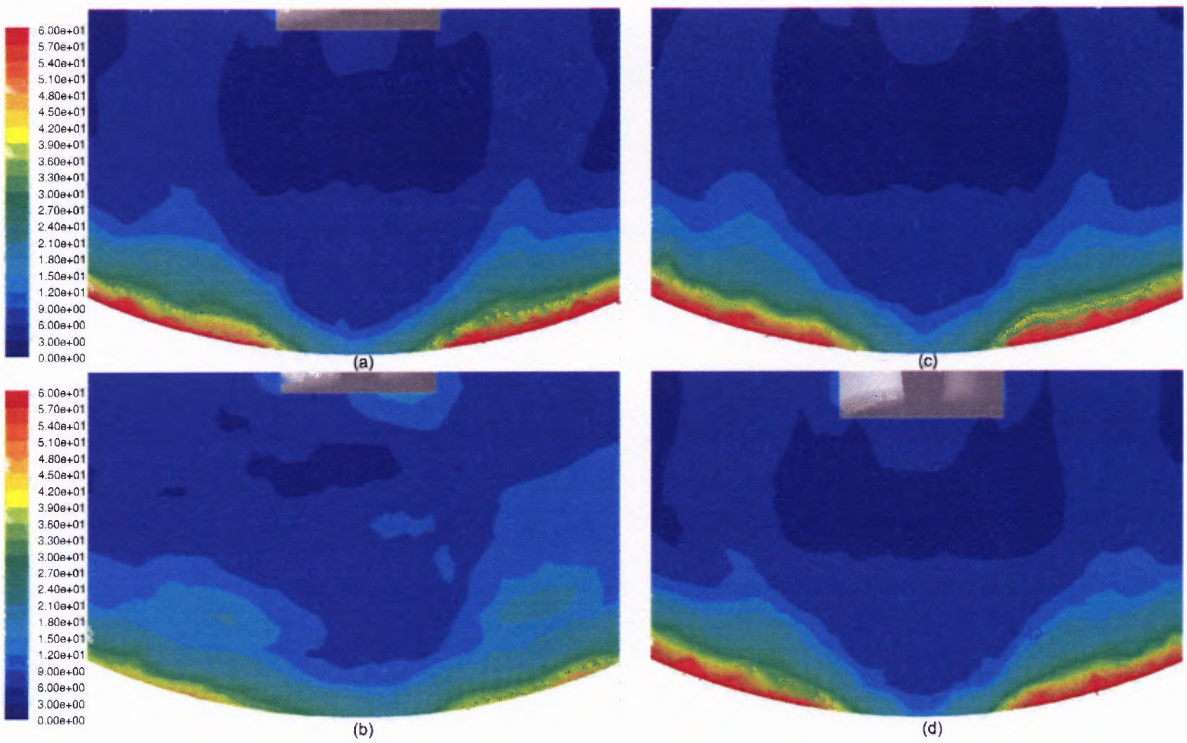

Figure 4.47 CFD predictions of contours of the strain rate (1/s) on the plane perpendicular to the impeller plane (x-plane) at the vessel bottom for different locations of the impeller: (a) Operating Condition 1, (b) Operating Condition 7, (c) Operating Condition 5, (d) Operating Condition 6.

The strain rate distribution is dramatically altered when the impeller is off-center under Operating Condition 7 (Figures 4.46b and Figure 4.47b). In this case, the strain rate along the vessel wall is more evenly distributed, and the central low strain rate region at the wall is significantly reduced, in terms of both size and difference in strain rate magnitude with respect to the surrounding area. In addition, the location of the now reduced low strain rate region moves with the impeller, as one can see comparing Figure 4.46b to Figure 4.47b.

Figure 4.46 and Figure 4.47 can only provide a qualitative but visual description of the strain rate distribution. Figure 4.48 and Figure 4.49 give quantitative CFD-based predictions of the strain rates along the wall of the hemispherical portion of the vessel wall in the y-plain and x-plain, respectively. The abscissa in these figures is the angle φ, originating from center of the sphere comprising the hemispherical vessel bottom and measured starting from the vertical centerline to the point of interest, (i.e., φ=0° for the central point below the impeller, and φ=±90° of the points at the intersection between the hemispherical and cylindrical sections of the vessel). The raw strain rate predictions were very smooth in the domain mapped with the structured Cooper-type hex mesh. However, numerical scatter was observed at the interface between the structured upper mesh and the lower unstructured, tetrahedral mesh. Since this phenomenon occurred independently of where the partition between the two domains was located, a total of six points (three for φ<0° and three for φ>0°) located at the domain interface, were discarded out of some 150. Some scattering was also observed in the lower structured Cooper-type hex mesh domain. In order to produce a smoother strain rate curve in the entire range -90°<φ<90° the CFD-predicted data were interpolated with a 10^{th} order polynomial passing through the predicted value at φ=0° and having a horizontal tangent there. The results are shown in Figure 4.48 and Figure 4.49. Panels (a), (c) and (d) in these figures should be symmetric with respect to the centerline because of the central location of the impeller in these Operating Conditions. The fact that they are not point-by-point symmetric is an artifact of the mesh generator and the solver, which typically produce slightly asymmetric grids to avoid numerical stability problem during numerical iterations. This is especially the case for the fine grid in the bottom region of the vessel.

Three regions can be identified in the strain rate-φ plots in Panels (a), (c), and (d) in Figure 4.48. In the first region, extending from 0° to about 10°, and from 0° to about -10°, the strain rate increases linearly from near zero to about 80-100 s^{-1}. In the second region, which goes from about 10° to about 20° and from about -10° to about -20° the strain rates reach a peak value approximately equal to 100 s^{-1} to 110 s^{-1}. In the third region extending beyond $|\varphi|>20$ °, the strain rate decreases monotonically to about 30 s^{-1} at $|\varphi|=90°$.

A similar picture emerges from the curves on the x-plane for the corresponding cases (Panels (a), (c), and (d) in Figure 4.49). The strain rate plot for the initial region ($0°<|\varphi|<10°$) is similar to the *y*-plane case. The peak region is still in the same φ range ($10°<|\varphi|<20°$), although the peaks are less sharp and more in the shape of a plateau (Figures 4.49a and Figure 4.49c). In the outer region after the peak, the strain rates decreases monotonically, reaching an even lower value at $|\varphi|=90°$.

The magnitude of the strain rate was also predicted on the vertical portion of the cylindrical wall and was found to be equal to ~30 s^{-1}, and slowly decreasing with height, over a significant portion of the wall of the on the y-plane (results not shown). A similar profile was found for the strain rate on the vertical wall in the *x*-plane, although the average value was lower ($\dot{\gamma} \approx 15\ s^{-1}$).

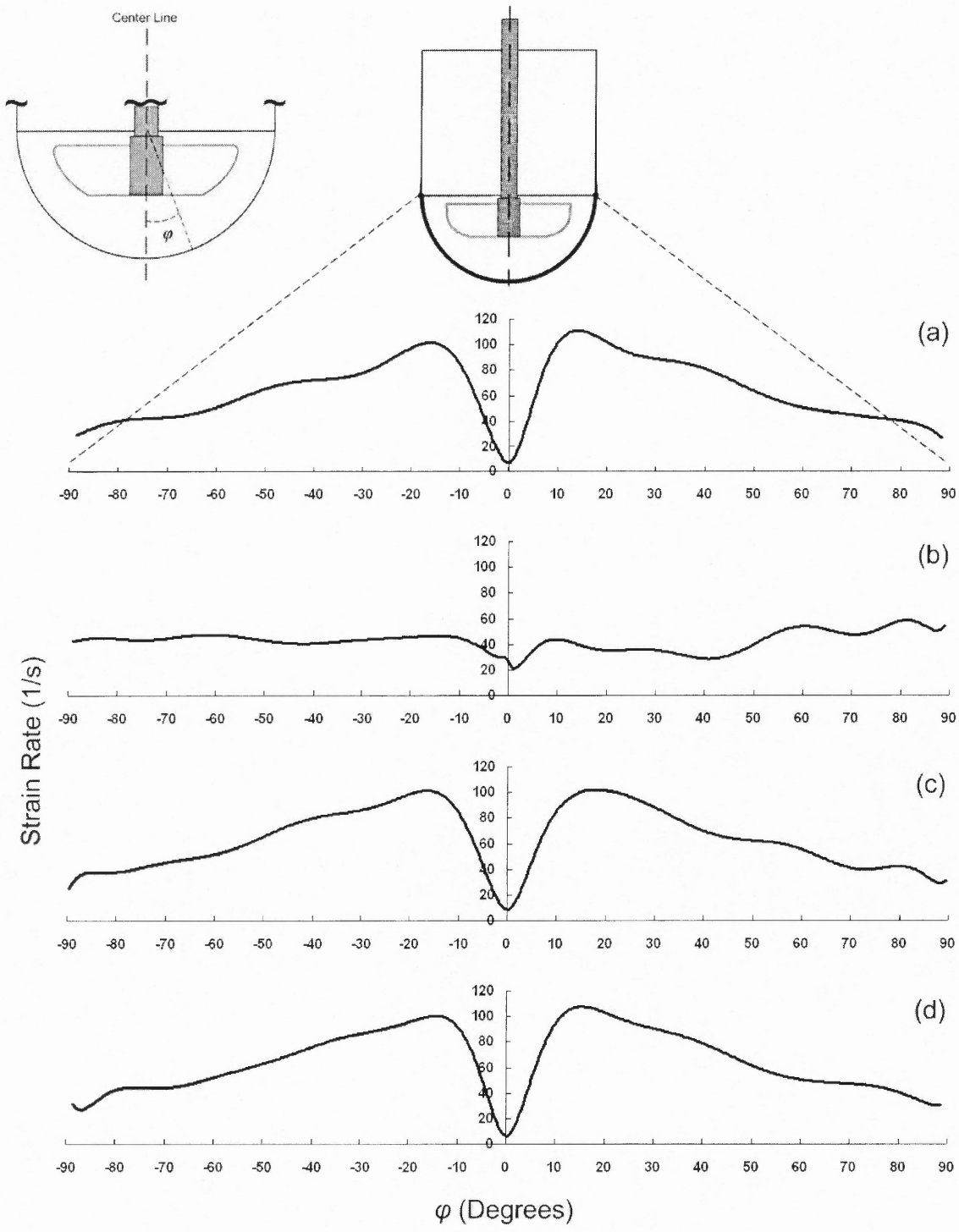

Figure 4.48 CFD predictions of strain rate (1/s) along the bottom of the vessel wall on the impeller plane (y-plane) as a function of angular position from centerline for different locations of the impeller: (a) Operating Condition 1, (b) Operating Condition 7, (c) Operating Condition 5, (d) Operating Condition 6.

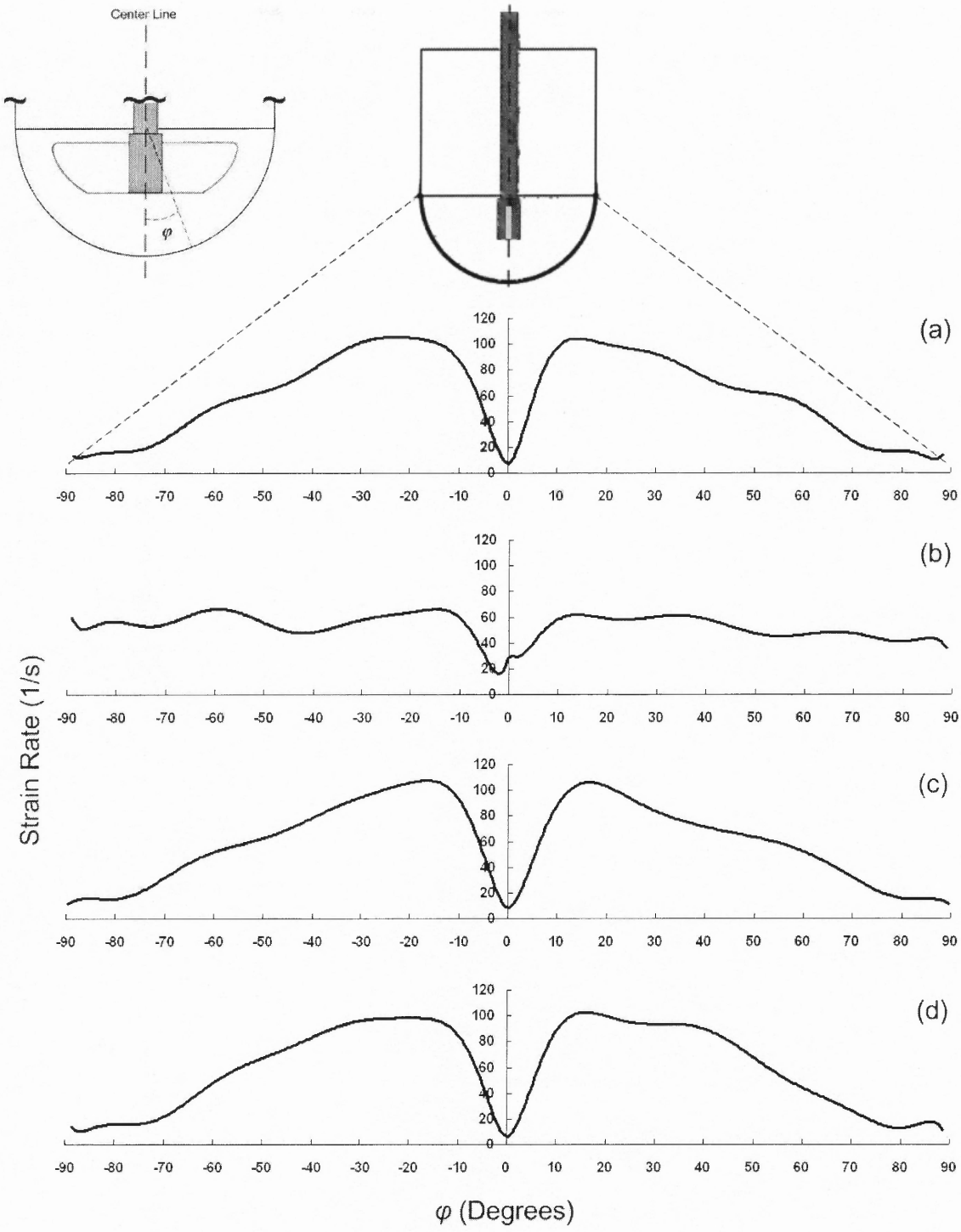

Figure 4.49 CFD predictions of strain rate (1/s) along the bottom of the vessel wall on the plane perpendicular to the impeller plane (x-plane) as a function of angular position from centerline for different locations of the impeller: (a) Operating Condition 1, (b) Operating Condition 7, (c) Operating Condition 5, (d) Operating Condition 6.

The strain rates profiles were found to be very different under Operating Condition 7 (Figure 4.48b and Figure 4.49b). In this case, the strain rate is relatively constant irrespective of φ ($\dot{\gamma} \approx 40\text{-}50\ s^{-1}$ for the y-plane and $\dot{\gamma} \approx 60\ s^{-1}$ for the x-plane) and, overall, much smaller than the peak value under Operating Condition 1, 5 and 6. A small drop for $\dot{\gamma}$ can be see in the central region, for $-10° < |\varphi| < 10°$. This drop is non-symmetric and more pronounced in the x-plane than in the y-plane. Overall, the shapes of the strain rate curves under Operating Condition 7 are very different from those for the other symmetric cases (Operating Conditions 1, 5 and 6), even in the central region.

4.5.4 Discussion of Flow Fields under Operating Conditions 5, 6 and 7

The USP Dissolution Apparatus II is designed to conduct dissolution testing for oral solid dosage forms in pharmaceutical industry. Therefore, one of its characteristics should be to provide a homogeneous dissolution environment for the tablet undergoing testing in order to generate accurate and reproducible results, especially if the equipment is built and operated according to USP specifications. However, the above results of this work, as well as those previously reported by this and other groups, clearly show that the velocity distribution in the region just below the impeller is highly non-homogenous, and changes rapidly with position along the vessel bottom, even when the impeller is centrally and symmetrically located within the vessel (Bai et al. 2006). A similar conclusion can be drawn for the strain rate experienced at the tablet surface, which is likely to have an even greater impact than the velocity flow field on the tablet-liquid mass transfer, and hence the dissolution rate.

The computational results of the current investigation under Operating Condition 1, previously validated experimentally via LDV, are in qualitative agreement with the few previously reported results obtained using quantitative data for the velocity flow field and, especially, strain rates (Kukura et al. 2004, Baxter et al. (2005). Kukura et al. (2004) and Baxter et al. (2005) generated CFD-predicted strain rate distribution profiles along the vessel wall of a USP Apparatus II. Their results can be directly compared to those reported here in Figure 4.48a, showing similarities but also significant differences. Both their and our profiles show that the strain rate increases from a very low value in the center of the vessel to a peak in correspondence of $\varphi \approx 15° \pm 5°$. However, the results of those authors show that the strain rate has an additional and even higher peak at $\varphi \approx 85°$, i.e., very close to the end of the hemispherical section, whereas no such peak appears in our strain rate curves. Instead, curves in Figure 4.48a show that the strain rate reaches a maximum for $\varphi \approx 20°$, and it decreases beyond this value.

Another substantial difference between our strain rate results and those of Kukura et al. (2004) and Baxter et al. (2005) is that the strain rate values along the vessel wall are much lower then those found in our work. In their studies, those authors reported that the highest strain rate value for N= 50 RPM is less than 10 s^{-1} for $-90° < \varphi < 90°$, whereas in our work the average strain rate values in the same range can be calculated to be between 60 and 70 s^{-1} on both y-plane and x-plane. The strain rate reported by these investigators for the vertical portion of the cylindrical wall section ($\dot{\gamma} \approx 10 \pm 5$ s^{-1}) was also lower than that found here ($\dot{\gamma} \approx 30$ s^{-1} on the y-plane and $\dot{\gamma} \approx 15$ s^{-1} on the x-plane). These differences could possibly be attributed to the differences in mesh size and type, CFD solver, discretization method, and turbulence model used. Despite the differences, both our

results and the results of Kukura et al. ()and Baxter et al. () show that the distribution of strain rate on the bottom of the USP Apparatus II is a strong function of location.

Our results additionally show that the impeller clearance off the tank bottom, at least within the USP specifications, does not appreciably change the velocity distribution in the bottom portion of the vessel (Figure 4.41, Figures 4.43 and Figure 4.44). More significantly, the strain rate values in the same region, and especially along the bottom vessel wall, do not appear to be significantly affected the impeller clearance (Figures 4.46-4.49). This is somewhat surprising since one would expect that the distance from the impeller, especially in a region so close to the impeller blades, would play a more dominant role. Instead, it appears that the presence of a low-turbulence, low-shear rate region near the center under the impeller shaft is the dominant features under all Operating Conditions in which the impeller is centrally located.

The results of the present study clearly show that the velocity distribution and the strain rate distribution are strongly affected by the off-center placement of the impeller, even when the off-center displacement is only 2 mm under Operating Condition 7, as allowed under USP specifications (Panels (b) in Figures 4.39-4.49). Also under Operating Condition 7, the flow is dominated by the tangential component of the velocity (Figure 4.41b), as in all unbaffled stirred vessels. However, the loss of symmetry resulting from the off placement of the impeller partially disrupts the rotational flow associated with a centrally located impeller, resulting in stronger axial and radial flows in the region below the impeller (Figures 4.44b and 4.45b). The velocity changes also affect the magnitude and distribution of the strain rate near the vessel bottom, which

become much more uniformly distributed than under all operating conditons in which the impeller is centrally located (Figures 4.48and 4.49).

It should be stressed, again, that the results presented here were obtained with only a 4% lateral translation of the impeller. Although the results presented here were obtained with the largest off-center impeller placement allowed by the USP (2 mm), one could speculate that smaller off-center impeller locations could also have similar effects, although not of equal intensity. It is therefore conceivable that some of the variability and, possibly, even failures, associated with dissolution testing and reported in the literature (FDC Reports, 2001, 2002, 2003) could be attributed to the off-center location of the impeller, especially if this effect is combined with other geometric effects, such as an off-center resting location of the tablet resulting from the randomness of the tablet vertical trajectory while sinking after its introduction in the vessel at the beginning of the test. Loss of central impeller symmetry could be the result of a number of factors, especially in older equipment, such as operator's error, worn couplings, misplacement of the vessel, or a bent shaft.

Given absence of baffles, the flow and shear rate in the USP II apparatus are expected to be highly sensitive to any geometric factors that may affect its symmetry (or lack thereof). This is one of the reasons why equipment manufacturers have tried over the years to reduce any mechanical defects that could result in loss of symmetry, e.g., by introducing self-centering shafts, certified vessels, and tools to determine eccentricity. Interestingly, one could propose that a possible method to reduce variability during the test would be precisely the opposite, i.e., to deliberately introduce non-symmetry in the

system, e.g., through the off-center placement of the impeller, which would result in a more uniform shear rate near the vessel bottom where the tablet is located.

Further studies need to be conducted in order to find out quantitatively how the non-uniform distribution of strain rate can affect the dissolution rates.

4.6 Results and Discussion on Power Dissipation in USP Dissolution Apparatus II

The values of the numerically computed power dissipation values and power numbers under different Operating Conditions for the USP Dissolution Apparatus II are given in Table 4.4 for the different Operating Conditions examined here. As mentioned previously, no comparison with experimentally derived power dissipation data was possible because of the extremely low values of the power consumed.

Table 4.4 CFD-Computed Power and Power Numbers for Different Operating Conditions

Operating Conditions	P (watts)	N_p
1	0.000877	0.678
2	0.002557	0.586
3	0.005246	0.507
4	0.000686	0.530
5	0.000890	0.689
6	0.000900	0.695
7	0.000960	0.743

The CFD-computed power data for Operating Condition 1, 2, and 3 (which are associated with the same geometric system operated at three different impeller speeds) are presented in Figure 4.50, and, as a logarithmic plot, in Figure 18. Equation 3.37 shows that P increases with the cube of the agitation speed N, assuming that the power number remains constant. However, N_p is a function of the impeller Reynolds number, Re, and becomes independent of Re only if the flow is highly turbulent and the system is baffled. If the system in unbaffled, N_p is a function of Re even in the turbulent regime, with N_p decreasing with increasing N.

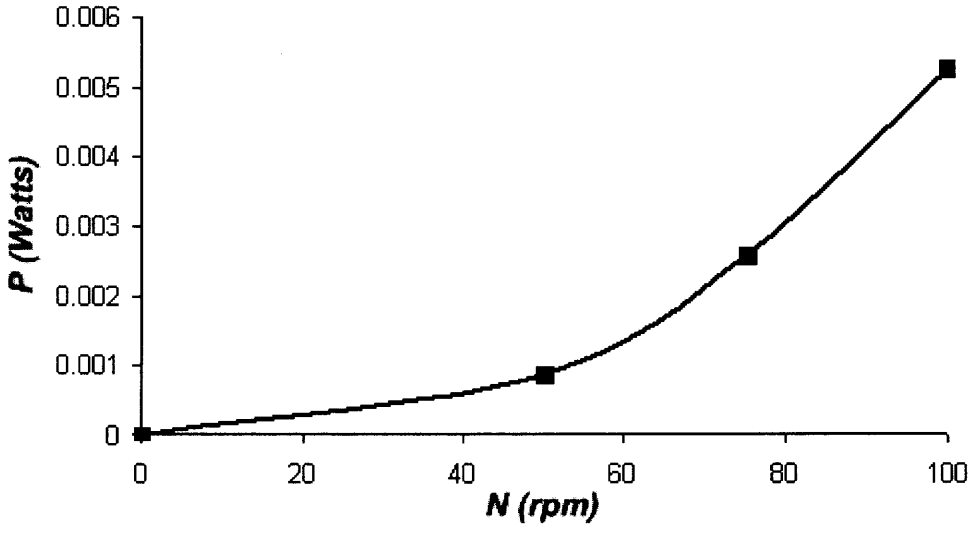

Figure 4.50 CFD-computed power data for Operating Condition 1, 2, and 3.

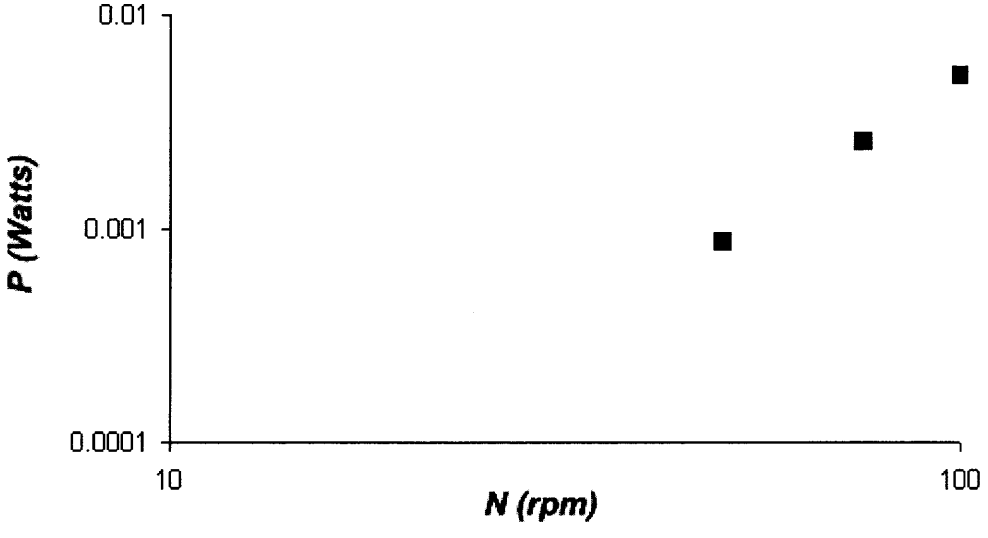

Figure 4.51 Logarithmic CFD-computed power data for Operating Condition 1, 2, and 3

The points in Figure 4.51 lie on the same line. Regression of the data in this figure shows that the slope of this line is 2.58, i.e.:

$$P \propto N^{2.58} \tag{4.16}$$

This result indicates that N_p is not a constant, but decreases with *Re*, as expected, since the USP II system is unbaffled.

In order to have a better idea of whether the data in Table 4.4 are meaningful, especially in the absence of any experimental validation, a comparison with literature results was made. Since no power data or correlations are available for the USP II apparatus, the comparison was made with a correlation produced by Nagata (1975) for rectangular, two-blade, flat-blade paddles in unbaffled, flat-bottomed, cylindrical tanks. For flat paddles with $0.3<D/T<0.9$ and $0.05<b/T<0.9$ (where b is the height of the paddle blade), Nagata (1975) obtained the following empirical correlation:

$$N_p = \frac{A}{\mathrm{Re}} + B\left(\frac{1000+1.2\,\mathrm{Re}^{0.66}}{1000+3.2\,\mathrm{Re}^{0.66}}\right)^{p} \cdot \left(\frac{H}{T}\right)^{\left(0.35+\frac{b}{T}\right)} \tag{4.17}$$

Where:

$$A = 14 + \frac{b}{T} \cdot \left[670\left(\frac{D}{T}-0.6\right)^2 + 185\right] \tag{4.18}$$

$$B = 10^{\left[1.3-4\left(\frac{b}{T}-0.5\right)^2-1.14\frac{D}{T}\right]} \tag{4.19}$$

$$p = 1.1 + 4\frac{b}{T} - 2.5\left(\frac{D}{T}-0.5\right)^2 - 7\left(\frac{b}{T}\right)^4 \tag{4.20}$$

The power and power numbers obtained from Equation 4.20 are given in Table 4.5. For Operating Conditions 1, 2, and 3, no liquid height correction was included in the calculations (i.e., the term H/T was taken to be equal to 1) since this correction was

supposed to be applied to cases where $H/T<1$. A comparison between the results of Table 4.4 and Table 4.5 shows that the power and power numbers for corresponding Operating Conditions is close, although difference exists between the actual numerical values predicted via CFD and those derived from the Nagata equation. Such differences are in the range 1.81% to 8.75% for Operating Conditions 1, 2, and 3, and 10.2% for Operating Condition 4. This is not surprising for a number of reasons.

Table 4.5 Power and Power Numbers Under Operating Conditions 1, 2, 3, and 4 Calculated From Nagata Equation (1975)

Operating Conditions	P (watts)	N_p	Remarks
1	0.000859	0.665	no H/T correction
2	0.002603	0.597	no H/T correction
3	0.005703	0.551	no H/T correction
4	0.000755	0.584	H/T correction

Equation 3.37 shows that P is a very strong function of the impeller diameter D ($P \propto D^5$). In the calculations made using Nagata equation the maximum dimension of the USP II paddle was used (i.e., D=74.1 mm). However, this paddle is not rectangular, as assumed in Nagata equation, but it has a trapezoid shape with the shorter side equal to 42 mm. Therefore, it is debatable which impeller diameter should be used in Nagata equation for this case. For example, the same power dissipation predicted from the CFD simulation for Operating Condition 1 (0.000877 watts) can be obtained if a value of 73.2 mm is used in Nagata equation. Furthermore, Nagata equation was derived for unbaffled, flat-bottomed, cylindrical tanks, and its use for vessels with hemispherical bottoms, as in the USP II case, can be expected to introduce certain degree of errors. Interestingly, Nagata equation does not contain any term accounting for the effect on P of the impeller

clearance, *C*, although this variable can be expected to play a role in general, and especially in the USP II apparatus, as clearly shown in Table 4.4. In summary, although no experimental validation could be presented, the CFD-predicted values of the power and power number are likely to be correct.

4.7 Results and Discussion on Effect of Locations of Tablet on Dissolution under Operating Conditions 8 and 9

4.7.1 Results for Prednisone Tablets under Operating Condition 8

The centrally located prednisone tablets became totally disintegrated into granules of different sizes within about 8 minutes from the beginning of the experiment (the latter time being defined when the first sample was taken and the agitation was started). The granules formed a rotating "cone" at the center of the vessel bottom, as previously reported (Qureshi and Shabnam, 2001). The off-center tablets became totally disintegrated in about 5 minutes, i.e., significantly more rapidly than the centrally located tablets. Although the off-center tablets were initially bonded to their location with polybutene, the granules that were formed after they disintegrated moved from the off-center location to the center of the vessel bottom where they formed a rotating "cone".

Figure 4.52 shows the prednisone dissolution profiles, i.e., the prednisone concentration ratio C/C^* in the dissolution medium (with C^* being the prednisone concentration when the tablet is completely dissolved) as a function of time, for different locations of the prednisone calibrator tablets at the bottom of USP II vessel. This figure shows that the dissolution results for the centrally located tablets were reproducible. The largest and smallest standard deviations were, respectively, 3.72% at t=0 minutes and 1.28% at t=40 minutes. The variability at t=0 minutes was similar to that observed by previous researchers (Baxter et al. 2005), and can be attributed to disintegrating characteristics of prednisone tablets. When the dissolution medium was added to the vessel, a significant amount of prednisone became rapidly dissolved before the

experiment starts. At times larger than 5 minutes, the fractions of dissolved prednisone were significant higher for off-center located tablets than for centrally located tablets.

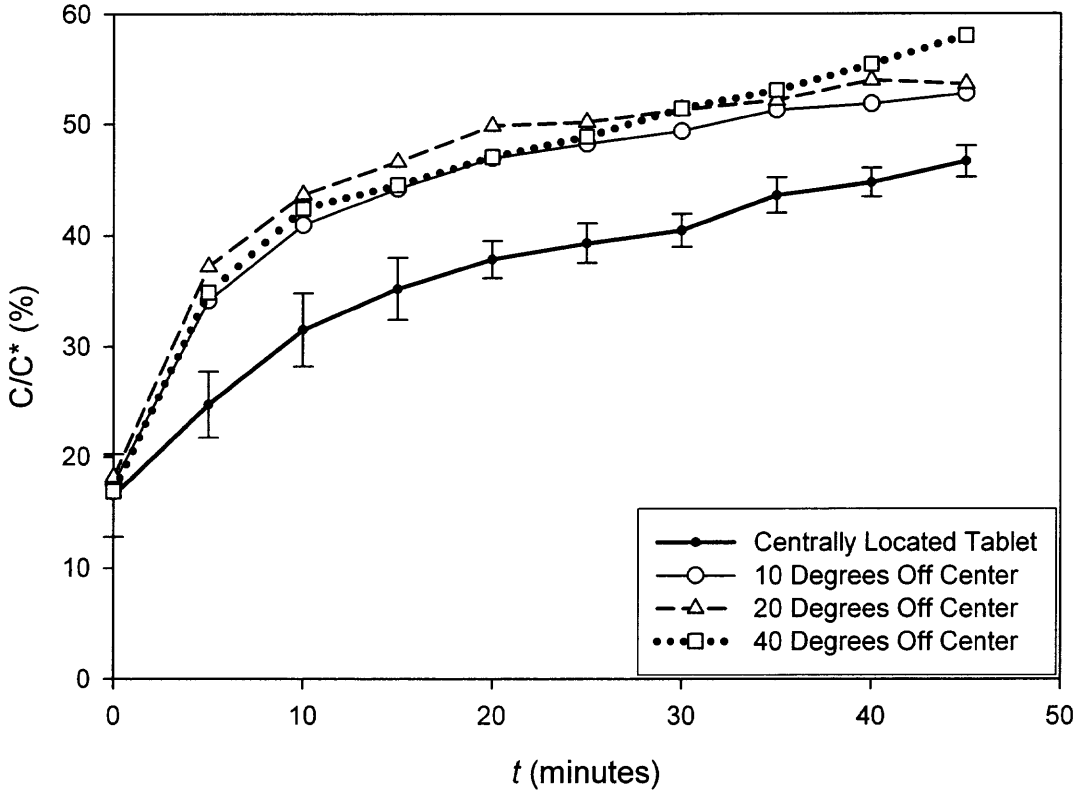

Figure 4.52 Experimental dissolution profiles for prednisone tablets at different tablet locations.

The criteria for dissolution profile comparison described in Equations 2.4 and 2.5 were applied to the profiles for each of the centrally placed tablet with respect to the average dissolution profile at that location. In all cases the f_1 values and the f_2 values were, respectively, much lower than 15 and at least above 77, indicating that the centrally placed tablets produced statistically similar dissolution data.

According to the DDA Dissolution Test Performance Standard #2 (Division of Drug Analysis, 1995), a dissolution profile should result in a dissolved fraction of prednisone between 28% and 44% of the total amount of prednisone contained in the tablet (10 mg) when sampling at 30 minutes. All the three profiles obtained for the centrally located tablets satisfied this criterion (dissolved fractions of prednisone at 30 minutes equal to 39.4%, 41.1%, 39.9%, respectively), implying that the equipment was well calibrated and appropriate to conduct dissolution testing on prednisone tablets.

The experimental results reported in Figure 4.52 show that the dissolution profiles for the off-center tablets were, in general, different from those for the centrally placed tablets. However, the initial C/C^* values were found to be similar irrespective of where the tablet was initially located, and were equal to 17.03%±2.45%. Since this value is significantly different from zero, this implies that appreciable dissolution resulted from the addition of medium to the vessel prior to the starting of the agitation and the beginning of the experiment. For $t \geq 5$ minutes the dissolution profiles diverged, with the off-center tablets dissolving significantly faster than the centered tablets (Figure 4.52). Although the profiles for all off-center tablets are similar to one another, the tablet located 10° off-center has the lowest dissolution profile among the three off-center tablets. For $t \leq 25$ minutes, the 20° off-center tablet located has higher C/C^* values than the 40° off-center tablet, but the reverse is true for $t > 25$ minutes.

The f_1 and f_2 factors (Equations 2.4 and 2.5) were calculated for the experimental dissolution profiles for each of the off-center tablets with respect to the average dissolution profile for the centrally located tablets. The f_1 values, f_2 values, and P-values from the Student's t-test are reported in Table 4.6. In all cases, f_1 was larger than 15, and

f_2 was about 50, implying that the off-center dissolution profiles were statistically different, according to the FDA criteria, from the baseline profile obtained with the centrally located tablets. At t=30 minutes the dissolved prednisone fractions were found to be 49.38%, 51.30%, and 51.40% of the amount of prednisone originally contained in the tablet (10 mg), for the 10°, 20°, and 40° off-center tablets, respectively. These values are all outside the 28%-44% range specified by the DDA Dissolution Test Performance Standard #2 (Division of Drug Analysis, 1995), indicating that the test did not produced the expected results and was invalid as a calibration test.

Table 4.6 Statistical Evaluation of Similarity Between Dissolution Profiles of Off-Center Tablets and Centrally Located Tablets for Prednisone and Salicylic Acid Tablets at Different Locations With Different Statistical methods (Gray Boxes Indicate A Failing Value According to FDA Criteria)

Prednisone Tablets			
	P-Value	f_1	f_2
10° off center tablet	0.0544	21.26	54.55
20° off center tablet	0.0251	26.63	49.67
40° off center tablet	0.0370	25.47	50.60
Salicylic Acid Tablets			
	P-Value	f_1	f_2
10° off-center tablet	0.1226	33.45	61.37
20° off-center tablet	0.0531	51.94	52.54
40° off-center tablet	0.1132	35.35	60.17

CFD simulations were conducted to determine the velocity flow field with and without prednisone tablets, and with the tablets at different locations. The results are presented in Figure 4.53 as velocity vectors originating on the plane of the impeller (y-plane). The key feature of the flow below the impeller is that the recirculation loop generated by the radial flow emanating from the paddles is not able to penetrate the inner core region located just at the center under the impeller. Consequently, the flow in this inner region, roughly as wide as the shaft, is very weak, as previously described. The

axial velocities change rapidly with location along the vessel bottom especially when the vertical boundaries of the inner core region are crossed (Figure 4.53).

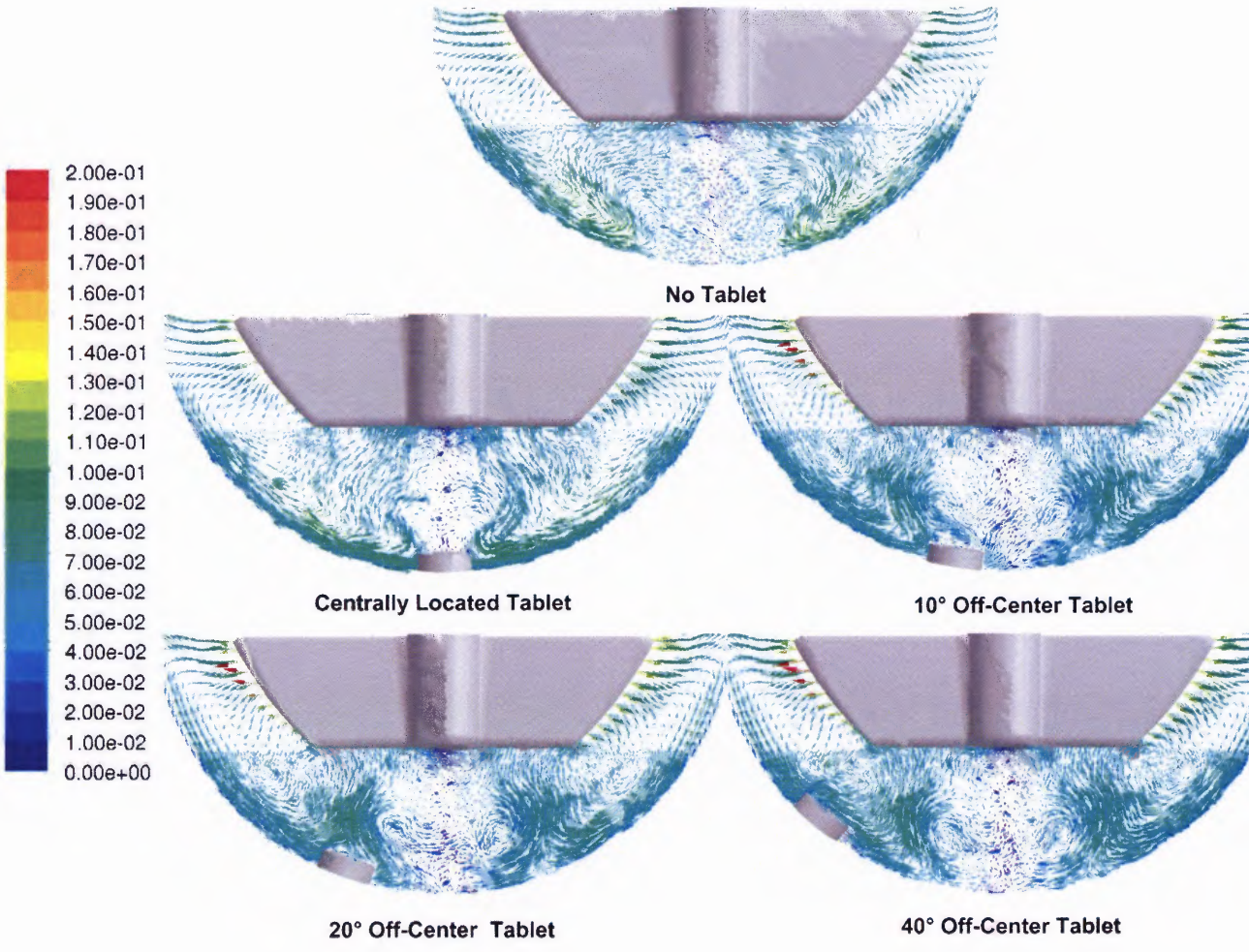

Figure 4.53 CFD-predicted velocity vectors (in m/s) on the impeller plane (y-plane) in the lower region of the USP Apparatus II vessel with and without prednisone tablets and at different tablet locations.

The presence of a tablet affects the overall and local flow, but the flow around the tablet is strongly determined by the exact location of the tablet. When the tablet is placed at the center of the vessel bottom, the tablet experiences a weak flow on its top surface. The overall flow in this case is still symmetrical, and similar to that obtained with no

tablet. When the tablet is off-center, the overall flow becomes, in general, asymmetric but only slightly, since the tablet is small. The flow in the central inner core region is still very weak, but the tablet may be more or less affected by it depending on its exact location on the vessel bottom.

The flow field around the 10° off-center tablet is stronger than that around the centered tablet, but it is affected by the proximity with the poorly mixed inner core region and the presence of the tablet itself, straddling the core region and the region surrounding it (Figure 4.53). Even in this case, the flow field near the upper surface of the tablet can be seen to be significantly different from, and stronger than, that experienced by the centered tablet. Figure 4.53 also shows that the velocity fields surrounding more off-center tablets (20° and 40°) are much stronger than that for the centered tablet. Interestingly, the tablet 20° off-center is in a region where the axial velocities are relatively strong, as a result of the closing of the recirculation loop generated by the impeller, as one can visually see from Figure 4.53.

Figure 4.54 shows the distribution of strain rates near the vessel bottom in the absence and presence of prednisone tablets at different locations. The red regions indicate strain rate values of 60 s^{-1} and above. Of importance here is the strain rate at the tablet surfaces. For both the centrally located tablet and the 10° off-center tablet, high strain rate values occur mainly on the side surfaces of the tablets. However, for tablets located 20° and 40° off-center, high strain rate values can be seen not only on the side surfaces but also on the top surfaces of the tablets, with possible implication for the tablet-medium mass transfer coefficient.

In order to better quantify the strain rate experienced by an integral prednisone tablet prior to disintegration, the average strain rate values on the exposed surfaces of the tablet (including the top face and the side surface, but not the bottom face in contact with the vessel bottom) were calculated from the strain rate maps obtained from the CFD simulations. The results, presented in Table 4.7, indicate that the off-center tablets experience 22.5% (10° off-center tablet), 64.7% (20° off-center tablet) and 57.0% (40° off-center tablet) higher strain rates, respectively, than the centrally located tablet. Higher strain rate values can result in higher mass transfer rate at the tablets, but only prior to tablet disintegration, which typically occurred within 5 minutes from the beginning of the experiments. Once the tablet disintegrated, the resulting fragments migrated toward the center of the vessel to form a cone there.

Table 4.7 CFD-Predicted Average Strain Rate Values on The Top and Side Surfaces of Prednisone Tablets for Different tablet Locations Prior to Tablet Disintegration

Tablet Location	Predicted Average Strain Rate on Tablet Surface (s^{-1})
Centrally located tablet	58.50
10° off-center tablet	71.70
20° off-center tablet	96.38
40° off-center tablet	91.85

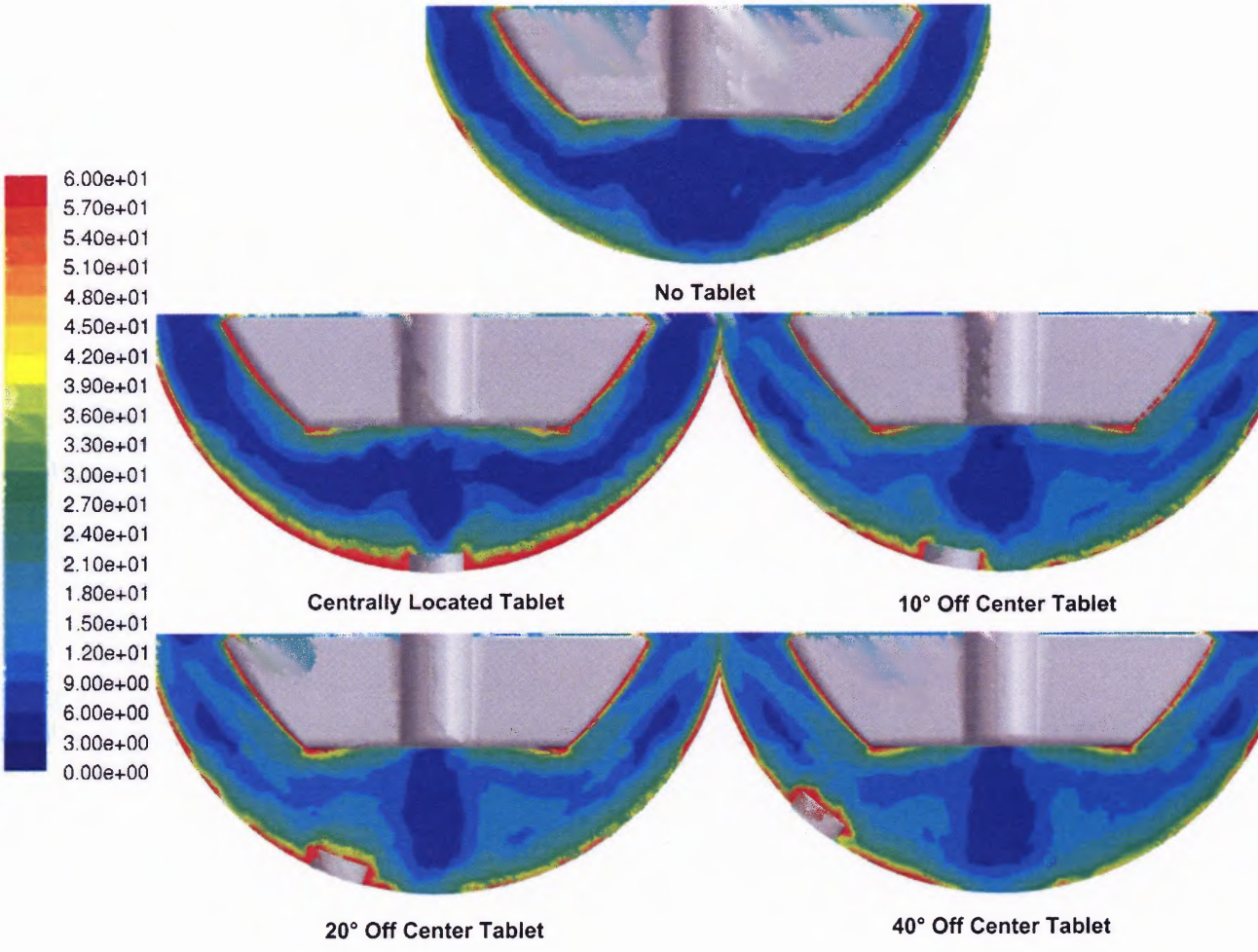

Figure 4.54 CFD-predicted strain rate (in s^{-1}) on the impeller plane (y-plane) in the lower region of the USP Apparatus II vessel with and without prednisone tablets and at different tablet locations. Red regions indicate strain rate values of 60 s^{-1} and above.

4.7.2 Results for Salicylic Acid Tablets under Operating Condition 9

In all dissolution tests, the salicylic acid tablets remained at their initial location for the entire duration of the experiment. Since the tablets did not disintegrate, the dissolution process was driven by erosion. Figure 4.55 shows the salicylic acid concentration ratio C/C^* vs. time during the experiments, for different locations of the tablets. All the experiments with the centrally located salicylic acid tablets gave similar dissolution profiles, with a high standard deviation value of 0.95% at 45 minutes and a low value of 0.21% at 5 minutes (Figure 4.55). The f_1 value and the f_2 value (Equations 2.4 and 2.5) were calculated in order to compare each of the profiles for the centered tablets to the average profile at the same central location. In all cases f_1 and f_2 were, respectively, lower than 4.7 (i.e., much lower that 15, the FDA upper limit for similarity) and larger than 911 (i.e., much greater than 50), indicating that the centrally placed salicylic acid tablets produced statistically similar dissolution profiles.

Based on the USP specifications for the salicylic acid calibrator tablets used in this work (USP Lot Q0D200, Rockville, Maryland) (USP Certificate, 2006), each individual run should produce a dissolved amount of salicylic acid between 17%-25% of the total amount contained in the tablet (300 mg) when sampling at 30 minutes. This is the case here, since the experimentally obtained fractions at 30 minutes were found to be 20.17%, 18.61%, and 19.87%, respectively, implying that the equipment was suited to conduct dissolution testing with salicylic acid tablets.

The off-center tablets have different dissolution profiles than the centrally located tablets (Figure 4.55), even though the initial C/C^* values were found to be similar to one another (3.38%±0.89%) irrespective of where the tablets were initially located. This low

variability is consistent with the fact that salicylic acid tablet is non-disintegrating. Therefore, the effect on tablet dissolution of the initial addition of dissolution medium is smaller than for the case of disintegrating prednisone tablets. For $t \leq 25$ minutes, the 10° off-center tablet has slightly higher C/C^* values than the 40° off-center tablet, but the reverse is true for $t > 25$ minutes. The dissolution profiles for the tablets located 10° and 40° off-center are very similar to each other, but always above the profiles for the centered tablets. The profile for 20° off-center tablet is always higher than all the other profiles, except at $t=0$.

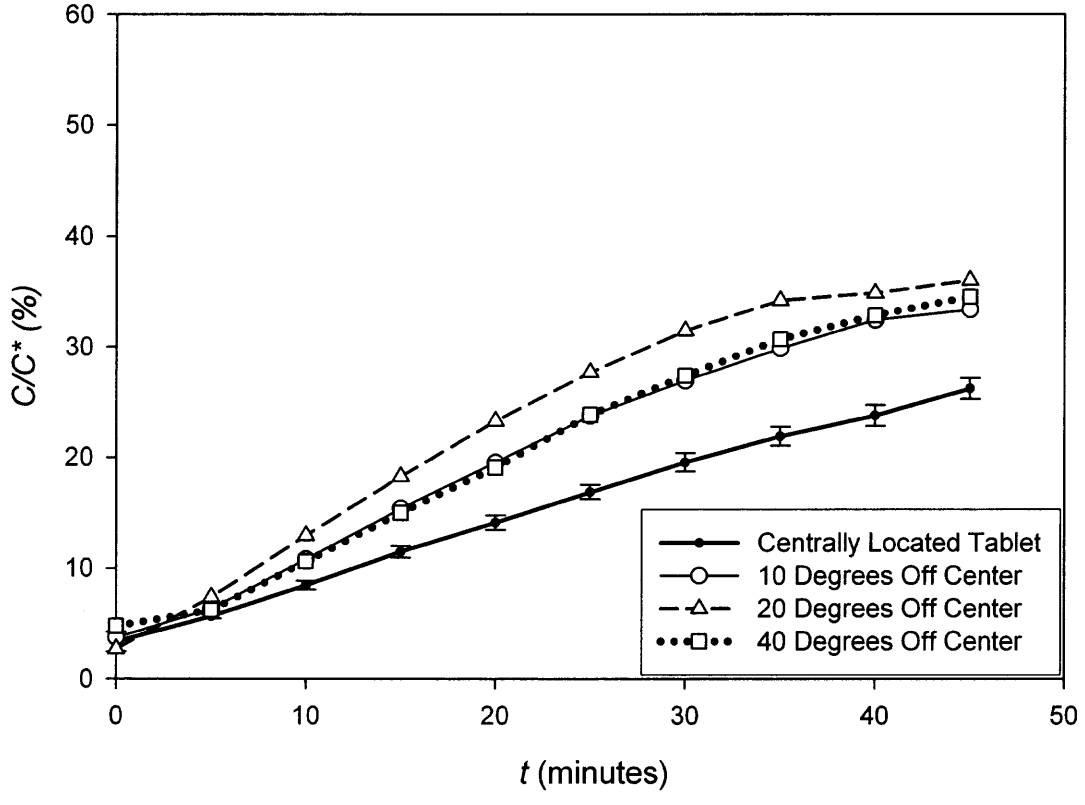

Figure 4.55 Experimental dissolution profiles for salicylic acid tablets at different tablet locations.

Table 4.6 shows the f_1 values, f_2 values, and P-values from the Student's t-test when the off-center dissolution profiles are compared with the average dissolution profile for the centrally located tablets. In all cases, the f_1 values were in the range 33-52, i.e., much larger than the required 15, and the f_2 values were around in the 50-60 range, implying that the off-center dissolution profiles were statistically different, according to the FDA criteria, from the baseline profile obtained with the centrally located tablets. At t=30 minutes the dissolved salicylic acid fractions were found to be, respectively, 26.92%, 31.45%, and 27.38% of the amount of salicylic acid originally contained in the tablet (300 mg) for the 10°, 20°, and 40° off-center tablets. These values are all outside the 17%-25% range specified by the USP (USP Certificate, 2006), which would indicate that the apparatus is off calibration.

Figure 4.56 shows the CFD-predicted velocity vectors originating on the plane of the impeller (y-plane) when the salicylic acid tablets are at different locations. Although the impeller speed is twice as large for salicylic acid as that used in the prednisone dissolution cases, the two sets of velocity distributions are similar when appropriately scaled (Figure 4.56 vs. Figure 4.53), including the presence of a poorly mixed central inner core region just under the impeller. The flow around the tablet is strongly affected by the exact location of the tablet. When the tablet is centrally located a weak flow sweeps its top surface; when the tablet is 10° off-center the flow is stronger but still affected by the nearby poorly mixed inner core region. However, when the tablet is 20° off-center and, to a lesser extent, 40° off-center, the flow is appreciably stronger.

The distribution of strain rates near the vessel bottom in the absence and presence of salicylic acid tablets at different locations is reported in Figure 4.57. The red regions indicate strain rate values equal to 120 s^{-1} or above. The strain rate at the tablet surfaces vary with tablet location, as in the prednisone case. The strain rate at the top face of the salicylic acid tablets is weaker when the tablet is centrally located, followed in order of increasing magnitude, by the tablets 10° off-center, 40° off-center, and finally 20° off-center, where the strain rate is the highest among the locations tested.

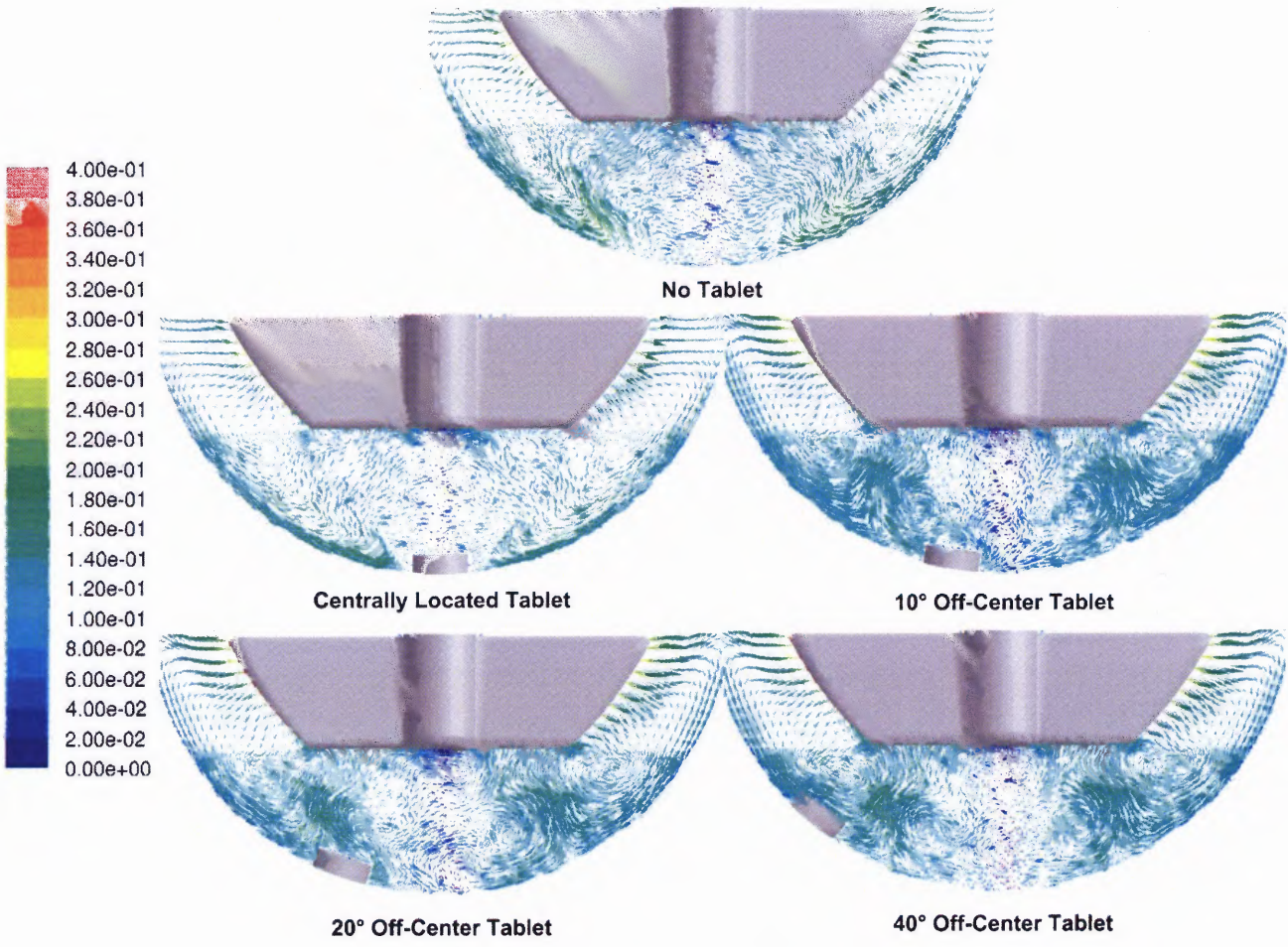

Figure 4.56 CFD-predicted velocity vectors (in m/s) on the impeller plane (y-plane) in the lower region of the USP Apparatus II vessel with and without salicylic acid tablets and at different tablet locations.

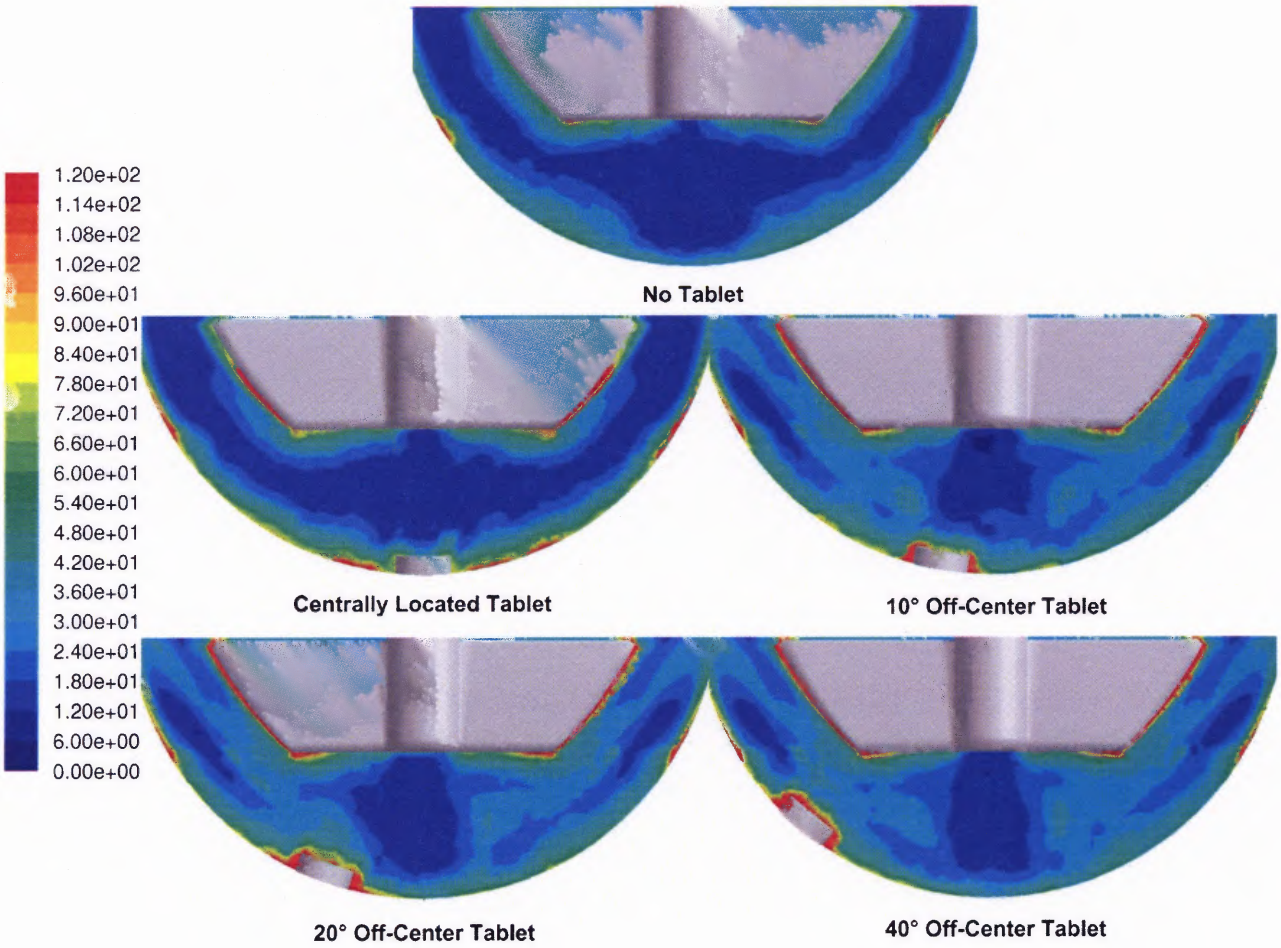

Figure 4.57 CFD-predicted strain rate (in s^{-1}) on the impeller plane (y-plane) in the lower region of the USP Apparatus II vessel with and without salicylic acid tablets and at different locations. Red regions indicate strain rate values of 120 s^{-1} and above.

The average CFD-predicted strain rate values on the surfaces of the tablet exposed to the medium (i.e., top and side surfaces) are summarized in Table 4.8. The off-center tablets experience strain rates that are, respectively, 73.7% (10° off-center tablet), 123.8% (20° off-center tablet) and 87.2% (40° off-center tablet) higher than the strain rates experienced by the centrally located tablet, with possible implication for the tablet-medium mass transfer coefficient.

Table 4.8 CFD-Predicted Average Strain Rate Values on The Top and Side Surfaces of Salicylic Acid Tablets for Different Tablet Locations

Tablet Location	Predicted Average Strain Rate on Tablet Surface (s^{-1})
Centrally located tablet	77.91
10° off-center tablet	135.32
20° off-center tablet	174.33
40° off-center tablet	145.81

4.7.3 Tablet-Medium Mass Transfer Coefficients for Salicylic Acid Tablets

The experimental dissolution data, from 0 to 30 minutes, presented in Figure 4.55 for the salicylic acid tablets, and the properties of the salicylic acid tablet and dissolution system reported in Table 4.9 were used as input in Equation 2.14 to obtain the average mass transfer coefficients, k, for the tablet-dissolution medium system for each tablet location. The k values were obtained via numerical integration of Equation2.14. The results, reported in Table 4.10, show that the centrally located tablet had the smallest k value among all cases. The tablets that were 10°, 20°, and 40° off-center had k values that were, respectively, 67.9%, 89.5% and 62.3% larger than the base value for the centrally located tablet.

Table 4.9 Properties of Salicylic Acid Tablet and Dissolution System

C_s	3.14 kg/m^3
ρ_T	1253.09 kg/m^3
V_L	9.00×10^{-4} m^3
β	0.35
d_{T0}	9.57×10^{-3} m

Table 4.10 Overall mass transfer coefficients for salicylic acid tablets at different tablet locations, calculated from experimental dissolution data

Tablet Location	Mass Transfer Coefficient from Experimental Dissolution Data, k_{exp} (m/s)
Centrally located tablet	5.04×10^{-5}
10° off-center tablet	8.59×10^{-5}
20° off-center tablet	10.31×10^{-5}
40° off-center tablet	8.43×10^{-5}

The strain rate represents the rate at which the velocity varies with distance when moving away from the point of interest. According to the boundary layer theory (Bird et al., 2002) the mass transfer from a solid surface to the surrounding fluid is proportional to the velocity gradient in the boundary layer surrounding the solid, i.e., the strain rate at that surface (typically through $Sc^{1/3}$, where Sc is the Schmidt Number, $Sc=\mu/D_{AB}\cdot\rho$). Therefore, one can expect that regions where the local strain rate is high will be associated with high mass transfer rates. In this work, the experimentally derived mass transfer coefficients k reported in Table 4.10 for different locations of the salicylic acid tablets were plotted against the CFD-predicted strain rate values on the surface of salicylic acid tablets listed in Table 4.8. The results are shown in Figure 4.58. The straight line through the points was obtained by regressing the data. The line was additionally forced to go through the origin since no strain should produce no mass transfer (Remark: this is not entirely correct since molecular diffusion also contributes to mass transfer, even in the absence of flow. However, it can be shown that this contribution would be negligible in this case). One can see that the there is a direct proportionality between the mass transfer coefficient and strain rate at the tablet surface. The tablet located 20° off-center experiences the highest strain rate, has the highest overall mass transfer coefficient, and thus the highest dissolution rate.

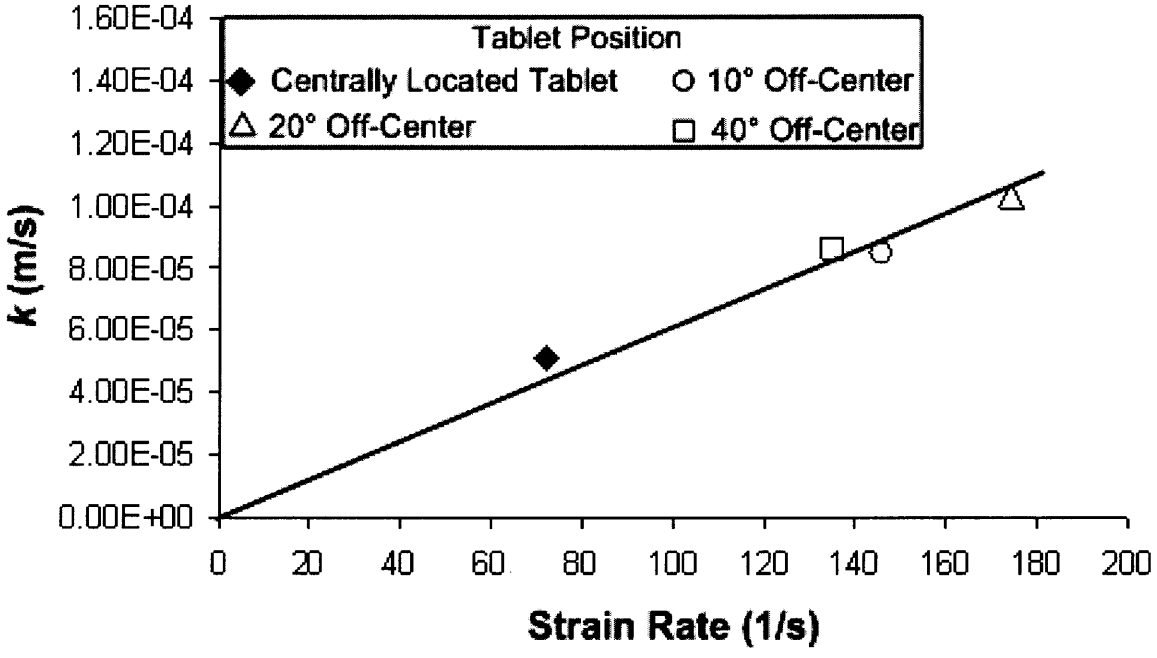

Figure 4.58 Correlation between the experimentally derived overall mass transfer coefficient for salicylic acid tablets and the CFD-predicted average strain rate values on the surfaces of tablets.

In addition to determining the mass transfer coefficients from experimental data, an attempt was also made to predict them using the literature equations listed above (Equations 2.15, 2.17, 2.19, and 2.21), for which the velocity input were obtained through CFD. Figures 4.59 and 4.60 present, respectively, the CFD-predicted flows above the centered tablet and above the 40° off-center tablet. The flows on the top and side surfaces of 10° and 20° off-center tablets are similar to those of 40° off-center tablet (results not shown). Figure 4.59 shows that the centrally located tablet experiences a rotating liquid flow on its top surface, thus partially justifying the use of the rotating disk and rotating cylinder equations for k_{top} and k_{side} (Equations 2.15 and 2.17). Similarly, Figure 4.60 shows that the 40° off-center tablet is exposed to a cross-over flow on its top surface (Figure 4.60a) and around its side (Figure 4.60b), thus partially justifying the use of the

mass transfer equations for flow parallel to a flat plate for the top surface (Equation 2.19), and around a cylinder for its side surface (Equation 2.21). The predictions for the mass transfer coefficients at the top and side surfaces are shown in the second and third column in Table 4.11. These mass transfer coefficients can be used to calculate the area-averaged k value for the entire tablet as follow:

$$\frac{dC_P}{dt} \cong K\frac{A}{V}(C_{Ps}) = \alpha \tag{4.21}$$

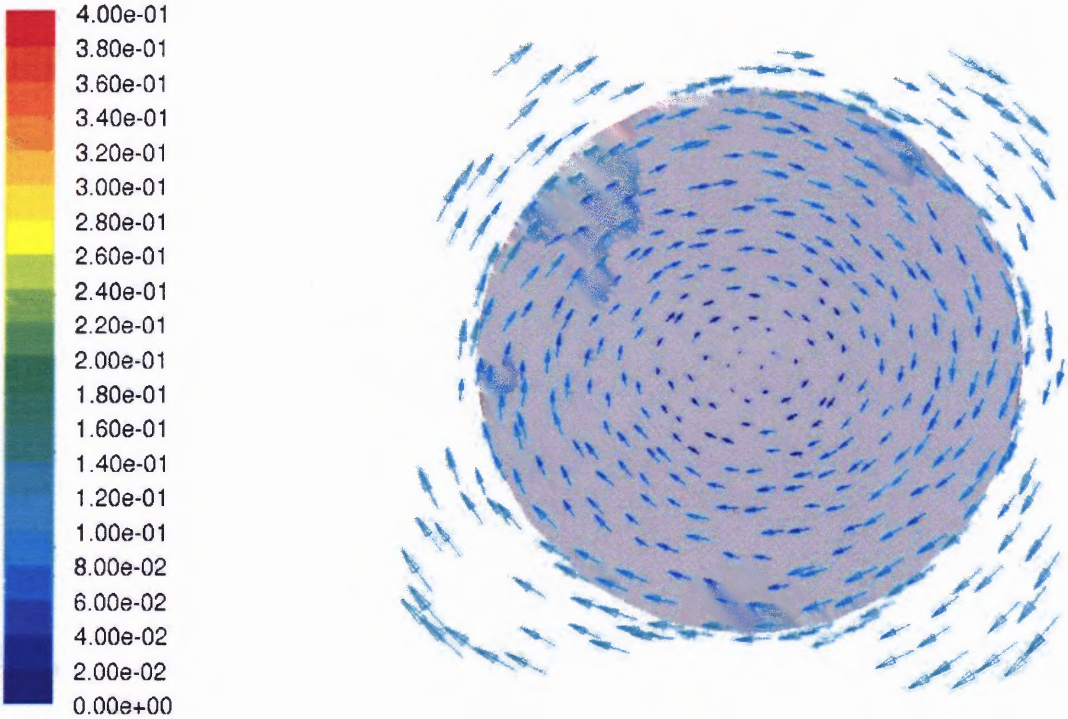

Figure 4.59 CFD-predicted velocity vectors (in m/s) on the top surface of the centrally located salicylic acid tablet.

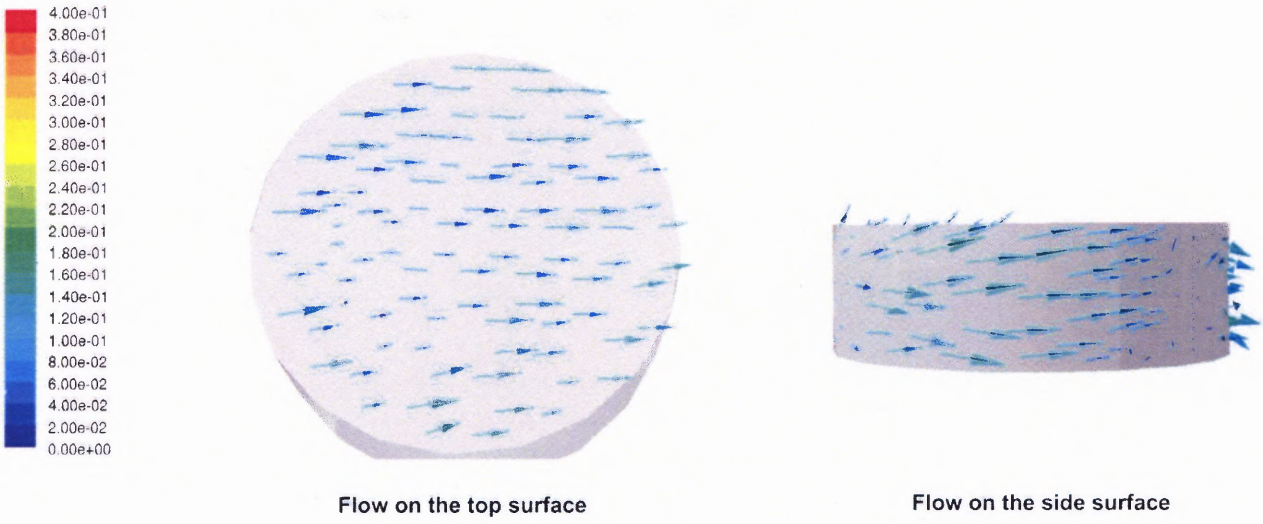

Figure 4.60 CFD-predicted velocity vectors (in m/s) on the top surface and side surface of the 40° off-center salicylic acid tablet.

The last column in Table 4.11 presents these CFD-predicted area-averaged overall k values for different tablet locations. These data show that the predicted mass transfer coefficients for the 10°, 20°, and 40° off-center salicylic acid tablets are about 90%, 126% and 84%, larger, respectively, than the base value for the centrally located tablet.

Table 4.11 Mass Transfer Coefficients for Salicylic Acid Tablets at Different Locations Predicted from CFD Simulations

Tablet Location	Predicted Mass Transfer Coefficient at Top Surface of Tablet, k_{top} (m/s)	Predicted Mass Transfer Coefficient at Side Surface of Tablet, k_{side} (m/s)	Predicted Area-Averaged Mass Transfer Coefficient for Tablet, k_{prd} (m/s)
Centrally located tablet	3.06×10^{-5}	1.31×10^{-5}	2.04×10^{-5}
10° off-center tablet	4.81×10^{-5}	3.21×10^{-5}	3.88×10^{-5}
20° off-center tablet	5.72×10^{-5}	3.83×10^{-5}	4.62×10^{-5}
40° off-center tablet	4.66×10^{-5}	3.11×10^{-5}	3.76×10^{-5}

The predicted mass transfer coefficients in Table 4.11 can be compared with the corresponding mass transfer coefficients derived from the experimental data (Table 4.10). From these tables one can see that k_{prd} is on the same order of magnitude as k_{exp}, and that a proportionality exists between the k_{exp} values obtained for a given tablet location and the corresponding values of k_{prd}.

The results of Tables 4.10 and 4.11 are quantitatively compared in Figure 4.61. Two conclusions emerge. The experimental mass transfer coefficient k_{exp} correlates well with the predicted mass transfer coefficient k_{prd} and the correlation equation is:

$$k_{\exp} = 2.247 \cdot k_{prd} \tag{4.22}$$

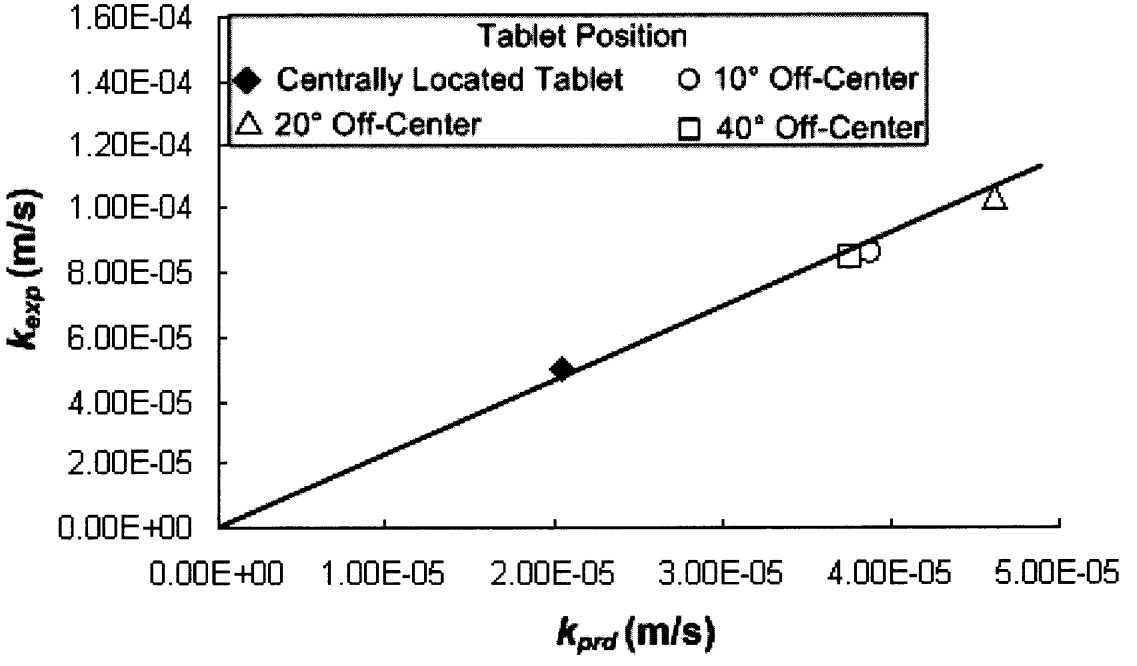

Figure 4.61 Comparison between the mass transfer coefficient experimentally derived from dissolution tests, k_{exp}, and that predicted in this work, k_{prd}.

However, since the proportionality constant is not equal to 1, k_{prd} significantly underpredicts k_{exp}. It should be remarked that equations such as Equations 2.19, and 2.21 have margins of error of ±40% and ±30% respectively. In addition, these equations were originally developed for systems (such as long cylinders rotating in unagitated fluids) that are very different from the system modeled here (such as the side surface of a short tablet in a complex flow field). Therefore, the agreement can be considered satisfactory.

Finally, the values of k_{esp} and k_{prd} obtained for each case and reported in T Tables 4.10 and 4.11 were used to predict the dissolution profiles by inserting them in Equation 2.6 as follows:

$$\frac{dC}{dt} = \frac{k_{\exp} A(C)}{V_L}(C_s - C) \tag{4.23}$$

$$\frac{dC}{dt} = \frac{2.247 \cdot k_{prd} A(C)}{V_L}(C_s - C) \tag{4.24}$$

Since the tablet-medium transfer area $A(C)$ is a function of the drug concentration in the medium C, these equations were numerically integrated using the Runge-Kutta method. The results, shown in Figure 4.62, indicate that the predictions adequately match the experimental data. Since k_{exp} was obtained by regressing the experimental data, the agreement between the data and Equation 4.23 is marginally better than that with Equation 4.24.

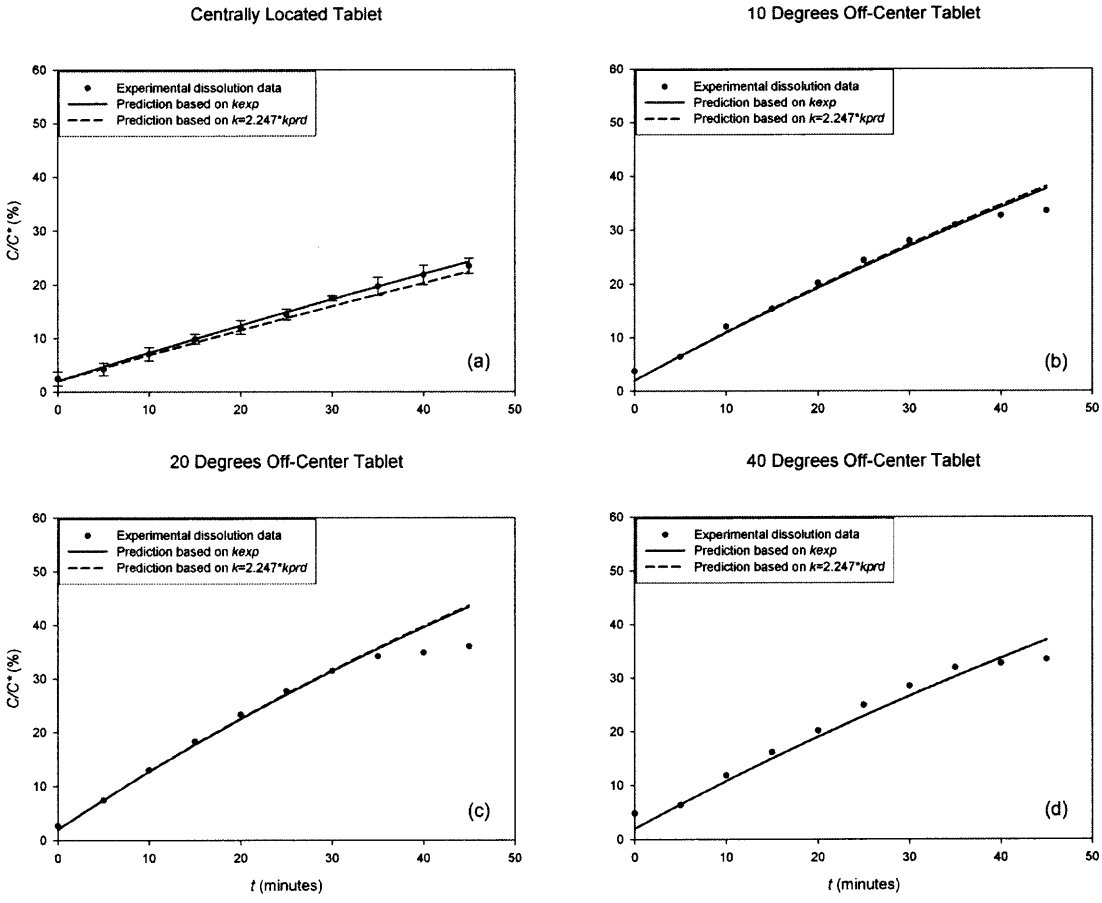

Figure 4.62 Comparison between the experimental dissolution data and the dissolution profiles predicted by numerically integrating Equations 21 and 22.

In conclusion, Equation 4.22 can be used to calculate k_{exp} using the CFD results as input, together with literature equations for k (Equations 2.15, 2.17, 2.19, and 2.21), and Equation 4.21. More significantly, Equations 4.23 and 4.24 can be used to predict the dissolution profiles for any non-disintegrating dissolution system operating at the same agitation system, fill volume, and tablet shape even for drugs other than those used here, since the hydrodynamics of the dissolution system is not a function of tablet composition. In such cases however, the values of k_{exp} and k_{prd} must be scaled using the physical

characteristics of the drug, such as the diffusivity D_{AB}, which appear in the equations for the mass transfer coefficients.

4.7.4 Discussion

Both experimental and theoretical/computational results have been presented here to assess the importance of tablet location during dissolution testing. The experimental dissolution data for both disintegrating and non-disintegrating tablets clearly indicate that the location of the tablet produces statistically different dissolution testing results. This is in good agreement with the previous results of Baxter et al. (2005).

The statistical difference between the results obtained here for different tablet locations can be quantified by examining the value of the difference factor, f_1, which is always outside the range established by FDA for statistical similarity (Table 4.6). The difference factor f_2 calculated for the off-center tablets vs. the centered tablets produces more ambiguous results, since many of the values reported in Table 4.6 for this factor are within the FDA limits (50-100), although always borderline. This apparent conflict between the factors recommended by the FDA is caused by the fact that f_2 is not a very sensitive statistical tool to assess differences among dissolution curves. The contradictory outcome of these two factors has also been reported by other researchers (Baxter et al. 2005, Costa. and Lobo, 2001), who have pointed out that the conflict between the two methods shows that the similarity factor f_2 may not be very robust for its intended task.

While the difference between dissolution curves obtained at different tablet locations may make sense for non-disintegrating, eroding tablets (since the complex hydrodynamics of the Apparatus II can be expected to produce different flows around tablets at different locations), it is more difficult to justify for disintegrating tablets, since the tablet fragments, once the tablet disintegrates, move toward the center of the vessel, thus possibly eliminating any further effect of the initial tablet location on the remaining portion of the dissolution process. The explanation for this apparent contradiction comes from a closer examination of Figure 4.52. This figure shows that at t=0 all curves start at the same point, and that the concentration ratio C/C^* at this time is appreciably high (17.54%). Within 5 minutes, the curves for the off-center tablets diverge from those for the centrally located ones. However, after this time the two sets of curves remain nearly parallel to each other. One can conclude that what happens during the first 5 minutes is critical to promote dissolution and disintegration, and that the remainder of the dissolution process simply add to that initial basis. In fact, it was visually observed that by t=5 minutes the off-center tablets were nearly completely disintegrated, whereas it took about 8 minutes for the centered tablet to do the same. Apparently, the improved hydrodynamics experienced by off-center tablets results in a more rapid dissolution *and* disintegration of the tablet, generating a higher dissolved concentration of the drug during the initial phase of the dissolution process. Once this initial process is complete and the tablet is fully disintegrated, the dissolution process proceeds at a similar rate irrespective of the initial location of the tablet in the vessel.

The process is different for non-disintegrating tablets. Here, since the tablets remain at their initial location during the whole process, the improved hydrodynamics experienced by off-center tablets results in their faster dissolution rate throughout the entire dissolution test. This can be clearly seen in Figure 4.55, where the gap between the curves keeps growing as times goes by (obviously this cannot go on forever, as predicted by Equation 2.6, since eventually all curves must reach the same C/C^* ratio of 1 if $C^*<C_s$). Unlike the disintegrating prednisone tablets, the non-disintegrating salicylic acid tablets are subjected to higher dissolution rates during the entire test, and not only until disintegration occurs.

Although a major difference in dissolution performance can be seen between off-center and centered tablets, not all off-center tablet positions are equal. A small tablet off-center displacement of only 10° is already capable of producing significantly and statistically different dissolution results. One can only speculate on how many dissolution tests routinely fail simply as a result of such small random variations in the tablet resting position after it has been dropped in the vessel. However, greater off-center deviations of the tablet location from the centerline can produce even larger variations in test results. Both Figure 4.52 and Figure 4.55 show that the dissolution curves for tablets 20° off-center deviate the most from the curves for the centered tablets. This is especially significant for the salicylic acid tablets, resulting in deviations in dissolved concentration even higher than 40% when placed 20° off-center. Higher tablet locations in the vessel (e.g., 40° off-center) do not result in greater deviations in the concentration profiles.

The dissolution results nicely match the hydrodynamics in the vessel. Figures 4.53 and 4.55 show that centrally located tablets experience a very weak flow around them, whereas slightly off-center tablets (e.g., 10°) are immersed in much stronger flow. This can only improve the mass transfer rate and the dissolution rate. These figures additionally show that even if the tablet was displaced by an angle smaller than the smallest angle tested here (10°), it would still be likely exposed to a flow significantly different from that of a perfectly centered tablet, and hence produce different dissolution profiles. When the tablet is displaced by 20° off-center the flow that it experiences is stronger than in the other cases as a result of the upswinging recirculation flow in which the tablet is immersed, feeding the impeller from the bottom. This can be clearly seen in Figures 4.53 and 4.55. If the angle displacement is greater, the flow around the tablet is still strong but weaker than at 20°. The contour plots for the strain rate, shown in Figures 4.54 and 4.57, also match the dissolution test results. These figures, as well as Tables 4.7 and 4.8, show that the strain rate around a centered tablet is much weaker than that for off-center tablets, especially at 20°. The increase is especially large for salicylic acid tablets (Table 4.8). The hydrodynamics around the tablet and especially the strain rate experienced by the tablet appear to be the key variables in predicting mass transfer rates. This is evident from correlations, such as that shown in Figure 4.58, and visual representation of the CFD-predicted flow around tablets at different locations, such as those shown in Figures 4.59 and 4.60.

Finally, the approach proposed here to correlate and predict dissolution profiles represents a first attempt to combine the results of actual dissolution data regression (to predict the mass transfer coefficient) with a basic mass transfer model. This approach,

based as it is on the use of k values extracted from experimental data, appears to reproduce well the behavior of system under study and can be simply extrapolated to be employed with other tablet shapes and drugs, provided that the geometric characteristics of the tablet and the physical properties of the drug are known. However, this approach requires that the tablet be always at the same location, which is not the case in the current dissolution testing USP Apparatus II, and appears to be a major drawback of this dissolution system.

A more complex predictive approach based on combining together several standard equations for mass transfer coefficient, the CFD-predicted velocity profiles, and the mass transfer-based mass balance equations, appears to be yield interesting results. The mass transfer coefficients obtained with this model correlate very well with the experimentally derived mass transfer coefficients, but are typically, and consistently, some 50% smaller than the experimental coefficients. It appears that the model still needs to be refined if one expects to fully predict the mass transfer coefficient and hence the dissolution profiles with this approach, especially since the expressions for the mass transfer coefficients obtained from the literature are adaptations from different systems than those examined here. However, when appropriately scale by a constant factor (2.247) even this approach seems to produce results in good agreement with the experimental dissolution data. More accurate mass transfer models must be developed to better estimate the mass transfer coefficients using CFD simulation and accurately predict the dissolution rates of drug tablets entirely from first principles.

4.8 Results and Discussion for Particle Suspension Study

The experimentally determined true density of Avicel PH 102 was found to be 1.38 g/cm^3 whereas the density of "wet" Avicel PH 102 obtained with the experimental method described above was 1.29 g/cm^3. The density of the "wet" resin particles was found to be 1.27 g/cm^3, which is very close to that of the "wet" Avicel PH 102.

Experiments were initially conducted with Avicel PH 102. When 400 mg of Avicel PH 102 were placed in the vessel and the paddle speed was set to 50 rpm, a "cone" of Avicel PH 102 was readily apparent directly under the rotating paddle. The cone was about 15 mm in diameter and 5 to 10 mm in height. When the paddle speed was increased to 75 rpm, the cone partially disappeared. When the agitation speed was increased to 100 rpm, the cone disappears entirely. The process was completely reversible. The cone re-appeared when the paddle speed was subsequently reduced back to 50 rpm.

Thus, at about 100 rpm the axial flow velocities in the cone region are able to overcome Avicel sedimentation. However, a major problem with these particles was that agglomerates could be clearly observed during the experiment. Even impeller rotational speeds as high as 100 rpm did not break the aggregates.

This implies that the corresponding CFD simulation could not be conducted since two parameters for the particles must be known in order to simulate the particle suspension via CFD, i.e., the particle size distribution and the particle density. In this case, although the density of the "wet" Avicel PH 102 particles was obtained experimentally, it could not be used in the simulation since the corresponding density of the agglomerates was unknown. Furthermore, the particle size distribution of the Avicel

PH 102 agglomerates could not be determined. Thus, no CFD simulations were conducted for the Avicel particles.

Resin particles with a size distribution range of 250 microns to 300 microns were then used to conduct particle suspension experiment. When the agitation speed was 50 rpm, the resin particles remained on the vessel bottom. When the impeller rotational speed was increased to 150 rpm the particles became fully suspended. No agglomeration was observed when using resins particles in the suspension experiments.

Since the particle size distribution and the experimentally determined density of the resin were known, the trajectories of the particles in the vessel could be simulated with CFD. In the simulations, 6 particles with a linear size distribution ranging from 250 microns to 300 microns were computationally added to a cell near the liquid surface in the dissolution medium Figure 4.52. The unsteady state FLUENT solver was used with a time step of 0.01 seconds.

Figure 4.63 shows the positions of the particles in Apparatus II at 1 second and at 4 minutes at two agitation speeds, i.e., 50 rpm and 150 rpm, as obtained from the simulations. When the agitation speed was 50 rpm the simulation predicted that all the resin particles would be "settled" by t=4 minutes, i.e., that they would all reside in the same computation cell next to the vessel bottom at that time (Figure 4. 63, upper panels). However, when the agitation speed was increased to 150 rpm the simulations predicted that the particles would remain in suspension even after 4 minutes (Figure 4.; lower panels), as indeed experimentally observed. The good match between the experimental results and the simulation shows that CFD can be used to conduct particle suspension

studies, provided that the physical and geometric characteristics of the particles are known.

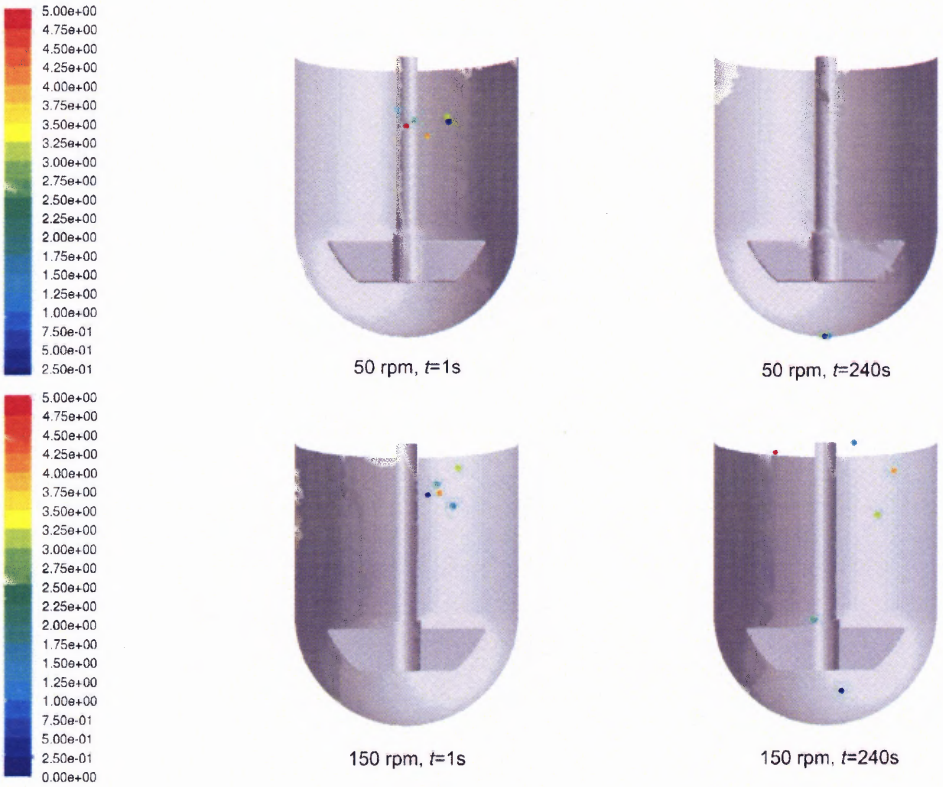

Figure 4.63 CFD predicted movement of resin particles (250-300 microns) with impeller rotation speed of 50 RPM and 150 RPM at 1 second and 240 seconds after being put into the USP Dissolution Apparatus II.

CHAPTER 5

CONCLUSIONS

The approach used in this work to determine the velocity distribution in the vessel was both experimental, through the use of LDV, and computation, through the use of computation fluid dynamics (CFD). This approach was especially valuable to compare the predictions of the velocity distributions against a significant amount of experimental data for the most common impeller configurations and operating conditions. The significant agreement between the results of the two methods was not only important for the validation of the computational approach, but also for a deeper analysis of the performance of the system under those configurations, since it helped to draw additional conclusions about the hydrodynamics of those systems.

The validation of CFD method was also important when other cases were examined, in which the location of the impeller, the agitation speed, or the fill level were changed to determine the sensitivity of the system to critical operating parameters. These cases were examined only computationally. Additionally, CFD was used to obtain other hydrodynamic results such as blend time and power dissipation. When possible these results were compared with experimental data.

Finally, dissolution tests were conducted under different operating conditions to determine the impact of some key variables on the dissolution profiles. The experimental results could be justified on the basis of the hydrodynamics of Apparatus II, and a model was developed that could partially explain such a complex phenomenon.

In the end, a rather complete picture emerges for the analysis of all the data, from which a number of conclusions can be drawn. Some of them are intuitive; other less so. The most important of such conclusions are now presented and briefly discussed.

1. **Influence of turbulence model on CFD results**

   a. Preliminary simulations were conducted with different turbulence models (standard k-ε, realizable k-ε, and k-ω), as well as with no turbulence model (i.e., under laminar conditions). The predictions were compared with LDV data.

   b. The laminar model produced by far the worst predictions, indicating that a turbulence model must be used with CFD to appropriately describe the hydrodynamics of the USP II apparatus when low viscosity aqueous solutions are used.

   c. Predictions based on the k-ω model are superior to the predictions with all other turbulence models tested here.

   d. The k-ω model was used in all the other simulations in this work.

2. **Hydrodynamics of the USP Dissolution Apparatus II under Operating Condition 1**

   a. The LDV measurements and the CFD velocity predictions are, in general, in substantial agreement.

   b. All tangential velocities, irrespective of where in the vessel they are obtained from, are oriented in the same direction as the impeller rotation, indicating a strong tangential flow. The highest tangential velocity is typically between 40% and 50% of the impeller tip speed on all iso-surfaces, both above and below the impeller.

   c. The axial velocities are all significantly smaller than the tangential velocities, with magnitudes typically ranging between 0% and 15% of the tip speed. This implies that top-to-bottom recirculation in the USP II apparatus is weak, as in most unbaffled vessels. The radial velocities are even smaller than the tangential and axial velocities.

   d. The flow in the region below the impeller is complex, and it is strongly dominated by the tangential component while the radial and axial components are very weak. The presence of a vertical recirculation loop having a pulsating component generated by the passing of the impeller blades can be observed. When this pulsating effect decays, the flow is extremely weak.

e. In the region below the impeller, the vertical recirculation loop is not able to penetrate the inner core region located just under the shaft. The flow in this core is nearly quiescent in the vertical plane and is dominated by the tangential velocity. This weakly swirling but otherwise nearly stagnant core region extends all the way from the vessel bottom to the lower edge of the impeller. At its vertical boundaries, the axial velocities change rapidly with time and location, while remaining weak. This can explain the "coning" effect often observed at the center of the vessel bottom.

f. The strain rate is highly not uniform in the region below the impeller. The shear rate is very week below the shaft but increases rapidly to reach a peak value some 15°-20° away from the centerline. The shear rate then declines with distance from the centerline in the outer region on the vessel bottom.

g. The location of the tablet could affect the tablet dissolution rate much because the distribution of strain rate is not uniform along the vessel bottom.

3. **Effect of higher impeller rotation speeds**

a. To a significant extent all velocities scale well with tip speed. The non-dimensional velocity profiles relative to the tip speed are nearly superimposable at most iso-surfaces, irrespective of tip speed. However, the non-dimensional tangential velocity profiles at 100 RPM are typically slightly higher than at 50 and 75 RPM.

b. When the impeller speed is increased from 50 RPM, to 75 RPM, or 100 RPM the nearly quiescent zone below the impeller shaft does not change in size appreciably. However, the magnitude of the velocities surrounding the quiescent zone does increase significantly with agitation speed.

c. Higher impeller rotation speeds doesn't change the fact that the distribution of the strain rate is highly not uniform along the bottom of the vessel.

4. **Effect of lower dissolution medium volume**

a. The non-dimensional velocity profiles are similar in trend, but not identical, to those at the higher dissolution medium volume.

b. The lower dissolution medium volume doesn't change the fact that the distribution of the strain rate is highly not uniform along the bottom of the vessel.

5. **Effect of vertical impeller location**

   a. With 2 mm higher impeller or 2 mm lower impeller, the axial and radial components of the velocity are symmetrically distributed with respect to the vessel centerline and are very weak in the region below the impeller, especially in the region under the shaft.

   b. Change in impeller vertical location does not change the fact that the distribution of the strain rate is highly not uniform along the bottom of the vessel. The shear rate is very week below the shaft but increases rapidly to reach a peak value some 15°-20° away from the centerline. The shear rate then declines with distance from the centerline in the outer region on the vessel bottom.

6. **Effect of impeller off-center location**

   a. When the impeller is placed 2 mm off center the symmetrical structure and the poorly mixed region below the shaft observed in the standard case are largely removed, thus promoting better mixing and recirculation in the lower vessel region where the tablet resides.

   b. Placing the impeller off center even within the limits specified in the USP (2 mm) can have significant effects on the flow field, velocity magnitude, and strain rate near the vessel bottom. This, in turn, is likely to significantly affect the liquid-tablet mass transfer rate and hence the rate of dissolution.

   c. When the impeller is placed 2 mm off center the strain rate distribution is significantly more uniform nearly everywhere along the vessel bottom wall.

   d. Given the extreme sensitivity of the USP Dissolution Apparatus II to loss of symmetry, it is conceivable that smaller off center impeller displacements, such as those introduced by operator's error, equipment wear, and improper impeller misalignment, could also lead to appreciable variations in the fluid flow and strain rate, potentially introducing variability in the test results.

7. **Blend time**

   a. Only non-intrusive methods should be used to experimentally determine blend time is the USP Apparatus II. Intrusive methods, such as conductivity detection using a conductivity probe, can result in the introduction of baffling effects that may alter the results of the experiments. The discoloration method, coupled with calibration with a conductivity method, was found here to be appropriate to generate reproducible results.

b. Under the Operating Condition 1, both experimental results and CFD simulations show that the blend time to achieve a 95% uniformity level was found to be on the order of 30 s. The good agreement between experiment and CFD simulation validates the CFD approach to predict blend time.

c. Changing the locations of the measuring point, injection point of the tracer, and impeller vertical position (±2 mm) had only a limited effect, and did not appreciably change this result.

d. The precise location of the sampling point affects the level of homogeneity achieved at a given time. However, the time required to achieve a significant level of homogenization ($U \approx 95\%$) in most regions of the vessel is still about 30 s, with the possible exception of the core region next to the impeller shaft in the upper portion of the vessel. This implies that the system is relatively insensitive to sampling location and that the time that most regions of the vessel need to achieve similar level of homogeneity is small in comparison to the time scale of the dissolution process.

e. The CFD-predicted results for blend time at different agitation speeds and same geometry fit well the blend time equation typically used for mixing vessels ($N \cdot \theta$=constant), indicating that blend time is inversely proportional to the agitation speed. This equation is useful to estimate the blend time for cases in which the dosage form needs to be tested at agitation speeds lower than the 50 RPM standard value, as when fast dissolving oral dosage forms are tested, or at speeds higher than 50 RPM, as when slow dissolving tablets are tested.

f. The blend times experimentally obtained and computationally predicted in this work appear to be some two orders of magnitude smaller than the time usually required for appreciable tablet dissolution during the typical dissolution test, which is on the order of tens of minutes. Therefore, it can be concluded that the USP Apparatus II is always relatively well mixed, as far as the liquid phase is concerned, if compared to the typical time scale of the dissolution process that this device is supposed to follow during a test. However, if an oral dosage form dissolves at a much higher rate than the typical case, blending and dissolution could have similar time scales, and the location of the sampling point could have an effect on the dissolution curve obtained from collected samples. The approach outlined here and the equations for blend time presented in this work can be used to calculate the relative magnitudes of these time scales, and hence help determine whether blending and the location of the sampling point can affect the results of the dissolution test.

8. **Power dissipation**

   a. Power dissipation was predicted via CFD but could not be measured experimentally because of its extremely small values.

   b. The CFD-based power dissipation values agree to an appreciable extent with the results of correlations from the literature for unbaffled tanks.

9. **Particle suspension**

   a. "Coning" could be observed under Operating Condition 1 when Avicel PH 102 particles were introduced in the USP Dissolution Apparatus II. This phenomenon could be eliminated by increasing the impeller rotation speed (Operating Condition 3).

   b. Ion exchange particles with a size distribution range of 250 microns to 300 microns were additionally used to conduct particle suspension experiment. The particle could be suspended by increasing the agitation speed to 150 rpm.

   c. Particle suspension could be appropriately simulated with CFD as long as the density and size information of the particles were known.

10. **Tablet location effect on dissolution rate**

   a. The exact location of the tablet in the USP Dissolution Testing Apparatus II has a significant impact on the dissolution profile generated during the test. In all cases experimentally tested here with calibrator tablets, displacing and keeping the tablet off-center by 10°, 20°, and 40° resulted in failing the dissolution test, as indicated by the systematic and statistically significant off-specification values of the similarity factor f_1. In the same experiments, the difference factor f_2 was less sensitive to detect difference in dissolution profiles, and its values were either off-specification or borderline.

   b. Test failures occurred with both disintegrating and non-disintegrating tablets, although the reasons for the failures are different. Non-disintegrating tablets fail because the flow field surrounding them is appreciably different from that surrounding centrally placed tablets throughout the entire dissolution process. Disintegrating tablets fail because the initial disintegration and dissolution process during the first few minutes of the test is sufficiently different between off-center and centered tablets to generate different dissolution profiles even though the fragments produced by the tablet migrate towards the vessel center.

c. CFD can be used to predict the flow around tablets. CFD predictions indicated that the flow field and especially the shear rate at the tablet surface are significantly different depending on the location of the tablet. The flow field experienced by centrally located tablets consists of a rotating flow centered on the tablet, as opposed to that for off-center tablets, which is typically dominated by a cross-over flow around the tablet.

d. Tablets that are 20° off-center experience the highest shear rate and the most intense flow around them among all the tablet locations studied here.

e. Tablet-medium mass transfer coefficients can be obtained from the experimental dissolution data for non-disintegrating tablets using a simple mass transfer model to fit the data.

f. The CFD-predicted strain rate values at the tablets correlate well with the experimentally observed dissolution rates and the experimentally derived mass transfer coefficients, confirming that the hydrodynamics of the system, and especially the strain rate at the tablet, are critical to the dissolution process.

g. A model was developed to predict the mass transfer coefficient from first principles, using as input literature equations mass transfer coefficients, CFD-predicted velocity profiles, and mass balance equations. The predicted coefficients correlate well with the experimentally derived mass transfer coefficients, but are typically about 50% smaller.

h. The result of this work clearly indicate that the velocity distribution and strain rates in the bottom region of the USP Apparatus II vessel are intrinsically very non-uniform, and that even small changes in the tablet location, possibly even smaller than the smallest deviation in tablet location examined here (10° off-center), significantly alter the flow around the tablet and hence the dissolution profile. It is possible that some of the variability and test failures historically associated with this testing device can be attributed to the high sensitivity of the dissolution profiles to tablet location.

REFERENCES

Akiti, O. and Armenante, P. M., (2004). Experimentally-Validated Micromixing-Based CFD Model for Fed-Batch Stirred-Tank Reactors. AICHE Journal, 50, 566-577.

Armenante, P. M., Chou, C. C. (1994). Experimental LDV Measurement and Numerical CFD Determination of the Fluid Velocity Distribution in an Unbaffled Mixing Vessel. AIChE Symp. Ser., 90, 33-40.

Armenante, P. M., Chou, C., Hemrajani, R. R., (1994). Comparison of Experimental and Numerical Fluid Velocity Distribution Profiles in an Unbaffled Mixing Vessel Provided with a Pitched-Blade Turbine. IChemE Symp. Ser., 136, 349-356.

Armenante, P. M., Luo, C., Chou, C. C., Fort, I. and Medek, J. (1997). Velocity Profiles in a Closed, Unbaffled Vessel: Comparison between Experimental LDV Data and Numerical CFD Predictions. Chemical Engineering Science, 52, 3483-3492.

Armenante., P.M., Kirwan, D. J., (1989). Mass transfer to microparticles in agitated systems. Chemical Engineering Science, 44(12), 2781-2796.

Bai, G., Armenante, P. M., Plank, R. V., Gentzler, M., Ford, K. and Harmon, P., (2006). Hydrodynamics Investigation of USP Dissolution Apparatus II. Journal of Pharmaceutical Science, In Press.

Batchelor, G. K., (1967). An Introduction to Fluid Dynamics. Cambridge University Press, Cambridge, England.

Baxter, J. L., Kukura, J., Muzzio, F. J., (2005). Hydrodynamics-induced Variability in the USP Apparatus II Dissolution Test. International Journal of Pharmaceutics, 292, 17-28.

Bird, R. B., Stewart, E.W., Lightfoot N.E., (2002). Transport Phenomena. John Wiley & Sons, Inc., New York.

Bocanegra, L. M., Morris, G. J., Jurewicz, J. T., Mauger, J. W., (1990). Fluid and Particle Laser Doppler Velocity Measurements and Mass Transfer Predictions for USP Paddle Method Dissolution Apparatus. Drug Development and Industrial Pharmacy, 16, 1441-1464.

Brown, A.R.D., Jones, N. P., Middleton, C. J., Papadopoulos, G., Arik, B. Engin, (2004). Experimental Methods, Chapter 4 of Handbook of Industrial Mixing, edited by by Paul, L. E., Atiemo-Obeng, A. V., Kresta M. S., Jonh Wiley & Sons, Inc., Hoboken, New Jersey.

Campolo, M. and Soldati, A., (2004). Numerical evaluation of blend time in a tank reactor stirred by a magnetically driven impeller. Industrial and Engineering Chemistry Research, 43 (21), 6836-6846.

Choudhury, D. (1993). Introduction to the Renormalization Group Method and Turbulence Modeling. FLUENT Inc. Technical Memorandum TM-107.

Ciofalo, M., Brucato, A., Grisafi, F., and Torraca, N. (1996). Turbulent Flow in Closed and Free-Surface Unbaffled Tanks Stirred by Radial Impellers. Chem. Eng. Sci., 51, 3557-3573.

Cohen, J. L., Hubert, B. B., Leeson, L. J., Rhodes, C. T., Robinson, J. R., Roseman, T. J., Shefter, E., (1990). The Development of USP Dissolution and Drug Release Standards, Pharmaceutical Research, 7, 983-987.

Costa, P., Lobo, J. M. S., (2001). Influence of Dissolution Medium Agitation on Release Profiles of Sustained-Release Tablets. Drug Development and Industrial Pharmacy, 27, 811-817.

Cox, D.C., Furman, W.B., (1982). Systematic Error Associated With Apparatus 2 of the USP Dissolution Test I: Effects of Physical Alignment of the Dissolution Apparatus. Journal of Pharmaceutical Sciences, 71, 451-452.

Coy, D., (1996). Computer simulation helps design laboratory equipment that accurately models production plant. Simulation, 67(3), 206-208.

Cox, D.C., Furman, W.B., Thornton, L.K., (1983). Systematic Error Associated With Apparatus 2 of the USP Dissolution Test III: Limitation of Calibrators and the USP Suitability Test. Journal of Pharmaceutical Sciences, 72, 910-913.

Division of Drug Analysis, Food and Drug Administration, (1995). Dissolution Test Performance Standard #2.

Dong, L., Johansen, S. T. and Engh, T. A. (1994a). Flow Induced by an Impeller in an Unbaffled Tank-I, Experimental. Chemical Engineering Science, 49, 549-560.

Dong, L., Johansen, S. T. and Engh, T. A., (1994b). Flow Induced by an Impeller in an Unbaffled Tank-II, Numerical Modeling. Chemical Engineering Science, 49, 3511-3518.

FDC Reports, (2001). Recalls Prompted By FDA on the Increase. The Gold Sheet 35, 1.

FDC Reports, (2002). Counterfeits Pose Special Recall Challenge. The Gold Sheet 36, 1.

FDC Reports, (2003). Spike in Potency-Related Problems Contributes to Overall Rise in 2002 Recalls. The Gold Sheet 37, 1.

FLUENT 6.2 User's Guide (2005), FLUENT, Inc., New Hampshire

GAMBIT 2.2 User's Guide (2005), FLUENT, Inc., New Hampshire

Geankoplis, J. C., (2003). Transport Processes And Seperation Process Principles. Prentice Hall, Upper Saddle River, New Jersey.

Grenville, K. R., Nienow, W. A., (2004). Blending of Miscible Liquids. Chapter 9 of Handbook of Industrial Mixing, edited by Paul, L. E., Atiemo-Obeng, A. V., Kresta M. S., Jonh Wiley & Sons, Inc., Hoboken, New Jersey.

Grenville, R. K., (1992). Mixinging of viscous Newtonian and pseudo-plastic fluids. Ph.D. dissertation, Cranfield Institute of Technology, Cranfield, Bedfordshire, England.

Guidance for Industry - Dissolution Testing of Immediate Release Solid Oral Dosage Forms, Food and Drug Administration, 1997.

Hanjalic, K., Nagano, Y., Tummers, M. (2003). Turbulence, Heat and Mass Transfer 4. Begell House Inc., Redding, Connecticut, pp. 625-632.

Harvey III, A. D., Rogers, S. E., (1996). Steady and unsteady computation of impeller-stirred reactors. AIChE Journal, 42(10), 2701-2711.

Hass, V. C., Nienow, A. W., (1989). A new axial pumping agitator for the dispersion of gas in liquids. Chem Ing Technik, 61, 152-154 (in German).

Jaworski, Z. and Dudczak, J., (1998). CFD Modelling of Turbulent Macromixing in Stirred Tanks: Effect of the Probe Size and Number on Mixing Indices. Computers and Chemical Engineering, 22, Supplement, S293-S298.

Kresta, M. S., Mao, D. and Roussinova, V., (2006). Batch blend time in square stirred tanks. Chemical Engineering Science, 61, 2823-2825.

Kukura, J., Arratia, P. C., Szalai, E. S., Muzzio, F. J., (2003). Engineering Tools for Understanding Hydrodynamics of Dissolution Tests. Drug Development and Industrial Pharmacy, 29, 231-239.

Kukura, J., Baxter, J. L., Muzzio, F. J., (2004). Shear distribution and variability in the USP Apparatus 2 under turbulent conditions. International Journal of Pharmaceutics, 279, 9-17

Labraga, L., Berkah, T., (2004) Mass transfer from a rotating cylinder with and without crossflow. International Journal of Heat & Mass Transfer 47, 2493–2499.

Launder, B. E., Spalding, D. B., (1972). Lectures in Mathematical Models of Turbulence. Academic Press, London, England.

Levins, D.M., Glastonbury, J.R., (1972). Application of kolmogoroff's theory to Particle-liquid mass transfer in agitated vessels. Chemical Engineering Science, 27 (3), 537-543.

Manna, L., (1997). Comparison between physical and chemical methods for the measurements of mixing times. Chemical Engineering Journal, 67, 167-173.

Mauger, J.W., Brockson, R., De, S., Gray, V.A., Robinson, D., (2003). Intrinsic Dissolution Performance of USP Apparatus 2 Using Modified Salicylic Acid Calibrator Tablets: Proof of Principle. Dissolution Technologies, 10, 6-15

McCarthy, L., Bradley, G., Sexton, J., Corrigan, O., Healy, A. M. (2004). Computational Fluid Dynamics Modeling of the Paddle Dissolution Apparatus: Agitation Rate, Mixing Patterns, and Fluid Velocities. AAPS AAPS PharmSciTech, 5 (2), Article 31.

McCarthy, L., Kosiol, C., Healy, A. M., Bradley, G., Sexton, J., Corrigan, O. (2003). Simulating the Hydrodynamic Conditions in the United States Pharmacopeias Paddle Dissolution Apparatus. AAPS PharmSciTech, 4 (2), Article 22.

Moore, J.W., Flanner, H.H., (1996). Mathematical Comparison of Dissolution Profiles. Pharmaceutical Technology, 20, 64-74

Moore, T.W., Hamilton, J.F.,Kerner, C.M., (1995). Dissolution Testing: Limitations of the USP Prednisone and Salicylic Acid Calibrator Tablets. Pharmacopeial Forum, 21, 1387-1396.

Murthy Shekhar, S., Jayanti, S. (2002). CFD Study of Power and Mixing Time for Paddle Mixing in Unbaffled Vessels. Chemical Engineering Research and Design, 80(5), 482-498.

Myers, K. J., Reeder, M. F., Fasano, J. B., (2002). Optimize mixing by using the proper baffles. Chemical Engineering Progress, 98(2) 42-47.

Nagata, S., (1975). Mixing Principles and Applications. Kodansha Ltd., Tokyo.

Nere, N. K., Patwardhan, A. W. and Joshi, J. B., (2003). Liquid-phase mixing in stirred vessels: Turbulent flow regime, Industrial and Engineering Chemistry Research, 42 (12), 2661-2698.

Nienow, W. A., (1997). On impeller circulation and mixing effectiveness in the turbulent flow regime. Chemical Engineering Science, 52 (15), 2557-2565.

Nishkawa, M., Ashiwake, K., Hashimoto, N. and Nagata, S., (1979). Agitation Power and Blend time in Off-centering Mixing. International Chemical Engineering, 19 (1), 13-159.

Qureshi, A. A., (1996). Calibration – The USP Dissolution Apparatus Suitability Test. Drug Information Journal, 30 (4), 1055-1061.

Qureshi, S. A., McGilveray, I. J., (1999). Typical Variability in Drug Dissolution Testing: Study with USP and FDA Calibrator Tablets and a Marketed Drug (Glibenclamide) Product. European Journal of Pharmaceutical Sciences, 7, 249-258

Qureshi, S.A.. Shabnam, J., (2001). Cause of high variability in drug dissolution testing and its impact on setting tolerances. European Journal of Pharmaceutical Science, 12, 271–276

Reynolds, W.C. (1987). Fundamentals of turbulence for turbulence modeling and simulation. Lecture Notes for Von Karman Institute, Agard Report No. 755.

Schafer, M., Hofken, M., Durst, F. (1997). Detailed LDV Measurements for Visualization of the Flow Field within a Stirred-tank Reactor Equipped with a Rushton Turbine, Chemical Engineering Research and Design, 75 (8), 729-736.

Shih, T.H., Liou, W.W., Shabbir, A., Yang, Z., Zhu, J. (1995). A New k-ϵ Eddy-Viscosity Model for High Reynolds Number Turbulent Flows - Model Development and Validation. Comuter Fluids, 24(3), 227-238.

The United States Pharmacopeia & The National Formulary. The Official Compendia of Standards, USP 29–NF 24 (2005). Pharmacopial Convention Inc., November 2005.

Uehara-Nagamine, E., (2001). Modeling and Experimental Validation of a Single-Feed Semi-Batch Precipitation Process. Ph.D. Dissertation. New Jersey Institute of Technology.

USP Certificate, USP Salicylic Acid Tablets RS, Lot Q0D200, United States Pharmacopeia, 2006

Wilcox, D.C., (1993). Turbulence Modeling for CFD, DCW Industries. Inc., La Canada, California.

Yeoh, S. L., Papadakis, G., Yianneskis, M., (2005). Determination of Mixing Time and Degree of Homogeneity in Stirred Vessels With Large Eddy Simulation. Chemical Engineering Science, 60, 2293-2302.

Zhang, Z. and Kleinstreuer C., (2003). Low-Reynolds-Number Turbulent Flows in Locally Constricted Conduits: A Comparison Study. AIAA Journal, 41 (5), 831-840.

Zhang, Z., Kleinstreuer, C. (2003). Low-Reynolds-Number Turbulent Flows in Locally Constricted Conduits: A Comparison Study. AAIA Journal, 41(5), 831-840.

Zhou, G., Shi, L. and Yu, P., (2003). CFD Study of mixing Process in Rushton Turbine Stirred Tanks. Third International Conference on CFD in the Minerals and Process Industries, CSIRO, Melbourne, Australia, Dec. 10-12.